PROCESSING OF ECHOCARDIOGRAPHIC IMAGES WITH REFERENCE TO MITRAL REGURGITATION

Ph.D. THESIS

by

KALPANA SAINI

DEPARTMENT OF ELECTRICAL ENGINEERING
INDIAN INSTITUTE OF TECHNOLOGY ROORKEE
ROORKEE - 247 667 (INDIA)

JUNE, 2013

PROCESSING OF ECHOCARDIOGRAPHIC IMAGES WITH REFERENCE TO MITRAL REGURGITATION

A THESIS

Submitted in partial fulfilment of the

requirements for the award of the degree

of

DOCTOR OF PHILOSOPHY

in

ELECTRICAL ENGINEERING

by

KALPANA SAINI

DEPARTMENT OF ELECTRICAL ENGINEERING
INDIAN INSTITUTE OF TECHNOLOGY ROORKEE
ROORKEE - 247 667 (INDIA)

JUNE, 2013

INDIAN INSTITUTE OF TECHNOLOGY ROORKEE
ROORKEE

CANDIDATE'S DECLARATION

I hereby certify that the work which is being presented in the thesis entitled **"PROCESSING OF ECHOCARDIOGRAPHIC IMAGES WITH REFERENCE TO MITRAL REGURGITATION"** in partial fulfilment of the requirement for the award of the Degree of Doctor of Philosophy and submitted in the Department of Electrical Engineering of the Indian Institute of Technology Roorkee, Roorkee is an authentic record of my own work carried out during a period from August, 2009 to June, 2013 under the supervision of Dr. M. L. Dewal, Assistant Professor, Department of Electrical Engineering, Indian Institute of Technology Roorkee, Roorkee, India and Dr. Manojkumar Rohit, Additional Professor, Advanced Cardiac Center, Post Graduate Institute of Medical Education and Research, Chandigarh, India.

The matter presented in this thesis has not been submitted by me for the award of any other degree of this or any other Institute.

(KALPANA SAINI)

This is to certify that the above statement made by the candidate is correct to the best of our knowledge.

(Manojkumar Rohit)
Supervisor

(M. L. Dewal)
Supervisor

Date:

The Ph.D. Viva - Voce Examination of **Ms. KALPANA SAINI**, Research Scholar, has been held on …….

Signature of Supervisor (s) Chairman, SRC Signature of External Examiner

Head of the Department/Chairman, ODC

ACKNOWLEDGEMENTS

At this momentous occasion of completing my research I would like to acknowledge the contribution of all those benevolent people, I have been blessed to associate with. All the data collection, theories, models would have failed to serve their purpose for me if blessings of God would not have joined hands with my efforts.

I would like to express my sincere gratitude to those who helped me throughout the years at IIT Roorkee. First of all, I would like to thank my thesis supervisors, Dr. M. L. Dewal and Dr. Manojkumar Rohit, for their advice, support and encouragement. I have been impressed by their enthusiasm, the breadth of their knowledge, and their deep in sight. In regular meetings, they have not only shown me the big picture but also challenged me with critical questions, which often transformed my half-baked ideas into gems. I am also grateful to Dr. M. L. Dewal for his favor of reviewing each research paper and chapters of my thesis even over weekends, tremendously increasing the clarity of my work. The completion of my Ph.D. research reflects the importance of a close cooperation between engineers and clinicians, which has been the key for the success. At the early stage of the thesis, I was very much preoccupied by all sorts of technical problems without knowing the practical situation in clinics. Dr. Manojkumar Rohit, with his years of experience in clinical research, dragged me out of my pure technical thinking and helped me to find a practical way of meeting clinical requirements.

I would like to thank the Ministry of Human Recourse and Development, Govt. of India (MHRD) for the financial support and the Head of the Department of Electrical Engineering IIT Roorkee for his support and for providing the facilities for the completion of my Ph.D. research work.

Finally I would like to thank my husband, Mr. Rajeev Kumar for his enormous patience in my frustrations and long working days, and for his impatience that pushes me through, for his kindness, and for being who he is.

I would also like to thank my parents who have always loved and supported me. Without my parent's support it is not possible to achieve this goal. They always taught me many essential values in life, such as positivity, stability, lovability, loyalty, self respect and independence. A

great thanks for their everlasting support and understanding. The Successful completion of my thesis is a reward for them.

My special thanks go to my elder sister Mrs. Anju Saini who supports and guides me to do work with positive thinking. After marriage my in- law's support was very positive for my thesis. Their encouragement pushes me to do my thesis work within time.

(Kalpana Saini)

ABSTRACT

The present thesis deals with the research work carried out for the automatic severity evaluation of the mitral regurgitation (MR). MR is a common heart valve disorder. In present days, the clinicians carry out this task by extracting the regurgitant jet area from the echocardiographic images, manually. Since, the echocardiographic images primarily suffer from the multiplicative speckle noise, efforts have been made to clean the echocardiographic images to enable clinicians to obtain higher MR assessment accuracies. Here after, in the thesis, only the word images shall be used to refer to the echocardiographic images. Digital image processing has been done in the MATLAB environment.

To facilitate the manual analysis of the MR images by the clinicians the research efforts have been worked out to provide clinicians with the much better contrasted enhanced and almost completely de-speckled images with the view to improve accuracy of his assessment because of the improved visual enhancement. The contrast enhancement has been achieved using the proposed modified log transformation technique and the images has been de-speckled using the newly developed two techniques; the Hybrid Speckle Reducing Anisotropic Diffusion (HSRAD) filter and the Modified Non-linear Complex Diffusion (MNCD) filter for cleaning the images of the multiplicative speckle noises.

For the contrast enhancement the log transformation has been modified to give better contrast enhanced images than the one which are obtainable using conventional log transformation. Results demonstrate that the proposed modified version of log transformation gives better image enhancement one obtainable using conventional log transformation technique. The results are better balanced contrasted images bearing much higher quality indices proving to be more useful for manual processing in assessing the MR severity.

For de-speckling the two newly developed algorithms have been proposed which produce much better results when compared with the results obtainable using existing filters which are also employed on echocardiographic images besides other types of images. These two new filters allow clinicians to carry out flawless diagnosis.

One of the proposed de-speckling filters is a hybrid filter, namely HSRAD filter is a combination of speckle reducing anisotropic diffusion (SRAD) filter and the relaxed median filter.

Experiments are carried out on a number of images. Results show significant reduction in speckle noise while retaining the edges at the same time. The proposed filter removes speckle noise as well as the impulse noise and enhances the edges. The second proposed de-speckling filter MNCD filter is developed to remove speckle noise more effectively from the images and provides much better enhancement even of the finer details of the image. The performance of the MNCD filter has been found to be much better than the existing de-speckling filters with particular reference to echocardiographic images. The results are compared with the results of the other existing filters.

The clinicians' assessment of MR, carried out manually, is thus, taken as the ground truth to compare with the results obtained from the following designed and developments of algorithms for 'Automatic MR Severity Evaluation' techniques.

The thesis presents the three novel approaches for automatic MR severity grade evaluation. The first approach is the boundary detection of heart's chambers. Two new algorithms viz. the Fast Region Based Active Contour Model (FRACM) and the New Selective Binary and Gaussian Filtering Regularized Level Set (NSBGFRLS) model have been proposed for the purpose of above stated boundary detection.

The second approach is the detection of MR jet area which employs the two newly proposed techniques; A Region Growing based Mosaic Jet Segmentation (RG-MJS) and the Combined Wavelet and Watershed Transformation based Mosaic Jet Segmentation (CWW-MJS), for carrying out automatically the MR mosaic jet segmentation and evaluation of its area.

The third approach has been the Vena Contracta Width (VCW) detection. A technique which automatically finds out the location of VC and calculates the VCW has been developed and proposed. The results evaluated automatically using the proposed technique and assessed manually by the clinicians are compared. The comparison corroborates results within very close limits.

In case of significant MR, left ventricle has to accommodate both the stroke volume and regurgitant volume with each heart beat so it leads to volume overload of the left ventricle. The left ventricle dilates and becomes hyper-dynamic for compensation. The left atrial and pulmonary venous pressures increase sharply in case of acute severe MR, leading to pulmonary congestion and pulmonary edema. A gradual increase in left atrial size and compliance compensates in chronic MR, so that left atrial and pulmonary venous pressures do not increase until late in the course of the disease. An increase in after load, contractile dysfunction, and heart failure occur in case of progressive left ventricular dilation. This entails the detection of boundaries of heart's chambers, for which two new models, viz. the Fast Region Active Contour Model (FRACM) and

the Novel Selective Binary Selective Regularized Level Set (NSBGFRLS) have been developed and presented in the thesis. The proposed models the FRACM and the NSBGFRLS are the much faster algorithms than the existing algorithms to detect the boundaries of the heart chambers.

The performance of these two boundary detection models has been experimented and the results are tabulated, plotted and compared with the performance of other existing models which are also employed for boundary detection of echocardiographic images. The performance of the models has been found to be much superior to other existing models.

The second approach to detect the severity grades of MR is to evaluate the value of the MR jet area. The objective is to segment out the color mosaic pattern from the color Doppler image. At present the clinicians draw this area and assess the value of the regurgitation jet area manually. If this area is found out automatically then it will save a lot of time of the clinicians and allow higher measurement accuracies.

The two novel methods, RG-MJS and CWW-MJS have been proposed for the automatic evaluation of the mosaic MR jet area. The methods have been applied on some ten patients who were suffering from varied grades of MR severity from mild to severe. The RG-MJS method is recommended for those patients who are suffering from moderate or severe MR. Whereas the method CWW-MJS is recommended for all the patients who may be suffering from MR of any one of the three severity grades viz. mild, moderate and sever. The results of experiments have been compared with the results of manual assessment of MR assessed by the clinicians as the ground truth.

The third approach to detect the severity grading of MR is to calculate the vena contracta width (VCW) of the MR jet. The narrowest part of the jet that appears just downstream from the orifice is referred to as the vena contracta. High velocity and laminar flow are the characteristics of the vena contracta. A mathematical expression has also been proposed for the calculation of VCW. The VCW is smaller than the anatomic regurgitant orifice to some extent due to boundary effects. It is difficult to locate this narrowest part exactly in TTE or TEE images. It entails to develop a method which should process the MR images to locate and find out the numerical value of VCW. A simpler method than the complexity of the mathematical derivation has been developed and proposed for getting the numerical value of the vena contracta width. The proposed method also automatically finds out the location of the VCW for which it does not require zooming out of the vena contracta width portion of the MR jet images.

Clinical values have been taken as ground truth for the jet area and vena contracta width comparisons. MR severity comparison has been done between clinical values and values obtained from proposed methods. Results are very much in agreement and within very close limits.

The results of experiments are very encouraging and the proposed developments find clinical applications. To demonstrate application a Graphical User Interface (GUI) which is supported by all the existing and the proposed algorithms has been designed. With the help of the proposed GUI the clinicians or any other user will be able to process images just by selecting the name of the method from the GUI panel; without going in to complexity of the mathematical treatment of the techniques. The GUI facilitates processing of images, provides comparison between different methods, and also displays the measured values of MR jet area and VCW in terms of numerical digits.

TABLE OF CONTENTS

LIST OF FIGURES

LIST OF TABLES

LIST OF ABBREVATIONS AND ACRONYMS

2-D	Two Dimensional
3-D	Three Dimensional
ad	Perona and Malik Anisotropic Diffusion Filter
adsr	Speckle Reducing Anisotropic Diffusion Filter
AV	Atioventricular Valve
CAD	Coronary Artery Disease
CV	Chan-Vese
CW	Continuous Wave
CWWT-MJS	Combined Wavelet and Watershed Transformation based Mosaic Jet
ECG	Electrocardiogram
EF	Ejection Fraction
EM	Expectation Maximization
EROA	Effective Regurgitation Orifice Area
ESF	Edge Stopping Function
FA	Feature Asymmetry
fdf	Frequency Domain De-Speckle Filter
FFT	Fast Fourier Transform
FRACM	Fast Region Based Active Contour Model
FSI	Fast Sprash Surface Interpolation
GAC	Geodesic Active Contour
GACV	Geodesic Aided Chan-Vese

gf4d	Geometric De-Speckle Filter
gfminmax	Geometric De-Speckle Filter Utilising Minimum Maximum Values
GVF	Gradient Vector Flow
homo	Homomorphic De-Speckle Filter
homog	Most Homogeneous Neighborhood De-Speckle Filter
HSRAD	Hybrid Speckle Removing Anisotropic Diffusion
ICE	Intra-Cardiac Echocardiography
IVC	Inferior Vena Cava
KL	Kullback Leibler
LA	Left Atrium
lecasort	Linear Scaling and Sorting De-Speckle Filter
lemva	Mean and Variance Local Statistics De-Speckle Filter
LPND	Laplacian Pyramid Bade Nonlinear Diffusion
ls	Linear Scaling of the Gray Level Values De-Speckle Filter
lslog	Linear Scaling of Gray Values Logarithmic De-Speckle Filter
lsmedc	Diffusion Exponential Damp Kernel De-Speckle Filter
lsmedcd	Lee Diffusion De-Speckle Filter
lsminsc	Minimum Speckle Index Homogeneous Mask De-Speckle Filter
lsminv1d	Minimum Variance Homogeneous 1-D Mask De-Speckle Filter
lsmv	Mean and Variance Local Statistics De-Speckle Filter
lsmv_lee	Lee Local Statistics De-Speckle Filter
lsmvsk2d	Mean Variance, Higher Moments Local Statistics De-Speckle Filter
lsmvske1d	Mean, Variance, Skewness, Kurtosis 1-D Local Statistics De-Speckle Filter
LV	Left Ventricle

MAE	Mean Absolute Error
MAP	Maximum A Posterior
median	Median De-Speckle Filter
MI	Mitral Infarction
ML	Maximum Likelihood
MMSE	Minimum Mean Square Error
MNCDF	Modified Nonlinear Complex Diffusion Filter
MR	Mitral Regurgitation
MS	Mitral Stenosis
MSE	Mean Square Error
MV	Mitral Valve
MVP	Mitral Valve Prolapses
NCD	Nonlinear Coherent Difference
NCDF	Nonlinear Complex Diffusion Filter
nldif	Non Linear Coherent Diffusion De-Speckle Filter
NN	Neural Networks
NSBGFRLS	New Selective Binary and Gaussian Filtering Regularized Level Set
PDE	Partial Differential Equation
PRF	Pulse Repetition Frequency
PSNR	Peak Signal to Noise Ratio
PV	Pulmonary Valve
PW	Pulse Wave
Q_i	Quality Index
RA	Right Atrium

RF	Radio Frequency
RG-MJS	Region Growing based Mosaic Jet Segmentation
RHD	Rheumatic Heart Disease
RMSE	Root Mean Square Error
ROI	Region of Interest
RV	Right Ventricle
R_{vol}	Regurgitation Volume
SAR	Synthetic Aperture Radar
SBGFRLS	Selective Binary and Gaussian Filtering Regularized Level Set
SNR	Signal to Noise Ratio
SPF	Singed Pressure Force Function
SRAD	Speckle Reduction Anisotropic Diffusion
SRG	Seeded Region Growing
SV	Semiluner Valve
SVC	Superior Vena Cava
TEE	Trans-Esophageal Echocardiography
TTE	Trans-Thoracic Echocardiography
TV	Tricuspid Valve
VCW	Vena Contracta Width
VF	Ventricular Fibrillation
waveltc	Wavelet De-Speckle Filter
wiener	Wiener De-Speckle Filter

LIST OF SYMBOLS

F_d	The Doppler Frequency
f_o	The Original Frequency
V	The Blood Flow Velocity
c	The Velocity of Light
θ	The Transducer Angle
s	The Value of Pixels after Processing
r	The Value of Pixels Before Processing
c	A Constant in Log Transformation
a	A Variable under user Control
$C_{Orignal}$	The Contrast of the Original Image
$C_{\mathrm{Pr}ocessed}$	The Contrast of Image after Applying the Contrast Enhancement Technique
C_{II}	Contrast Improvement Index
$mean(P_f)$	The Mean of Foreground Pixels
$mean(P_b)$	The Mean of Background Pixels
$z_{i,j}$	The Noisy Pixel in the Middle of the Moving Window
$x_{i,j}$	The Noise-Free Pixel
$n_{i,j}$	The Multiplicative and Additive Noise
$a_{i,j}$	The Additive Noise (Independent of $z_{i,j}$, with Mean 0)
i, j	The Indices of the Spatial Locations that Belong in the 2D Space if Real Numbers, $i, j \in R^2$
μ	Mean
σ	Standard Deviation
σ^2	Variance

μ/σ	Rayleigh Distribution
σ_n^2	Noise Variance
σ_p^2	The Variance of the Noise in the Selected Windows
$\bar{g}_p$	The Mean of the Noise in the Selected Windows
p	The Index Covering all Windows in the Whole Image
$f_{i,j}$	Noise Free Pixel after Logarithmic Compression
$nl_{i,j}$	Noise Free Component after Logarithmic Compression
f_i	The Mean Gray Level Value of the Original Image
g_i	The Gray Level Value of the Pixels of Noise-Removed Image
N	The Total Number of Pixels in the Image
e_i	The Error Between Input and Output Signal
$I_0(x,y)$	Intensity Image Having Finite Power
$I(x,y;t)$	The Output Image
Ω	The Bounded and Open Subset of R^2
$\partial\Omega$	The Border of Ω
$\vec{n}$	The Outer Normal to the $\partial\Omega$
$c(q)$	The Diffusion Coefficient
$q(x,y;t)$	The Instantaneous Coefficient of Variation
$q_0(t)$	The Speckle Scale Function
$\mathrm{var}[z(t)]$	The Intensity Variance over a Homogeneous Area at t
$\overline{z(t)}$	The Intensity Mean over a Homogeneous Area at t
ρ	A Constant in the Determination of $q_0(t)$
$\dot{q}_0(t)$	The First Derivative of $q_0(t)$ with Respect to t

$\{X_i\}$	A $m-$Dimensional Sequence, Where the Index $i \in Z^m$
$W \subset Z^m$	A Sliding Window is Defined as a Subset
W	Sliding Window
$med\{.\}$	The Median Operator
l	Lower Bound
u	Upper Bound
Δt	Time Space Step Size
$\mathrm{Im}(I)$	The Imaginary Part of the Image
$d(\mathrm{Im}(I))$	The Coefficient of Diffusion for Nonlinear Complex Diffusion Filter
k	The Threshold Parameter
$\theta \in (-\pi/2; \pi/2)$	A Phase Angle Close to Zero
∇_s	The Discrete Gradient Operator
Δ_s	The Laplacian Operator
t_i	The i^{th} Element from the time Population
u_0	An Image, Considered here aReal-Valued Bounded Function Defined on $\overline{\Omega}$, in Case of Boundary Detection
$\omega \subset \Omega$	An Open Subset
φ	Lipschitz Function
$\mu \geq 0, \nu \geq 0, \lambda_1, \lambda_2 > 0$	Fixed Parameters
$X(s) = (X(s), Y(s)), s \in [0,1]$	A Curve Which Moves Though the Spatial Domain of an Image to Minimize Energy Functional
E_{int}	The Internal Energy of Snake
E_{ext}	The External Energy of Snake
$\frac{\partial}{\partial S}\left(\alpha \frac{\partial X}{\partial S}\right)$	The Elastic Energy of Curve

$\frac{\partial^2}{\partial S^2}\left(\beta\frac{\partial^2 X}{\partial S^2}\right)$	The Bending Energy of Curve
$\nabla P(X)$	The Potential Energy
$\varphi[X(s,t),t]$	A Level Set Function with Contour $X(s,t)$
$\nabla\phi$	The Gradient of ϕ
k	The Zero Level Set
$E^{MS}(u,c)$	Mumford-Shah Energy Functional
$H(.)$	The Heaviside Function
δ_0	One-Dimensional Dirac Measure
$\frac{\partial\phi}{\partial\vec{n}}$	The Normal Derivative of φ at the Boundary
α	The Real Constant Called the Balloon Force in GAC
$G_\sigma * I$	The Convolution between Image and the Gaussian Kernel
$f_{ROI}(x)$	ROI Region in the Image Containing Jet Area
$x \geq 0$	A Particular Contrast Level
F	The Focused Region
DF	The Defocused Region
μ_j	The Mean Contrast of the j^{th} Class
μ_1	Corresponds to the Contrast Distribution in the Focused Region
$fL_{ROI}(x,y)$	Transformed Grayscale Image
ζ	The Covariance Matrix of the Color Channels
$Var(fL_{ROI})$	The Variance of the Transformed Grayscale Image
$A_b(fL_{ROI})$	The Average Brightness
$\lvert D_i(x,y)\rvert$	Complex Magnitude of the Output from the DT-CWT
$M_i(x,y)$	Output of the Median Filter

$\left[\varepsilon_B(f)\right](x)$	Morphological Erosion
E_{tex}	The Texture Energy
$TA(x,y)=e^{\Re_h\left(\frac{E_{tex}(x,y)}{\alpha}-\beta\right)}$	The Texture Activity
$\Re_h(\varsigma)$	The Just Half-Wave Rectification to Suppress Negative Exponents
β	The Threshold Below which Activity Measure is Unity
$M_{IG}(x,y)$	The Modulated Intensity Gradient
$H_{median}(x,y)$	The Median of Intensity Gradient
$T_G(x,y)$	The Texture Gradient of Each Sub-Band
$T_{Gmedian}$	The Median of Texture Gradient
$G_T(x,y)$	The Total Intensity Gradient
$T_f(p,q)=\inf_\gamma\int\left\|\nabla f(\gamma(s))\right\|ds$	The Topographical Distance between Points p and q in Connoting Domain D
$\inf_\gamma$	The Overall Paths (Smooth Curve) Inside D
$CB(m_i)$	The Catchment Basin of a Minimum m_i
F	The Blood Flow
P	The Pressure
R	The Resistance, ν is Fluid Viscosity, L is Length of Tube, and r is Radius Orifice
$\frac{dp}{dt}=\rho\left(v_2^3A_3-v_1^2A_1\right)\approx\rho v_3^2A_3\approx 2P_1A_3$	The Momentum Flux, When Blood Passes Through the Orifice
A_1	The Area of Jet on Ventricle
A_2	The Area of Jet on Atrium
A_3	The Area of Jet in the Vena Contracta
v_1	The Velocity of the Blood in the Ventricle
v_2	The Velocity of the Blood in the Atrium

v_3	The Velocity of the Blood in the Vena Contracta
P_1	The Pressure of the Blood on the Ventricle
P_2	The Pressure of the Blood in the Atrium
P_3	The Pressure of the Blood in the Vena Contracta
$\nabla^2\phi = 0$	The Laplace's Equation
$w(z) = \phi + i\psi$	The Analytic Function of Complex Variable $z = x + iy$
$\frac{\partial\phi}{\partial x} = \frac{\partial\psi}{\partial y},\ \frac{\partial\phi}{\partial y} = -\frac{\partial\psi}{\partial x}$	Cauchy-Riemann Equations
$\alpha, \beta,$ and γ	The Three Transform Coefficients to Transform f_{ROI} into a Grayscale $fL_{ROI}(x,y)$
$\pi_j^{'}$ s	The Mixing Proportions $(0 \le \pi_j \le 1), \sum_{j=1}^{2} \pi_j = 1$

CHAPTER 1

INTRODUCTION

---

1. 1 INTRODUCTION

The heart is a muscular structure and is central component of the vertebrate cardiovascular system. It pumps the oxygenated blood from the lungs to the body and back again de-oxygenated blood from the body to the lungs in a closed system. Blood is carried away from the heart in arteries and arterioles, and returned to the heart in venules and veins. Blood transport is vital to bring oxygen and nutrients to the body's tissues, as well as to remove carbon dioxide and waste products/ chemicals [286].

The human heart is located between the lungs. Because of slight tilting of its apex on the left side of the chest it creates heart rhythm or beating on the left side of the chest and makes an illusion that the heart is located just there. The size of a human heart is that of the tightly closed fist. It beats about 100,000 times in a day.

1.2 COMMON HEART FUNCTION

Although the heart pumps blood, delivering oxygen to the entire body's muscles and organs in order for them to function, it also needs its own oxygen enriched blood to work properly. The heart functions as a large muscular pump with arteries, veins, valves and an electrical system. The electrical system triggers the pulses for; thereby stimulating the heart to beat. The heart muscles then squeeze the blood to push the oxygenated blood throughout the entire body in one large arterial circuit and the deoxygenated blood through the pulmonary arteries to the lungs. The two, one-way, valves create separation between the four different chambers, namely, LA and LV, and RA and RV, for forming the dual pumps of the heart adjusting both rate and flow of the oxygenated and deoxygenated blood throughout the each cardiac cycle or the heart beat. The more activity one performs, the more the heart muscles have to work in order to supply needed quantity of the blood to the muscles to be utilized during the activity.

1.3. HEART VALVES

Heart valves can be categorized as follows:

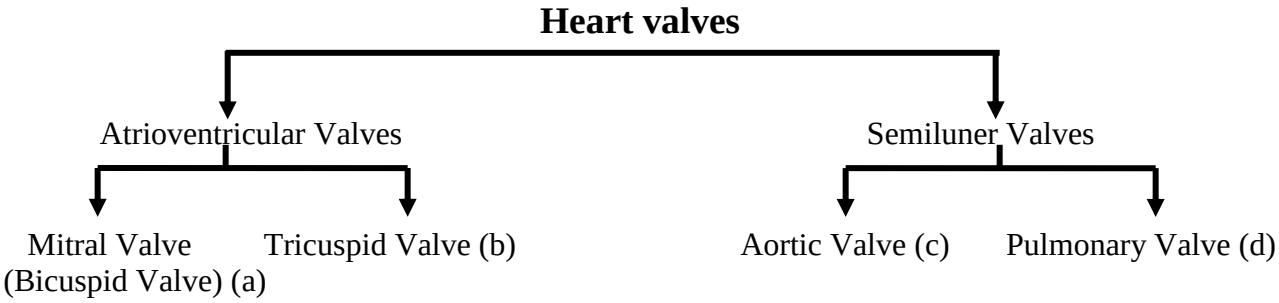

Figure 1.1 Chart to classify heart valves

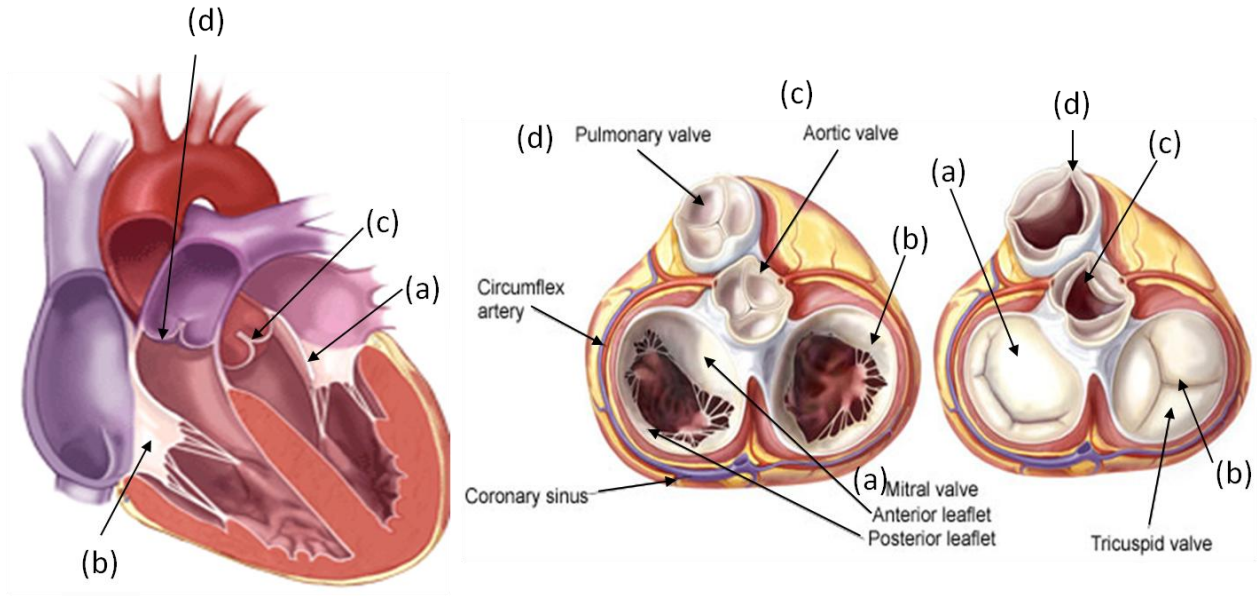

Figure 1.2 Heart Valves (Courtesy: D. H. Adams. 2010)

The two atrioventricular one-way valves are thin structures that are composed of endocardium and connective tissues. These valves, namely, the bi-cuspid/ mitral and the tricuspid atrioventricular valves are located between the left atrium and the left ventricle, and the right atrium and right ventricle, respectively. The two semiluner one-way valves are made up of three flaps each of endocardium and connective tissues reinforced by fibers which prevent the valves from turning inside out, shaped like a half moon so the name semiluner aortic and pulmonary valves, respectively. These valves are located between aorta and left ventricle and between the start of pulmonary artery and right the ventricle.

The one-way-blood flow in the heart is maintained with the help of four heart valves that lie at the exit of each of the four chambers of the heart. These four heart valves allow only the one-way flowing of the blood in the forward directions and restrict the backward flow of the blood. Sequence of blood flow is from the right and the left atria into the right and left ventricles through the open tricuspid and mitral valves, respectively. The atrio-ventricular valves open and close passively according to the changes in pressure in the chambers. They close when the pressure in ventricular systole (contraction) the pressure in the ventricles rises above that in the atrium and the valves snap shut, preventing backward flow of blood. The contraction of the ventricles leads to forced opening of the pulmonic and aortic valves, to pump the blood from the right and left ventricles through the open valves into the pulmonary artery toward the lungs, and through the aortic valve to the aorta, and the body. At the end of ventricle contraction it begins to relax and the aortic and pulmonic valves snap shut during the diastole. These valves prevent blood from flowing back into the ventricles. This pattern keeps on going again and again, causing blood to flow continuously from the heart to the lungs and the body.

1.4 MITRAL VALVE

The normal mitral valve opens when the left ventricle relaxes (diastole) allowing blood from the left atrium to fill the decompressed left ventricle.

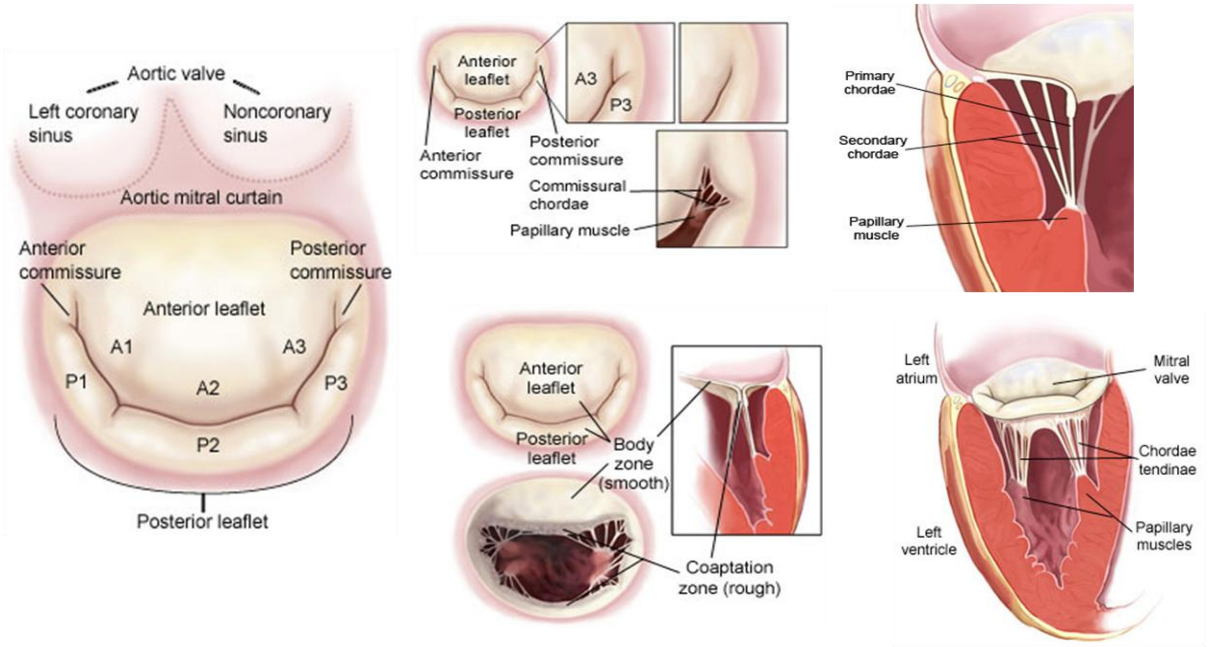

Figure 1.3 Mitral Valve Parts (Courtesy: D. H. Adams. 2010)

Pressure in the left ventricle increases during the systole or the contraction of the left ventricle. This increased pressure leads to close the valve, and restricts the flow of blood from leaking into the left atrium. At this time the blood flows through the aortic valve to the aorta and to the body. All the valvular apparatus such as annulus, leaflets and subvalvular apparatus work in a complex manner for the proper functioning of the valve. (Fig. 1.3).

The mitral leaflet tissues are organized in three layers: fibrosa, spongiosa, and ventricularis Table 1.1 [131] [250] describes location, composition and functions of these layers.

Table 1.1: The Layers of Valve Tissue: Fibrosa, Spongiosa, and Atrialis/Ventricularis

Layer	Location	Composition	Function
Fibrosa	Faces the LV	High concentration of collagen, thickest layer	Bears most of the load during coaptation
Spongiosa	Middle layer	High concentration of glycosaminoglycans (GAG) and proteoglycans (PG)	Provides shear between outer support layers and diffuses gasses and nutrients
Atrialis (Ventricularis for Semilunar valves)	Faces the LA	High concentration of collagen and elastin, thinnest layer	Elastin allows for strain when valve is open

(Courtesy J. D. Bronzino, *The Biomedical Engineering Handbook*.: CRC Press, 1995)

1.5 HEART DISEASES

Different heart diseases are the abnormalities which affect the heart valves functions, the function of heart's electrical system, the heart muscle itself, and the coronary arteries malfunctions. Some common heart diseases are as follows:

1. Coronary Artery Disease or CAD.
2. Myocardial Infarction (MI) — a severe type of heart disease.
3. High blood pressure (Hypertension).
4. Heart Valve Disease.
5. Cardiomyopathy, or Heart Muscle Disease.
6. Pericarditis.
7. Rheumatic Heart Disease

1.5.1 Mitral Valve Diseases

Mitral Valve diseases broadly can be of three types- Mitral Stenosis: Narrowing of the mitral valve orifice impeding the diastolic flow of blood from the left atrium into the left ventricle, Mitral Regurgitation: The backward flow of blood into the left atrium during systole; may be acute or chronic. The mitral valve prolapse: Posterior displacement or the anterior posterior or both mitral valve leaflets bent towards the left atrium may be the reason. Out of all these diseases the mitral valve regurgitation has been chosen as the topic of the present research work as the mitral valve diseases are the second most common valvular lesions, preceded only by the aortic stenosis. Study of mitral regurgitation is understood to cover all the other mitral valve diseases.

1.5.2 Mitral Regurgitation

A common heart valve disorder is mitral regurgitation (MR), or mitral insufficiency. When the heart is affected by the mitral regurgitation, blood flows backwards through the mitral valve during the heart contraction and there is a reduction in the blood which is to be supplied to the body.

If MR does not progress then the amount of MR is small; the backward leak has no significant consequences. But if there is significant MR then the left ventricle has to do more work to fulfill the oxygenated blood demand of the body. To fulfill this increased demand the heart muscles i.e. myocardium and the circulatory system undergo a sequence of changes. These types of changes take a long period of time, sometimes several years or decades which depend upon the severity of the regurgitation. The causes of mitral regurgitation also determine how quickly the heart begins to fail i.e. they give the information of failer in terms of weakening of heart apparatus. Weak apparatuses are the sources of a sudden heart attack.

1.5.3 Mitral Regurgitation Causes

Mitral regurgitation may increase from mild to severe due to the various cardiac diseases or other heart valve abnormalities. Some of these are as follows:

- ***Mitral valve prolapse***— Due to deformation and elongation of valve leaflets, the normal coaptation of the leaflets gets restricted. This is known as mitral valve prolapse. Due to this abnormality in valve motion, the blood flow direction gets partially reversed. The blood leaks backward from left ventricle to the left atrium. The mitral prolapse may ranges from mild to severe.

- ***Infective endocarditis*** — Sometimes heart valves are infected by bacteria, fungus or by some other organisms that affect the blood stream. This infection is known as infective endocarditis (IE). They stuck on the valves and some abnormal structure grows up known as vegetation. This vegetation makes the valve thick and changes their direction, thus, restricting leaflets to join during the closing operation. Endocarditis develops faster on the previously abnormal heart valves than in case of a normal heart valve.
- ***Rheumatic fever*** — Rheumatic fever occurs due to the throat infection. If this infection is not treated then it creates body illness. Inflammation on the heart valves and some more valvular complications occur because of the rheumatic fever. Rheumatic fever can be easily seen in the patients from the developing countries, while it is less seen in the patients from the developed countries because of the awareness about this disease.
- ***Congenital heart abnormality*** — Mitral regurgitation may also occur in the patients having child-born abnormalities in the heart.
- ***Other types of heart disease*** — Heart attacks, and muscle injuries and abnormalities may also lead to mitral regurgitation.
- ***Trauma*** — When the valve chords are broken than there is a sudden displacement of the leaflets and leaflets are not able to withstand their normal position. These flailed leaflets are not able to join and allow the valvular leakage which is severe.

1.5.4 Mitral Regurgitation Signs and Symptoms

Some patients show up no symptoms of mitral regurgitation. In case of mild and moderate regurgitation patients may never show up the symptoms and serious complications. Sometimes patients who may be suffering from severe mitral regurgitation, they may not show up any signs and symptoms. MR symptoms in these patients may be seen if their left ventricle becomes abnormal, atrial fibrillation occurs or pulmonary hypertension occurs. When the blood pressure gets increased in the pulmonary artery, the pulmonary hypertension occurs. This increases the workload on right side of the heart and it becomes difficult to supply an adequate oxygenated blood to the body.

If the left ventricle gets enlarged in the severe manner there will be some severe heart disease to the patients and there may be chances of heart failure. In these patients some abnormal signs

may seem like weakness, breath shorting during work, and there may be collection of fluid in the lower legs and abdomens leads to swelling in foot.

1.5.5 Mitral Regurgitation Diagnosis

Mitral regurgitation may be diagnosed if a heart murmur is heard by the clinician with a stethoscope. The change in heart sound is due to back-flow of blood through the mitral valve. The turbulent backward flow of blood is the main source of the heart murmuring.

Reasons of heart murmur may be one or more. Some diagnostic tests may be done to determine the reasons of the murmur. Other tests like ECG examining, Chest X-ray, Echocardiogram etc. may be essential to calculate the main cause of MR.

Echocardiography and color Doppler have their own utility in the evaluation of MR extent, however, they exhibit their own advantages/disadvantages and limitations. Table 1.2 is presented to describe these characteristics along with the use of Doppler parameters in evaluating MR severity.

Doppler parameters and grading severity of MR are presented in Table 1.3. These quantitative parameters help clinicians to sub-classify the moderate regurgitation group into mild to moderate and moderate to severe.

Doppler is the method which detects the mitral regurgitation. The M-mode or two-dimensional echocardiography is not able to find out the specific sign of the MR. It is possible to see the progress of the mitral regurgitation by the continuous echocardiographic examination. These changes can be seen by taking echocardiograms on a time interval.

The volume overloading in the left atrium or in the left ventricle is the initial echocardiographic feature of mitral regurgitation. Volume overloading occurs due to the stroke volume transfer between the two chambers. However, the thickness of wall is normal (because the wall mass increases at the time of enlargement). If the end-diastolic dimension become greater than 5.5 cm, and a noticeable hyperdynamic wall motion is seen on the interventricular septum than the left ventricular volume overload is easily recognized.

Table 1.2: Mitral Regurgitation Severity Evaluation Parameters: Utility, Advantages and Limitations (curtsey: publication by Pinjari Abdul Khayum)

	Utility/advantages	Limitations
Structural parameters:		
LV and LA size	Sensitive to enlargement for a chronic significant MR, generally outcomes are important. Significant chronic MR is excluded with normal size virtually.	In other conditions enlargement can be seen. In acute significant MR, it may be normal
MV leaflet/support Apparatus	Ruptured papillary muscle and flail valve specific for significant MR.	In significant MR Other abnormalities do not imply.
Doppler parameters:		
Jet area-color flow	Quick and simple, screen for mild or severe central MR; spatial orientation of jet evaluation.	Subject to variation of technical, hemodynamic; significantly under-estimates severity in wall-impinging jets.
Vena contracta width	Simple, good, quantitative at identifying mild or severe MR	Not useful for multiple MR jets; confirmation is required for intermediate values. Small values; thus small error leads to large % error.
PISA method	Quantitative; Presence of flow convergence at Nyquist limit of 50-60 cm sec^{-1} alerts to significant MR. Provides both, volume and lesion severity (EROA) overload (R Vol)	Less accurate in eccentric jets; not valid in multiple jets. Provide peak flow and maximal EROA.
Flow quantization-PW	Quantitative, valid in multiple jets and eccentric jets. Provides both lesion severity (EROA, RF) and volume overload (R Vol)	Measurement of flow at MV annulus less reliable in calcific MV and/or annulus. without the use of pulmonic site Not valid with concomitant significant AR.
Jet profile-CW	Simple, readily available	Qualitative; complementary data.
Peak mitral E velocity	Simple, readily available, A-wave dominance excludes severe MR	Influenced by LA pressure, LV relaxation, MV area and atrial fibrillation. Complementary data only, does not quantify MR severity.
Pulmonary vein flow	Simple, Systolic flow reversal is specific for severe MR	Influenced by atrial fibrillation, LA pressure. Not accurate if MR jet directed into the sampled vein.

LV: Left Ventricle, CW: Continuous Wave Doppler; EROA: Effective Regurgitant Orifice Area; LA: Left Atrium; PISA: Proximal Isovelocity/Surface Area, PW: Pulsed Wave Doppler; MR: Mitral Regurgitation; RVol: Regurgitant Volume

Table 1.3: Qualitative and Quantitative Parameters useful in Grading Mitral Regurgitation Severity (curtsey: publication by Nuasheen Akhter)

	Mild	Moderate	Severe
Structural parameters:			
LA size	Normal*	Normal or dilated	Usually dilated**
LV size	Normal*	Normal or dilated	Usually dilated**
Mitral leaflets or support apparatus	Normal or abnormal	Normal or abnormal	Abnormal/flail leaflet/ruptured papillary muscle
Doppler parameters:			
Color flow jet area x	Small, central jet (usually <4 cm^2 or <20% of LA area).	Variable	Large central jet (usually >10 cm^2or >40% of LA area) or variable size wall impinging jet flowing in LA.
Mitral inflow-PW	A wave dominant ϕ	Variable	E wave dominant f (E usually 1.2 m sec^{-1})
Jet density-CW	Incomplete or faint	Dense	Dense
Jet contour-CW	Parabolic	Usually parabolic	Early peaking-triangular
Pulmonary vein flow	Systolic dominance§	Systolic blunting §	Systolic flow reversal ↑
Quantitative parameters Ψ::			
VC width (cm)	<0.3	0.3-0.49	≥ 0.5
RVol (mL $beat^{-1}$)	<30	30-44, 45-59	≥ 50
RF (%)	<30	30-39, 40-49	≥ 60
EROA (cm^2)	<0.20	0.20-0.29, 0.30-0.39	≥ 0.40

LV minor axis ≤ 2.8 cm m^{-2}, LV end-diastolic volume ≤ 82 mL m^{-2}, maximal LA antero-posterior diameter ≤ 2 cm m^{-2}, maximal LA volume ≤ 36 mL m^{-2} (2,33,35); RF: Regurgitant Fraction; RVol: Regurgitant Volume, VC: Vena Contracta; *: Unless there are other reasons for LA or LV dilation. Normal 2D measurements: **: Exception: acute mitral regurgitation; x: At a Nyquist limit of 50-60 cm sec^{-1}; ↑: Pulmonary venous systolic flow reversal is specific but not sensitive for severe MR; f: Usually above 50 years of age or in conditions of impaired relaxation, in the absence of mitral stenosis or other causes of elevated LA pressure; §: Unless other reasons for systolic blunting (e.g., atrial fibrillation, elevated left atrial pressure); Y: Quantitative parameters can help sub-classify the moderate regurgitation group into mild-to-moderate and moderate-to-severe.

The present thesis is devoted on (i) the enhancement and de-speckling of the two-dimensional echocardiographic images for the better view, (ii) the automatic LA and LV boundary detection for making it convenient for the clinicians to recognize and assess the enlargement of the two

chambers due to mitral regurgitation. , (iii) the automatic jet area detection and assessment, which is directly related to the severity level of mitral regurgitation, and (iv) on the automatic detection and measurement of vena contracta width.

1.6. ECHOCARDIOGRAPHY

The size of cardiac chamber, wall motion, wall thickness, valve motion, valvular anatomy, the proximal great vessels and the pericardium can be detected by the echocardiography. Cardiac functionality and their anatomic relationships can be seen as a live picture with echocardiography. Echocardiography is a very sensitive tool in regard to find out the pleural and pericardial fluid, to find out the mass lesions which may be inside or near the heart. Echocardiography is effective to find out the congenital heart diseases, diagnose the myocardial or valvular related pathology. It is safe because the transthorasic echocardiography (TTE) is done without the use of chemicals insertion, which may damage the myocardium.

1.6.1 Principles of Echo

Ultrasound has high frequency (>20,000 Hz), pulsed sound waves. When ultrasound waves enter the tissues they transmit through the tissues and based on the acoustic impedance of the tissues they are reflected back. The density of the tissue times the velocity at which sound wave travels through the tissues is the acoustic impedance of a tissue. Ultrasound reflection depends upon the mismatching of the impedances between the two tissues. Higher the difference higher is the reflection. The bones have high acoustic impedance, whereas, the air has low acoustic impedance, relatively. Therefore, the bone-tissue and the air-tissue interfaces exhibit very high mismatch of acoustic impedance resulting in high reflection of ultrasound waves. So imaging of the deeper structures is restricted when the ultrasound beam intersects the air filled and bony structure because they reflect the beam to image their outer structure. Therefore, some suitable places have been selected to take the image of the heart. So, for echocardiography, intercostal spaces within the cardiac windows (where the heart is against the thorax, without intervening lungs) or from subcostal windows (depending upon the species) have been chosen.

Speed of ultrasound wave varies depending upon the tissue type through which it is propagating. Through the soft tissue the speed of ultrasound beam is seen to be approximately 1540 m/sec. On the basis of the relation with the transducer’s parameters, the size, thickness and

the location of the soft tissues can be calculated at any point and at any instant. The reflection, refraction and transmission rules of the ultrasound wave are as the laws of geometric optics. Reflection, refraction and absorption of the ultrasound wave depend upon the difference of acoustic impendence at the interference. As the ultrasound beam is distanced from the transducer its intensity gets decreased because of the scatter, divergence, absorption, and reflection of energy of the wave at the interferences of the tissues. When the ultrasound beam is perpendicular to the images-structure it forms the highest reflection to create a strong echo. Transducer receives theses reflected echoes and creates an image on the ultrasound machine. Most of the time (about 99% of the total time) the transducer acts as a receiver. The images which are formed by the transducer can be displayed on the monitor, or recorded for future use, or printed on a paper. Optical Cd's can be recorded to form a data bank.

1.6.2 Modes of Echocardiography

Echocardiography used in clinical areas can be classified into three modes: M-mode, two-dimensional (2-D, B-mode or real time), and Doppler echocardiography. These different modes of echocardiography are used during the each echocardiographic examination. One type of echocardiographic examination creates a complimentary finding from the other modes of the examination. Different modes are performed simultaneously.

1.6.2.1 M-mode Echocardiography

A high sampling rate is used in M-mode echocardiography. High clarity images are obtained from the M-mode echocardiogram, which leads to accurate measurements of cardiac dimensions and for the evaluation of cardiac motion. It is very difficult to place the M-mode beam at the appropriate location in the heart and therefore it is difficult to obtain the clear echoes, and carry out critical measurements. It is difficult to obtain meaningful results from the calculations performed on the obtained measurements. The right parasternal position permits the standard view of M-mode. To avoid the inclusion of the papillary muscles which are in the left ventricle free wall the M-mode cursor should be positioned within the heart in case of the right parasternal short axis view. There are the mitral valve, the left ventricle wall (at the level of the chordae tendineae), and the aortic root (aorta/ left atrial appendage) views, are included through the standard M-mode view. A linear sweep is added to show motion patterns, as a graphic displays as shown in Fig. 1.4.

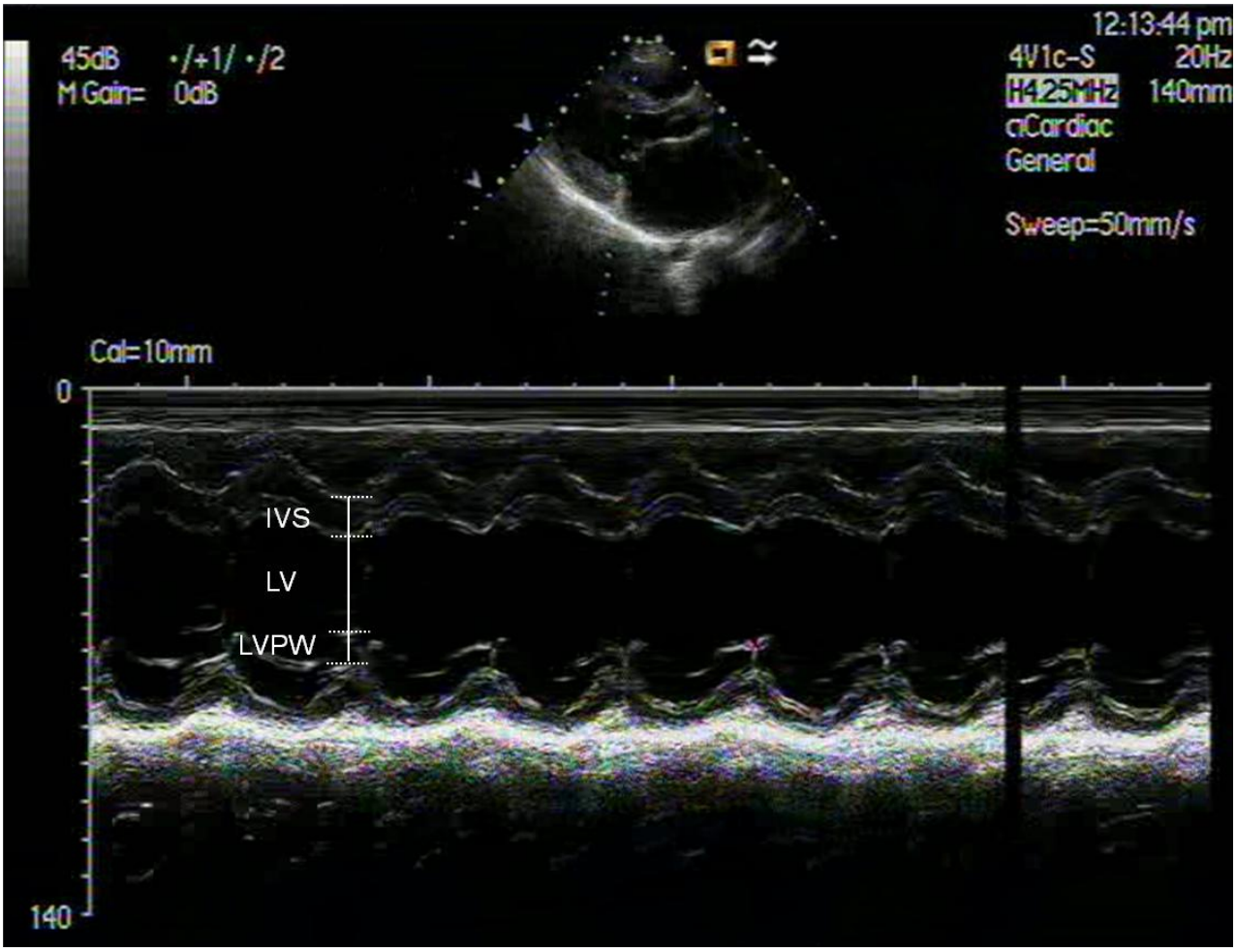

Figure 1.4 "M-Mode" Display of the Motion Pattern of the Mitral Valve. The Beam Direction is indicated on the Small Image Icon at the Top of the Display.

1.6.2.2 Two-Dimensional Echocardiography

A real time image of both depth and width of a plane of tissue is obtained in two-dimensional echocardiography. So it is easier to obtain the various results of the different structures of the heart than with the M-mode echocardiographic images. It is possible to take infinite number of imaging planes through the heart; however, there are some standard views, which are used to evaluate the extra cardiac and intra cardiac structures.

More information about the shape and size of the heart is obtained in two-dimensional echocardiography than M-mode. Two-dimensional echocardiography also gives the spatial relationships of its structures during the cardiac cycle. M-mode and two dimensional recordings

both are done simultaneously for getting the more information about cardiac anatomy and clinical values. This makes echocardiography a major diagnostic tool. Fig. 1.5 shows the image obtained with the help of 2-D echocardiography.

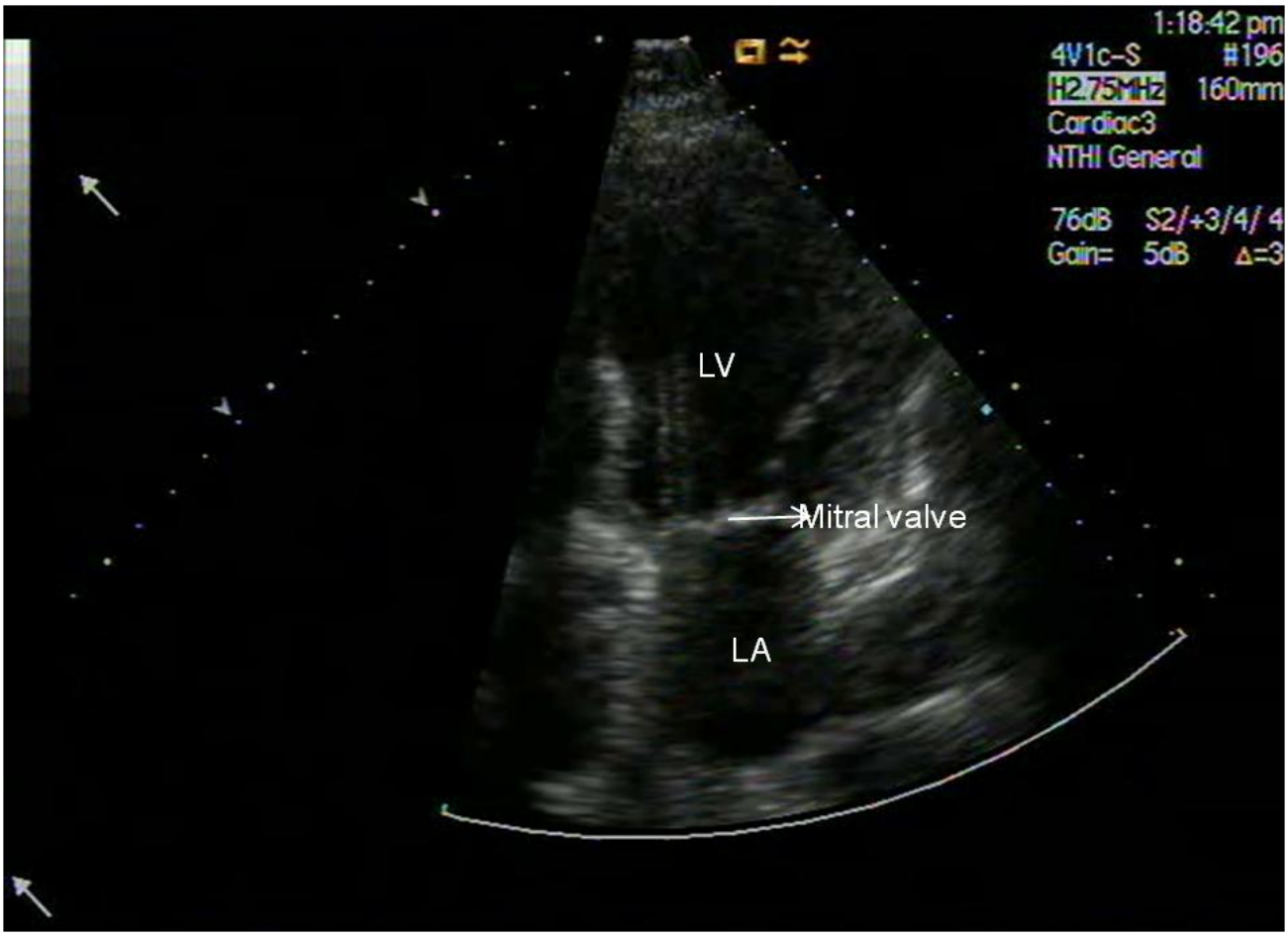

Figure 1.5 Two-Dimensional Echocardiography of Mitral Valve.

1.6.2.3. Doppler Echocardiography

Blood flow patterns, velocity and direction is obtained using Doppler imaging. Color Doppler works based on the detection of change of frequency of reflected ultrasound waves. The phenomenon is referred to as Doppler shift. This change I frequency occurs as the ultrasound waves reflect off the moving blood cells, which are either moving towards the transducer or away from the transducer. In this way the color Doppler helps us in documenting and quantifying the insufficiency of the mitral valve which is also referred to as Mitral stenosis or MR. An accurate

measurement of blood flow velocity is possible if the direction of blood flow is precisely parallel to the direction of US beam. The results become increasingly inaccurate as the angle θ, shown in fig. 1.6, deviates from zero angle between the blood flow direction and the direction of beam. The equation (1.1) describes the relationship that determines the blood flow velocity.

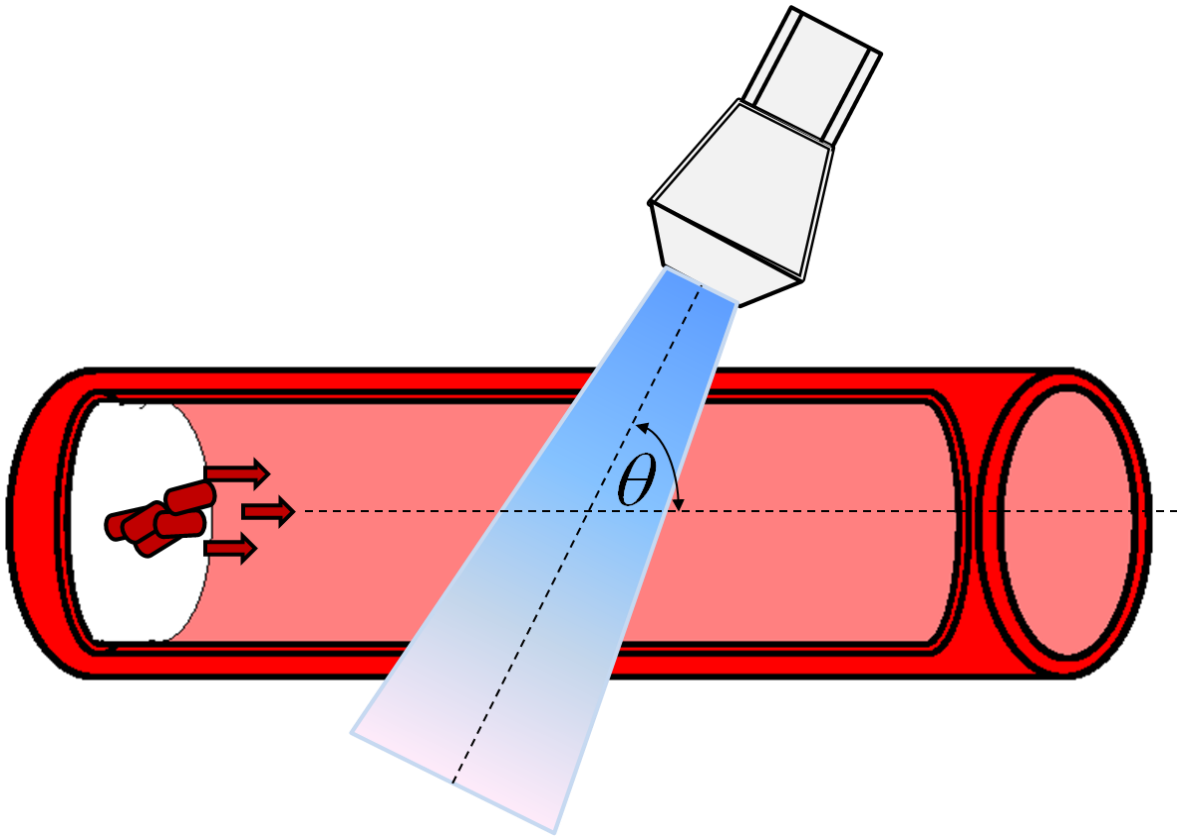

Figure 1.6 The Doppler Phenomena

$$F_d = \frac{2 f_o}{c} V \cos\theta \tag{1.1}$$

Where F_d is the Doppler frequency, f_o is the original frequency, V is the blood flow velocity, c is- the velocity of light and θ is the transducer angle.

Clinically, two types of Doppler echocardiography are employed generaaly, viz one is pulsed wave (PW) Doppler shown in fig. 1.7 and other is continuous wave (CW) Doppler shown in fig. 1.8.

In ***PW Doppler*** the ultrasound beam is transmitted as short bursts, to a point which is (fixed as the "sample volume") on a distance from the transducer. The advantage of this type of Doppler is

that from a specified point in the heart or blood vessel, blood flow velocity, direction and spectral characteristics can be calculated. The measured maximum velocity is limited because of the limited pulse repetition frequency and is the major disadvantage. Transducer used in pulsed wave (PW) Doppler systems alternates transmission and reception of ultrasound as in the M-mode transducer (Fig. 1.6). One main advantage of pulsed Doppler is that it is able to provide Doppler shift data selectively along the ultrasound beam from a small segment, also known as "sample volume".

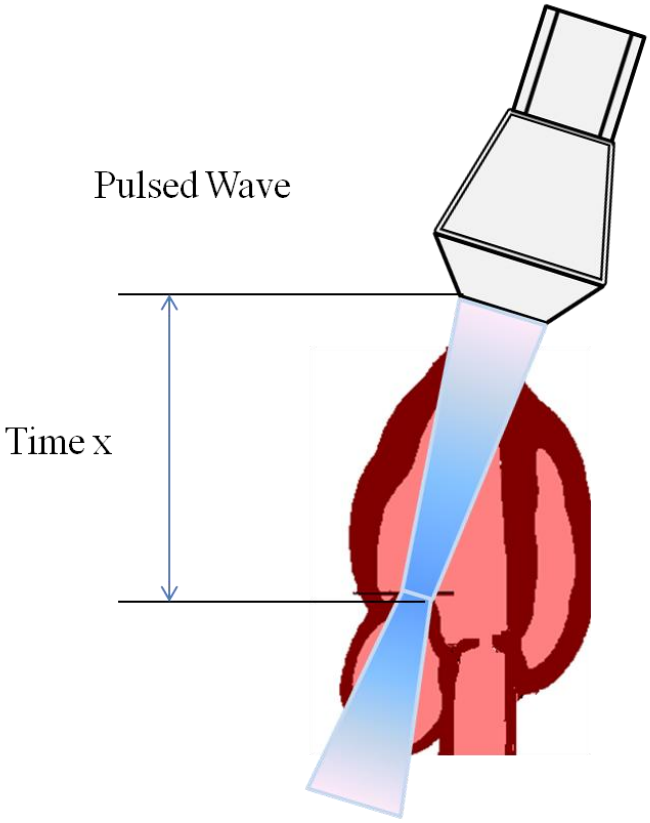

Figure 1.7 In PW Doppler, the Transducer Alternately Transmits and Received the Ultrasound Data to a Sample Volume. This is also known as Range-Gated Doppler

Dual crystals are used in ***CW Doppler*** to simultaneously and continuously sent and receive ultrasound waves. High velocity flows can be also be measured with CW because there is no maximum measurable velocity (Nyquist limit). The direction and velocity of sampled blood flow is in the spread form not in the specific area in case of CW Doppler which is a disadvantage of CW Doppler. According to its name in CW Doppler continuous ultrasound waves are generated with

continuous ultrasound reception. Fig. 1.8 shows the two crystal transducer, one crystal for each function, and accomplishes this dual function.

Color Flow Doppler Echocardiography is a combination of M-mode and 2-D modalities with blood flow imaging and a type of PW Doppler ultrasonography. Multiple scan can be carried out for taking the multiple samples along the scan line with color flow Doppler. A color coding is assigned to the mean frequency shift obtained from many sample volumes for velocity and directions. There are several types of mapping which are usually available for this purpose. There is a BART (blue away and red towards) system used in most systems. The presence of multiple velocities and differences in relative velocity of flow can be obtained. Different maps which depend upon the brightness and color are used to indicate multiple velocities. The blood flow is displayed on the two-dimensional echocardiographic image during the mitral regurgitation into the left atrium at the time of systole is shown in fig 1.9. The colors (red and blue) in color flow imaging, represent direction of a given color jet and the different velocities that can be represented by the hues from dull to bright. A turbulent jet shows a mosaic of many colors. A two-dimensional display of flow is now shown according to the size, direction, and velocity.

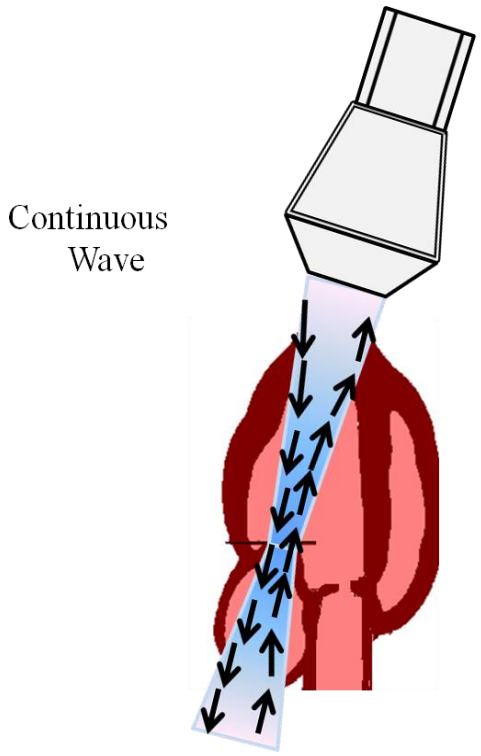

Figure 1.8 In CW Doppler, the Transducer is Constantly Emitting and Receiving Ultrasound Data

Meaning of Color There is useful information in the flow map of an image. According to the direction, red color is assigned to the flow which is towards the transducers and blue for the flow away from the transducers.

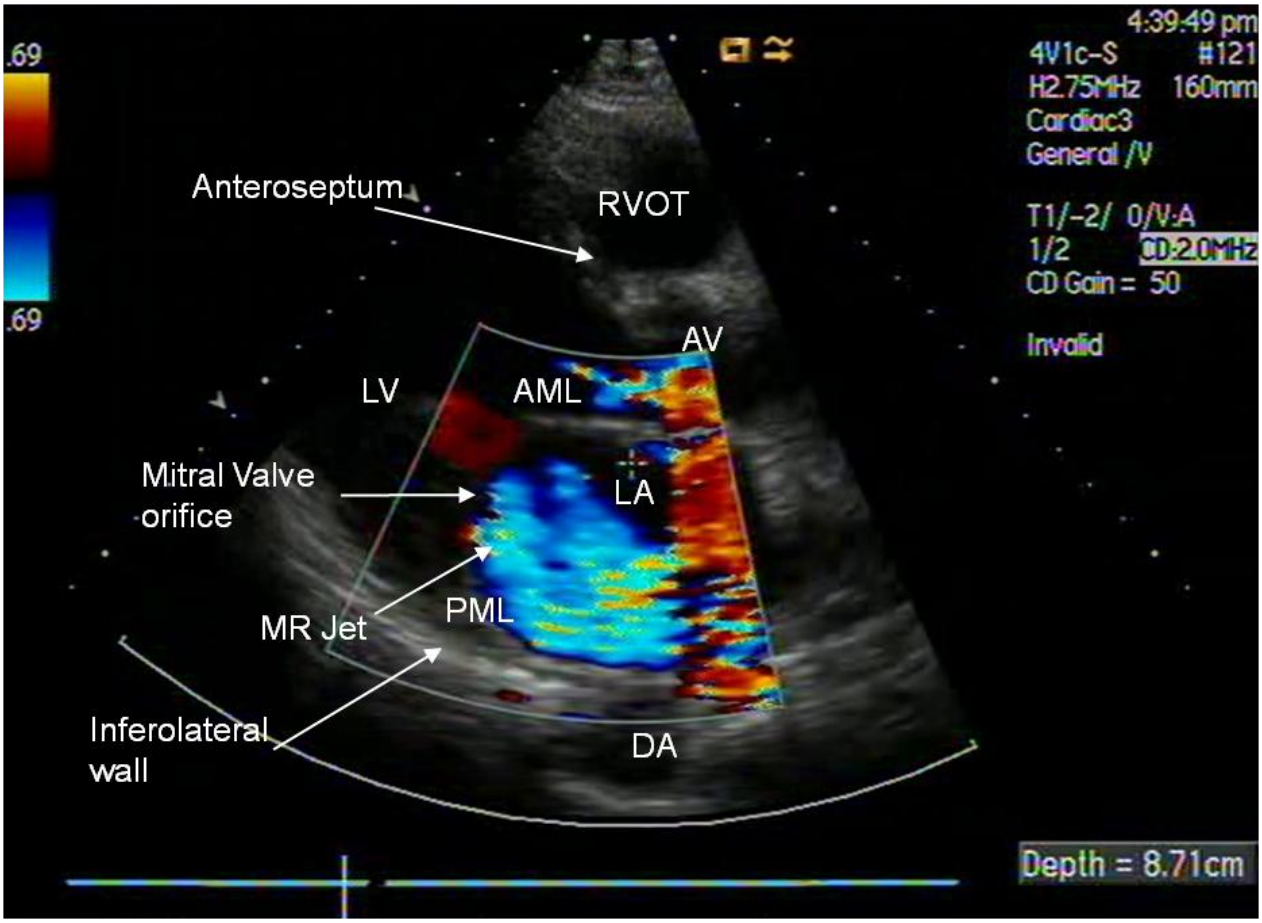

Figure 1.9 Systolic Parasternal Long-Axis Color Flow Image of Mitral Regurgitation. The Mitral Regurgitation Jet Comprises a Mosaic Of Varying Colors. A Variance Map is used. Note the Direction of Flow Indicated by the Color Bar on the Right. LV-Left Ventricle, LA-Left Atrium, AV-Aortic Valve, AML-Anterior Mitral Valve Leaflet, PML-Posterior Mitral Valve Leaflet, RVOT-Right Ventricular Outflow Tract, And DA-Descending Aorta

1.6.2.4 Two-Dimensional Recording Technique

Transducer Manipulation

In both M-mode echocardiography and two-dimensional echocardiography the same recording techniques is used. In 2-D Mode echocardiography a stationary ultrasound beam is used as a flashlight. At a particular time this illuminates on a small area of the heart. A two-dimensional

transducer is like a circular saw, which is rotated on the chest at the time of rest, It is rotated around the point considering the index mark printed on the transducer. The index marl on the transducer corresponds to the right-hand side of the machine display. A more complex maneuver is necessary during the two-dimensional examination, in order to align the scan plane with the desired anatomic axis of the heart. Manipulation of the echocardiography transducer for two-dimensional can be described as follows. *Rotating* the transducer pivots the scan plane about the transducer axis. For example, to change from the parasternal long axis to the parasternal short axis rotation through 90 degrees is used,. *Tilting* the transducer displaces the scan to form a series of radial planes. *Angling* the transducer moves its axis in the plane of the scan, for example to bring an object at an edge to the center of the view-field. Fig. 1.10 shows the location of the planes to access the heart.

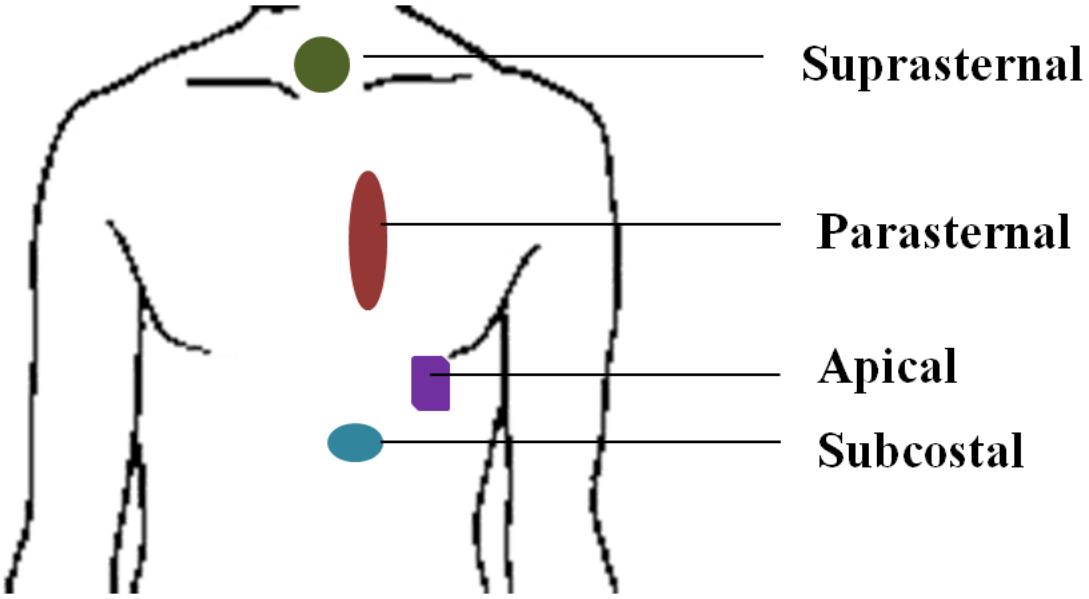

Figure 1.10 Planes for Accessing Heart to Perform Echocardiography

1.6.3 ADVANTAGES AND LIMITATIONS OF ECHOCARDIOGRAPHY

1.6.3.1 Advantages

- Portable – can bring equipment to sick patient rather than move patient to test facility.
- Does not limit access to sick patient for clinician, nurse or monitoring equipment.
- Can be performed in upright position in severely orthopnoeic patients.

- Non-invasive and safe – therefore also highly suitable for follow-up investigations.
- Relatively cheap.
- Widely available.

1.6.3.2 Limitations

- Image quality is dependent on operator's skills, patient anatomy and position; generally best in the left lateral position. It may be severely impaired by air between chest wall and heart, e.g. hyperinflated lungs in obstructive airways disease, patients on mechanical ventilator, pneumothorax, supine or right lateral position etc. Narrow rib spaces and obesity may also cause technical difficulty.
- Information is often qualitative rather than quantitative. Significant intra- and inter-observer variation are seen when images are suboptimal.
- Left atrial appendage and in adults, superior vena cava and majority of aorta and pulmonary arteries above valve/root level, cannot be imaged.
- Image quality is generally inferior to transesophageal echo.
- Offers limited capacity for differentiation between different types of tissues and fluids.

1.7 LITERATURE REVIEW

Almost no work is available in literature delivering technical information on processing of echocardiographic image with reference to segmentation of mosaic patterned regurgitant jet against the colored background. A few research papers are available on speckle noise removal and enhancement of echocardiographic images. Only a fewer research papers are seen on boundary detection of heart chambers; that too, presenting very little technical information. Most of the research papers on echocardiography deal with the clinical aspects of the regurgitant jet and the vena contracta width assessment. There is hardly any research papers delivering technical knowhow on computer based echocardiographic image processing and severity assessment to corroborate with the clinicians opinion.

1.7.1 Echocardiographic Image Enhancement

Only a very little material is available in literature on echocardiographic image enhancement. A research paper [186] presents a technique to assess an experimental model of coronary occlusion, whether the spatial and temporal variability in myocardial enhancement can interfere

with quantitative measurements of myocardial perfusion. [135] proposes a feature enhancement approach; First, in which Feature Asymmetry (FA) is used to detect image features [209]. This provides a normalized likelihood image in which the intensity value at any location is proportional to the significance of the detected features. After that, the sparse data at feature locations are interpolated by a Fast Sparse Surface Interpolation (FSI) technique using the likelihoods to estimate the degradation field [197]. In, the final step, a non-linear processing method is applied using the degradation field to the original data to enhance feature values. [136] used a feature-based contrast enhancement approach to enhance the quality of noisy ultrasound images. The approach uses a phase-based feature detection algorithm, followed by sparse surface interpolation and subsequent non-linear post-processing. The first step to select a set of relevant image features in the data is to exploit the intensity-invariant property of phase-based acoustic feature detection. Then, a fast surface interpolation algorithm is used to obtain an approximation to the low-frequency components of the sparse set of selected features. The final step is a non-linear post-processing. After that, they presented results of applying the method to Echocardiographic sequences (2-D + T). The results show that the interesting features in the image are enhanced by this method.

An important and useful part both for manual processing and assessment by a clinician and for computer analysis of the sequence is the contrast enhancement. The balanced contrasted images in the case of echocardiographic data and their quantitative results are important. Image filtering via generalized scale is proposed in [141]. Filtering method is based on generalized scale (*g*-scale for short) [26]. Within the largest, homogeneous, fuzzily connected region containing *p*, the *g*-scale at any image element *p* is considered to be the set of all image elements. Roughly speaking, the largest set (of any shape whatsoever) of elements within which there is a spatial contiguity of intensity homogeneity is the *g*-scale at *p*. *g*-scale imposes no shape, size, or anisotropic constraints on the homogeneous regions that is why it differs from *b*-scale and other local morph metric scale models. For the purpose that the diffusion rate is greater deep within the region than in its border filtering is controlled by *g*-scale regions. In [176], a digital filtering technique has been developed for enhancement of two-dimensional ultrasonic images of the heart. The lateral axis normal to the direction of scan lines was taken for applying filtering. Both filtering off-axis artifacts and

interpolation within the scanning plane give the enhancement results. Simple filters of this design, which significantly increase the quality of images, have been implemented.

During the last two decades, modality specific image enhancement schemes have been developed and studied in the literature [146], [108]. Specifically, various spatial and frequency-based techniques [87], [279], and [204] have been developed for ultrasound image enhancement.

1.7.2. Speckle Noise Removal of Echocardiographic Images

The speckle and scene models used as the basis for filter development decide the speckle filter performance. The multiplicative and the product speckle models are the well known models, which have been used as the basis for the development of almost all the existing speckle filters. The multiplicative speckle model serves for the development of the minimum mean-square error (MMSE) filters Lee [152], Kuan [73], and Frost. [310], whereas the product model has been used as the basis for the development of the maximum *a posteriori* (MAP) Bayesian Gaussian [80], Gamma [261], [50], and model-based de-speckling [212] filters. Various mathematical expressions have been developed and used for the named "multiplicative speckle model" [310], [73], [152], [41], [99]. All these speckle-scene models implicitly incorporate certain assumptions about speckle, observed signals and scene and this strongly influences speckle filtering, as well as scene reconstruction, during the inversion process based on these models [190], [11], [243].

Recently, the well known single-stage speckle filter, the refined Lee filter [154] and the Frost [310] filter that have been used for many years, were prematurely rejected in [56]: "Single-stage filters are inadequate for effective speckle removal; MMSE reconstruction can be rejected because structure is not retained upon iteration" [56]. On the other hand, the Hagg edge-preserving optimized speckle filter [315], which is basically a multiresolution box (average) filter, has been recognized as the best speckle filter [147], [98].

Grainy appearance of speckle noise can mask features which are useful in diagnosis and also this affects the accuracy of segmentation algorithms [235], [120]. The statistical mechanism of laser speckle formation was first presented in [161]. This study presents the theoretical results; and elaborates that speckle noise can be rejected by linear filtering. Later in [248], [46] and [310] it is concluded that linear filtering, the way it was presented in [161], suppresses the noise at the cost of smoothing out image details.

In [81], [80] and [151] the product model was used as the basis to generate of the maximum *a posteriori* (MAP) Bayesian Gaussian [50], Gamma [41], [99], and model-based de-speckling [212] filters. Many papers used the "multiplicative speckle model" [81], [80], [152] and [212].

Several filters are proposed in the literature for reducing speckle noise: linear filters are used in [212] temporal averaging filter is proposed in [139] and median filter in [16]. These filtering methods are useful in reducing additive random noise and have little success in speckle noise removing. In case of nonlinear diffusion methods [169], [330], [63] and [66] regarded as an adaptive filtering method, smoothing direction and strength are controlled by an edge detection function. A coefficient of variation is used as an edge detector for speckled imagery in speckle reducing anisotropic diffusion (SRAD) [324]. A nonlinear coherent diffusion (NCD) model [170] has jointly used three different models viz. isotropic diffusion, anisotropic coherent diffusion and mean curvature motion.

Non linear filters which are size and shape sensitive [31], [27], [238] and [231] are found to be good in removing speckle noise patterns based on mathematical morphology. Morphological filters are also used as despeckling filters [116], [35], [241] and [118]. Recent literature available in [180], [259], [91], [105], [143], [164] and [19] has shown this extensively.

In [332], [287] SRAD algorithm is made capable of enhancing volumetric ultrasound data by generalizing the 2D SRAD algorithm. A partial differential equation (PDE) is developed in [335] for speckle reduction by minimizing a cost functional of the instantaneous coefficient of variation. A new PDE has been proposed in [288]. It combines the enhancement of speckle reducing anisotropic diffusion (SRAD) with the mechanism of deconvolution. In [167] a method is implemented to remove speckle noise from ultrasound images by minimization of total variation.

A novel algorithm has been introduced in [23] for speckle reduction in medical ultrasound imaging while preserving the edges. It has an additional advantage of adaptive noise filtering and speed. Laplacian pyramid-based nonlinear diffusion (LPND), is proposed in [331]. With this method, speckle is removed by nonlinear diffusion filtering of band-pass ultrasound images in Laplacian pyramid domain.

1.7.3. Boundary Detection of Echocardiographic Images

Two-dimensional echocardiography is a good method for finding out left atrium and ventricle dilation in case of mitral regurgitation. There are many papers in the literature which discuss the

different measurements related to left atrium and left ventricle [319], [132], [15], [217] and [233]. There are different techniques for left atrium and ventricle boundary detection. In [121], the LV center and LV edge points were detected using neural network classifiers with new input feature vectors. These neural classifiers combined with knowledge-based techniques in the center detection stage refine the center estimate. In [318], double thresholding method is used for left ventricle endocardium detection. First step of this method was to suppress the noise by taking mean of two adjacent frames four times. Next step was ternary thresholding in which two thresholds divide the image into three regions. Final step was second thresholding, in which a binarized image is obtained. In [140], snake-based algorithm is used for endocardial boundary detection. A correlation between geometrically normalized images from the patient and from the database is also proposed.

Here the objective is to detect the left atrium and left ventricle boundaries using active contour method. Active contour model is firstly proposed in [206]. There are many research papers which are based on deformable models or active contour models [121], [94], [115], [14], [317], [9] , [72] [86]and [321]. An energy minimizing deformable spline influenced by constraint and image forces that pull it toward object contours is called active contour. Snakes are largely used in applications like boundary detection object tracking, shape recognition, segmentation, edge detection, stereo matching [206], etc.

Segmentation is a well known step which is carried out for the clinical diagnosis from medical images. But the major problem encountered during the segmentation of echocardiographic images. The literature shows that the active contour based segmentation techniques are being extensively used in medical imaging [206], [307], [277] and [285]. Active contour models can be categorized as edge based active contour models [206], [307], [277], [106], [54], [219] and [62] and region based active contour models [294], [258], [59], [12], [77], and [173].

Some of the edge based active contour models are used as the edge-detector. The operation of edge detector depends on the gradient of the image [61] to stop the initial contour on the boundary of the interested objects. This technique has advantage when the objects and background of segmented image are heterogeneous. Drawbacks of these active contour models are that the satisfactory results cannot be achieved in case of objects with discrete or with the presence of blur boundaries or noise. Some active contour models as in [106] introduce the balloon force to shrink

and enlarge the capture range of the force. However some undesired effects occur during balloon method. If weak balloon force is there then contour is not able to pass through the narrow part of the object, and if the balloon force is large, the contour will pass through the weak edges of the object. The geodesic active contour (GAC) [106] is the most popular methods in this category. This method uses an edge stopping function (ESF) which stops the contour on the object boundaries.

Region based active contour models have several advantages over edge based active contour models. Region based active contour models use the statistical information inside and outside the initial curve to evolve the contour towards the boundaries of the desired object. This renders it the less sensitive to noise and gives better performance in case of weak edges. It is also suitable for regions having no edges. Another advantage is the less sensitivity about the location of the initial contour to make it, in turn, easy to detect exterior and interior boundaries efficiently. The most popular method based on the Mumford- Shah model [173], in the category of region based active contour without edges is given by Chan-Vese (C-V) [294].

There are some hybrid models that are proposed in literature to drive the advantages of both GAC and C-V models. In [181] a geodesic-aided C-V (GACV) model had been proposed which includes region and local detector in the level set flow function. In [291] a variation method has been proposed using discriminating function for color image segmentation. In [291], the region was combined with the photometric invariant edge information for color-texture image segmentation. In [340] an integrated model is established by combining the edge location with statistical region information. Recently, in [171] signed pressure force function active contour model has been proposed. This model has the advantages of both GAC and C-V models. In this, a level set method for active contour model is developed with a new signed pressure force function.

1.7.4. Regurgitation Jet Area

There are some literatures on clustering in color space. Pixels are assigned to the given region using NN rule in [92]. Prototypes for the region are derived by multiediting and next condensing technique. Clustering with NN algorithm. Number of prototypes reduction using multiediting and condensing. Pixels are classified by minimum distance to single representatives (prototypes) of classes in [268]. In [200] regions are defined by 19 given hue clusters.

Another method of segmentation is Fuzzy clustering in color space. In [333] pixel had been allocating to the region using maximum of the fuzzy membership function. However, from coarse segmentation most of pixels were already assigned to regions using hexahedra bounds. Fuzzy c-means clustering had been used.

Area base segmentation in the literature is regrowing and region merging. In [251] region R is uniform if average distance $D_{(R)}$ of its color points to its cancroids is less than threshold D_{max} (experimentally set to 10% of distance between black and white points in the color space). Boundary relaxation technique had been used. In [182] a region is uniform if a seven dimensional predicate D holds in several levels of hierarchy. Regions are homogeneous sets of pixels in [303]. Pixels are merged based on the minimum Euclidean color distance in a four-connected neighborhood. In [304] Regions are homogeneous sets of pixels. Homogeneity is verified based on the color difference between two adjacent pixels and the average edge contrast between adjacent regions. Both values have to be less than corresponding thresholds to create a region. Image enhancement employing a Symmetric Nearest Neighbor operator and region growing based on hierarchical connected components analysis have been used. In [188] regions are defined by a simulated mass moving through an irregular held of forces. [227], [51], [64], [338], [88], [207], [337], [322] describes the color texture based segmentation. In these papers color texture has been taken as region property to segment the specific region. A new graph-theoretic criterion for measuring the goodness of an image partition means normalized cut is developed in [160]. [213] represents an example of fuzzy cluster based segmentation. [290] implemented algorithm for finding a minimum ratio cut, proved its correctness, and discussed its application to image segmentation, and presented the results of segmenting a number of medical and natural images using these techniques.

One example of Multiscale Clustering and Graph Theoretic Region Synthesis is [282]. A novel generative model and an EM algorithm for Markov-based image segmentation is proposed in [12]. The proposed model assumes that the hidden class labels of the pixels are generated by prior distributions that share similar parameters for neighboring pixels. A pseudo likelihood quantity that couples neighboring priors by means of entropic quantities such as the KL divergence is introduced to define a notion of similarity between neighboring pixels priors. An EM algorithm that iteratively maximizes an appropriately constructed lower bound on the data log-likelihood has

been derived to estimate the unknown parameters of the pixels prior distributions, as well as the parameters of the observation model.

In [327] fast dominant color extraction scheme based on nonparametric density estimation has been developed. His method automatically determines the number of dominant colors and effectively reduces the representative colors in an image. A definition of region salience and accordingly develop a novel merge strategy, which takes into account not only the homogeneity but also the geometric properties of regions have also been explained. [296] presented a modified graph-cut technique using a novel energy function without the regularizing parameter for image segmentation. In addition, a mixture color model is employed to apply the proposed technique to color image segmentation effectively.

To achieve better segmentation boundary detection and region growing tend to combine and this technique is called hybrid methods of segmentation [299], [137], [48], [325], [183], [237], [179], [244], [28]. One of the hybrid methods is seeded region growing (SRG) as proposed in [135]. It requires a seed, and regions are grown by merging a pixel into its nearest neighboring seed region. For color images automatic seeded region growing is proposed in [326].

Color Doppler echocardiography gives the almost accurate results for finding out severity of mitral regurgitation. Valvular regurgitation can be diagnosed with the help of color Doppler [267]. Doppler echocardiography plays an important role in the diagnosis of mitral regurgitation and in its surgery [194], [199] and [198].

Color image segmentation produces additional difficulties in the segmentation. Due to complexity and problems which are dependent on image to image basis there are many researches that are carried out in this area [43], [113], [226], [270], [281], [283], [95], [30], [222], [276], [220] [236], [160], [142], [127], [183], [303]. [339] and [328].

The watershed transformation for the gray scale images is proposed in [52]. Advance researches had been done in many literatures in the area of watershed segmentation transformation [266], [265], [159] and [183]. Over-segmentation is a major drawback of the watershed transformation and it increases excessively in case of certain images. Some techniques such as region merging [264], hierarchical watersheds [264], marker based watershed segmentation [264] and adaptive smoothing [133] morphological filtering [229], are the examples of advanced watershed transformations.

Decomposing data in to different frequencies is the main objective of the wavelet transform. Wavelet produces four images with the size of each one as half of the original image [58]. Recent work for segmentation using wavelet is in [252].

1.7.5. Vena Contracta Width Detection

At present interest in color Doppler imaging for vena contracta for the assessment of mitral regurgitation is increasing progressively [60] and [111]. The vena contracta is the narrowest part of the regugitant jet can also be called as 'neck' of the jet [224] and having location just downstream from the orifice and before the jet area [122]. Vena contracta is slightly smaller than the mitral orifice due to boundary effects, so the effective regurgitant orifice area (EROA) can be measured by the vena contracta [323]. If the orifice is fixed then the size of the vena contracta is independent of driving pressure and flow rate [112]. But for dynamic regurgitant orifice vena contracta may change with hemodynamic or during the cardiac cycle [24]. Research [314], [149], [193] and [111] shows that the regurgitant orifice size can be presented by the vena contracta width obtained from the color Doppler imaging. Hence in recent studies measurement of vena contracta is the mostly used method for the MR assessment [60], [262], [271], [314] and [323].

In [262], [274], [149], [60] vena contracta is to be assumed as the accurate method for finding out the severity of MR, using TTE or TEE method. Literature [262] and [228] shows that vena contracta diameter can also be measured by TTE with a good feasibility (between 95% and 97%). But recent study shows that the determination of vena contracta is more feasible by TEE [272]. In case of mitral regurgitation, the vena contracta diameter can vary over time, particularly in the case of mitral regurgitation [269]. In some literature [168] and [93] it is suggested that vena contracta diameter should be measured at the time of its maximal width for mitral regurgitation.

1.8. AUTHOR CONTRIBUTIONS

- To analyze the enhancement, suitable for echcardiographic images log enhancement has been taken and modified for getting the suitable results according to the image. A modified log transformation has been developed, which gives better results than that obtainable using conventional log transformation. Results thus obtained demonstrate that log transformation, as already existing in the literature, does not work well with echocardiographic image but proposed modified log transformation, gives better results. Better balanced contrasted

images are obtained, and these are both important and useful for manual processing as well as for assessment by a clinician, and also for computer analysis.

- Two methods have been developed for speckle noise removal. One is Hybrid Speckle Reducing Anisotropic Diffusion (HSRAD) filter and other is Modified Nonlinear Complex Diffusion (MNCD) filter.

  In first case a hybrid filter is introduced. This filter is combination of speckle removal SRAD and Relaxed median filter. Experiments are carried out on echocardiographic images. Results show speckle reduced edge preserved images. This hybrid filter removes speckle noise as well as removes impulse noise. This model also enhances the edges in the image.

  In second case a new formulation has been proposed for a well-known nonlinear complex diffusion filter. Its diffusion coefficient and the time step size are modified to give fast processing and better results. The proposed MNCD filter smoothes the homogeneous area and enhances the fine details.

- Two methods have been developed for boundary detection. One is Modified Chan-Vese method which is much faster than the Chan-Vese method. In second method a new singed pressure force function (SPF) has been developed for level set method.

  First model; the Fast Region Based Active Contour Model (FRACM) evolves the automatic boundary detection for carrying out segmentation of echocardiographic images. Active contour method is selected for this purpose. There is an enhancement of Chan–Vese paper on active contours without edges. Our algorithm is based on Chan–Vese paper active contours without edges, but it is much faster than Chan–Vese model. Here we have developed a method by which it is possible to detect much faster the echocardiographic boundaries. The method is based on the region information of an image. The regionbased force provides a global segmentation with variational flow robust to noise. Implementation is based on level set theory so it easy to deal with topological changes. In our proposed method, Newton–Raphson method is used which makes possible the fast boundary detection.

  A second model; the New Selective Binary and Gaussian Filtering Regularized Level Set (NSBGFRLS) model deal with novel region based active contour method is developed by

formulating a new signed pressure function (SPF). The method has been applied to the echocardiographic images. The method is useful for other images as well. Level set method in combined with original SPF has not been able to give satisfactory results during the segmentation of echocardiographic images. There are lots of noises present in the echocardiographic images that create difficulties in the segmentation process. The proposed method resolves all these difficulties. The new method also gives the fast response in terms of time taken by CPU and the number of iterations. The presented model is an advancement of Selective Binary and Gaussian Filtering Regularized Level Set (SBGFRLS) method. Proposed model is more robust against images with weak edge and intensity in-homogeneity when compared with the performance of earlier methods.

- Automatic jet area has been obtained by proposing two methods of segmentation.

  The first method; the Region Growing based Mosaic Jet Segmentation (RG-MJS) is base on region based segmentation and is suitable for every image obtained from the echo lab.

  Second method; the Combined Wavelet and Watershed transformation based Mosaic Jet Segmentation (CWW-MJS) having a multistep algorithm has been applied. The first stage of the proposed algorithm is dual-tree complex wavelet transform. Next stage is the watershed transform and then similarity measure has been done to get the final segmented image.
- Vena contracta is the smallest width in this jet area. Region based segmentation has been used which is proceeded by pixel count for getting the smallest width. An automatic method for vena contracta width detection for the severity of the mitral regurgitation (MR) has been developed.

1.9. THESIS ORGANIZATION

Chapter 1 begins with a description of the introduction of the heart. Next section describes the heart physiology explaining the functionality of the heart and blood circulation. Then we discuss the heart related disease. Heart valve related diseases also discussed in the same section. Next we discuss the mitral valve anatomy and mitral valve diseases including mitral regurgitation cause symptoms and diagnosis, which is our main concern. It is also related to the echocardiography basics. After a brief description about echocardiography in introduction section, principles of echo

are discussed in the second section of this chapter. Next section deals with the description of the modes of echocardiography. Two dimensional scanning have been discussed in details on the preceding section. Artifacts during the echocardiography also discussed. Then planes for echocardiography has been discussed which helps in understanding the echocardographic images. Last section shows the advantages and limitations of echocardiography.

Then the literature review is presented according to the problems and objectives. Brief description of my contribution is also given. Then thesis organization has been given in the next section and the last section gives the publication details.

Chapter 2 deals with our first objective i.e. contrast enhancement of echocardiographic images related to second objective i.e. de-speckling of echocardiographic images. After a brief introduction point processing techniques have been discussed. Then next section related to our proposed method i.e. modified log transformation. Results have been discussed in the result section and then chapter closes with some conclusions. Next section gives knowledge about speckle noise. Then some de-speckling methods have been discussed in the next section. A section discussed the performance parameters used to analyze the filter performance. Next section discussed the proposed methods there algorithm, results and performance. The last section concluded the proposed methods.

Chapter 3 related to boundary detection methods related to our objective boundary detection of echocardiographic images. Introduction of this chapters discuss some method of boundary detection in literature. Second section deals with the basics of deformable models. Next section deals with the proposed methods, with their algorithms, results and comparisons. The last section concludes the chapter.

Chapter 4 discusses the automatic jet area detection which is the next objective of this thesis. Giving a brief knowledge about regurgitate jet area in introduction next two section discuss the two different method for finding out the regurgiatnt jet area automatically. This section shows the results with algorithms of the methods. Comparison with clinical data has been performed. Last section concludes the chapter.

Chapter 5 related to automatic vena contracta width detection, our next objective. After an introduction next section presents the algorithm. Results have been shown in the other section. Comparisons have been done with the clinical data. A conclusion closes the chapter.

Chapter 6 conclude the finding outs of the thesis and future scope.

A GUI 'Echocardiographic Image Processing System' has been made to give a man machine interface for clinical use. User manual gives knowledge about the operating method of the GUI. This user manual is attached just after the list of the references in the thesis from pages 163 to 172. Appendix I, Appendix II and Appendix III related to some knowledge about echocardiographic machine, cardiac measurements and transducers used respectively.

1.10. LIST OF PATENTS AND PUBLICATIONS

Patents:

1. A patent entitled "Design and Development of Direct Echocardiographic Read-Out for Evaluation of Cardiac Diseases", has been submitted in the IPR cell of IIT Roorkee for filing on 28-Aug-2012.

Publication in Journals:

1. Kalpana Saini, M. L. Dewal, Manojkumar Rohit, "Detection of Mitral Reguirgitation Severity using Color Histogram", International Journal of Research in Biomedicine and Biotechnology, URP Journels (Accepted).
2. KalpanaSaini, M. L. Dewal, ManojkumarRohit, "A Mathematical Evaluation of Mitral Regurgitation Severity with EROA" Engineering in Medicine and Biology Magazine, IEEE (SCI IP: 2.057) (Communicated).
3. M. L. Dewal, KalpanaSaini, ManojkumarRohit, "Assessment of Mitral Regurgitation Severity with Intensity based Region Growing", Journal of Medical Imaging and Health Informatics, American Scientific Publishers (Communicated).
4. KalpanaSaini, M. L. Dewal, ManojkumarRohit, "Automatic Detection of Vena Contracta Width for the Mitral Regurgitation Assessment", International Journal of Computer Science and Management Research, vol. 2, no. 5, pp. 2455–2460, May 2013.
5. KalpanaSaini, M. L. Dewal, ManojkumarRohit, "Level Set based on New Signed Pressure Force Function for Echocardiographic Image Segmentation", International Journal of Innovation and Applied Studies (Accepted).
6. Kalpana Saini, M. L. Dewal, Manojkumar Rohit, "Automatic Jet Area Detection during Mitral Regurgitation", International Review on Computers and Software (IRECOS), vol. 7 no. 6, pp. 2891-2898, Praise worthy Prize, (Index Copernicus (Journal Master List): Impact Factor 6.14)
7. KalpanaSaini, M.L.Dewal, ManojkumarRohit, "Modified nonlinear complex diffusion filter (MNCDF)", Journal of Echocardiography (Springer), vol. 10, pp.48-55, 2012 .
8. KalpanaSaini, M. L. Dewal, ManojkumarRohit, "A Fast Region-Based Active Contour Model for Boundary Detection of Echocardiographic Images", Journal of Digital Imaging, Springer, vol. 25, no. 2, pp. 271-278, 2012 (SCI IP: 1.421).
9. KalpanaSaini, M. L. Dewal, ManojkumarRohit, "A Modified Hybrid Filter For Echocardiographic Image Noise Removal", International Journal of Signal Processing, Image

Processing and Pattern Recognition,Science and Engineering Support SoCiety(SERSC) Korea, pp.61-72, vol.5, No.2, 2012.

10. Kalpana Saini, M. L. Dewal, Manojkumar Rohit, "Spatial Enhancement and Modified Log Transformation for Echocardiographic Images", International Journal of Biomedical Engineering and Technology (IJBET), Inder Science Vol. 7, No. 4, pp. 327-338, 2011.

Proceedings in E-Books:

1. Kalpana Saini, M. L. Dewal, Manojkumar Rohit, "Statistical Analysis of Speckle Noise Reduction Techniques for Echocardiographic Images", International Conference on Methods and Models in Science and Technology (ICM2ST-11), published in e-book of American Institute of Physics, New York, USA, pp. 95-99, Nov 2011 (Best paper award).
2. Kalpana Saini, M. L. Dewal, Manojkumar Rohit, "Comparitive Study of Edge Detectors in case of Echocardiographic Images" International Conference on Methods and Models in Science and Technology (ICM2ST-10), published in in e-book of American Institute of Physics, New York, USA , pp. 267-271, 25-26 Dec.2010.

Conferences:

1. Kalpana Saini, M. L. Dewal, Manojkumar Rohit, "Segmentation of Mitral Regurgitant Jet Using the Combination of Wavelet and Watershed Transformation", 8th IEEE Colloquium on Signal Processing & Its Applications, Melaka, Malaysia, pp. 74- 79, 23-25th March 2012 (Best paper award).
2. Kalpana Saini, M. L. Dewal, Manojkumar Rohit, "Role of Transducers and Signal Processing in Echocardiography and Effect of Instrument Artifacts", International Conference on Biomedical Engineering and Assistive Technologies (BEATS), National Institute of technology Jalandhar, 17-19 Dec. 2010.
3. Kalpana Saini, M. L. Dewal, Manojkumar Rohit, "Echocardiographic Image Segmentation with Threshold Operation", Proceeedings of 4th International Confrenece on Advance Computing & Communication Technologies Technicallycally sponserd by IEEE, Asia Pacific Institute of Information Technology SD, India, pp.272-275, Oct 30, 2010.

CHAPTER 2

PRE-PROCESSING OF ECHOCARDIOGRAPHIC IMAGES

2.1. INTRODUCTION

The very first thing that a clinician does is the visual examination of the echocardiographic images. The problems that usually encounter are due to the low contrast and noisy appearance of such images besides the limitations in obtaining suitable view of the heart. For the accurate diagnosis of the cardiac disease, it is important that the image is enhanced and made free from the speckle noise.

First section of this chapter devoted to contrast enhancement of echocardiographic images. Image enhancement techniques are used to highlight certain features of interest in an image. Two important examples of image enhancement are: (i) increasing the contrast, and (ii) changing the brightness level of an image so that the image looks better. It is a subjective area of image processing. Logarithmic transform helps us to show the frequency content of an image. This transformation maps a narrow range of low gray level values in the input image into a wider range of the output level. The opposite is true of higher values of input level. This type of transformation is used to expand the values of dark pixels in an image while compressing the higher level values.

Second section of this chapter devoted to de-speckling echocardiographic images. The speckle noise is the kind of noise that immerges on the image on account of de-phased echoes. There are a number of methods that are proposed in the literature by various authors for the enhancement and de-speckling of the echocardiographic images. The chapter intends to present some two newly devised methods which produce much better results in terms of processing the image to render it more suitable for the clinicians to carry out flawless diagnosis.

2.2 CONTRAST ENHANCEMENT OF ECHOCARDIOGRAPHIC IMAGES

This section is devoted to spatial enhancement of echocardiographic images. The log transformation has been modified to give better contrast-enhanced images than the images which are obtainable using conventional log transformation. Log transformation has not given satisfactory results and thus, the need is felt to modify log transformation for echocarcadiographic

images. The results thus obtained thereafter using modified version of the log transformation has drawn better balanced and contrasted images with required contrast improvement index. The images, thus, become more useful for manual processing as well as for assessment by a clinician**.** These images become more suitable for processing using computer.

2.2.1 Log Transformation

The general form of log Transformation is:

$$s = c\log(1+r) \tag{2.1}$$

Where c is a constant, and it is assumed that $r \geq 0$. This transformation maps a narrow range of low intensity values in the input into a wider range of output levels and vice versa. Figure 2.1 shows (a) original image and (b) its log transformation.

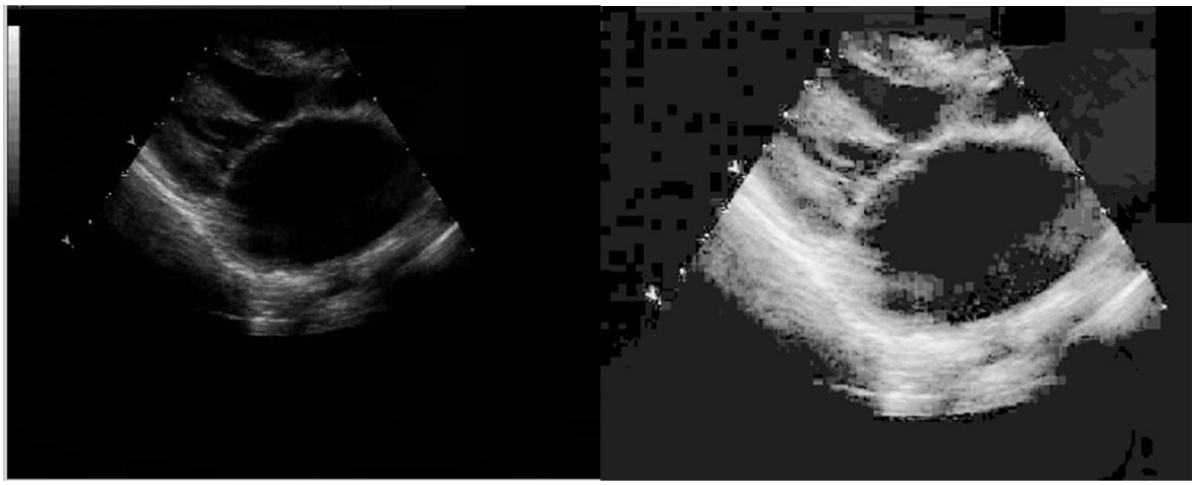

Figure 2.1 (a) Original Image and (b) its Log Transformation

Here, we notice that in case of Echocardiographic images log transformation does not give favorable results because there is no option to change the histogram shifting according to the need of echo cardiographer. So in our next section we have developed a modified log transformation for echocardiographic images.

2.2.2 Modified Log- Transformation for Echocardiographic Images

By considering all the facts discussed in section 2.2.1, we have to choose a technique which enhances the image according to the visual perception of the clinicians and works according to the image. As in previous section 2.2.1, it has been seen that the log transformation does not give

satisfactory results in the contrast enhancement of echocardiographic Images, due to the high white pixel spreading. This white spreading overlaps the important features. Reason of this problem is that more number of pixels will shift in the high intensity value when the log transformation is applied. In order to overcome this problem the figure of 1 of log-transformation is replaced by a variable say a. Thus, named as modified- log-transformation. Which offers a flexible way to analyze the image at different values of a. This value can be changed by the clinician according to the better visualization of the image.

$$s = c\log(a + r) \tag{2.2}$$

2.2.3 Quantitative Measure of Contrast Improvement

Improvement in contrast can be measured by contrast improvement index and can be calculated as in eq. (2.3)

$$C_{II} = \frac{C_{\text{Processed}}}{C_{Orignal}} \tag{2.3}$$

Where $C_{Orignal}$ is the contrast of the image before processing and $C_{\text{Processed}}$ is the contrast of image after applying the contrast enhancement technique.

According to the optical definition, contrast is defined as:

$$C = \frac{mean(P_f) - mean(P_f)}{mean(P_f) + mean(P_b)} \tag{2.4}$$

Where $mean(P_f)$ is the mean of foreground pixels and $mean(P_b)$ is the mean of background pixels.

2.2.4 Results

Figure 2.2 shows the curves between input intensity and output intensity at different values of a .These values varying from 1 to 15,000.

It is noticed that :

- For the value of a ranging from 1 to 25 the images show more growth of white areas.

- For the value of $25 < a \leq 500$ significantly reduce white areas and good contrast image is obtained.
- For the value of $500 < a \leq 1500$ contrast is gradually reduced significantly.
- For the value of $a > 1500$ transformation gives results as identity transformation.

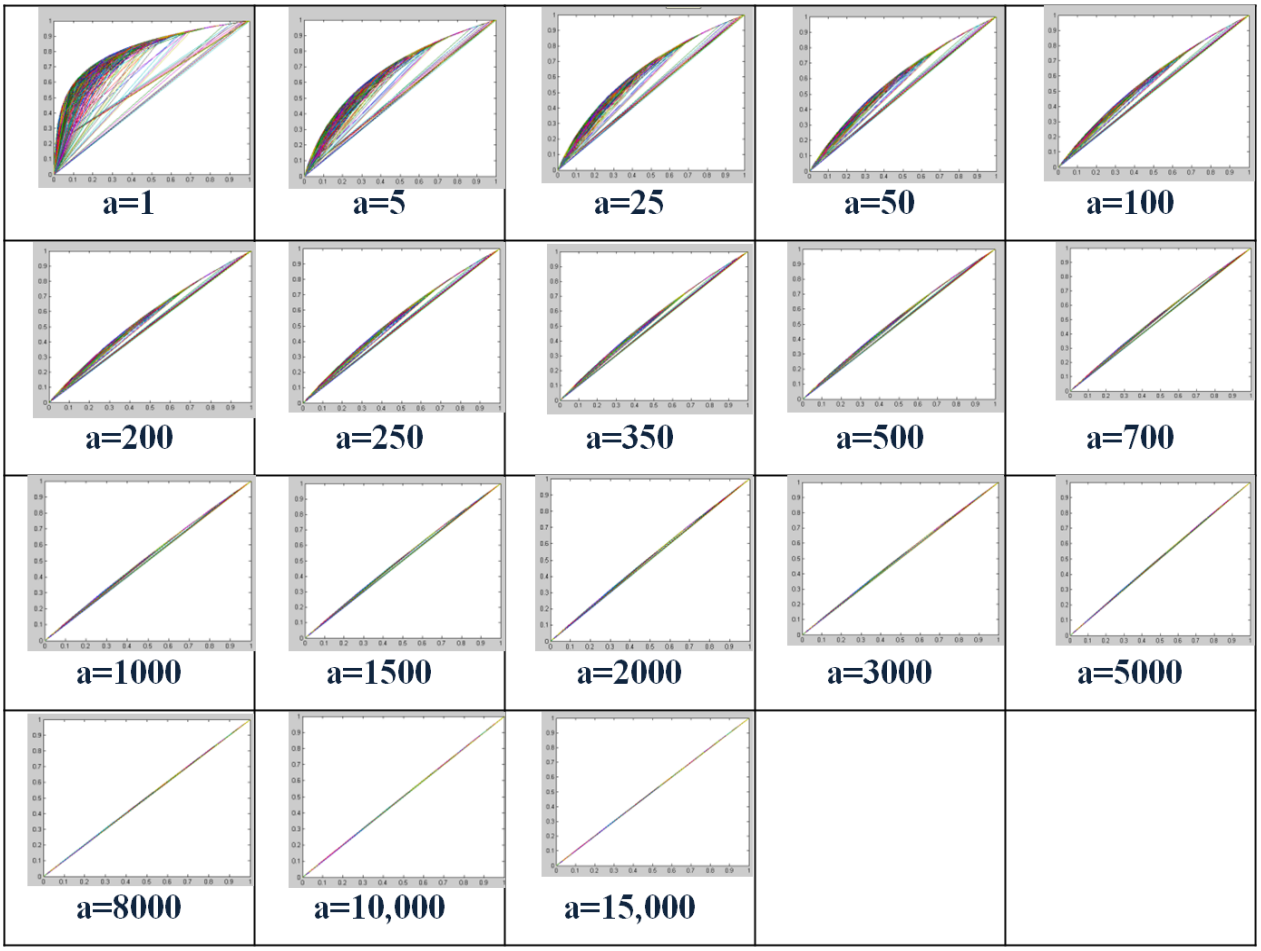

Figure 2.2 Curves between Input Intensity and Output Intensity with Different Values of a in Modified Log Transformation

The corresponding print outs of images are presented in fig. 2.3. So it is shown that there is no change in contrast after a >1500. For example in fig. 2.3a when there is log-transformation $a = 1$, it can be seen that there is a lot of white portion spreads abruptly in the image. So it is very difficult to visualize the chambers. This white noise spreads even inside the chambers of the heart in the image. When the value of a increases such as in case of fig. 2.3 at value of $a = 5$ then this white

effect gets reduced and chambers become slightly free from this white noise. This effect reduces gradually on increasing the value of a from $a=5$ to $a=1500$ for the particular image. This variation changes from image to image. The appearance of chamber and their boundaries remain unchanged on further increase in the value of a . In short we can say that if the value of a is equal to 1, then this transformation maps a narrow range of low intensity values in the input into a wider range of output levels. As the value of a increases this range is decreased.

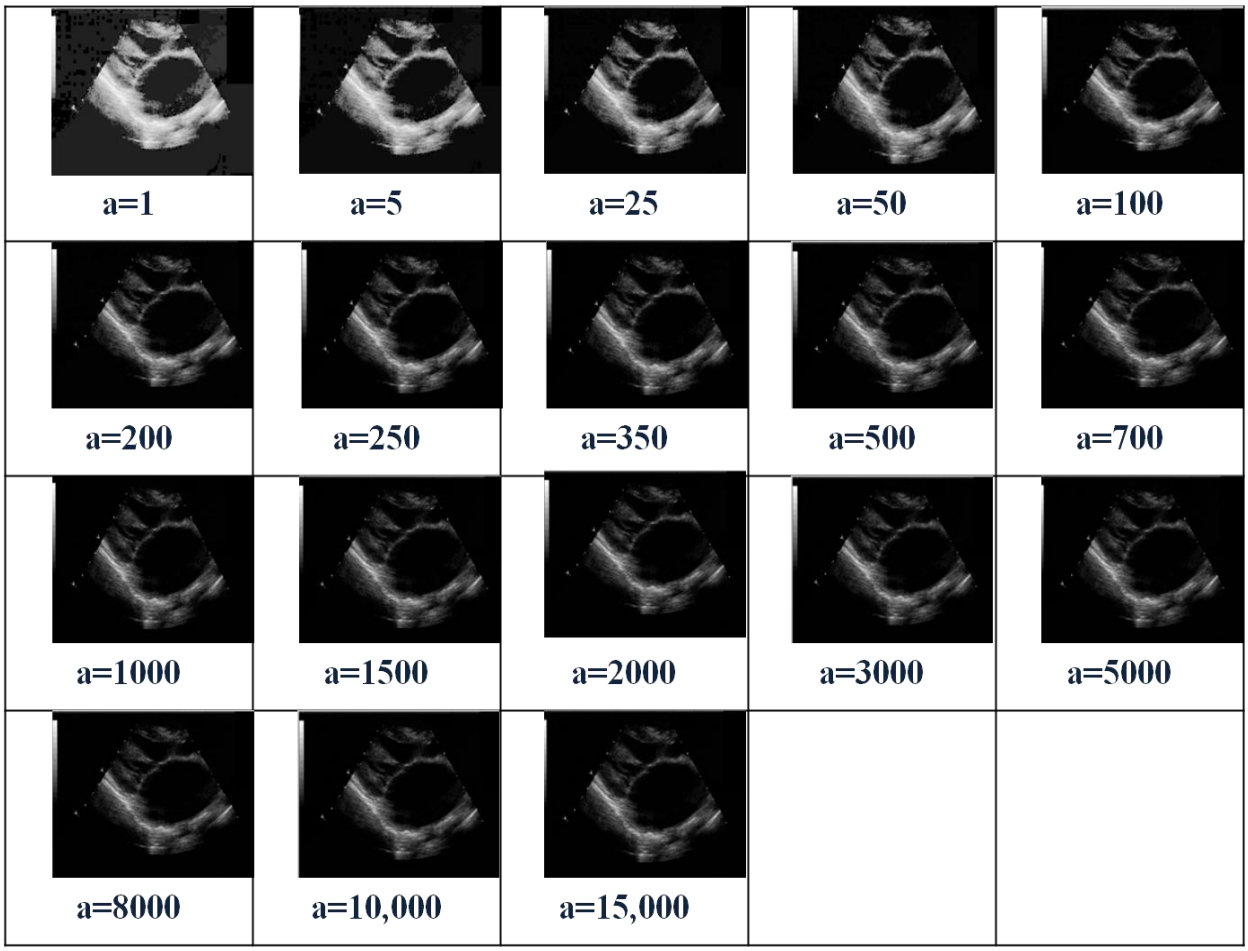

Figure 2.3 modified Log Transformed Image with Different Value of a

The log function has the important characteristic that it compresses the dynamic range of images with large variation of pixel values. However, the histogram of this data is usually compact and uninformative and there are less or more changes in the contrast of the image. This change can only be seen by the quantitative analysis of the image such as contrast improvement index.

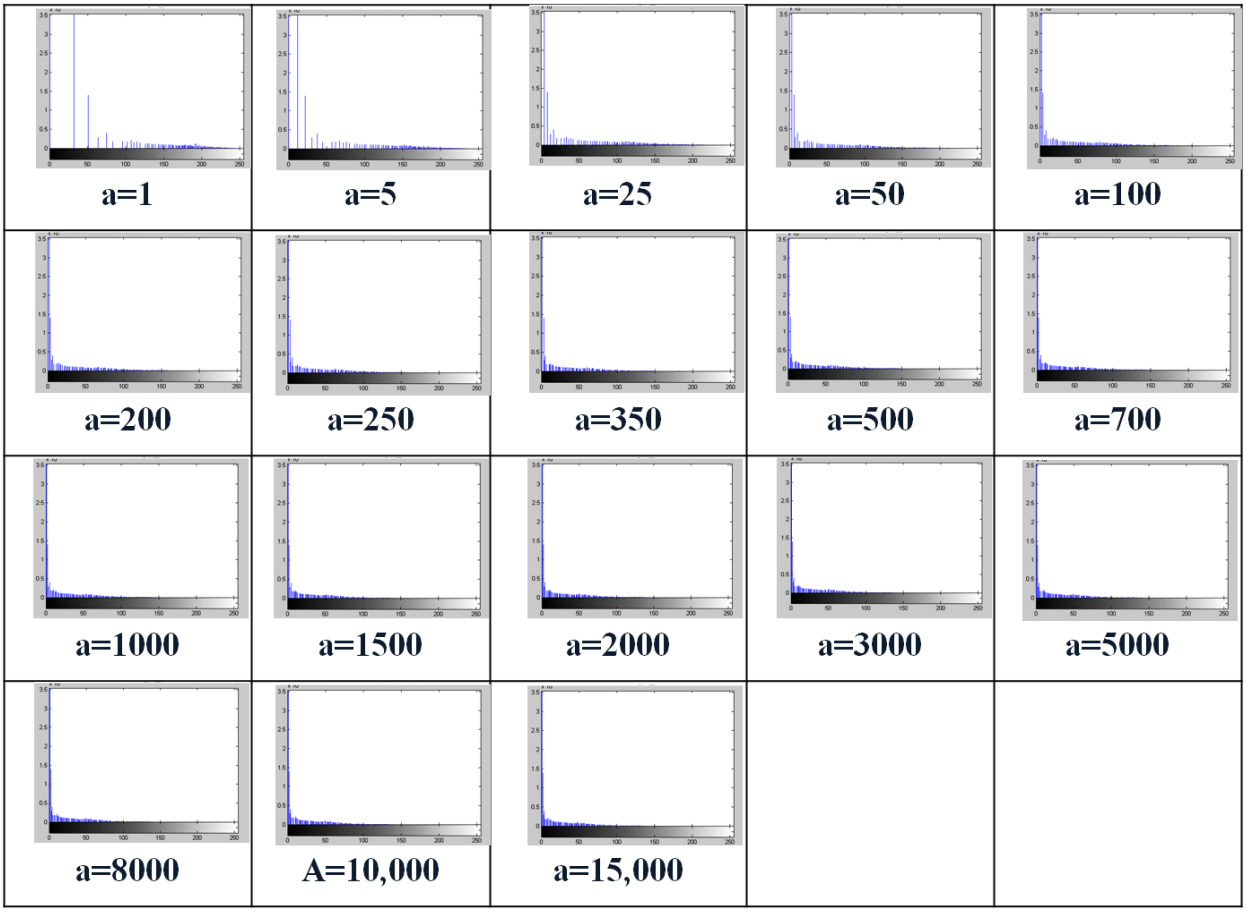

Figure 2.4 Intensity Histogram on Different Values of a in Modified Log Transformation

Figure 2.4 explains that histogram of the images with different values of a. When a is 1 histogram having the most pixels on the higher intensity value region hence the image having the much white portion. As we move on increasing values of a histogram spreads over the intensity level. At a stage shafting of pixels get constant. From this figure it is clear that at different values of a intensity span is changed. Value of a can be changed to get an image with highest contrast image.

Table 2.1 shows the contrast and contrast improvement indices of the image on different values of a. When $a=1$, this is the case of log transformation. In this case contrast is very poor as can be seen in table 2.1; but by using the proposed transform clinicians are able to get the image with varaiable contrast according to their requirement. In this case after $a \geq 1500$, C_{II} value becomes close to 1. This means at that condition transform behaves like an identity transform.

Table 2.1: Quantitative Evaluation of Contrast Improvement with $C_{Orignal}$ = 0.9023

Value of a	Contrast value of processed image $C_{Processed}$	Contrast improvement index C_{II}
1	0.3129	0.34678
5	0.5012	0.555469
25	0.6911	0.765932
50	0.72	0.797961
100	0.7703	0.853707
200	0.7812	0.865787
250	0.8084	0.895933
350	0.8249	0.914219
500	0.8352	0.925634
700	0.9167	1.015959
1000	0.9117	1.010418
1500	0.9102	1.008755
2000	0.9092	1.007647
3000	0.9082	1.006539
5000	0.9074	1.005652
8000	0.9069	1.005098
10000	0.9067	1.004876
15000	0.9065	1.004655

2.3 DE-SPECKLING OF ECHOCARDIOGRAPHIC IMAGES

Noise models can be classified as additive and multiplicative noise. Reduction of additive noise is quite easy, but the multiplicative noise depends on the properties of the images. Its modeling is difficult so it is very tough job to remove this multiplicative noise. Speckle noise is a type of multiplicative noise which generates due to the de-phased echoes from the scatters. Grainy appearance of speckle noise masks the features and makes diagnosis difficult. It also affects the performance of segmentation.

One of the main problems associated with the enhancement of the echocardiographic image as well in ultrasound images [40] is the presence of speckle noise. This type of noise, which is coherent with the nature of the ultrasound, is one of the main sources of impoverishment in the resolution and lack of ability to detect the objects of the image, which makes up the content of the clinical information. Images containing multiplicative noise have the characteristic that the brighter the area the noisier it is. A starting condition in any scheme oriented to the reduction of this type of noise is that the designed procedure must not imply a loss of contrast in the most significant features of the image. The primary goal of speckle filtering ought to be the reduction of speckle noise without sacrificing the information content to enhance the diagnostic value of the image and for future segmentation or tracking of non-rigid anatomical structures.

2.3.1 Speckle Noise

A system of images is named as coherent when the system is subjected to the action of a coherent illumination, that is, when the source points of the luminous radiation have relations of fixed phase and, though their phases fluctuate randomly, they do it in a synchronized way in order to keep a fixed relative phase. In this class of systems, and because of fluctuation of the source points in tune, the relations of the fixed phase allow to establish patterns of both destructive and constructive interferences. When a coherent ultrasonic radiation is reflected on a surface which has the same size as the radiant wave length, the interference of the waves produces a noise called speckle, whose nature is different from the so called additive noise.

If the received envelope signal from the ultrasound imaging system output of the beam former is captured before the logarithmic compression, the approximation of speckle noise model is given as multiplicative and it may be defined as:

$$z_{i,j} = x_{i,j} n_{i,j} + a_{i,j},\ j,i \in N \tag{2.5}$$

Where $z_{i,j}$, is the middle pixel having noise in the middle of the moving window, $x_{i,j}$, represents the pixel which is free from noise, $n_{i,j}$ and $a_{i,j}$ represent the multiplicative and additive noise (independent of $z_{i,j}$, with mean 0), respectively, and i, j, are the indices of the spatial locations that belong to in the 2D space of real numbers, $i, j \in R^2$.This model is particularly suitable for our purpose, as it can be applied on the images as displayed by the ultrasound machine rather than the envelope detected echo signal [276], [170], [308]. De-speckling consists in estimating the true intensity of $x_{i,j}$, as a function of the intensity of the pixel $z_{i,j}$, and some local statistics calculated on a neighbourhood of this pixel. Wagner et al. [248] has shown that the histogram of amplitudes within the resolution cells of the envelope detected RF-signal backscattered from a uniform area with a sufficiently high scatterer density has a Rayleigh distribution with μ proportional to the σ, $\left(\mu/\sigma = 1.91\right)$. This implies that speckle could be modeled as multiplicative noise. However, the signal processing stages inside the scanner, (mainly the logarithmic compression) in order to adjust the large echo dynamic range (50-70dB) to the 8-bits of the digitization in the scan converter modify the statistics of the original signal. The model in (2.2.1) has been shown to be valid for images as displayed by the ultrasound scanner in studies [247], [170], [230], [254]. In particular it should be noted, that speckle is no longer multiplicative in the sense that on homogeneous regions, where $x_{i,j}$, can be assumed constant, the mean is proportional to the variance $\left(\mu \approx \sigma^2\right)$, rather than the standard deviation $\left(\mu \approx \sigma\right)$, [2], [170], [320], [308].

The computation of variance of the speckle noise, σ^2, may be from the image which is compressed logarithmically, by considering the dimensions of many windows larger than the filtering window and taking the average noise variance over them. The noise variance in each window is computed as [308]:

$$\sigma_n^2 = \sum_{i=1}^{p} \sigma_p^2 / \overline{g}_p \tag{2.6}$$

Where σ_p^2 and $\bar{g}_p$, are the variance and the mean of the noise respectively in the selected windows and p, is the index covering all windows in the whole image [166], [308]. We may therefore calculate the variance of the speckle noise, σ_n^2 from the noise image characteristics, namely from $\bar{g}_p$, and σ_p^2, over the image. The speckle noise variance, σ_n^2 will be used in some of the de-speckle filters.

As shown earlier, nonlinear processing such as logarithmic compression, employed on ultrasound echo images, affects the speckle statistics in such a way that the local mean becomes proportional to the local variance rather than the standard deviation. More specifically, logarithmic compression affects the high intensity tail of the Rayleigh and Rician PDFs more than the low intensity part. As a result the speckle noise becomes very close to white Gaussian noise corresponding to the uncompressed Rayleigh signal [308].

Since the effect of additive noise, such as sensor noise, is considerably smaller and less significant compared with that of the multiplicative noise component [2], [166] such as:

$$\left(\left\|\alpha_{i,j}\right\|^2 << \left\|n_{i,j}\right\|^2\right) \tag{2.7}$$

then the filters utilizing first order statistics such as the variance and the mean of the neighborhood, may be derived from (2.5) with the following multiplicative model as:

$$z_{i,j} \approx x_{i,j} n_{i,j} \tag{2.8}$$

The logarithmic amplification transforms the model in eq. (2.8) into the classical signal in additive noise form as:

$$\log\left(z_{i,j}\right) = \log\left(x_{i,j}\right) + \log\left(n_{i,j}\right) \tag{2.9}$$

$$g_{i,j} = f_{i,j} + nl_{i,j} \tag{2.10}$$

In equation (2.10) the term $\log\left(z_{i,j}\right)$, is the after compression observed pixel on the display of the ultrasound, is denoted by $g_{i,j}$, and the terms $\log\left(n_{i,j}\right)$ and, $\log\left(x_{i,j}\right)$ which are the noise component and noise free pixel, as $f_{i,j}$ and $nl_{i,j}$ respectively, after logarithmic compression.

2.3.2 De-Speckling Methods

De-speckling is always a trade-off between noise suppression and loss of information, something that experts are very concerned about. It is therefore attractive to keep as much of important information as possible. Despeckle filtering can be used as a pre-processing step for image segmentation [57], or image registration [240], techniques. By suppressing the speckle the performance of these techniques can be improved.

There are some despeckle filters, originated from the Synthetic Aperture Radar (SAR) community [216], [152], [21], [22], [329], [249], [97], [157] and [34]. These techniques have later been applied to ultrasound imaging since the early 1980's [213], which may be described with the same statistical model as the one describing the SAR images. The most widely used filters in SAR and ultrasound imaging include the Frost [195], [311], Lee [151]-[154] and the Kuan [79], [80].

Most adaptive filters only use local statistical information related to the central pixel to be filtered [54], [295], [152-154], [56]. Some additional information may be used from the despeckle window (see next subsection) to improve despeckling, by utilising the higher order statistics of the image. Many adaptive despeckling methods have been proposed, such as the Lee filter [151]-[154], Frost [195], [311], Kuan [79], [80], and Lopes [21], [22]. Furthermore, the Gaussian filter function has been used for despeckling but it was shown [89] that this form of filtering is not suitable for speckle noise, as it does not take into consideration the true positions of object boundaries. However, the full removal of speckle noise without losing any information in ultrasound images is still a long way off. When additionally edges are present in the filtering window, the central pixel gray level replaced by the information from all its neighbourhood pixels will not be correct. Lee has therefore introduced [153] an edge detector, which was implemented in his old algorithm version [151].

Since the early 1980's, various researchers have presented the progress that has been made in quantitative ultrasound imaging and reported techniques that have been applied on ultrasound images for de-speckling [195]. The certain limitations which are present in despeckling filtering techniques in majority seen in the literature are summarized as follows:

a) They are sensitive to the size and shape of the window [54], [154], [82], [334], [57], [166]. The use of different window sizes will greatly affect the quality of the processed images. If the window is too large over smoothing will occur, subtle details of the image

will be lost in the filtering process and edges will be blurred. In case of small size window the smoothing capability of the filter will decrease and the speckle noise will not be removed and thus not effective. In homogenous areas, the larger the window size, the more efficient is the filter in reducing the speckle noise. In heterogeneous areas the smaller the window size, the more it is possible to keep subtle image details unchanged. Our experiments showed that a 7x7 window size is a fairly good choice. The images presented in this work have been processed either by 7x7 or by 5x5 pixel windows.

b) Some of the de-speckling methods, require thresholds for filtering process, known as window approaches [54], [177], [152], [53], the threshold is estimated empirically. If the threshold value is not selected properly, it may lead to filter averaging and noisy boundaries from leaving the sharp features unfiltered [177], [152], [53].

c) Most of the existing despeckle filters just inhibit smoothing near the edges and do not enhance edges. When in the filtering window there is an edge, the smoothing will be due high coefficient of variation at these places. Therefore, speckle will remain as it is in the neighborhood of an edge after filtering. On the edge, all smoothing is precluded so these types of filters are not directional filters. A parallel direction smoothing is allowed, instead of inhibiting smoothing in directions perpendicular to the edges of the images.

Speckle reduction techniques that have been proposed in the literature are shown in Table 2.1 and are summarized under the following categories: local statistics, median filtering, linear scaling, homogeneity, geometric, logarithmic, homomorphic, anisotropic diffusion, and wavelet filtering. Some of the local statistic filters are the Lee [151]-[154], Frost [195], [311], Kuan [79], [80], filters.

The Lee and Kuan filters having the same structure, in which the Kuan filters is a generalization of the Lee filter. Both filters form an output image by computing a linear combination of the central pixel intensity in a filter window with the average intensity of the window and a coefficient of variation inside the moving window. Kuan considered a multiplicative speckle model and designed a linear filter, based on the minimum-mean-square error (MMSE) criterion, optimal when the intensity image is Gaussian distributed. The Lee [152] MMSE filter was a particular case of the Kuan filter based on a linear approximation made for the multiplicative noise model. The Frost [195] makes a balance between the averaging and the all-pass filters. It was

designed as an adaptive Wiener filter that assumed an autoregressive exponential model for the image.

In the linear scaling group the gray level values are linearly scaled to de-speckle the image [53]. The despeckling in the homogeneity group is based on the most homogeneous neighbourhood around each image pixel [43]. Non-linear iterative algorithms are used in Geometric filters [177], [300], the pixel values are increased or decreased in a neighborhood according to their relative values. The similar method to the logarithmic point operation used in histogram improvement is homomorphic filtering [158], [289]. In this the bright pixels which are dominant, will de-emphasised. In the homomorphic filtering the logarithmic transformation of the image is done, then the FFT is applied on the image, and then despeckling will be done, next step is the inverse FFT calculation, to get Back the exponential transformed.

In present literature there are some non-linear filtering techniques for de-speckle filtering methods, such as anisotropic diffusion [221], [334], [273], [162], [166], [187] and [234], speckle reducing anisotropic diffusion [334], and coherence anisotropic diffusion [351], they utilize the coefficient of variation to simultaneously perform the contrast enhancement and noise reduction. [334]. Furthermore, in the wavelet filters category, a realistic distribution of the wavelet coefficients is used for suppressing the speckle noise [34], [2], [292], [324], [320] and [75], where only the useful documented wavelet coefficients are to be utilized. A pre-processing stage which consists of a logarithmic transform for the separation of noise from the original image is used in the wavelet methods. There are different wavelet shrinkage approaches, which are employed, based on Donoho's work [75].

Some other researchers have tried in the past to despeckle SAR images by averaging of uncorrelated images obtained from different spatial positions [178]. These temporal averaging and multi-frame methods aimed to increase the SNR by generating multiple uncorrelated images that are summed incoherently to reduce speckle [53], [263]. Despite being simple and fast, these approaches suffer from two limitations.

First, in order to produce uncorrelated ultrasound images, the transducer has to be translated at least by about half its element width for each of the generated frames [46]. Second, temporal averaging based on transducer movement causes the loss of small details such as small vessels and texture patterns because of blurring. For the above reasons this procedure has been proved to be

Table 2.2: An Overview of De-Speckle Filtering Techniques

Speckle Reduction Techniques	Investigator	Method	Filter Name
Local Statistics	[54], [295], [151]-[154], [156], [195], [311], [79], [80], [21], [22], [329], [249] [54], [295], [53] [54], [211] [54], [232] [250], [8], [158]	Moving window utilizing local statistics: a) Mean (μ), variance (σ^2) b) Mean $\sigma^2, \sigma^3, \sigma^4$. c) Homogeneous mask area filters. d) 1-D, μ and σ^2 filter. e) Wiener filtering.	**lsmvminmax, lsmv, lemva, lsmv1d, lsmv_lee** **lsmvske1d, lsmvsk2d** **lsminsc, lsminv1d, wiener**
Median Filtering	[250], [8], [158]	Median filtering	**median**
Linear Scaling	[54]	Linear scaling of the gray level values.	**ls, ca, lecasort**
Homogeneity	[54], [49]	Based on the most homogeneous neighbourhood around each image pixel.	**homog**
Geometric	[177], [300]	Non-linear iterative filter.	**gf4d, gfminmax**
Logarithmic	[126], [263]	Image is logarithmically transformed then filtered for suppressing additive noise (wiener or median [21]). Image is then exponentially back transformed.	**lslog**
Homomorphic	[158], [263], [289]	The idea is similar to the logarithmic point operations used in histogram improvement: de-emphasize the dominant bright image pixels.	**homo**
Anisotropic Diffusion	[263], [289], [273], [195] [311], [333] [333], [166]	Non-linear filtering technique for simultaneously performing contrast enhancement and noise reduction. Exponential damp kernel filters utilizing diffusion. Anisotropic diffusion based on the coefficient of variation. Coherence enhancing diffusion.	**ad, lsmedcd, lsmedc** **adsr** **nldif**
Wavelet	[34], [2], [96], [292], [364]	Realistic distribution of the wavelet coefficients. Only the useful wavelet coefficients are utilized.	**waveltc**

not suitable for despeckle filtering. It is most suitable for additive noise reduction [54], [85]. Another disadvantage of this method is that multiple images from the same object are required [177], [295], [154], [156]. Other researchers applied their techniques on ultrasound images of the kidney [2], echocardiograms [324], heart [166], abdomen [166], pig heart [320], liver [205], SAR images [90], [310], [82], [34], [96], [155], real world [79], [234], and artificial images [6], [117], [166], [320]. They used statistical measures like the mean, variance, median, MSE, image contrast, and visual perception evaluation made by experts, to evaluate their techniques. They compared their despeckling techniques with the Lee filter [152], homomorphic filtering [289], median filter [278], and diffusion filtering [187], [234].

2.3.3 Performance Evaluation Parameters

For evaluating the performance of filtering parameters chosen in the present work are Peak Signal to Noise Ratio (PSNR), Universal Image Quality Index (Qi), Mean Absolute Error (MAE), Mean Square Error (MSE) and Root Mean Square Error (RMSE).

The noise level is measured by standard deviation of the image

$$\sigma = \sqrt{\frac{1}{N}\sum(g_i - f_i)} \tag{2.11}$$

Where i=1, 2,3……..N, f_i is the mean gray level value of the original image and g_i is the gray level value of the pixels of noise-removed image, and N is the total number of pixels in the image.

PSNR is the ratio between the maximum possible power of a signal and the power of corrupting noise that affects the fidelity of its representation. Because many signals have a very wide dynamic range, PSNR is usually expressed in terms of the logarithmic decibel scale.

$$PSNR = 20.\log_{10}\left(\frac{MAX_g}{RMSE}\right) \tag{2.12}$$

Higher the value of PSNR better is the image quality.

The universal image quality index (Qi) measures the distortion between the two images. It is the combination of three factors; the loss of correlation, luminance distortion and the contrast distortion.

$$Qi = \left(\frac{4\sigma_{gu}\bar{g}\bar{u}}{\sigma_g^2 + \sigma_u^2\left[\left(\bar{g}\right)^2 + \left(\bar{u}\right)^2\right]} \right) \tag{2.13}$$

Where $g = \{g_i \,|\, i = 1, 2, ..., N\}$ and $u = \{u_i \,|\, i = 1, 2, ..., N\}$ are the original and the test images, respectively. And

$$\bar{g} = \frac{1}{N}\sum_{i=1}^{N} g_i \ , \ \bar{u} = \frac{1}{N}\sum_{i=1}^{N} u_i \ ,$$

$$\sigma_g^2 = \frac{1}{N-1}\sum_{i=1}^{N}\left(g_i - \bar{g}\right)^2 \ , \ \sigma_u^2 = \frac{1}{N-1}\sum_{i=1}^{N}\left(u_i - \bar{u}\right)^2 \ , \text{ and}$$

$$\sigma_{gu} = \frac{1}{N-1}\sum_{i=1}^{N}\left(g_i - \bar{g}\right)\left(u_i - \bar{u}\right)$$

In terms of three components as mentioned above we can break it into three parts as follows:

$$Qi = \frac{\sigma_{gu}}{\sigma_g\sigma_u} \cdot \frac{2\bar{g}\bar{u}}{\left(\bar{g}\right)^2 + \left(\bar{u}\right)^2} \cdot \frac{2\sigma_g\sigma_u}{\sigma_g^2 + \sigma_u^2} \tag{2.14}$$

It can be seen that first component is the correlation coefficient between input and output images with dynamic range [-1, 1]. Second component shows the closeness of the luminance between two images with range [0, 1] and the third component measures similarity in the contrast. Its range of values is also [0, 1].

The Mean Absolute Error (MAE) is used to measure how close forecasts or predictions are to the eventual outcomes. It is formulated as:

$$MAE = \frac{1}{N}\sum_{i=1}^{N}\left|g_i - u_i\right| = \frac{1}{N}\sum_{i=1}^{N}\left|e_i\right| \tag{2.15}$$

Here e_i is the error between input and output signal. Lower values of MAE, MSE and RMSE ensure a good quality filter.

The Mean Square Error (MSE) is defined as given below in eq. (2.16)

$$MSE = \frac{1}{N}\sum_{i=1}^{N}\left[g_i - u_i\right]^2 \tag{2.16}$$

And Root Mean Square Error (RMSE) is given by

$$RMSE = \sqrt{\frac{1}{N}\sum_{i=1}^{N}\left[g_i - u_i\right]^2} = \sqrt{MSE} \tag{2.17}$$

2.3.4 Proposed De-Speckling Methods for Echocardiograhic Images

2.3.4.1 Method 1: Hybrid Speckle Reducing Anisotropic Diffusion filter (HSRAD)

In the present method the SRAD [334] has been used in combination with relaxed median filter [6]. SRAD not only preserves edges but also enhances edges by inhibiting diffusion across edges and allowing diffusion on either side of the edge. SRAD is adaptive and does not utilize hard thresholds to alter performance in homogeneous regions or in regions near edges and small features. The new diffusion technique is based on the same minimum mean square error (MMSE) approach to filtering as the Lee (Kuan) and Frost filters. In fact, it has been shown that the SRAD can be related directly to the Lee and Frost window-based filters. So, SRAD is the edge sensitive extension of conventional adaptive speckle filter, in the same manner that the original Perona and Malik anisotropic diffusion [234] is the edge sensitive extension of the average filter. In this sense, the application of anisotropic diffusion has been extended to applications such as radar and medical ultrasound in which signal-dependent, spatially correlated multiplicative noise is present.

SRAD filter de-speckles the image with edge preservation but impulse noise is remained over the images. So a hybrid filter has been modeled in proposed method which is the combination of SRAD and relaxed median filter. This hybrid modal is able to give noise free image.

Given an intensity image $I_0(x,y)$ having finite power and no zero values over the image support Ω, the output image $I(x,y;t)$ is evolved according to the following PDE:

$$\begin{cases} \partial I(x,y;t)/\partial t = div[c(q)\nabla I(x,y;t)] \\ I(x,y;0) = I_0(x,y), (\partial I(x,y;t)/\partial \vec{n})\big|\partial\Omega = 0 \end{cases} \tag{2.18}$$

Where $\partial\Omega$ denotes the border of Ω, $\vec{n}$ is the outer normal to the $\partial\Omega$, and , the diffusion coefficient is:

$$c(q) = \frac{1}{1+[q^2(x,y;t)-q_0^2(t)]/[q_0^2(t)/[q_0^2(t)(1+q_0^2(t))]} \tag{2.19}$$

Or

$$c(q) = \exp\left\{-\left[q^2(x,y;t)-q_0^2(t)\right]/\left[q_0^2(t)(1+q_0^2(t)\right]\right\} \tag{2.20}$$

In (2.19) and (2.20), $q(x,y;t)$ is the instantaneous coefficient of variation determined by

$$q(x,y;t) = \sqrt{\frac{(1/2)\left(|\nabla I / I|\right)^2 - \left(1/4^2\right)\left(\nabla^2 I / I\right)^2}{\left[1+\left(1/4\right)\left(\nabla^2 I / I\right)\right]^2}} \tag{2.21}$$

And $q_0(t)$ is the speckle scale function. We call (2.21) the SRAD PDE.

In the SRAD, the instantaneous coefficient of variation $q(x,y;t)$ serves as edge detector in speckle imagery. The function exhibits high values at edges or on high-contrast features and produces low values in homogeneous regions. Speckle scale function effectively controls the amount of smoothing applied to the image by SRAD. It is estimated using

$$q_0(t) = \sqrt{\frac{\mathrm{var}[z(t)]}{\overline{z(t)}}} \tag{2.22}$$

Where $\mathrm{var}[z(t)]$ and $\overline{z(t)}$ are the intensity variance and mean over a homogeneous area at t, respectively.

Because of the need of computing eq. (2.22), the SRAD requires knowing a homogeneous area inside the image being processed. Although it is not difficult for a user to select a homogeneous area in the image, it is nontrivial for a computer. So, automatic determination of $q_0(t)$ is desired in real applications to eliminate heuristic parameter choice.

First of all, we state that $q_0(t)$ can be approximated by

$$q_0(t) \approx q_0 \exp[-\rho t] \tag{2.23}$$

Where ρ is a constant, and q_0 is the speckle coefficient of variation in the observed image. For fully developed speckle, $q_0 = 1$, for ultrasound intensity data (without compounding) and $q_0 = 1/\sqrt{N}$ for N -look SAR intensity data. For partially correlated speckle, q_0 is less than unity.

Here is the derivation of eq. (2.23). As we expected, in a uniform area the diffusion should be isotropic. Adopting the discrete isotropic diffusion update, we have

$$I_{i,j}^{t+\Delta t} = I_{i,j}^{t} + \frac{\Delta t}{4}(I_{i+1,j}^{t} + I_{i-1,j}^{t} + I_{i,j+1}^{t} + I_{i,j-1}^{t} - 4I_{i,j}^{t}) \tag{2.24}$$

Given $\sigma(t)$, the standard deviation of $I_{i,j}^{t}$ in a homogeneous region, we can estimate the standard deviation of $I_{i,j}^{t+\Delta t}$ in the region. Assuming that pixels in the region are stationary in dependent and identically distributed. Statistical formula for the variance of a sum of random variables

$$\sigma(t+\Delta t) = \sqrt{(1-\Delta t)^2\sigma^2(t) + (\Delta t/4)^2 4\sigma^2(t)} \tag{2.25}$$

On the other side, the local means remains the same before after one iteration. So, we have

$$q_0(t+\Delta t) = q_0(t)\sqrt{(1-\Delta t)^2 + (\Delta t)^2/4} \tag{2.26}$$

For $\Delta t << 1$, the $(\Delta t)^2$ terms in eq. (2.26) can be neglected, and we have

$$\sqrt{1-2\Delta t} \approx 1-\Delta t \tag{2.27}$$

By Taylor series expansion and neglecting the second and higher order terms. So eq.(2.26) becomes

$$\dot{q}_0(t) + q_0(t) \approx 0 \tag{2.28}$$

Where $\dot{q}_0(t)$ is the first derivative of $q_0(t)$ with respect to t. solving eq.(2.28), yields

$$q_0(t) \approx q_0 \exp[-t] \tag{2.29}$$

Relaxed median filter has been used here in combination with SRAD to remove large spike noises.

Let $\{X_i\}$ be a $m-$dimensional sequence, where the index $i \in Z^m$. A sliding window is defined as a subset $W \subset Z^m$ of odd size $2N+1$. Given Sliding window W, define $W_i = \{X_{i+r} : r \in W\}$ to be the window located at position i.

If we let X_i and Y_i be the input and the output at location i, respectively, of the filter, then we have for the standard median (SM) filter:

$$Y_i = med\{W_i\} = med\{X_{i+r} : r \in W\} \tag{2.30}$$

Where $med\{.\}$ denotes the median operator.

Denote by $[W_i]_{(r)}, r = 1,.....2N+1$ the r^{th} order statistic of the samples inside the window W_i:

$$[W_i]_{(1)} \le [W_i]_{(2)} \le .....[W_i]_{(2N+1)} \tag{2.31}$$

The relaxed median filter works as follows: two bounds l and u lower and upper, respectively—define a sub list inside the $[W_i]_{(.)}$, which contains the gray levels that we assume to be good enough not to be filtered.

If the input belongs to the sub-list, then it remains unfiltered, otherwise the standard median filter is output.

Let $m = N+1$ and l, u such that $l \le m \le u \le 2N+1$. The relaxed median filter with bounds l and u is defined as:

$$Y_i = RM_{lu}\{W_i\} = \begin{cases} X_i & if X_i \in [[W_i]_{(l)}, [W_i]_{(u)} \\ [W_i]_{(m)} & otherwise \end{cases} \tag{2.32}$$

Where $[W_i]_m$ is the median value of the samples inside the window W_i.

The discrete isotropic diffusion update from eq. (2.18) is

$$I_{i,j}^{t+\Delta t} = I_{i,j}^{t} + \Delta t(\nabla^2 I_{i,j}^{t}) \tag{2.33}$$

$$\text{Where} \qquad \nabla^2 I_{i,j}^{t+\Delta t} = \frac{\Delta t}{4}(I_{i+1,j}^{t} + I_{i-1,j}^{t} + I_{i,j+1}^{t} + I_{i,j-1}^{t} - 4I_{i,j}^{t})$$

Where Δt is time space step size.

Relaxed median filter has been used here in combination with SRAD to remove large spike noises. The proposed hybrid method is defined as follows:

$$I_{i,j}^{t+\Delta t} = RM_{l.u}[I_{i,j}^{t} + \Delta t(\nabla^2 I_{i,j}^{t})] \quad (2.34)$$

Where *RM* is the relaxed median filter with lower bound l and upper bound u .The lower bound and upper bounds for relaxed median used in the experiments are 3 and 5 respectively.

2.3.4.2 Results

Here we show example which results from proposed hybrid model. Fig. 3.5 shows the echocardiographic images taken from different views of heart of different patients.

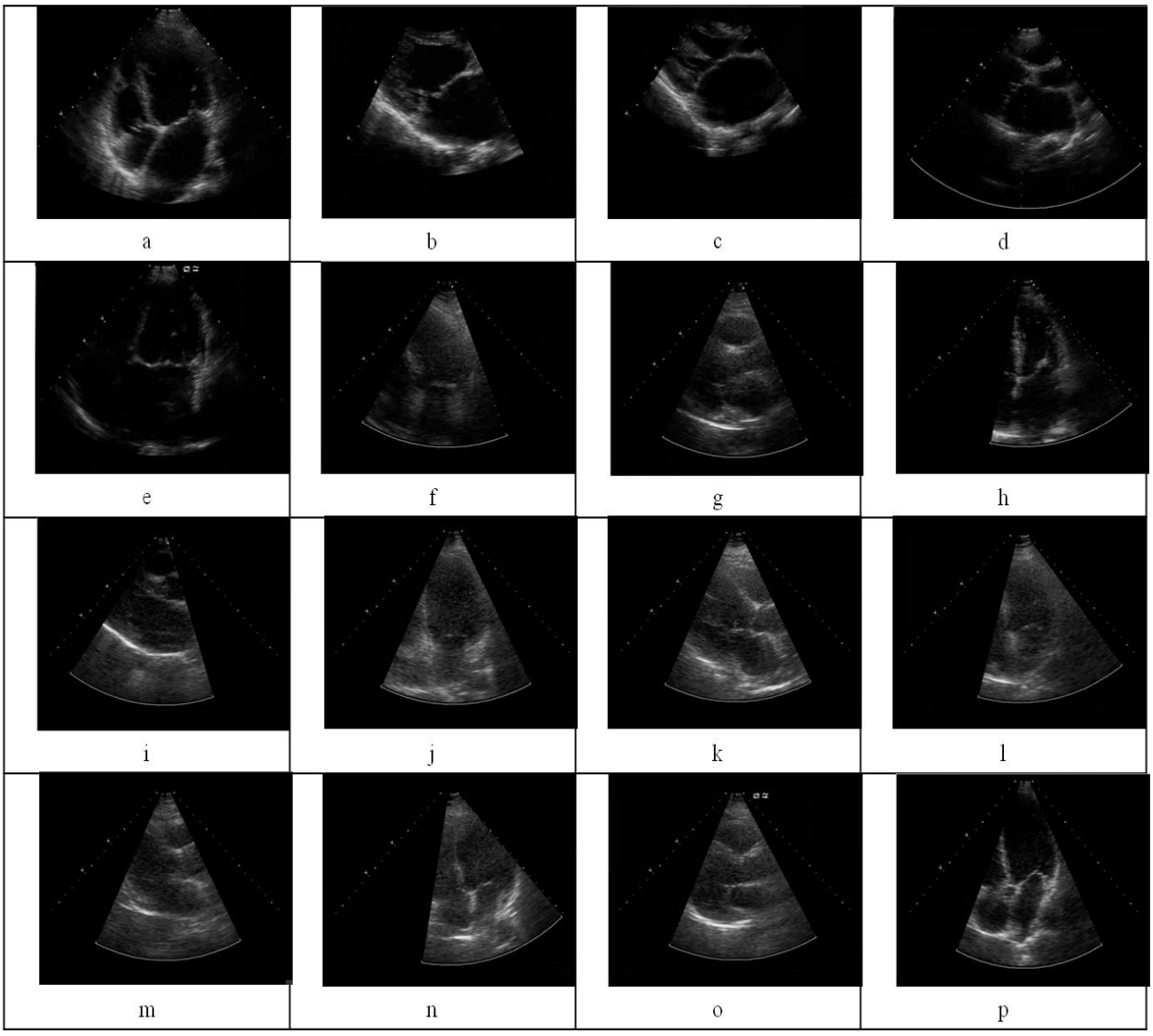

Figure 2.5 Original Echocardiographic Images

Here we can see that there is lots of speckle noise present in these images which makes it difficult to extract boundaries. Other important diagnosis also becomes difficult with this noise. By analyzing these image it can been that boundaries of chambers get dull due to this noise. In case of fig. 2.5f to fig. 2.5o, density of speckle noise is very high and this noise covers the boundaries as well as inside of the chambers.

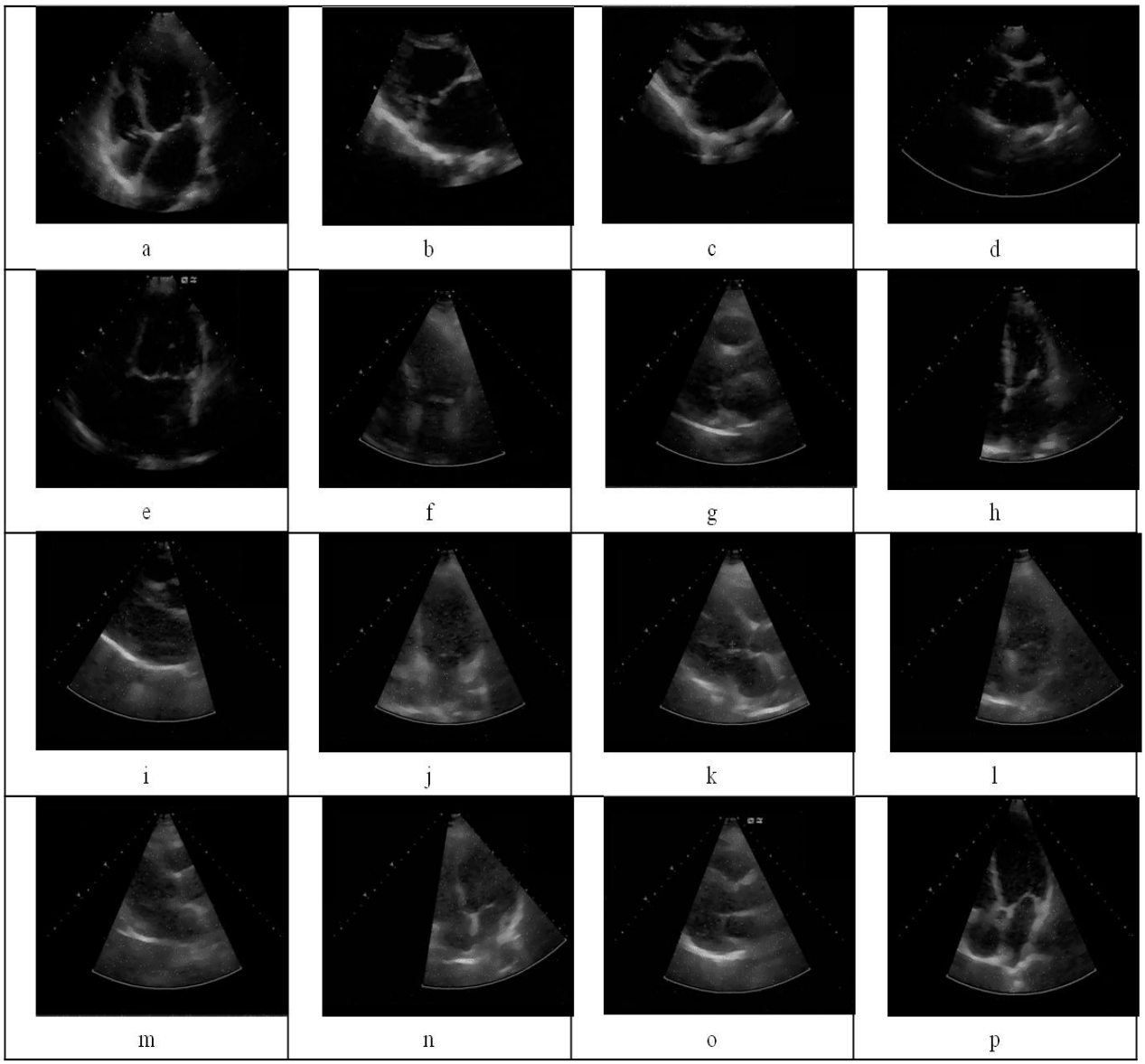

Figure 2.6 De-Speckled Image after Speckle Reducing Anisotropic Diffusion filter (SRAD)

Figure 2.6 shows the SRAD filtered images. We can see that these images are speckle free but impulse noise or salt and pepper noise is introduced. Which also creates problem in diagnosis. So there is requirement of a filter that removes these types of disturbing noises. As we can see in fig. 2.6a to fig. 2.6p, it is noticed that the impulse noise increases in the image which having the high speckle noise.

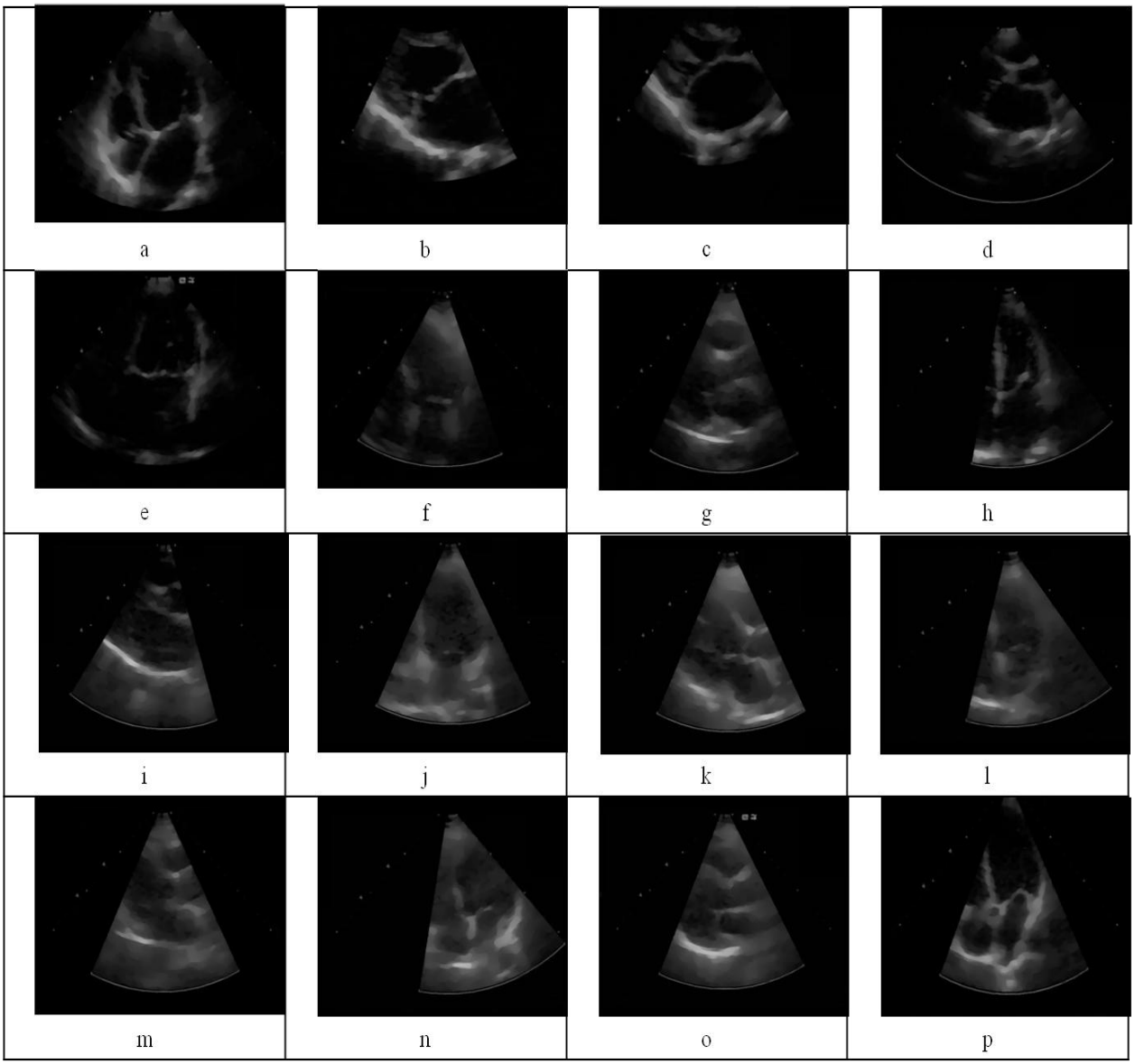

Figure 2.7 De-Speckled Images after Applying Proposed Hybrid Filter (HSRAD)

Proposed hybrid filter (HSRAD) removes speckle noise as well as impulse noise. Fig. 2.7 shows images filtered with proposed hybrid filter. Relaxed median filter hybrid with speckle reducing filter removes impulse noise in parallel. HSRAD removes the speckle as well as impulse noise even in case of high speckled noise images. Images in fig. 2.7f to fig. 2.7o prove this statement. Edges can be as well as chambers can be visualize properly in these images.

Table 2.3 shows the statistical analysis of these two filters. Here statistical parameters are Qi (quality index), PSNR (peak signal to noise ratio), MAE (mean absolute error), MSE (mean square error) and RMSE (root mean square error). High Qi and PSNR with low value of MAE, MSE and RMSE show the better filter. Analysis in table 2.3 shows that proposed filter have high PSNR and Low MSE and RMASE than SRAD in case of echocardiographic images.

Table 2.3: Performance of Proposed Hybrid Filter (HSRAD) with SRAD Filter

Images	SRAD					HSRAD				
	Qi	PSNR	MAE	MSE	RMSE	Qi	PSNR	MAE	MSE	RMSE
1	0.85	37.37	1.63	11.92	3.45	0.79	38.13	1.22	10.00	3.16
2	0.86	38.47	1.21	9.24	3.04	0.84	39.34	0.85	7.57	2.75
3	0.66	38.86	1.13	8.46	2.91	0.88	39.79	0.79	6.83	2.61
4	0.73	39.67	1.07	7.02	2.65	0.69	41.17	0.65	4.97	2.23
5	0.81	40.99	0.85	5.18	2.28	0.72	42.77	0.52	3.43	1.85
6	0.91	39.18	1.14	7.85	2.80	0.97	40.92	0.70	5.26	2.29
7	0.93	38.51	1.25	9.16	3.03	0.76	39.61	0.85	7.12	2.67
8	0.64	40.02	0.95	6.48	2.54	0.86	41.13	0.65	5.01	2.24
9	0.66	38.15	1.32	9.96	3.16	0.84	39.14	0.89	7.93	2.82
10	0.65	36.81	1.69	13.55	3.68	0.86	37.62	1.18	11.25	3.35
11	0.63	36.60	1.81	14.23	3.77	0.86	37.42	1.23	11.78	3.43
12	0.69	37.77	1.41	10.86	3.29	0.86	38.66	0.96	8.86	2.98
13	0.96	37.52	1.47	11.49	3.39	0.88	38.26	1.02	9.71	3.12
14	0.67	37.02	1.59	12.91	3.59	0.89	37.81	1.12	10.77	3.28
15	0.61	37.29	1.54	12.11	3.48	0.84	38.17	1.05	9.91	3.15
16	0.75	37.38	1.52	11.89	3.45	0.85	38.32	1.08	9.58	3.10

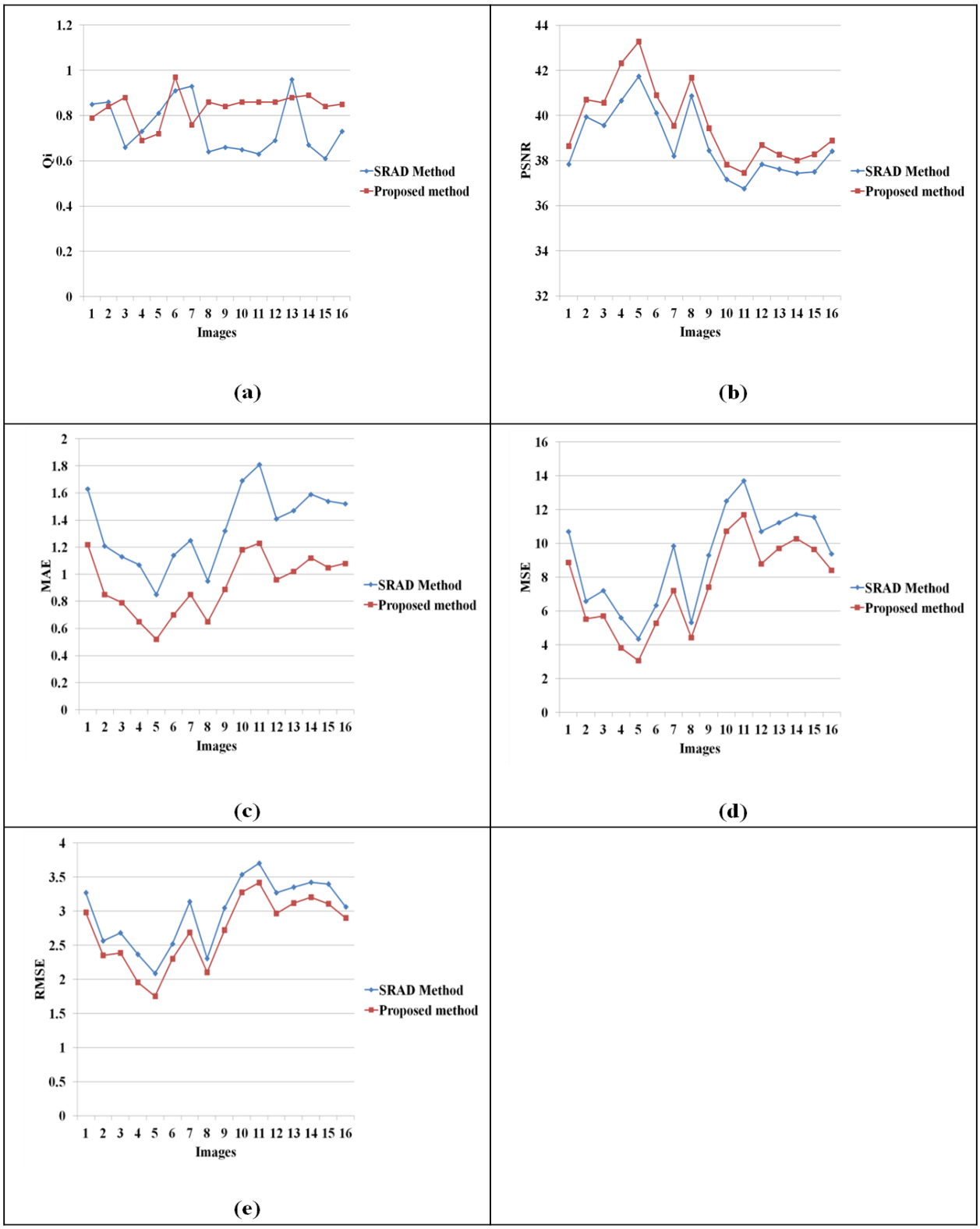

Figure 2.8 Comparison Between SRAD and MSRAD (a) for Qi , (b) for PSNR (c) for MAE (d) for MSE and (e) for RMSE

Fig. 2.8 shows the statistical comparison between two filters in graphical form. It can be seen that the data line related to SRAD filter is above the data line related to proposed method in case of Qi and PSNR. But in case of MAE, MSE and RMSE data line related to SRAD is below the data line related to proposed method.

2.3.4.3 Method 2: Modified Nonlinear Complex Diffusion (MNCD) Filtering

Second method is developed to improve the process of speckle noise reduction and to improve the preservation of edges and the image features. The filtering process is specific to echocardiographic images. A nonlinear complex diffusion based technique has been utilized to take the advantage of imaginary part of the image.

Nonlinear complex diffusion processes (2nd order PDE's) can behave like 3rd and 4th order real PDE's enabling a variety of new options with standard 2nd order numerical schemes. The imaginary value serves as a robust edge-detector with increasing confidence in time, thus handles noise well and may serve as a controller for nonlinear processes.

Equation for Non-linear complex diffusion filter is given as follows in the literature

$$\frac{\partial I}{\partial t} = \nabla.(d(\mathrm{Im}(I)\nabla I) \tag{2.35}$$

Where, $\mathrm{Im}(I)$ is the imaginary part of the image $d(\mathrm{Im}(I))$ is the coefficient of diffusion and it is defined as:

$$d(\mathrm{Im}(I)) = \frac{\exp(i\theta)}{1+\left(\mathrm{Im}(I)/k\theta\right)^2} \tag{2.36}$$

Where $i = \sqrt{-1}$, k is a threshold parameter, $\theta \in (-\pi/2; \pi/2)$ a phase angle close to zero and I is the image. As in this formulation, the definition of coefficient of diffusion does not involve the derivatives of the image; it is the advancement in comparison with real diffusion coefficients. Directional diffusion coefficient is used in this formulation. For small values of θ the imaginary part of I is a smooth function of its second derivatives and the ratios proportional to the laplacian of I, explained by [103] taking $\theta \to 0$. In this way, diffusion is facilitated for smooth areas and attenuated at image edges.

Equation (2.36) was discretized by finite difference scheme as:

$$I_{i,j,m}^{(n+1)} = I_{i,j,m}^{(n)} + \Delta t^{(n)} \left(\overline{(d(\mathrm{Im}(I)))}_{i,j}^{n} \Delta_s I_{i,j}^{(n)} + \nabla_s (d(\mathrm{Im}(I)))^n . \nabla_s I_{i,j}^{(n)} \right) \tag{2.37}$$

Where ∇_s and Δ_s are discrete gradient and laplacian operators respectively; i and j are indexes for pixels of I; and $\Delta t^{(n)}$ is the step in time for iteration.

Assuming that $0 \le \left| \mathrm{Im}\left(d(\mathrm{Im}(I))_{i,j}^{(n)} \right) \right| \le \mathrm{Re}\left(d(\mathrm{Im}(I))_{i,j}^{(n)} \right)$, for all i, j and n where Im(□) and Re(□) are imaginary and real parts. Work in [5] explains that the method is stable if:

$$\Delta t^{(n)} \le \frac{1}{\alpha \max_{i,j} \left[\mathrm{Re}((d(\mathrm{Im}(I))_{i,j}^{(n)} + \left| \mathrm{Im}((d(\mathrm{Im}(I)))_{i,j}^{(n)} \right| \right]} \tag{2.38}$$

From the above discussion it is seen that the choice of the diffusion coefficient and the time step function are very important as diffusion coefficient decides as to which area is to be smoothed out and which one to be enhanced. The iterations also depend on time step function. So, these parameters are of our main consideration.

a) Modified Nonlinear Complex Diffusion Coefficient

Equation (2.36) for diffusion coefficient seems to be good choice to preserve the edges, as mentioned in [120] , but for getting much better enhancement with edge preservation in echocardiographic images we formulate the diffusion coefficient as mentioned below:

$$d(\mathrm{Im}(I)) = \frac{\exp(i\theta).(\mathrm{Im}(I))}{1 + \left(\mathrm{Im}(I) / k\theta \right)^2} \tag{2.39}$$

The imaginary value serves as a robust edge detector with in creasing confidence in the time and thus handles noise well and may serves as a controller for nonlinear process. So in the eq. (2.39) weightage of imaginary value has been increased to get the edge enhancement as an advancement with the de-speckling.

b) Adaptive time step

The coefficient of diffusion depends on the gradient of the image. Due to noise, this gradient is much higher in the initial steps of the diffusion process. So an adaptive time step is formulated in the proposed method. An additional advantage of proposed time step function is that it also

increases the processing speed. The adaptive time step function has been formulated as in eq. (2.40)

$$\Delta t^{(n)} = \frac{1}{\alpha}\left[\frac{a}{\exp\left(-\max\left(\left|\mathrm{Re}\left(\partial I^{(n)}/\partial t\right)\right| \Big/ \mathrm{Re}\left(I^{(n)}\right)\right)\right)} + b\exp\left(-\max\left(\left|\mathrm{Re}\left(\partial I^{(n)}/\partial t\right)\right| \Big/ \mathrm{Re}\left(I^{(n)}\right)\right)\right)\right] \tag{2.40}$$

Where $\left(\left|\mathrm{Re}\left(\partial I^{(n)}/\partial t\right)\right| \Big/ \mathrm{Re}\left(I^{(n)}\right)\right)$ is the fraction of change of the image/volume at iteration n and α is as in eq. (2.38), and the a and b are the time step controlling parameters with $(a+b \le I)$.

2.3.4.4 Results

Fig. 2.9 shows the processed images of the original images from fig. 2.1 by NCDF filters. These filters remove noise in the homogeneous regions and the edges are left unaltered. But this filter produce some blurring in the echocardiographic images.

However, in case of echocardiographic images more enhanced images are required. The proposed MNCD applied to output the images as in fig. 2.10 has shown still better results. This filter removes the speckle noise from homogeneous regions and enhances the edges. Change in results is due to the change in diffusion coefficient value and the time step size.

The proposed method gives a new diffusion coefficient and time step size which enhances the image in much better way. The better outcome has been shown by discussing performance the parameters. Table 2.4 gives the values of these parameters in both the cases; when the traditional NCDF has been used and when the proposed MNCD has been used. It is clear from the table that the PSNR and the Qi are higher in case of proposed MNCD method and the value of MAE, MSE and RMSE are lower in the proposed method than the corresponding values obtained in case of the NCDF method. So the proposed filter is an advancement of the NCDF.

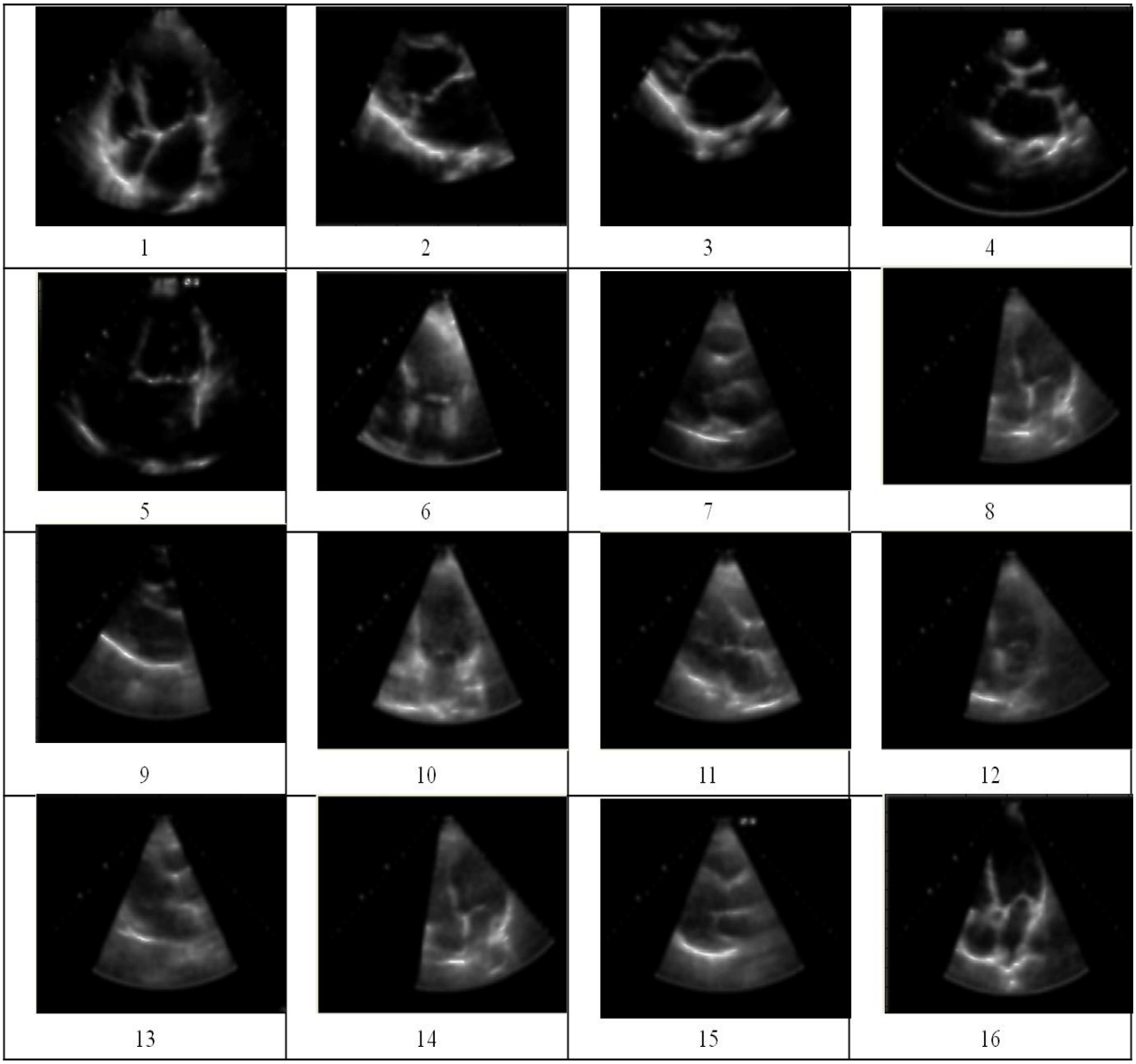

Figure 2.9 Processed Images by Traditional Non-linear Coefficient Diffusion Filter (NCDF)

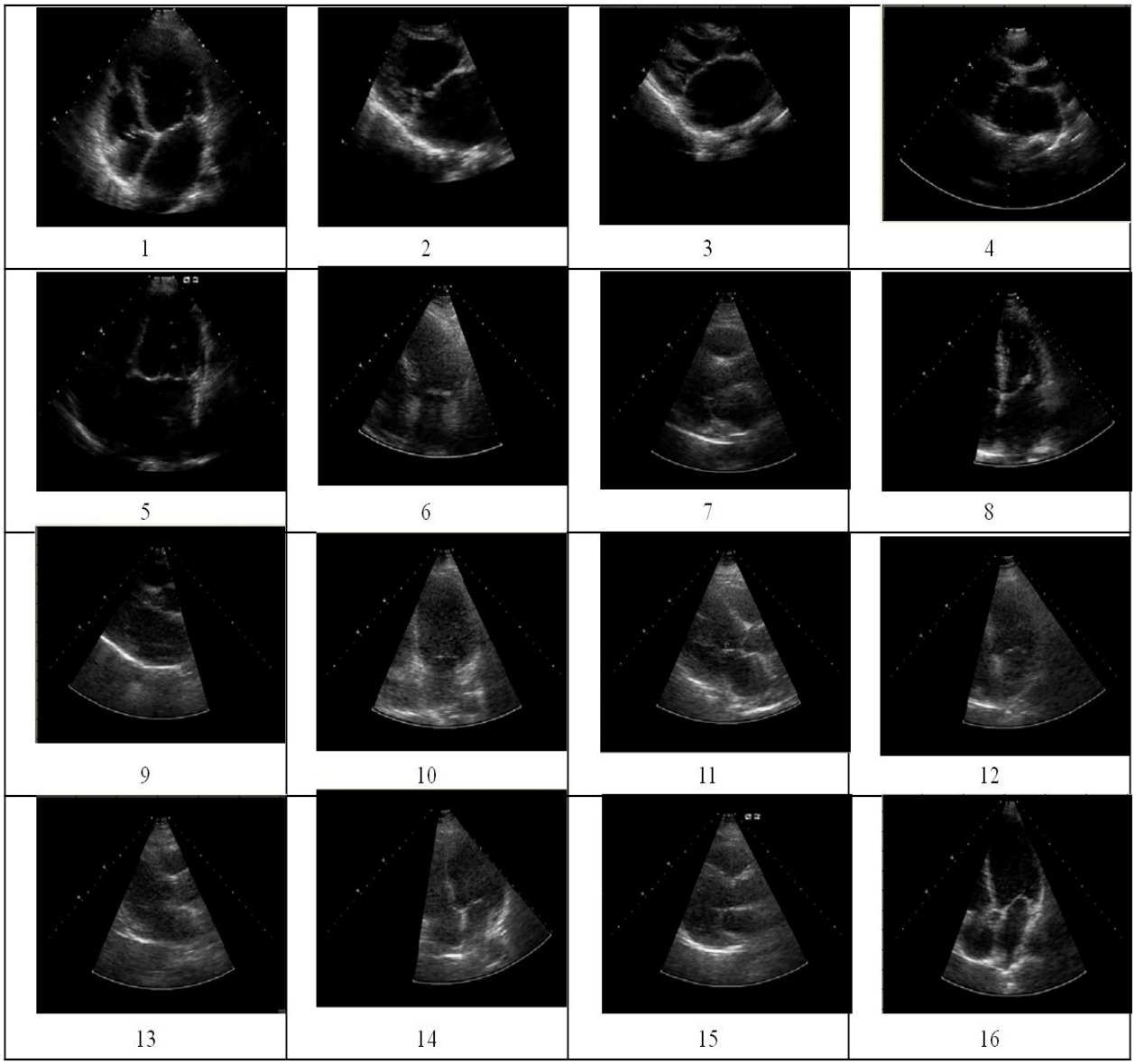

Figure 2.10 Processed images by proposed Modified Non-linear Coefficient Diffusion Filter

The graphical representation of the performance parameters is shown in fig. 2.11 From the graphs it can be seen that in case of PSNR and Qi the trend line of MNCD is above the trend line relating to NCDF. In case of MAE, MSE and RMSE the opposite is true. This clearly shows the higher performance index of the proposed filter than that of the traditional NCDF.

Table 2.4: Performance Parameters for Analyzing the Quality of Filter

Images	NCDF					MNCD				
	Qi	PSNR	MAE	MSE	RMSE	Qi	PSNR	MAE	MSE	RMSE
1	0.05	25.62	13.60	898.58	29.98	0.07	26.36	13.58	800.16	28.28
2	0.22	24.85	10.88	921.19	30.35	0.30	27.12	10.94	746.87	27.33
3	0.23	24.42	8.25	586.82	24.22	0.17	24.89	8.28	496.17	22.27
4	0.09	24.52	7.11	415.44	20.38	0.22	25.45	7.12	274.98	16.58
5	0.09	25.53	4.93	231.23	15.21	0.16	26.89	4.92	164.37	12.82
6	0.11	25.89	7.37	413.15	20.33	0.19	28.29	7.18	273.63	16.54
7	0.06	26.56	9.17	582.56	24.14	0.12	28.50	9.12	440.62	20.99
8	0.18	24.56	6.05	356.38	18.88	0.08	25.11	6.07	276.58	16.63
9	0.13	24.80	10.14	715.24	26.74	0.09	25.25	10.07	568.18	23.84
10	0.13	24.69	12.93	834.74	28.89	0.10	25.06	12.87	747.08	27.33
11	0.12	24.87	14.17	1006.86	32.68	0.09	25.31	14.14	956.23	30.92
12	0.15	24.89	10.33	586.80	24.22	0.09	25.26	10.29	514.06	22.67
13	0.04	26.87	11.64	681.57	26.11	0.06	29.26	11.76	583.96	24.16
14	0.14	24.75	13.17	910.04	30.17	0.08	25.09	13.11	819.15	28.62
15	0.12	24.69	12.72	887.53	29.79	0.08	25.02	12.66	788.75	28.08
16	0.03	26.67	12.18	958.85	30.97	0.07	28.87	12.07	705.52	26.56

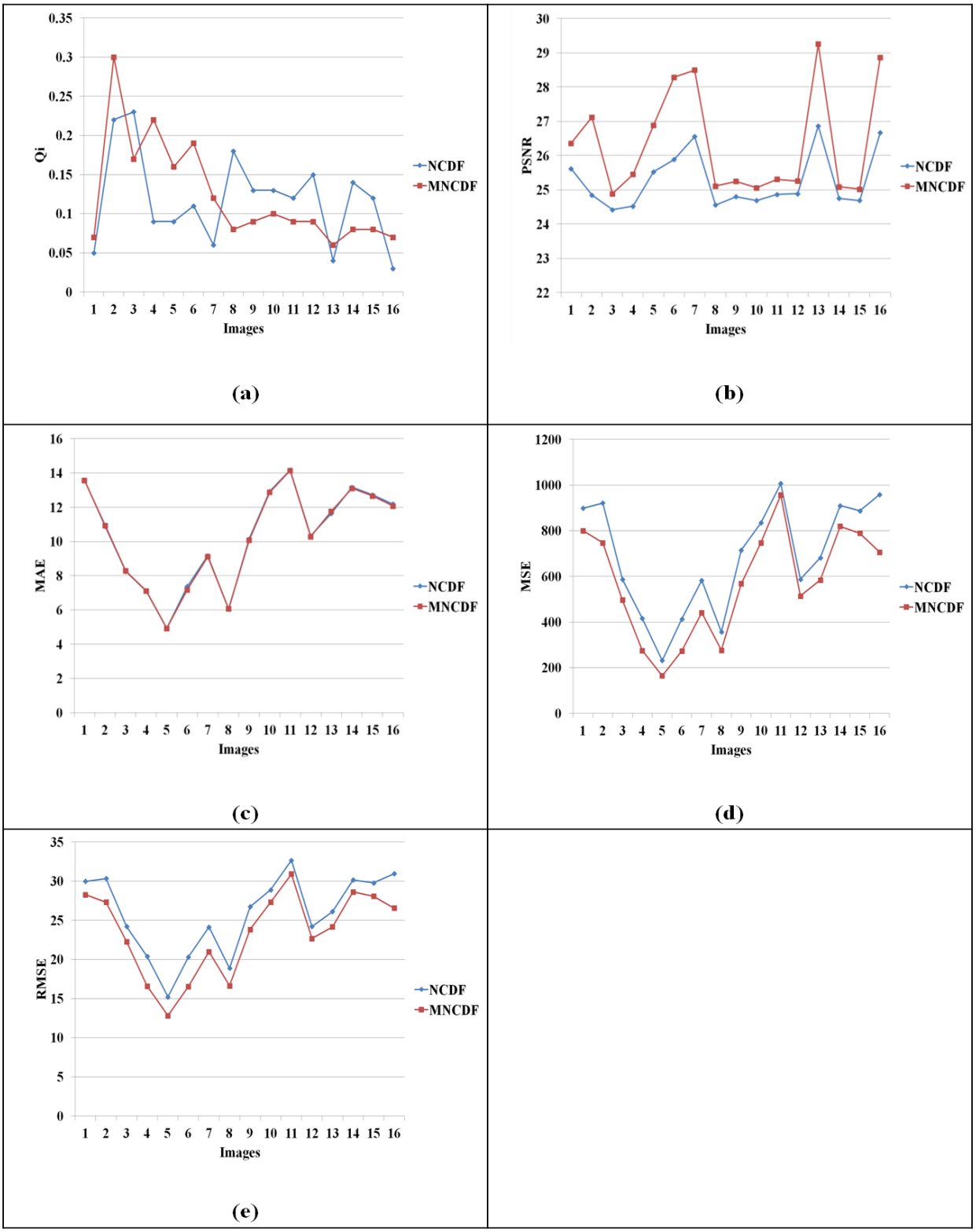

Figure 2.11 Comparison Between NCDF and MNCD (a) for Qi , (b) for PSNR (c) for MAE (d) for MSE and (e) for RMSE

2.4 SUMMARY

Echocardiographic images give different results on different intensity transformations. However, these results are tilted slightly from the results obtained in case of other types of images. Although spatial filtering gives fine results, images become complex for further processing. Proposed transformation is suitable for different kinds of low contrast images there is no requirement of different transformation for different kind of images as in the case of conventional transformations. Parameters are specified automatically and the enhancement procedure can work as automatic enhancement tool.

Here, we have applied the modified log transformation for gray-scale images; it can similarly work for color images also. This method is also applicable for 3-D echocardiographic images. And gives the satisfactory results with higher value of *a*.

The first proposed method for de-speckling is an improvement over Yongjian Yu and Scott T. Acton's paper Speckle Reducing Anisotropic Diffusion by additional quality of relaxed median filter. Proposed method has been implemented on different echocardigraphic images and has resulted in giving speckle and spike free images. Statistical analysis has also been carried out for comparison between SRAD and the proposed filter. This analysis shows that the proposed filter is better for echiocardiographic images.

In second a new formulation of the nonlinear complex diffusion filter has been proposed as the Modified Nonlinear Complex Diffusion (MNCD) filter. A modified filter is developed to remove speckle more effectively from the echocardiographic images and provides much better enhancement even of the smaller details. Five of the performance parameters as explained show the better quality of the filter. These parameters demonstrate advantages with regard to the edge preservation and speckle filtering capabilities. The adaptive time step proposed has its advantage with regard to better stability and the fast response. In addition to the echocardiographic images used for the present work this filter can also be used for other medical images, radar images and synthetic images.

CHAPTER 3

BOUNDARY DETECTION OF ECHOCARDIOGRAPHIC IMAGES

3.1 INTRODUCTION

There is an extensive literature on methods to automatically segmenting and tracking the left ventricle (normal assessment of the chamber for the diagnosis of heart disease). Tracking of the endocardium motion has been kept in mind for estimation of left ventricular size (areas/volumes) and derived measures such as the ejection fraction and for regional wall motion assessment. In particular, these measures are used in diagnosis and assessment of ischemic heart disease.

There is anisotropy in the acquisition of echocardiography images, there are some artifacts due to shadowing from lungs and a strong attenuation, these all things create some challenges in finding out the proper methods for segmentation. Segmentation methods used for echocardiography images should also have an ability to avoid problems created by the papillary muscles. A more challenge is in reliably finding the outer wall (also known as epicardial border detection), particularly from apical views. There are many papers on tracking of left ventricle which deal with the deformation model, which are independent of feature extraction or the imaging modality. In [146] motion analysis has been done for the systolic dysfunction of the left ventricle. A freehand ultrasound (synchronization of 2-D image acquisition to record the location of the slice with the help of a position sensor), rotational 3- D probes acquiring a sparse set of 2-D image sequences, or real-time 3-D echocardiography [125], [122] have been used based on the volumetric system [223], [293].

Contour finding approach is the most popular approach which is used for the endocardial segmentation. Due to uneven contrast around the left ventricle chamber border this is not straightforward. Contrast varies according to the relative orientation of the border to the transducer direction, and attenuation. So the conventional methods such as intensity gradient-based methods have had limited success on such types of images.

In [29] an active contour method has been discussed. In this the genetic algorithm was used for optimization. The first image is a preprocessed contour with the low pass filtering and

morphological operations and then optimized by using GA for rough boundary delineation to define an initial estimate of the contour at a fixed number of sample points. To minimize the energy functional a nonlinear mapping of the intensity gradient was used. To initialize contour finding in the next time frame a contour was used. The conventional constrained quasi-Newton method has been used to compare the convergence of the method to the active contour. The two experts have done manual delineations on 20 frames and the average compared to the automated algorithm showing that the intervariability between experts was similar to the difference between the manual and automated methods.

In [208] a statistical external energy [114], [76] has been used in a discrete active contour for the short axis parasternal images segmentation with an argument that this was well-suited in ultrasound images with missing boundaries and significant noise. To model gray levels statistics, a shifted Rayleigh distribution was used.

Oftently used alternative of active counters is the level set methods for the segmentation of echocardiographic images. Here, the evolving contour using a signed function, where it is zero level, corresponds to the actual contour. According to the motion equation of the contour, one can easily derive a similar flow for the implicit surface that when applied to the zero-level, will reflect the propagation of the contour. The level set method encodes numerous advantages: it is implicit, parameter free, provides a direct way to estimate the geometric properties of the evolving structure, can change the topology and is intrinsic. In [164] a level set method has been considered for applying on the echocardiographic images using fast marching method an adaptation. In this paper an average intensity gradient-based measurement has been used to reduce errors attributed to using local feature (intensity gradient) measurements. The method was applied to an apical four-chamber view sequence and parasternal short axis view. The results obtained in this study were discussed in there quantitative form only.

The ML blocky segmentation maps exhibit improper blood or muscle areas at lower levels (higher resolution levels of the pyramidal structure due to artifacts created by the ultrasound imagery process. The boundary of the endocardial contour cannot be efficiently extracted on these lower levels.

Segmenting abnormal from normal myocardium using high-frequency intracardiac echocardiography (ICE) images presents new challenges for image processing. Gray level intensity and texture features of ICE images of myocardium with the same structural/perfusion properties

differ. This significant limitation conflicts with the fundamental assumption on which existing segmentation techniques are based. Xiaohui Hao[330] concentrates on segmenting region shapes rather than automatically distinguishing abnormal from normal myocardial tissue. Segmentation results in the [330] were compared with the gross pathology images of the heart.

In the past four decades, computerized image segmentation has played an increasingly important role in medical imaging. Segmented images are now used routinely in a multitude of different applications, such as the quantification of tissue volumes [280], diagnosis [242], localization of pathology [33], study of anatomical structure [17], [45], treatment planning [312], partial volume correction of functional imaging data [123], and computer-integrated surgery [214], [313]. Image segmentation remains a difficult task, however, due to both the tremendous variability of object shapes and the variation in image quality. In particular, medical images are often corrupted by noise and sampling artifacts, which can cause considerable difficulties when applying classical segmentation techniques such as edge detection and thresholding. As a result, these techniques either fail completely or require some kind of post-processing step to remove invalid object boundaries in the segmentation results.

To address these difficulties, *deformable models* have been extensively studied and widely used in medical image segmentation, with promising results. Deformable models are curves or surfaces defined within an image domain that can move under the influence of *internal forces*, which are defined within the curve or surface itself, and *external forces*, which are computed from the image data. The internal forces are designed to keep the model smooth during deformation. The external forces are defined to move the model toward an object boundary or other desired features within an image. By constraining extracted boundaries to be smooth and incorporating other prior information about the object shape, deformable models offer robustness to both image noise and boundary gaps and allow integrating boundary elements into a coherent and consistent mathematical description. Such a boundary description can then be readily used by subsequent applications. Moreover, since deformable models are implemented on the continuum, the resulting boundary representation can achieve sub-pixel accuracy, a highly desirable property for medical imaging applications. Main part is contour detection a reference for contour detection is in [102].

3.2 DEFORMABLE MODELS

Although the term *deformable models* first appeared in the work by Terzopoulos and his collaborators in the late eighties [85], [206], [84] and [86] the idea of deforming a template for extracting image features dates back much farther, to the work of Fischler and Elschlager's spring-loaded templates [184] and Widrow's rubber mask technique [44]. Similar ideas have also been used in the work by Blake and Zisserman [7], Grenander et al. [305], and Miller et al. [201]. The popularity of deformable models is largely due to the seminal paper "Snakes: Active Contours" by Kass, Witkin, and Terzopoulos [206]. Since its publication, deformable models have grown to be one of the most active and successful research areas in image segmentation. Various names, such as snakes, active contours or surfaces, balloons, and deformable contours or surfaces, have been used in the literature to refer to deformable models. There are basically two types of deformable models: *parametric deformable models* (cf. [206], [1], [175] and [298]) and *geometric deformable models* (cf. [306], [256], [307], [36] and [260]). Parametric deformable models represent curves and surfaces explicitly in their parametric forms during deformation. This representation allows direct interaction with the model and can lead to a compact representation for fast real-time implementation. Adaptation of the model topology, however, such as splitting or merging parts during the deformation, can be difficult using parametric models. Geometric deformable models, on the other hand, can handle topological changes naturally. These models, based on the theory of curve evolution [107], [37], [254], [38], [180]and [172] and the level set method [284], [129], [130] and [131], represent curves and surfaces implicitly as a level set of a higher-dimensional scalar function. Their parameterizations are computed only after complete deformation, thereby allowing topological adaptivity to be easily accommodated. Despite this fundamental difference, the underlying principles of both methods are very similar. Finite element methods [298], [125] and [83] have been used to implement deformable surfaces. Recently a method [65], [128] is developed which casts the speed extension problem as a boundary value problem, which can then be solved efficiently using the fast marching method.

Deformable contour is a curve $X(s) = (X(s), Y(s)), s \in [0,1]$ which moves though the spatial domain of an image to minimize the following energy functional:

$$E(X) = E_{\text{int}}(X) + E_{ext}(X) \tag{3.1}$$

Internal energy of snake is the summation of elastic energy and bending energy and is given as:

$$E_{\text{int}} = \frac{\partial}{\partial S}\left(\alpha \frac{\partial X}{\partial S}\right) - \frac{\partial^2}{\partial S^2}\left(\beta \frac{\partial^2 X}{\partial S^2}\right) \tag{3.2}$$

The first term discourages stretching and makes the model behave like an elastic string. The second term discourages bending and makes the model behave like a rigid rod. The external energy is given as the potential energy:

$$E_{ext} = -\nabla P(X) \tag{3.3}$$

External energy attracts the curve towards the desired object boundaries. To find the object boundary, parametric curves are initialized within the image domain and are forced to move toward the potential energy minima under the influence of both the forces.

The level set method has the property of automatic topology adaptation. In the level set method, the curve is represented implicitly as a level set of a 2-D scalar function referred to as the level set function which is usually defined on the same domain as the image. The level set is defined as the set of points that have the same function value. Instead of tracking a curve through time, the level set method evolves a curve by updating the level set function at fixed coordinates through time. This perspective is similar to that of an Eulerian formulation of motion. An advantage of level set function is that it remains a valid function while the embedded curve can change its topology.

Given level set function $\phi[x, y, t]$ with contour $X(s,t)$; as its zero level set, we have

$$\varphi[X(s,t),t] = 0 \tag{3.4}$$

Differentiating the eq.(3.4) with respect to t and using the chain rule we obtain:

$$\frac{\partial \varphi}{\partial t} + \nabla \varphi \cdot \frac{\partial X}{\partial t} = 0 \tag{3.5}$$

Where $\nabla \phi$ denote the gradient of ϕ.

Assuming that ϕ is negative inside the zero level set and positive outside. Accordingly, the inward unit normal to the level set curve is given by:

$$N = -\frac{\nabla\varphi}{|\nabla\varphi|} \tag{3.6}$$

Using the curve evolution theory we can rewrite eq. (3.5) as

$$\frac{\partial\varphi}{\partial t} = V(k)|\nabla\varphi| \tag{3.7}$$

where k , the zero level set is given by

$$k = \nabla\frac{\nabla\varphi}{|\nabla\varphi|} = \frac{\varphi_{xx}\varphi_y^2 - 2\varphi_x\varphi_y\varphi_{xy} + \varphi_{yy}\varphi_x^2}{\varphi_x^2 + \varphi_y^2} \tag{3.8}$$

3.3 ECHOCARDIOGRAPHIC IMAGE SEGMENTATION

In case of mitral regurgitation, atrium and ventricle may get dilated. To examine this, doctors draw the boundary manually. Aim of this piece of research work as explained is to evolve the automatic boundary detection for carrying out segmentation of echocardiographic images. In case of significant MR, left ventricle has to accommodate both the stroke volume and regurgitant volume with each heart beat leading to volume overload of the left ventricle. The left ventricle dilates and becomes hyperdynamic for compensation. The left atrial and pulmonary venous pressures increase quickly in case of acute severe MR, leading to pulmonary congestion and pulmonary edema. A gradual increase in left atrial size and compliance compensates in chronic MR, so that left atrial and pulmonary venous pressures do not increase until late in the course of the disease. An increase in after load, contractile dysfunction, and heart failure occur in case of progressive left ventricular dilation. Left atrial enlargement leads the patient to atrial fibrillation and arterial thromboembolism.

Two-dimensional echocardiography is a good method for finding out left atrial and ventricle dilation in case of mitral regurgitation. There are many papers in the literature which discuss the different measurement methods related to left atrium and left ventricle [319], [132], [15], [55] and [61]. There are different techniques employed for left atrium and ventricle boundary detection. In [121], the LV center and LV edge points were detected using neural network classifiers with new input feature vectors. These neural classifiers combined with knowledge-based techniques in the center detection stage refine the center estimate. In [318], double thresholding method is used for

left ventricle endocardium detection. First step of this method was to suppress the noise by taking mean of two adjacent frames four times. Next step was ternary thresholding in which two thresholds divide the image into three regions. Final step was second thresholding, in which a binarized image is obtained. In [140], snake-based algorithm is used for endocardial boundary detection.

Our objective is to detect the left atrium and left ventricle boundaries using active contour method. Active contour model is first proposed in [206]. There are many research papers which are based on deformable models or active contour models [121], [94], [115], [14], [317], [9] and [321]. An energy minimizing deformable spline influenced by constraint and image forces that pull it toward object contours is called active contour. Snakes are largely used in applications like boundary detection, object tracking, shape recognition, segmentation, edge detection, stereo matching [206], etc. The problem of finding a curve that minimizes the energy functional is known as a variational problem [246]. It has been shown that the curve that minimizes energy functional must satisfy Euler-Lagrange equation [206] and [175]. The value of the distance map at each pixel is obtained by calculating the distance between the pixel and the closest boundary point, based either on Euclidean distance [225] or Chamfer distance [100].

3.3.1 Statistical Parameters used for Performance Analysis

For getting the performance of the method statistical analysis has been done on the population of time taken per iterations. The four parameters mean, median, standard deviation and variance have been calculated.

Mean is defined as :

$$\mu = \sum t / n \tag{3.9}$$

Where μ is the symbol for representing mean and $\sum t$ is the sum of time taken for all the iterations and n is the number of total iterations taken for the boundary detection of particular image.

Median is related to the middle value of time from time population.

The *variance* is the average squared deviation from the group of time mean, as defined by the following formula:

$$\sigma^2 = \sum (t_i - \mu)^2 / n \tag{3.10}$$

Where σ^2 is the variance, μ is the mean and t_i is the i^{th} element from the time population.

The standard deviation is the square root of the variance. Thus, the standard deviation is defined as:

$$\sigma = \sqrt{\sigma^2} = \sqrt{\sum (t_i - \mu)^2 / n} \tag{3.11}$$

3.3.2 Proposed Method 1– A Fast Region-Based Active Contour Model (FRACM)

Our algorithm is based on Chan–Vese paper active contours without edges, but it is much faster than Chan–Vese model [294]. Here method has been developed by which it is possible to detect much faster the echocardiographic boundaries. The method is based on the region information of an image. The region based force provides a global segmentation with variational flow robust to noise. Implementation is based on level set theory so it easy to deal with topological changes. Newton–Raphson method has been used here to converge the fast boundary detection.

An image u_0 is usually considered a real-valued bounded function defined on $\overline{\Omega}$, where Ω is a bounded and open subset of R^2 with $\partial\Omega$ as its boundary.

According to level set theory originally proposed by Osher and Sethian in [285], a geometric active contour can be represented by zero level set of real valued function $\Phi : \Omega \subset R^2 \rightarrow R$ which evolves in an image u_0 according to variational [246] flow in order to segment the object from the image background.

3.3.2.1 FRACM Formulation

Given an observed image u_0, find decomposition Ω_i of Ω and an optimal piecewise smooth approximation u of u_0, such that u varies smoothly within each Ω_i and rapidly or discontinuously across the boundaries of Ω_i.

To solve this problem, Mumford and Shah (77) proposed the following minimization problem:

$$\inf\left\{ F^{MS}(u, C) = \int_{\Omega} (u - u_0)^2 \, dx\, dy + \mu \int_{\Omega \setminus C} |\nabla u|^2 \, dx\, dy + \nu |C| \right\} \tag{3.12}$$

A reduced case of the model is obtained by restricting the segmented image u to piecewise constant function, i.e. $u = \text{constant}\ c_i$ inside each connected component Ω_i. Then this problem is called “minimal partition problem” and its functional is:

$$E^{MS}(u,c)=\sum_i \int_{\Omega} (u-c_i)^2 dxdy+\nu|C| \tag{3.13}$$

It is easy to see that, for fixed C, the energy from equation (3.13) is minimized in the variable c_i by setting

$$c_i = mean(u_0)\, in\, \Omega_i \tag{3.14}$$

By the functional for "minimal partition problem", and given the curve $C=\partial\omega$, with $\omega\subset\Omega$ an open subset, and two unknown constants c_1 and c_2 denoting $\Omega_1=\omega$, $\Omega_2=\Omega-\omega$. They have proposed to minimize the following energy with respect to c_1, c_2 and C.

$$F(c_1,c_2,C)=\mu\cdot Length(C)+\nu\cdot Area(inside(C))+\lambda_1\int_{inside(C)}|u_0(x,y)-c_1|^2 dxdy + \lambda_2\int_{outside(C)}|u_0(x,y)-c_2|^2 dxdy \tag{3.15}$$

where, $\mu\geq 0, \nu\geq 0, \lambda_1, \lambda_2>0$, are fixed parameters and these values fixed as $\lambda_1=\lambda_2=1$ and $\nu=0$ for further calculations.

Using the Heaviside function H and the one-dimensional Dirac measure δ_0 and defined, respectively, by

$$H(z)=\begin{cases}1, & if\ z\geq 0\\ 0, & if\ z<0\end{cases},\quad \delta_0(z)=\frac{d}{dz}H(z) \tag{3.16}$$

(in the sense of distributions), we express the terms in the energy in the following way

$$\begin{aligned} Length\{\varphi=0\} &= \int_{\Omega}\left|\nabla H(\varphi(x,y))\right| dx\,dy \\ &= \int_{\Omega}\delta_0(\varphi(x,y))\left|\nabla\varphi(x,y)\right| dx\,dy, \\ Area\{\varphi\geq 0\} &= \int_{\Omega} H(\varphi(x,y))\,dx\,dy, \end{aligned} \tag{3.17}$$

and

$$\begin{aligned} \int_{\varphi>0}|u_0(x,y)-c_1|^2 dx\,dy &= \int_{\Omega}|u_0(x,y)-c_1|^2 H(\varphi(x,y))\,dx\,dy, \\ \int_{\varphi<0}|u_0(x,y)-c_2|^2 dx\,dy &= \int_{\Omega}|u_0(x,y)-c_2|^2 H(\varphi(x,y))\,dx\,dy. \end{aligned} \tag{3.18}$$

So the level set formulation of energy function

$$F(c_1, c_2, \varphi) = \mu \int_{\Omega} \delta(\varphi(x,y)) \left|\nabla \varphi(x,y)\right| dxdy + \nu \int_{\Omega} H(\varphi(x,y)) dxdy + \lambda_1 \int_{\Omega} \left|u_0(x,y) - c_1\right|^2 H(\varphi(x,y)) dxdy + \lambda_2 \int_{\Omega)} \left|u_0(x,y) - c_2\right|^2 (1 - H(\varphi(x,y))) dxdy \quad (3.19)$$

Where $H(\cdot)$ is Heaviside function, $u_0(x,y)$ is input image and φ Lipschitz function.

c_1 and c_2 are the mean intensities inside and outside the active contour defined as follows:

$$c_1 = \frac{\int_{\Omega} u_0(x,y) H(\varphi(x,y)) dxdy}{\int_{\Omega} H(\varphi(x,y)) dxdy} \quad (3.20)$$

and

$$c_2 = \frac{\int_{\Omega} u_0(x,y)(1 - H(\varphi(x,y))) dxdy}{\int_{\Omega} (1 - H(\varphi(x,y))) dxdy} \quad (3.21)$$

Chan-Vese used. Aim of in our proposed method the evolution equation has been find out using Newton Raphson method in place of gradient descent method for finding evolution as suggested which s used in [294]. The method differs from the Steepest Descent, in that the information of the second derivative is used to locate the minimum of the function. This results in faster convergence. This iterative process follows a set guideline to approximate one root, considering the function, its derivative, and an initial x-value. The Newton-Raphson method uses an iterative process to approach one root of a function. The specific root that the process locates depends on the initial, arbitrarily chosen x-value.

$$X_{n+1} = x_n - \frac{f(x_n)}{f'(x_n)} \quad (3.22)$$

Now applying the Newton Raphson method on eq. (3.19) for finding out evolution equation:

$$\frac{\partial \varphi}{\partial t} = \left\{ \delta_\varepsilon(\varphi) \left[\mu div\left(\frac{\nabla \varphi}{|\nabla \varphi|} \right) - \nu - \lambda_1 \left(u_0 - c_1 \right)^2 + \lambda_2 \left(u_0 - c_2 \right)^2 \right] \right\}^{-1} \bullet F_\varepsilon(c_1, c_2, \varphi) in \left(0, \infty\right) \times \Omega,$$

$$\phi\left(0, x, y\right) = \phi_0\left(x, y\right) in\, \Omega,$$

$$\frac{\delta_{\varepsilon(\phi)}}{\nabla \phi} \frac{\partial \phi}{\partial \vec{n}} = 0 \, on \, \partial\Omega \qquad (3.23)$$

Where $\vec{n}$ denotes the exterior normal to the boundary $\partial\Omega$, and $\frac{\partial \phi}{\partial \vec{n}}$ denotes the normal derivative of φ at the boundary.

Let h be the space step and Δt the time step then the discretization of (3.23) is as follows:

$$\frac{\varphi_{I,J}^{N+1} - \varphi_{I,J}^{N}}{\Delta T} = \left\{ \delta_h\left(\varphi_{i,j}^n\right) \left[\frac{\mu}{h^2} \Delta_-^x \left(\frac{\Delta_+^x \varphi_{i,j}^n}{\sqrt{\left(\Delta^x + \varphi_{i,j}^n\right)^2 / (h)^2 + \left(\varphi_{i,j+1}^n - \varphi_{i,j-1}^n\right)^2 / (2h)^2}} \right) \right.$$

$$+ \frac{\mu}{h^2} \Delta_-^y \left(\frac{\Delta_+^y \varphi_{i,j}^{n+1}}{\sqrt{\left(\varphi_{i+1,j}^n - \varphi_{i-1,j}^n\right)^2 / (2h)^2 + \left(\Delta_+^y \varphi_{i,j}^n\right)^2 / h^2}} \right)$$

$$\left. - \nu - \lambda_1 \left(u_{o,i,j} - c_1(\varphi^n) \right)^2 + \lambda_2 \left(u_{0,i,j} - c_2(\varphi^n)^2 \right) \right] \right\}^{-1} \bullet F_h\left(c_1, c_2, \varphi_{i,j}^n\right) \qquad (3.24)$$

Eq. (3.24) is a linear system equation and is solved by an iterative method.

The stationary problem obtained directly from the minimization problem could also be solved numerically, using a similar finite differences scheme. As in Chan-Vese method proposed FRACM, the re-initialization is optional. On the other hand, it should not be too strong, because, it prevents interior contours from growing.

Finally, the principal steps of the algorithm are:

1. Initialize ϕ^0 by ϕ_0, $n = 0$.

2. Compute $c_1\left(\phi^n\right)$ and $c_2\left(\phi^n\right)$ by eq. (3.20) and eq. (3.21).

3. Solve the PDE in ϕ from (3.24), to obtain ϕ^{n+1}.

4. Reinitialize ϕ locally to the signed distance function to the curve (this step is optional).

5. Check whether the solution is stationary. If not, $n = n + 1$ and repeat.

3.3.2.2. Results

In this section some results in the form of figures and tables have been shown. Table 3.1 explains that the proposed FRACM method gives the response faster than that GAC method and the method proposed by Chan-Vese.

Figure 3.1 shows the input images. These images are original images taken from Cardiology department of Postgraduate Institute of Medical and Education Research.(PGIMER) Chandigarh, India.

Patients suffering from mitral regurgitation are taken for the examination**.** Here 9 such images are presented as examples. The images have been obtained by a trained echocardiographer using standard parasternal and apical views of heart. Image a and b are in apical four chamber views of heart while images from b to h are in parasternal long axis views.

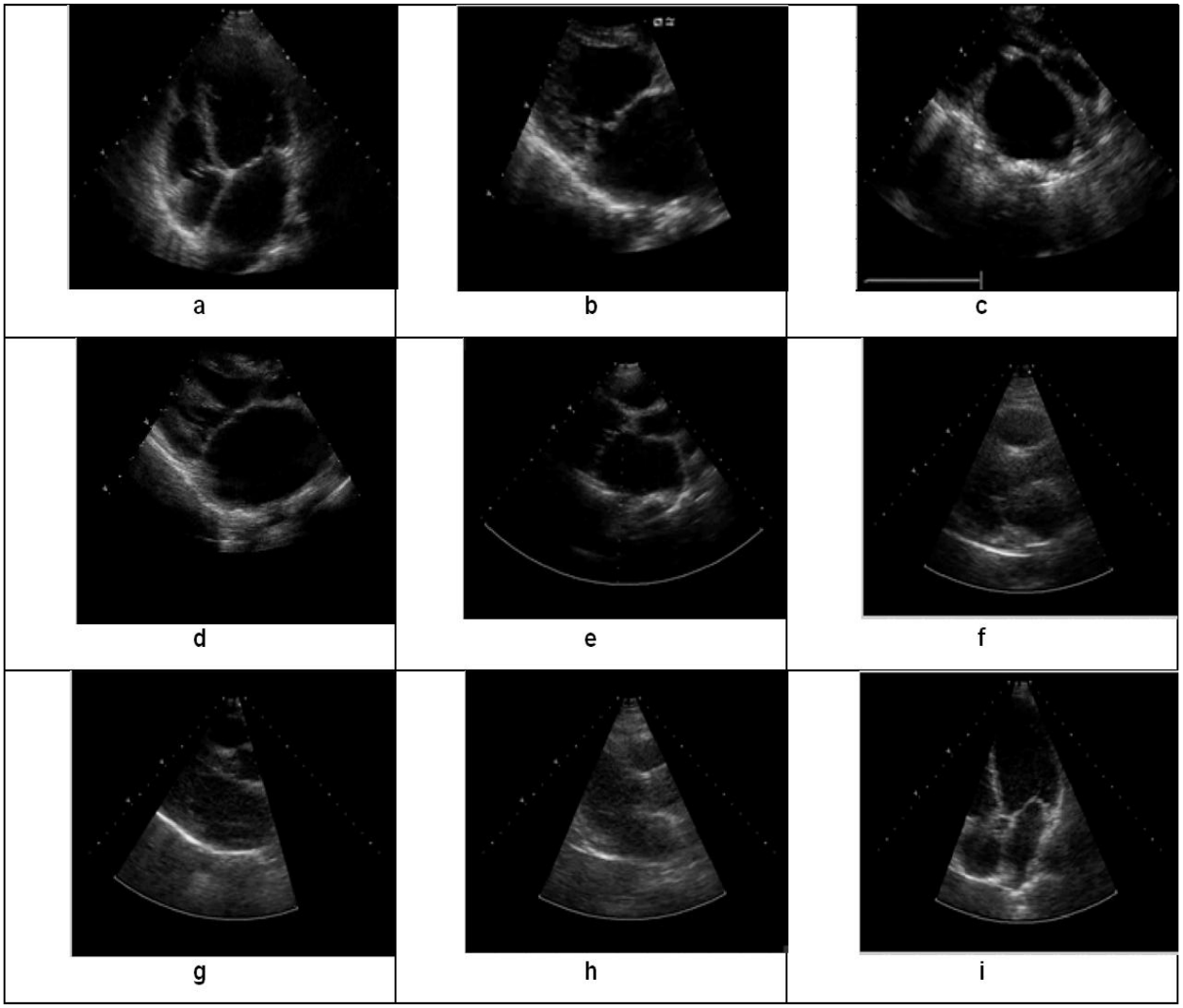

Figure 3.1 Images for Boundary Detection in Different Views of Heart

Figure 3.2 shows the images after boundary detection with GAC model. In this figure it can be seen that from among the nine cases none gives the satisfactory boundaries. For example if image a, b, c, d, e, f, g and i in this figure has been observed, the contour are not able to spread and converges on the chambers boundaries, it means that the contour leaks the required boundaries.

In fig. 3.1a there are four chambers left ventricle, left atrium, right ventricle and right atrium. When the GAC method has been applied to get the boundaries of these chambers then the result obtained is shown in fig 3.2a. Here it can be seen that the contour is leaked in such a way that it is not able to stop on the chamber boundaries. Contour stops only on the more shiny areas and chamber boundaries remains as it is. In figs 3.2b, 3.2c, 3.2d, there is left ventricle and left atrium

to be drawn by GAC. But behaves same as in the case of fig 3.2a. Contours in fig. 3.2e try to approach the chamber boundary but not able to make a continues drawing around the chamber. Contours in fig 3.2f gives totally false impressions of boundaries. GAC method fails in fig. 3.2g to draw boundary due to shiny effect of walls of the heart. Noisy image such as in case of fatty person or a small child, creates major problem in finding contour using GAC method, as can seen in fig. 3.2h. In this figure contour in not able to move inside the cambers and restricted by the high amount of noise. However GAC less useful, if image having less noise like in fig. 3.2i.

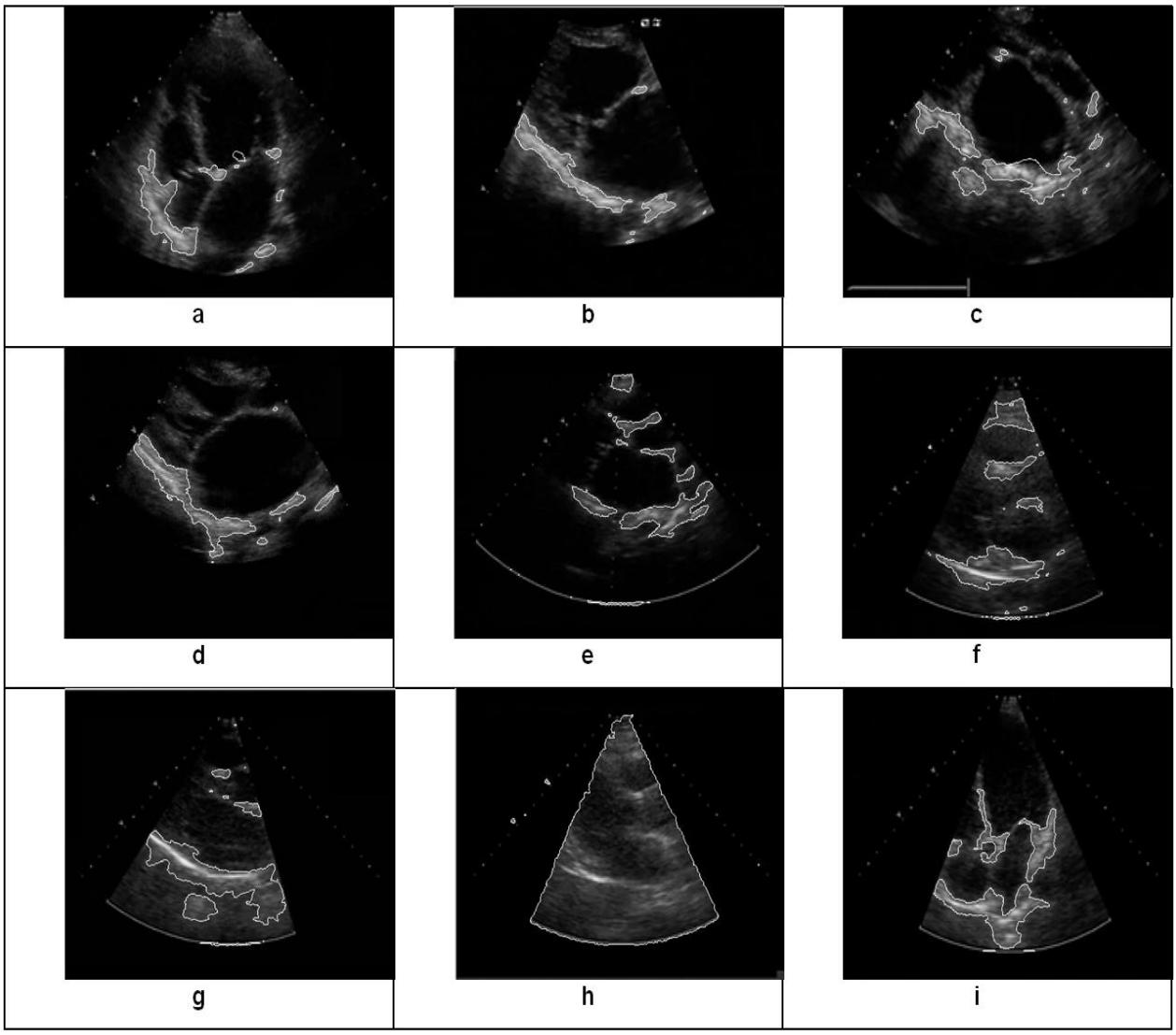

Figure 3.2 Boundary Detection with GAC Method in Different Views of Heart

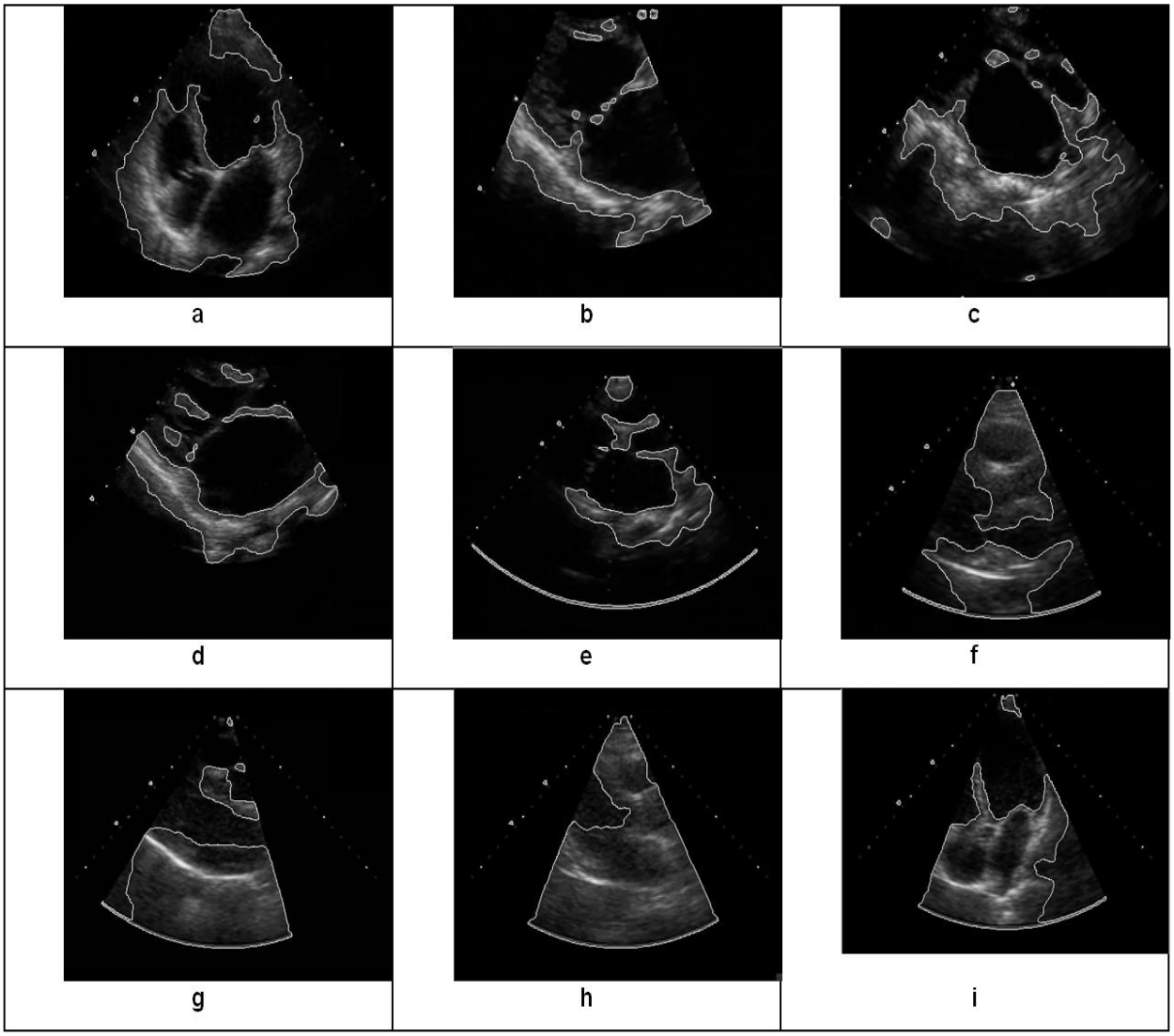

Figure 3.3 Boundary Detection with Chan–Vese Method in Different View of Heart

Fig. 3.3 shows the boundary detected images with C-V model. Here the results are better than the results obtained from the GAC model; however, here also the C-V model is not able to detect properly the boundaries of all the images. For example in fig. 3.3a and fig. 3.3i it is clearly seen that the contour is not able to detect all necessary boundaries and stops before approaching the chambers boundaries. In fig. 3.3a left ventricle has been detected but the contour just surrounds the other three chambers as the outer boundary. Whereas in case of fig. 3.3i upper two chambers i.e. left ventricle and left atrium have been detected properly but lower chambers i.e. left atrium and right atrium are just surrounded by the contour on the outer side. Similar deficiencies are also seen more or less in other images viz. fig. 3.3b to fig. 3.3h. In these cases contour try to approach the

chamber boundaries but not able to create a smooth continues boundaries of the all cambers. So it is difficult to distinguish chambers properly.

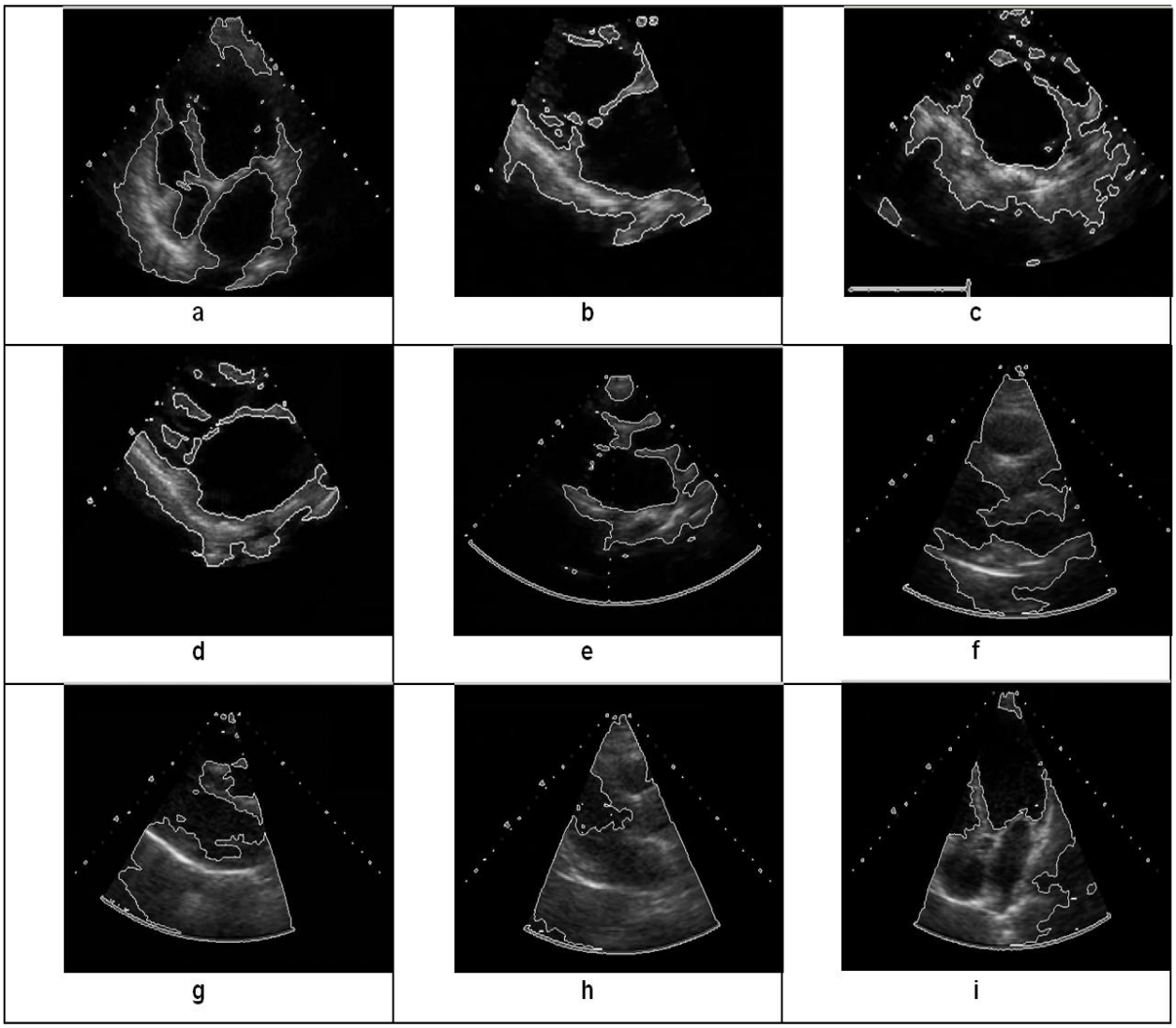

Figure 3.4 Boundary Detection with Proposed Method FRACM in Different View of Heart

Figure 3.4 shows the boundaries detected by proposed method. It can easily be seen that in the proposed FRACM method contour is able to draw all chamber boundaries accept in case of fig. 3.4f, fig. 3.4h and fig. 3.4i.

However these images also shows better results when compared with fig. 3.2f, fig. 3.2h and fig. 3.2i and fig. 3.3f, fig. 3.3h and fig. 3.3i. In fig. 3.4a boundaries of all four chambers viz. left atrium, left ventricle, right ventricle and right atrium have been detected properly such as chambers

and be indentify clearly. The difference can be seen by comparing this figure to fig. 3.2a and fig. 3.3a. Similar differences can be seen in fig. 3.4b, fig. 3.4c, fig. 3.4d, fig. 3.4e and fig. 3.4g with fig. 3.2b, fig. 3.2c, fig. 3.2d, fig. 3.2e and fig. 3.2g and fig. 3.3b, fig. 3.3c, fig. 3.3d, fig. 3.3e and fig. 3.3g.

FRACM method also takes less time and iteration for detecting same boundary as shown in table 3.1. Fast response is very important for clinicians. Table 3.1, shows the comparison between the GAC, Chan-Vese's and the proposed FRACM algorithm boundary detection techniques in terms of time and iterations to converge the contour on the boundaries taken by the CPU.

Table 3.1: Comparison between GAC, Chan–Vese and Proposed Algorithm FRACM

Images	GAC Model		C-V Model		Proposed FRACM Model	
	Iterations	**Time (sec.)**	**Iterations**	**Time (sec.)**	**Iterations**	**Time (sec.)**
1	2300	278.94	1500	36.35	1100	27.57
2	2500	250.49	1800	44.19	1200	29.91
3	2300	300.67	2500	62.86	1800	51.06
4	2500	270.73	1900	40.75	1400	34.38
5	2500	389.96	2000	47.98	1300	33.34
6	3000	386.51	1800	43.61	1300	33.61
7	4000	485.28	2000	46.47	1200	30.32
8	1400	142.79	1500	34.01	1000	24.94
9	3200	365.06	1600	36.84	1100	25.45

Fig. 3.5. represents the statistical analysis of the proposed method. Mean, Median, Standard deviation and variance has been taken for comparison. These four parameters have been calculated for all nine images based on GAC, Chan-Vese method and FRACM method. From the graphs in

fig. 3.5 it can be observed that line related to FRACM shows less fluctuations in the mean, median, standard deviation and variance of iteration time from image to image. This means that the method is almost suitable for all the images weather the images are less noisy or highly noisy.

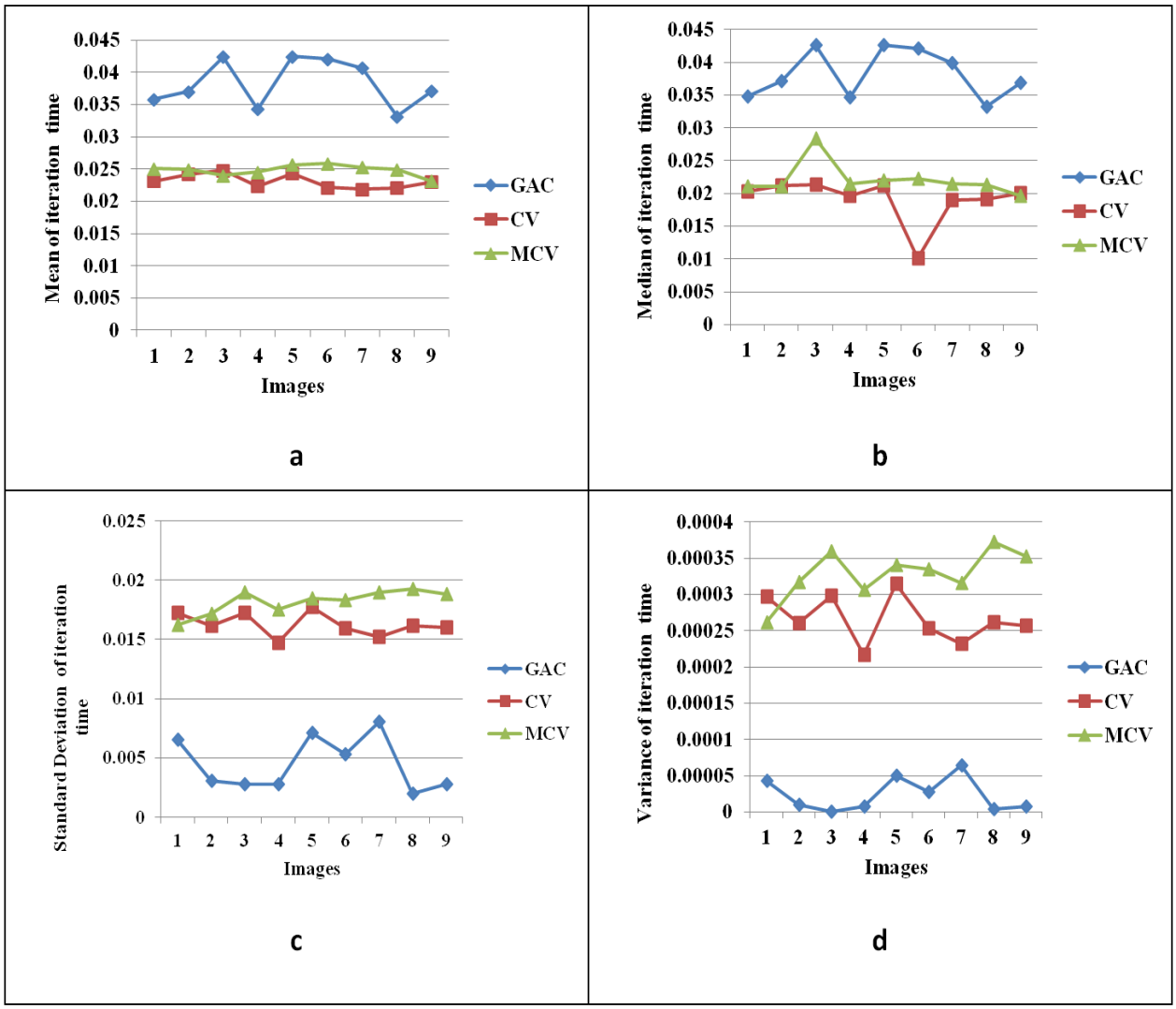

Figure 3.5 Comparisons of GAC, C-V and FRACM Methods (a) Mean, (b) Median (c) Standard Deviation and (d) Variance of Iteration Time

3.3.3 Proposed Method 2: New Selective Binary and Gaussian Filtering Regularized Level Set with New Signed Pressure Force Function (NSBGFRLS)

In this section a level set method for active contour model is developed with a new signed pressure force function. Proposed model is faster than the model proposed in [171]. This model having the ability to converge the contour on the all necessary boundaries so, improves the true value detection related to chambers. This model is used here for echocardiographic images but it is equally useful for other images also.

3.3.3.1 NSBGFRLS Formulation

Further improvements in the Selective Binary and Gaussian Filtering Regularized Level Set with New Signed Pressure Force Function (SBGFRLS) method have been done in the proposed method for faster iterations and required convergence of the contour on the boundaries. In the proposed model a new SPF function $spf_n(I(x,y)$ is developed to overcome the problems of SBGFRLS model. Proposed model also takes less time to converge and the lesser number of iterations to converge when compared with other models.

In GAC model active contours evolve according to the measures that belong to intrinsic geometrics of the image [163], [307] and [306]. Splitting and merging takes place for the simultaneous detection both in exterior and interior boundaries. Geodesic active contour approach is based on the computation of geodesics or minimal distance curves. This allows the connection between classical snakes which are based on energy minimization and geometric active contours which are based on the theory of curve evolution. Level set formulation for GAC model is given by

$$\frac{\partial \phi}{\partial t} = g|\nabla \phi|\left(div\left(\frac{\nabla \phi}{|\nabla \phi|} \right) + \alpha \right) + \nabla g.\nabla \phi \tag{3.25}$$

Where ϕ is the level set function, ∇ is the gradient operator, α is real constant called the balloon force [174] which controls the curve evolution and g is the edge based function and defined as in eq. (3.15)

$$g\left(|\nabla I|\right) = \frac{1}{1+|\nabla G_\sigma * I|^2} \tag{3.26}$$

Where, σ is the standard deviation, $G_\sigma * I$ shows the convolution between image and the Gaussian kernel.

Because GAC model is based on gradient information so it is not suitable for images with weak edges. In some cases balloon force, which is very difficult to design has been used. The weak balloon force doesn't allow the contour to pass through the narrow part of the object and in case of the large balloon force; contour will pass through the weak edges. When contour is far from the object boundary then also it is difficult to find interior or exterior boundaries of the object.

New selective Binary and Gaussian filtering regularized level set (NSBGFRLS) utilizes the advantages of both GAC and C-V model as in (SBGFRLS) [171]. In the substitution of Edge Stopping Function (ESF), a region based singed pressure force function has been (SPF) developed. This SPF function controls the direction of evolution. Opposite signs (range of SPF function is [-1 1]) around the boundaries of the object in this function enable the contour to expand when it is inside the boundary and to shrinks when it is outside the boundary.

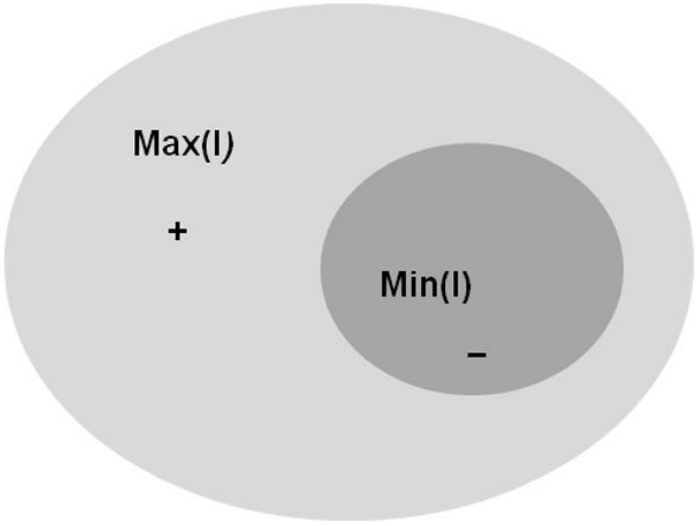

Figure 3.6 Signs of New SPF Function Inside and Outside of the Object

$$spf_n\left(I(x,y)\right)=\frac{\left(\left(c_1*c_2\right)*\left(I(x,y)-\frac{c_1+c_2}{2}\right)\right)}{\max\left(\left|\left(c_1*c_2\right)*\left(I(x,y)-\frac{c_1+c_2}{2}\right)\right|\right)},\ x,y\in\Omega \tag{3.27}$$

Where $spf_n\left(I(x,y)\right)$ is the new SPF function as explained in the proposed method.

The significance of new SPF explained in eq. (3.27) can be explained by referring fig. (3.6), which explains that $Min(I(x,y)) \le c_1, c_2 \le Max(I(x,y))$. Hence

$$Min(I(x,y)) < (c_1 * c_2)\frac{c_1 + c_2}{2} < \max(I(x,y)), x, y \in \Omega \tag{3.28}$$

Due to identical signs of the new SPF function in eq. (3.28) and in fig.3.6, eq. (3.27) can be used as SPF function. So substituting the new SPF function in the eq. (3.25), we get the level set formulation as expressed in eq. (3.29)

$$\frac{\partial \phi}{\partial t} = spf_n(I(x,y)).\left(div\left(\frac{\nabla \phi}{|\nabla \phi|}\right) + \alpha \right)|\nabla \phi| + \nabla spf_n(I(x,y)).\nabla \phi, x, y \in \Omega \tag{3.29}$$

The regular term $div\left(\frac{\nabla \phi}{|\nabla \phi|}\right)|\phi|$ is un-necessary because Gaussian filter utilized here to smooth the level set function to keep the interface regular. Also the term $\nabla spf_n.\nabla \phi$ can be removed because the method utilizes the statistical information of the regions.

$$\frac{\partial \phi}{\partial t} = spf_n(I(x,y)).\alpha|\nabla \phi|, x, y \in \Omega \tag{3.30}$$

The main procedures of the proposed algorithm are summarized as follows:

1. Initialize the level set function ϕ as

$$\phi\left(x, t=0\right) = \begin{cases} -\rho & x \in \Omega_0 - \partial\Omega_0, \\ 0 & x \in \partial\Omega_0, \\ \rho & x \in \Omega - \Omega_0, \end{cases} \tag{3.31}$$

Where $\rho > 0$ is a constant, Ω_0 is a subset in the image domain Ω and $\partial\Omega_0$ is the boundary of Ω_0.

2. Compute $c_1(\phi)$ and $c_2(\phi)$ using eqs. (3.20) and (3.21), respectively.

3. Evolve the level set function according to eq. (3.28).

4. Let $\phi = 1$ if $\phi = 0$; otherwise, $\phi = -1$.

This step has the local segmentation property. If we want to selectively segment the desired objects, this step is necessary; otherwise, it is unnecessary.

5. Regularize the level set function with a Gaussian filter, i.e. $\phi = \phi * G_\sigma$.

6. Check whether the evolution of the level set function has converged. If not, return to step 2.

Step 4 serves as a selective segmentation procedure, because it makes the deviation $|\nabla\phi|$ that is far from the interface of level set function ϕ close to zero, and only the $\phi(x)$ near the interface will evolve. Thus the evolution has local segmentation property. We can start the contour near the object of interest to obtain the desired segmentation. On the other hand, step 4 should be removed if we want to detect all the objects.

In step 5, the standard deviation σ of the Gaussian filter G_σ is a critical parameter, which should be chosen properly. If σ is too small, the proposed method will be sensitive to noise, and the evolution will be unstable. On the other hand, if σ is too large, edge leakage may occur, and the detected boundary may be inaccurate. In our experiments, we truncate the Gaussian kernel as a $K \times K$ mask for efficiency, which K is typically less than 6. σ ranges from 0.8 to 1.5.

3.3.3.2 Results

Results obtained from SBGFRLS are shown in fig. 3.7. It gives better results than GAC and C-V model but it is also not able to detect chambers of heart properly. Contour is not able to go in the narrow regions. In case of fig. 3.7a only left ventricle have been detected but the contour is not able to move to draw the binderies of the other three chambers. Contour drawn in fig 3.7f, fig 3.7g and fig 3.7h have not any significance in identifying the boundaries of the chambers. In case of fig 3.7i only upper two chambers have been detected but boundaries of the atriums have not been drawn.

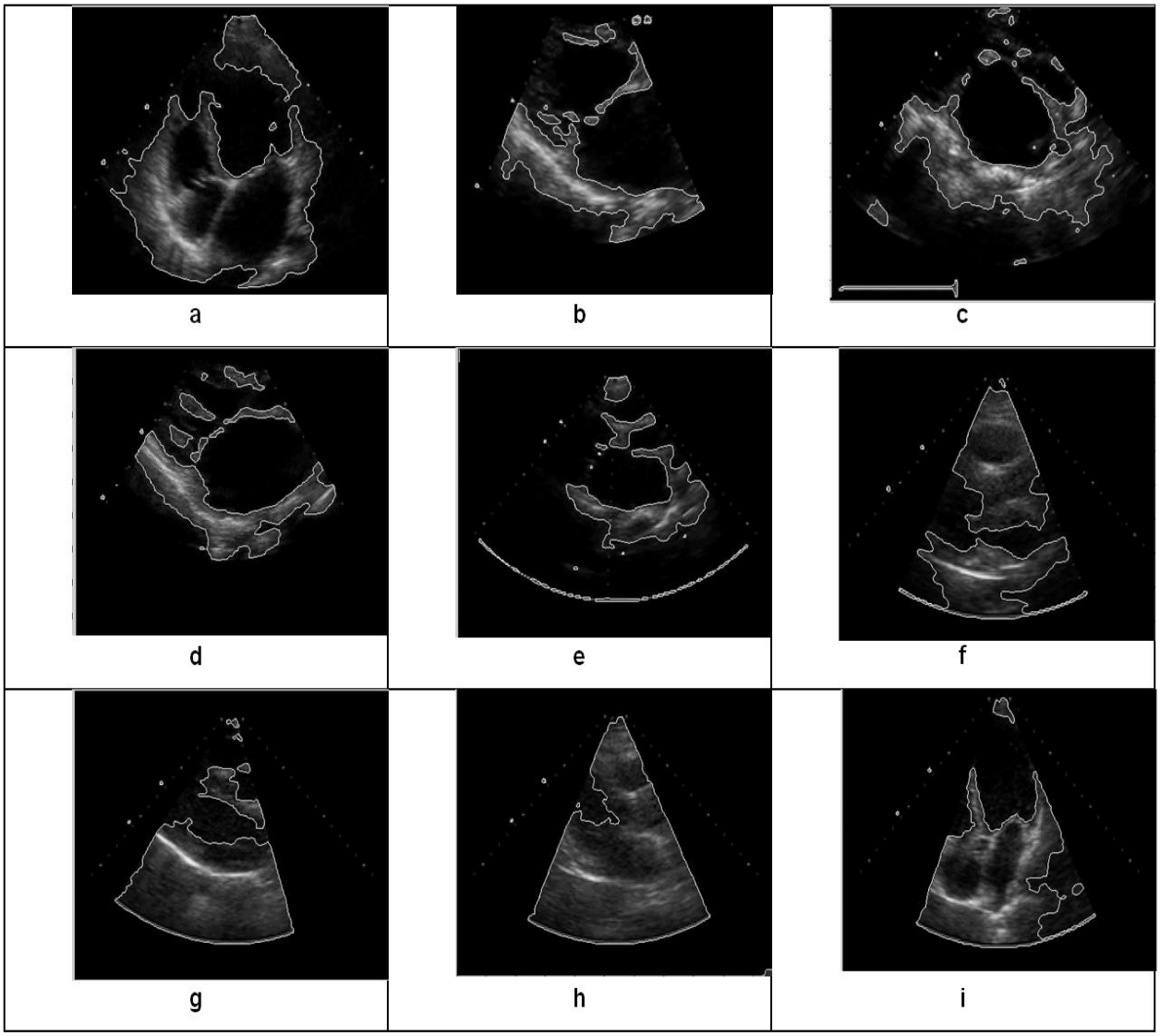

Figure 3.7 Boundary Detection of Echocardiographic Images with SBGFRLS Model

Fig. 3.8 shows the results which are obtained using the proposed method. It can be seen that the proposed model is able to detect all chambers boundaries. In fig. 3.8a all chambers have been drawn properly, difference can be seen by comparing with fig. 3.7a. Similarly significant boundaries have been detected as fig. 3.8f, fig. 3.8g and fig. 3.8h which were the exceptional cases for SBGFRLS method. From fig. 3.8i it can be seen that all chamber binderies have been detected using the proposed method. The proposed method has been able to detect the proper boundaries in those images also in which when processed through C-V and SBGFRLS. Proof of this can been seen by comparing fig. 3.3, fig. 3.7 and fig. 3.8.

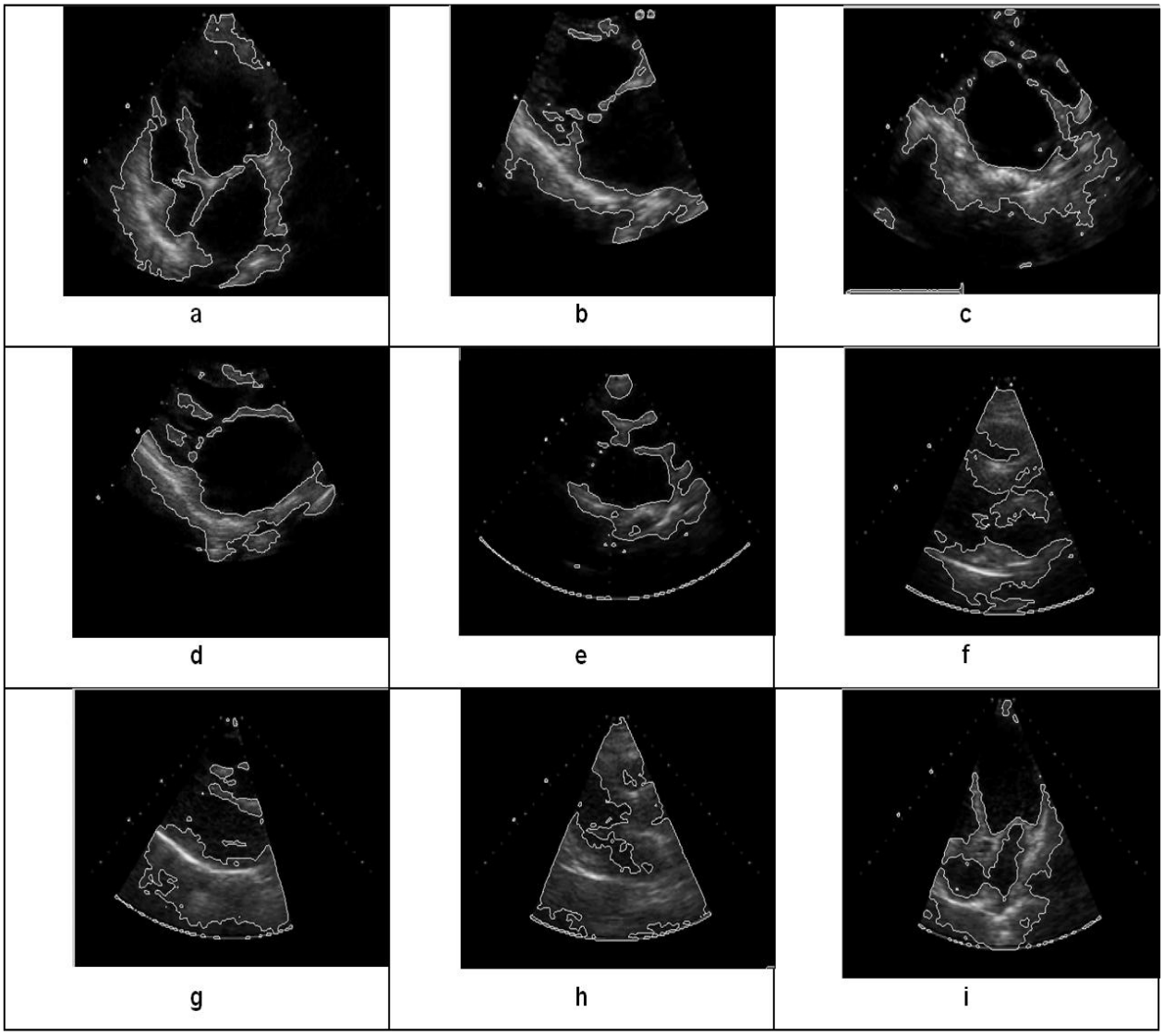

Figure 3.8 Boundary Detection of Echocardiographic Images with Proposed NSBGFRLS Model

The proposed model is also the most efficient when compared with the other models in terms of the number of iterations and the time it takes to converge. It takes the lowest time and the least iterations. Table 3.2 shows the number of iterations and time taken by GAC, C-V, SBGFRLS and the proposed model.

From observations from the table 3.2 it is seen, whereas the GAC model, C-V model and The SBGFRLS models takes 1400 to 4000, 1500 to 2500 and 100 to 200 iterations respectively, the proposed model takes only 30 to 60 iterations to converge; and whereas these three models take the total time to converge ranging from 142.79 to 485.28 seconds, 34.01 to 62.80 seconds and 2.15 to

4.68 seconds respectively, the proposed model takes total time ranging from 0.64 to 1.13 seconds only.

Table 3.2: Comparison between GAC, C-V, SBGFRLS and Proposed Model NSBGFRLS absed on Computer Efficiency

Images	GAC Model		C-V Model		SBGFRLS Model		NSBGFRLS Model	
	Iterations	Time (sec.)	Iterations	Time (sec.)	Iterations	Time (sec.)	Iterations	Time (sec.)
1	2300	278.94	1500	36.35	150	3.32	40	0.81
2	2500	250.49	1800	44.19	150	3.24	40	0.75
3	2300	300.67	2500	62.86	100	2.15	30	0.64
4	2500	270.73	1900	40.75	150	2.86	40	0.73
5	2500	389.96	2000	47.98	200	4.68	50	0.95
6	3000	386.51	1800	43.61	150	2.96	50	0.96
7	4000	485.28	2000	46.47	200	4.16	40	0.76
8	1400	142.79	1500	34.01	150	2.89	60	1.13
9	3200	365.06	1600	36.84	200	4.29	50	0.95

The statistical analysis has also been done to show graphically as in figs. 4.9 for mean, median, standard deviation and variance respectively, for the per iteration time taken to converge GAC, C-V, SBGFRLS and the proposed model. it can be observed that line related to SBGFRLS shows much less fluctuations in the mean, median, standard deviation and variance of iteration time from image to image. This means that the method is almost suitable for all the images weather the images are less noisy or highly noisy.

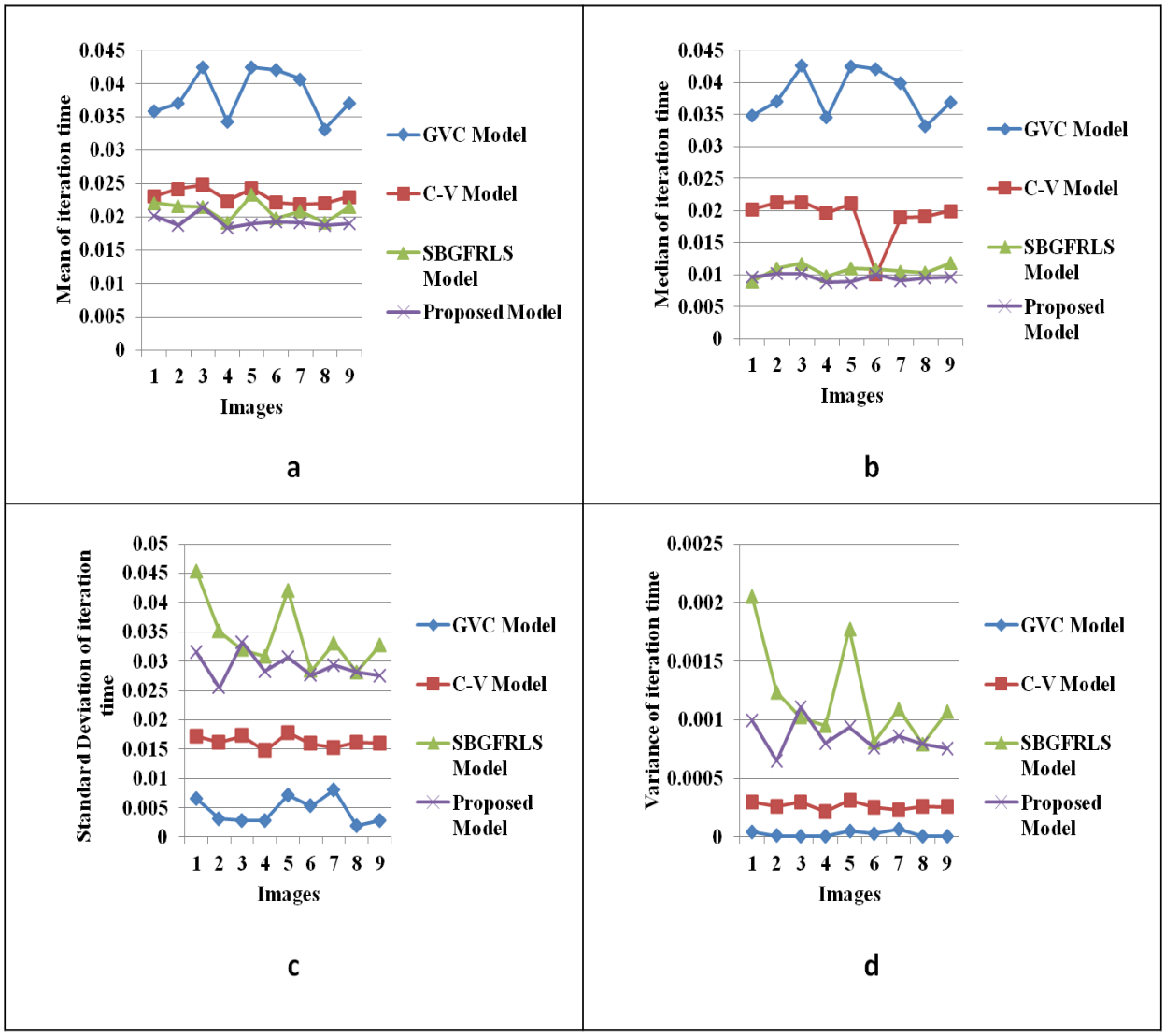

Figure 3.9 Statistical Analysis of the NSBGFRLS along with other Models for the per Iteration Time Taken to Converge

3.4 SUMMARY

The proposed first algorithm presented here gives a way to automatically find out the boundaries of left ventricle and left atrium which are dilated due to mitral regurgitation. Boundary detection is required for finding out the area which is a measure of severity of mitral regurgitation. Active contour method is best suitable for this work. An active contour model based on Mumford–Shah segmentation techniques and the level set method has been used. Our model is not based on an edge-function to stop the evolving curve on the desired boundary. Also, there is no need to smooth the initial image, even if it is very noisy and in this way, the locations of boundaries are

very well detected and preserved. By our model, we can detect the echocardiographic image boundaries which are not necessarily defined by gradient or with very smooth boundaries, for which the classical active contour models are not applicable. Results show that the proposed algorithm exhibits a faster response than with results obtained with Chan-Vese method. Proposed FRACM method takes less no. of iterations and less time to get desired boundaries.

The proposed NSBGFRLS model presents a method to detect boundaries of echocardiographic images automatically. Automatic detection of boundaries enables the clinicians to determine the chambers efficiently and carry out easy diagnosis. The proposed method is efficient in terms of detecting the proper boundaries with the highest clarity. It exhibits much higher CPU efficiency which is of very high significance to the clinicians for carrying out speedy diagnosis. The new SPF developed here can also be used with all types of active contours.

CHAPTER 4

AUTOMATIC DETECTION OF MITRAL REGURGITATION JET AREA

4.1 INTRODUCTION

Detection of valvular regurgitation is the most useful application of color flow imaging. Color flow techniques reduce the time required for interpretation and examination in comparison to the time consumed by the PW Doppler examination mapping techniques. During systole, the left atrium is usually free from color in normal cases. In abnormal cases the increased velocity and the turbulence caused through the closed valve orifice, results in aliasing and it appears as a mix of color mosaic patterns. Severity of valvular regurgitation is based approximately on the configuration and the size of the regurgitant jet. Very small jets, localized just to the proximal side of the regurgitant valve, usually signify mild valvular regurgitation. Large jets that fill the receiving chamber usually indicates sever valvular regurgitation.

Figure 4.1 Color Doppler Imaging during Mitral Regurgitation in Parasternal Long Axis View

Since the color flow mapping provides a fast response**,** currently**,** only the color flow approach is in practice for the detection of all valvular insufficiencies. For example, color Doppler study on a patient with mitral regurgitation would show a multicolored (mosaic color) turbulent mitral

regurgitation jet (MR) that can be seen in LA (Parasternal long axis view). Fig. 1 shows the regurgitation, left side image is a gray image without superimposing the pseudo color whereas the right side image is after the application of pseudo color in case of mitral regurgitation.

This shows that when the color pattern is not passive red or blue, and a mosaic pattern exists, then it indicates heart abnormality. Color Doppler image is a pseudo color image, since the velocity magnitude and direction are encoded into color patterns. Conventionally Blood cells moving away from the transducer are usually displayed in blue, while blood cells moving towards the transducer are displayed in red.

There are normally three methods with color Doppler echocardiography for quantifying the regurgitation severity. These are the evaluation of the regurgitation jet area, determining the proximal isovelocity surface area (PISA) and vena contracta width. However the most used method is the evaluation of MR jet and relative it to the severity level of MR. Fig. 5.2 shows the regions for the flow convergence, jet area and vena contracta formation.

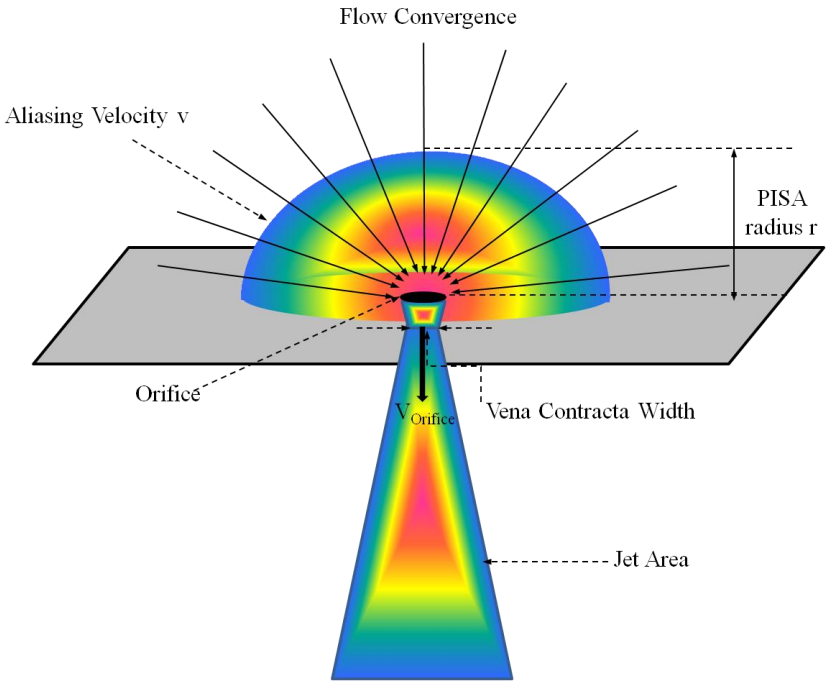

Figure 4.2 Representations of Different Zones for the Doppler Methods

The present work describes a technique developed for the automatic determination of the color jet area. Image processing methods are employed to detect the severity of regurgitation.

The most common approach for using color flow Doppler to quantify mitral regurgitation is to measure the area of the maximum regurgitant jet and to compute that value as a ratio to the area of the left atrium. This measurement is relatively simple and has wide appeal. In this research works following two methods have been developed for the jet area segmentation.

4.2. METHOD 1- REGION GROWING BASED MOSAIC JET SEGMENTATION (RG-MJS)

For accomplishing segmentation of mosaic patterned jet area out of the color background, one needs to carry out a good amount of preprocessing of the color Doppler image, which includes finding out (i) region of interest for getting color portion of the image and (ii) its conversion to gray scale to make it suitable for carrying out intensity based region growing segmentation. Region growing on the basis of intensity difference has been approached to get the MR jet area segmented. The value of the jet area is the dimensional value of the inner object in the segmented jet area. The post processing step has been included to remove the spurious areas around the actual jet area. The method proposed has the advantage of accurately estimating the jet area automatically and thereby save the time of clinicians and provide corroborative estimate with increased accuracy. Focusing and defocusing based techniques have been used for the selection of the ROI, and the advanced gray color to gray scale conversion has been applied to get the fine intensity and well contrast image.

Fig.4.3 shows the complete algorithm for Jet area segmentation and detection. There includes three stages. First two stages are related to Jet area segmentation algorithm and last stage for value detection of that area. In this section jet area segmentation is discussed.

4.2.1 Pre-Processing Stage

As said before, the pre-processing is done to carve out the object of interest and then convert it to format which is suitable for further processing.

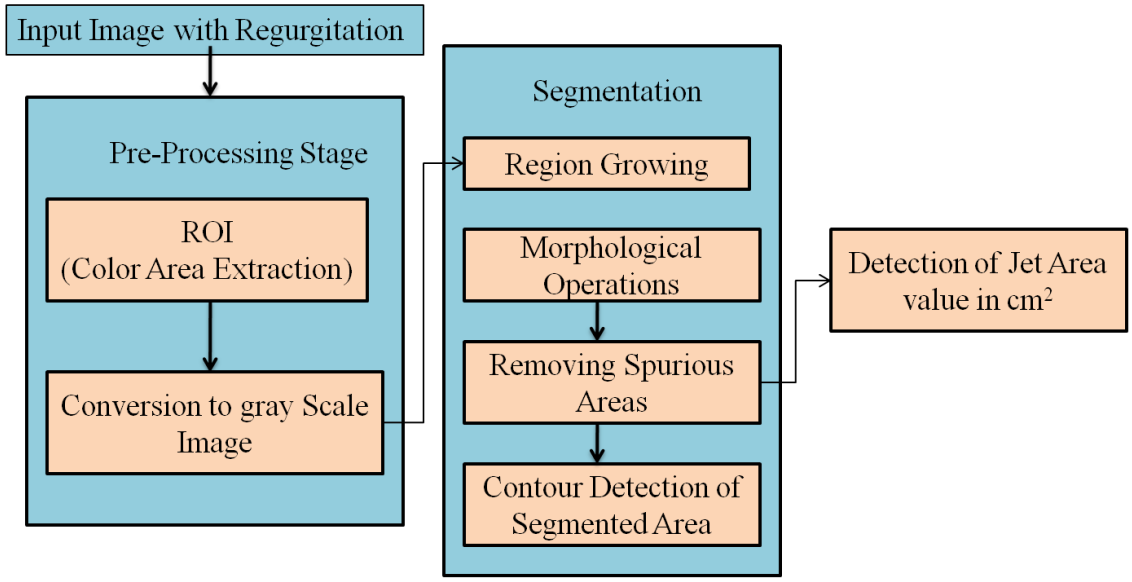

Figure 4.3 Block Diagram for Regurgitant Jet Area Segmentation using RG-MJS and Value Detection

4.2.1.1 Region Of Interest

This stage having two procedures first is Region of interest extraction and second is conversion of RGB image to gray scale image. Input color Doppler Echocardiography image with regurgitation is the combination of 2-d image and color Doppler image. Color shows the direction and flow of blood, So that color area is Region Of Interest in this case. This can be obtained by removing the background image.

This is possible if we have that image also on which that pseudo color is superimposed. There difference gives the ROI image, i.e color image.

ROI region can be given as:

$$f_{ROI}(x) = f(x|F|)\,p(F) + f(x|DF|)\,p(DF),$$
$$= \sum_{j=1}^{2} \frac{\pi_j}{\mu_j} \exp\left(-x/\mu_j\right) U_x. \qquad (4.1)$$

Where $x \geq 0$ denotes a particular contrast level, F and DF correspond to focused and defocused regions, respectively, $\pi_j^{'}$s are the mixing proportions $\left(0 \leq \pi_j \leq 1\right), \sum_{j=1}^{2} \pi_j = 1,$ and μ_j denotes the mean contrast of the jth class. μ_1 corresponds to the contrast distribution in the focused region so $\mu_1 > \mu_2$.

Where a1+a2, b1+b2……p1+p2 are random pixel values if image I1 and a1, b1…...p1 are random pixel values of image I.

4.2.1.2 Color to Gray Scale Conversion

Second step is conversion of that color image to gray scale image because region growing used is based on intensity of the image. Obtained image is multi intensity image on gray scale. The effective luminance of a pixel can be calculate as in eq. (4.2).

$$Y = 0.3R + 0.59G + 0.11B \tag{4.2}$$

Every color as well as color combination has its own intensity. Gray levels represent the interval number of quantization in gray scale image processing. Here the image is 8-bit image. There are 256 gray levels in an 8 bit gray scale image, and the intensity of each pixel can have from 0 to 255, with 0 being black and 255 being white.

Other method we apply is as follows:

Let $f_{ROI} = \{ f_{ROI}(x.y)\} = \{R(x,y), G(x,y), B(x,y)\}$ is a color image, we want to find three transform coefficients $\alpha, \beta,$ and γ to transform f_{ROI} into a grayscale image $fL_{ROI}(x,y) = \{ fL_{ROI}(x,y)\} = \{\alpha R(x,y) + \beta G(x,y) + \gamma B(x,y)\}$, where, (x,y) is the spatial co-ordinate of the pixels. The requirement of fL_{ROI} is to have the maximum variance in order to convey the maximum information. However, only maximizing the variance has no guarantee that fL_{ROI} will be visually pleasing or even visually meaningful. Therefore, extra constraints are necessary in order to produce visually plausible maximum variance grayscale image. It needs to set constraints; which may be as follows: First, the transform should be energy preserving.

We should not amply the image's energy but rather should preserve the energy in the grayscale. This means that $\alpha + \beta + \gamma = 1$; and second, the grayscale image should preserve the brightness of the original image. This is an equally important condition. An image and its negative have the same variance. The problem is, thus, formulated as:

Transform f_{ROI} to fL_{ROI} according to

$$fL_{ROI} = \{ fL_{ROI}(x,y)\} = \{\alpha R(x,y) + \beta G(x,y) + \gamma B(x,y)\}, \tag{4.3}$$

The transform coefficients are found as

$$(\alpha,\beta,\gamma) = \underset{\alpha,\beta,\gamma}{arg\,max}\left(Var\left(\left\{fL_{ROI}(x,y)\right\}\right)\right) \tag{4.4}$$

Subject to

$$\alpha+\beta+\gamma = 1 \tag{4.5}$$

And

$$\sum_{''(x,y)} fL_{ROI}(x,y) = \frac{1}{3}\sum_{''(x,y)}\left(R(x,y),G(x,y),B(x,y)\right) \tag{4.6}$$

Let the average of the Red, Green and Blue channels be M_R, M_G and M_B, respectively; the mean vector of the image $M = (M_R, M_G, M_B)$; Let $u = (\alpha,\beta,\gamma)$.

Let $R = \left(R(1,1),R(1,2).....R(M,N)\right)$ be the $M \times N$ dimensional array of the red pixels, Where $M \times N$ is the dimension of the image. We define *G* and *B* similarly for the green and blue pixels. The covariance matrix of the color channels is

$$\zeta\begin{bmatrix} R-M_R \\ G-M_G \\ B-M_B \end{bmatrix} = \left[\left(R-M_R\right)^T \left(G-M_G\right)^T \left(B-M_B\right)^T\right] \tag{4.7}$$

The variance of the transformed grayscale image, $Var(fL_{ROI})$, and the average brightness, $A_b(fL_{ROI})$, are

$$Var(fL_{ROI}) = u\zeta u^T \qquad A_b(fL_{ROI}) = Mu^T \tag{4.8}$$

4.2.2 Jet Area Segmentation

The intensity based region growing technique has been used for carrying out segmentation of the jet area. The following operations have been performed to accomplish the segmentation to get the true regurgitant jet area.

4.2.2.1 Region Growing

Region growing operation segments the image into different regions. The Regions either expand or contract based on the pixel properties and the properties of the neighborhood pixels.

Computation has been done for last iteration grown region R_i, (maximum likelihood estimation) ML estimates for the mean (available from last iteration) and standard deviation $\left(\overline{fL}'_{ROI(R_{i-1})}, \sigma_{f'_{ROI(R_{i-1})}}\right)$.

For every candidate pixel $x_{c_{i-1}}$ being connected to $R_{i-1}, x_{c-i} \in R_i$ if

$$fL'_{ROI}\left(x_{c_{i-1}}\right) \in \left[\overline{fL}'_{ROI(R_{i-1})} + k_i \sigma_{f'_{ROI(R_{i-1})}}\right] \tag{4.9}$$

The assessment function $O_i\left(\overline{fL}'_{ROI(R_{i-1})}, \overline{fL}'_{ROI(P_i)}\right)$ is derived as eq. (4.11) using the intensity average $\overline{fL}'_{ROI(R_i)}$ in R_i and the intensity average $\overline{fL}'_{ROI(P_i)}$ in the external perimeter P_i of R_i according to normalization equation $\overline{fL}_{ROI(N)} = \frac{1}{N}\sum_{x_k \in N} fL\left(x_k\right)$, and eq.(4.10):

$$P_i = \left\{x_{ci}\right\} \cap R_i^C \tag{4.10}$$

$$O_i\left(\overline{f}L'_{ROI(R_i)}, \overline{fL}'_{ROI(P_i)}\right) = \left|\frac{\overline{fL}'_{ROI(P_i)} - \overline{fL}'_{ROI(R_i)}}{\overline{fL}'_{ROI(P_i)} + \overline{fL}'_{ROI(R_i)}}\right| \tag{4.11}$$

If O_{i-1} was a local maximum, when compared to O_{i-2} and O_i (only when $i \geq 2$), then the algorithm stops and the output is R_{i-1}; otherwise it goes for another iteration.

4.2.2.2 Morphological Operation

These are local pixel transformations for processing region shapes. Mostly these are used on binary images. Morphological transformations are logically based on comparison of pixel neighborhoods with a pattern. Here the use of this operation is to smooth the region boundaries for shape analysis and Remove noise and artifacts from an imperfect segmentation. Another use of this operation is to match particular pixel configurations in an image for simple object recognition.

Morphological operations take two arguments, a binary image and a structuring element. A structuring element has been chosen and then comparison has been made between the structuring elements to the neighborhood of each pixel. This determines the output of the morphological operation. Structuring element having an origin. Here in this operation a square shape of the structuring element has been selected and opening of the area of less than 7 pixel radius has been removed.

4.2.2.3 Removing spurious areas

Upon implementation of the above procedures some small areas which are not objects of interest are generated. These areas introduce errors in the calculation of jet area and create complexity in finding regurgitant jet area. So it is important to remove these areas. For removing spurious areas there is a need of a threshold value of some pixels below which these areas are removed and a single object oriented area obtained in the image. Let P are the pixel below area is not acceptable. Then mathematically it can be represented as under:

$$\begin{cases} if\ Area > P\ then\ Area \in D_A \\ if\ Area \le P\ then\ Area \in S_A \end{cases} \quad and \tag{4.12}$$

Where P is the pixel size of the area. D_A is the desired area and S_A is the spurious area.

4.2.2.4 Contour Detection of the Segmented Area

Here the aim of contour drawing is only to represent the segmented area into within a single line. Enclosing area in desired jet area. Contour is a curve in two dimensions on which the value of a function $f(x, y)$ is a constant. Based on the minimum and maximum values of segmented image the number of contour levels and the values of the contour levels have chosen automatically.

Let ϕ is the desired contour, ϕ_i is inside of the contour and ϕ_o outside of the contour then:

$$D_A \in \varphi_i \tag{4.13}$$

And the boundary of this area is on ϕ.

4.2.3 Algorithm for Detection of Jet Area Value

In the previous section segmented area is obtained. But the main requirement in the medical is to find out the numerical value of that regurgitant jet area. Depending upon the numerical value clinician is able to decide the severity of the mitral regurgitation.

For obtaining the numerical value of the regurgitant area firstly pixel values under segmented region has been counted.

$$if\ P_i = 1 then\ P_i \in D_A \tag{4.10}$$

and numerical value of Regurgitant jet area in pixels is

$$A = \sum P_i \tag{4.11}$$

If $P_i = 0$ then ignore this region.

Aim is to find out the area in centimeter squares. So next step is to convert this pixel value into centimeter squares. Here is the procedure how pixels are converted into cm^2.

Pixels = Inches ×DPI (4.12)

4.2.4 Results

Total nine cases have been taken for this research work. Views selected for color Doppler Echocardiography are parasternal long axis view and Apical two chamber and four chamber view. Images which are taken here cover all views.

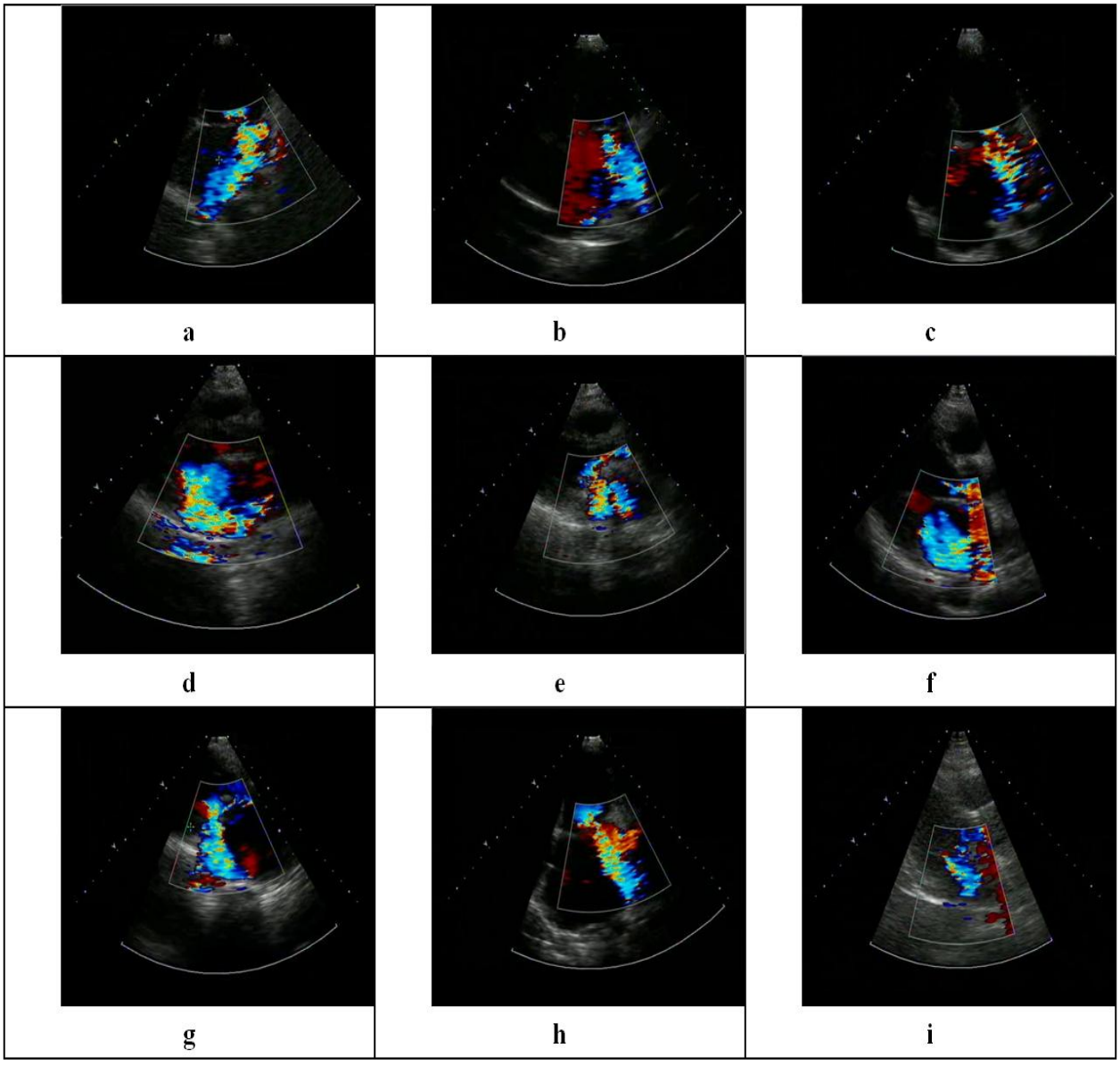

Figure 4.4 Color Doppler Images with Mitral Regurgitation

Fig.4.4 shows the color Doppler images with Mitral regurgitation. Images in fig.4.4a, fig.4.4b, and fig.4.4h are the apical two chamber view of heart with color Doppler. Chambers having large color jet are the left atriums and chamber above on this are the left ventricles and middle portion of these two chambers is the mitral valve. Image in fig.4.4 is the four chamber view of the heart. The left ventricle and left atrium lays just right side of the image. Images in fig.4.4d, fig.4.4e, fig.4.4f, fig.4.4g, and fig.4.4i are in the paresternal long axis view of the heart. In these images also the chambers having large color jet are the atriums. Ventricles are just left above from these chambers.

To extract the color jet portion we need images without pseudo color superimposition. These images are background images shown in Fig.4.5. chambers of the heart can be seen in these images clearly.

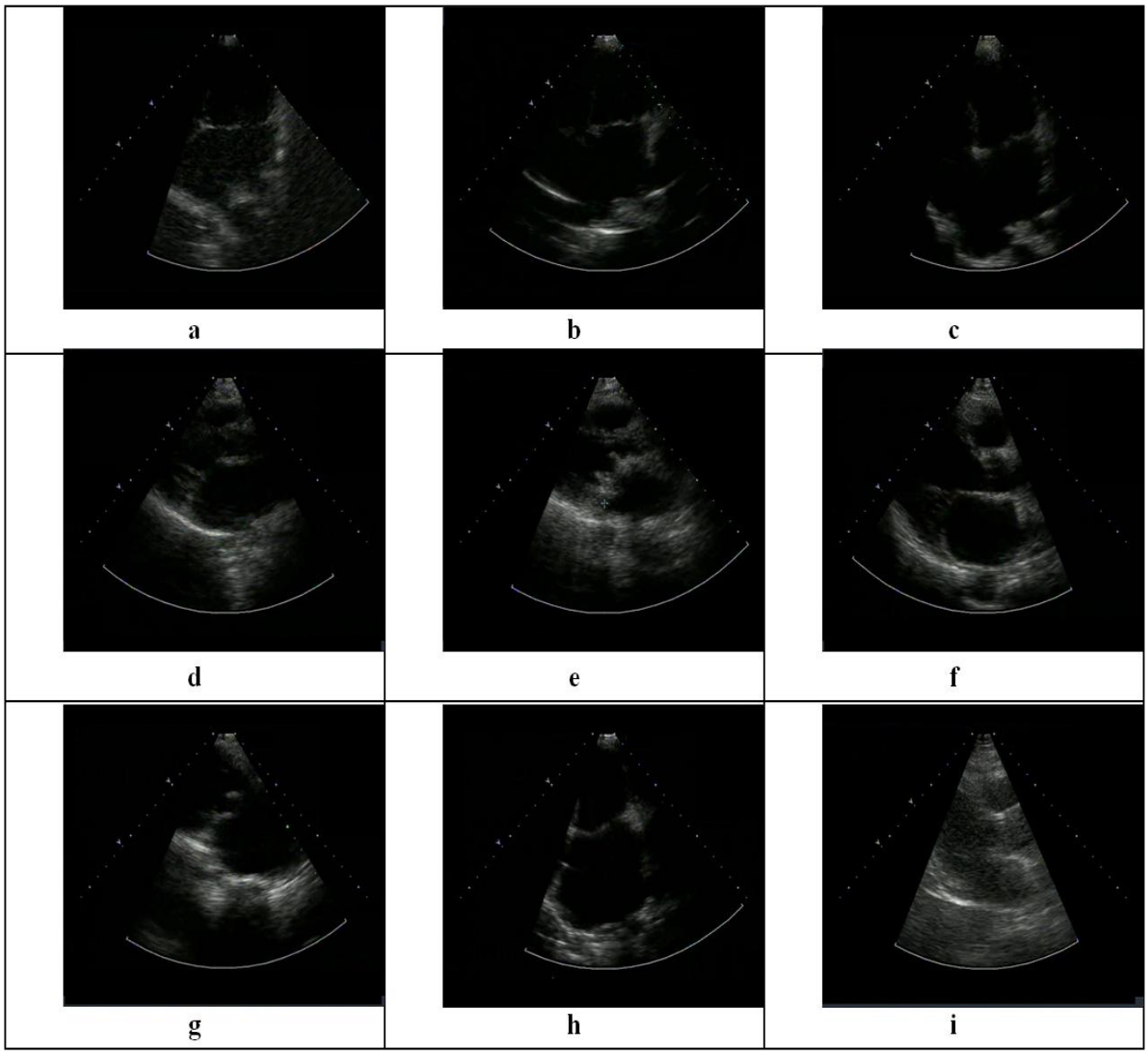

Figure 4.5 Background Images

When Region Of Interest (ROI) is extracted then all background pixels become zero and only color pixel remains a object as shown in fig. 4.6. it can be seen from the below figure that there is pure colors such as red and blue also be there with the mosaic pattern but our purpose is to segmenting only the mosaic pattern, which actually contains the MR jet area. This mosaic pattern is due to the combination of incoming and outgoing blood flow in the atrium at the same time.

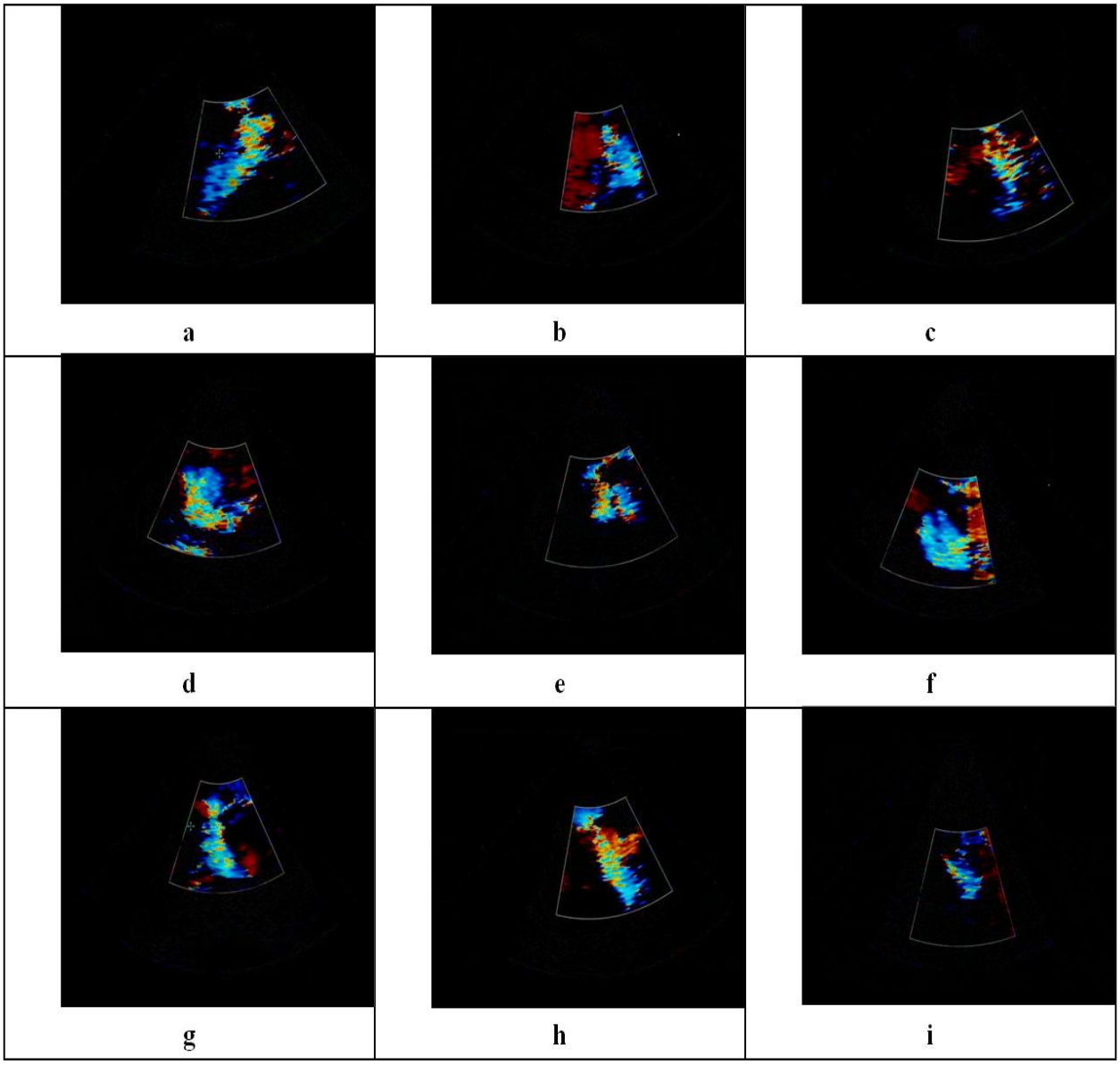

Figure 4.6 Object Extracted Images

Figure 4.7 shows the images that area obtained after applying segmentation and removing spurious areas. It can be seen from the comparison of fig. 4.6 and fig. 4.7 that only mosaic pattern get segmented by the proposed segmentation method while the pure red and blue colors had been

discarded. Images obtained after segmentation are in binary form. White object having pixel each value 1 is the part of the MR jet area.

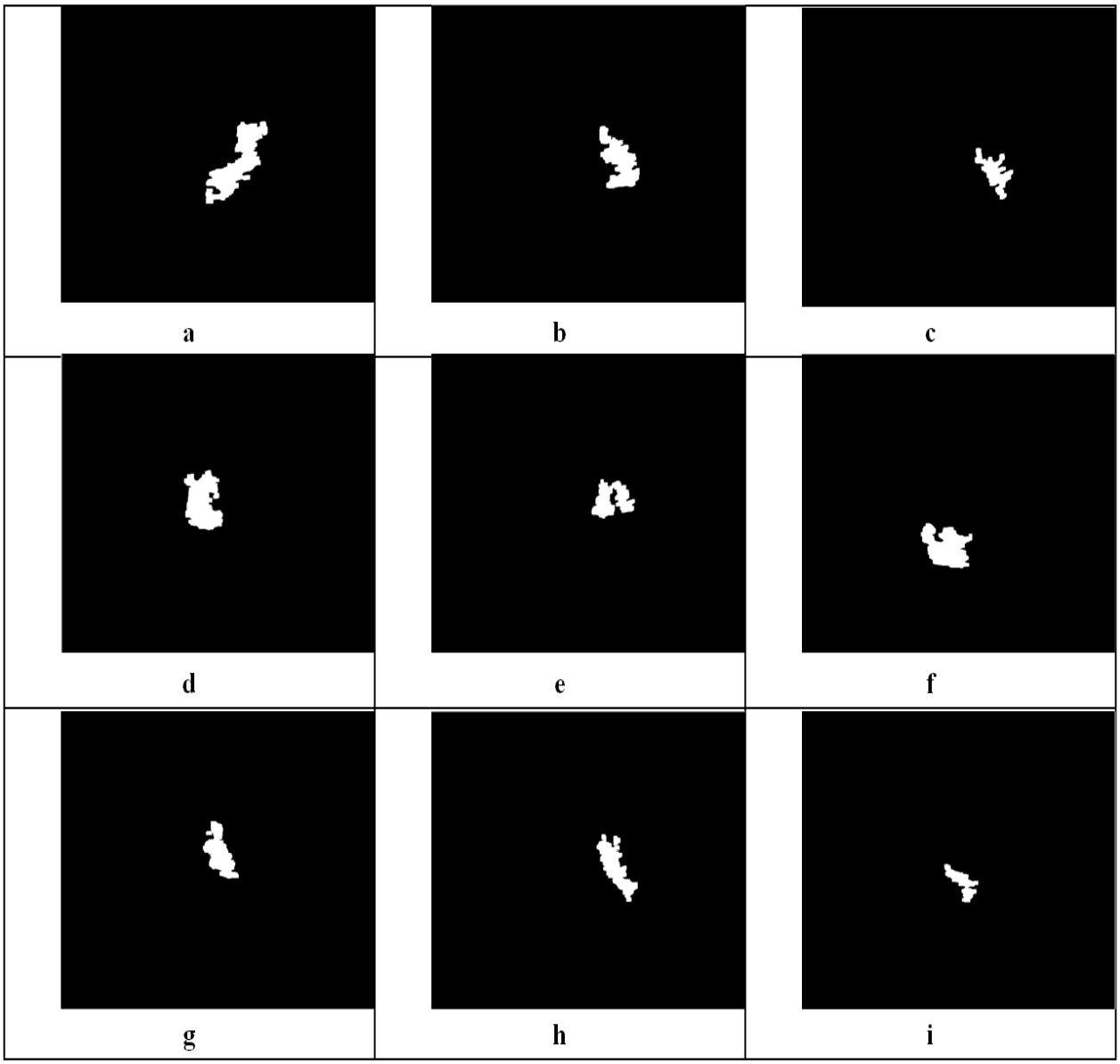

Figure 4.7 Final Jet Area after Segmentation

Figure 4.8 showing the contours of these images. These contours show just boundaries of the segmented jet areas. The purpose of contour drawing is to emphasize the mass and volume of the subject rather than the detail; the focus is on the outlined shape of the subject and not the minor details. Which is important for the clinician just for visualize the size of the MR jet.

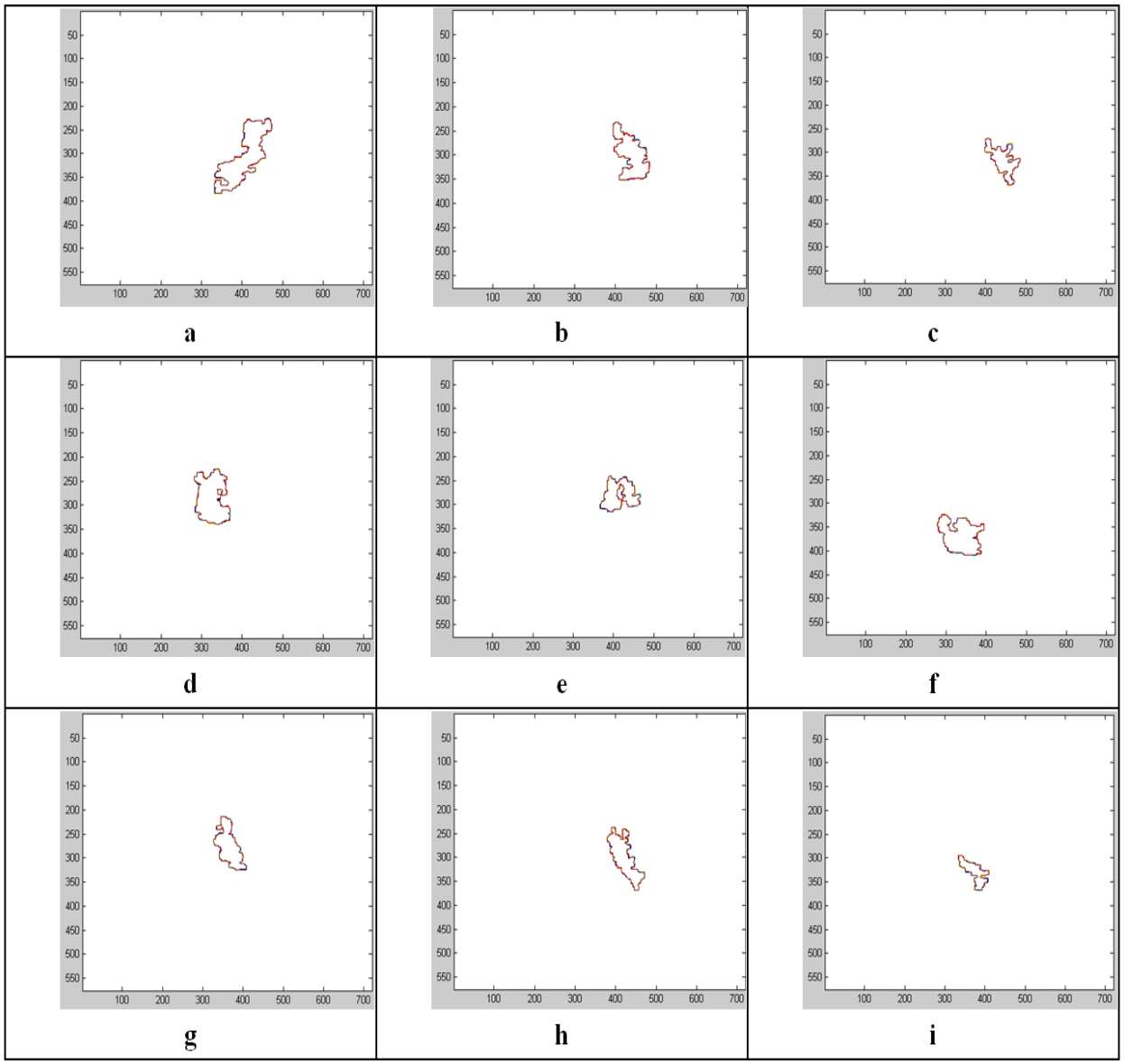

Figure 4.8 Contours of the Jet Areas

Depending upon the size of the regurgitant jet the regurgitation is either mild, moderate or severe. In this research this is calculated automatically. Numerical value of segmented jet area and clinician is as shown in Table. 4.1. This table also shows the comparison between these two values.

The work demonstrates the numerical values corresponding to the extent of severity of regurgitation directly. Table 4.1 shows the comparison between the values obtained through the technique presented here and the values obtained by an expert clinician manually.

Table 4.1: Value of Jet Area obtained from Proposed Segmentation RG-MJS and by Clinician

Images	Automatic Jet Area (Pixels) using RG-MJS	Automatic Jet Area (Cm^2) A using RG-MJS	Jet area drawn by clinician (Cm^2) M	Difference of |A-M |
1	8938	15.38	15.39	0.01
2	4541	10.96	10.86	0.10
3	3432	9.53	9.38	0.15
4	7006	13.61	13.23	0.38
5	4192	10.53	9.72	0.81
6	6300	12.97	12.94	0.03
7	4486	11.24	11.29	0.05
8	4855	11.35	11.86	0.51
9	2168	7.57	5.59	1.98

From fig. 4.9 it can be noticed that value of color jet area in both cases i.e. automatic segmentation proposed in this work and the one obtained by clinician are almost the same. There is very less variation in values. There difference is very-very close to zero line except in some values which are also quite near zero line. If the color jet area is less than $4cm^2$ then the condition of regurgitation is mild. But if it is up to $10cm^2$ then there is moderate regurgitation and if the jet area increases beyond $10cm^2$ then it is indication of severe mitral regurgitation.

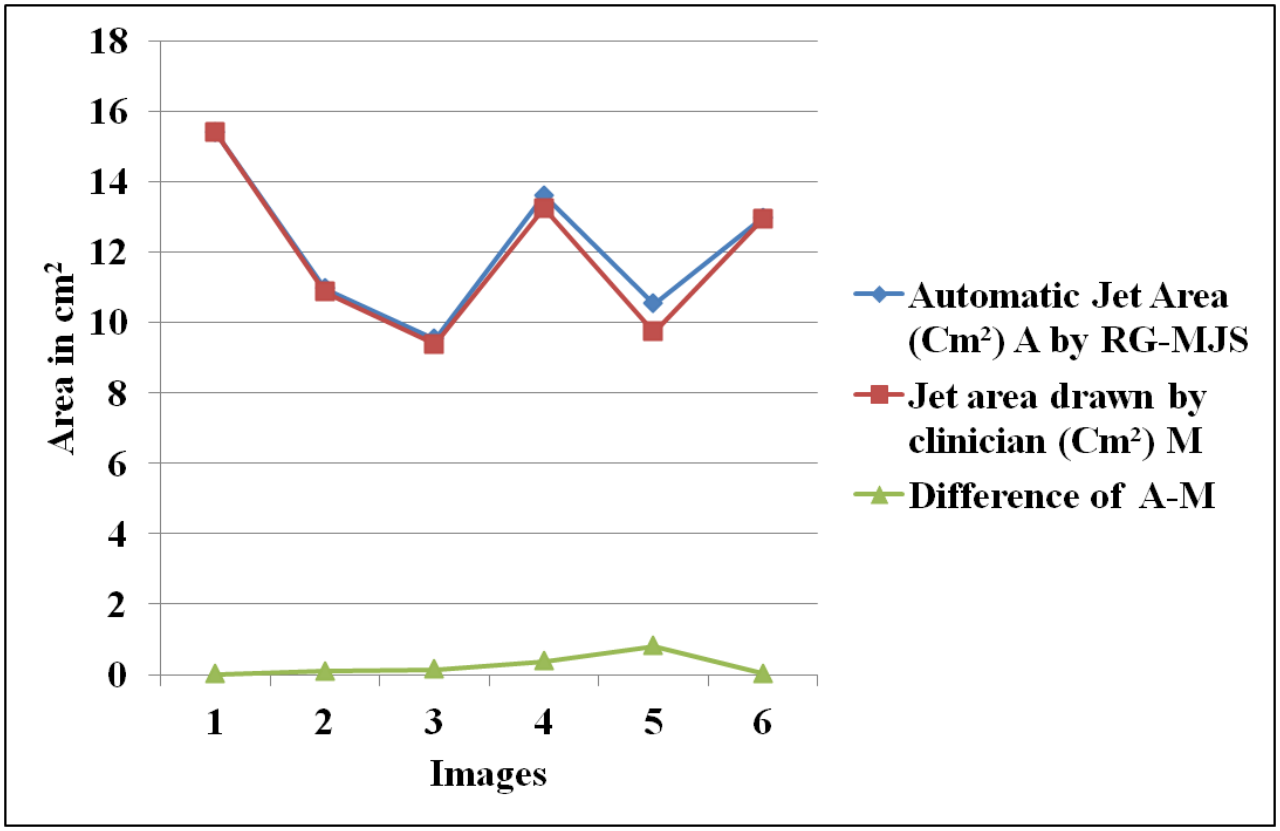

Figure 4.9 Graphical Comparison between Regurgitant Jet Areas Obtained from Proposed Algorithm (RG-MJS) and by Clinician

Table 4.2 shows the patients with mild, moderate and severe mitral regurgitation with proposed algorithm and Table 4.3 presents the findings carried out by clinician. There is no case of mild regurgitation in both cases. Patients are the same in both the cases.

Table 4.2 shows that proposed method categorized two patients in moderate condition and 7 patients in severe condition. Patients having moderate mitral regurgitation are Patient 3 having jet area 9.53 cm^2 and patient 9 having jet area 7.57 cm^2. Patients 1, 2, 4, 5, 6, 7, 8 having severe regurgitation having jet area 15.38 cm^2, 10.96 cm^2, 13.61 cm^2, 10.53 cm^2, 12.97 cm^2, 11.24 cm^2, 11.35 cm^2 respectively. Table 4.3 shows that according to area drawn by clinician three patents 3, 5 and 9 with jet area 9.53 cm^2, 9.72 cm^2 and 7.57 cm^2 respectively are having moderate mitral regurgitation; whereas the patients 1, 2, 4, 6, 7, and 8 with jet area 15.38 cm^2, 10.96 cm^2, 13.61 cm^2, 12.97 cm^2, 11.24 cm^2, 11.35 cm^2 having severe regurgitation.

Table 4.2: Severity Grades According Area Drawn By Proposed Method (RG-MJS)

Images	Mild	Moderate	Severe
1	_	_	15.38
2	_	_	10.96
3	_	9.53	_
4	_	_	13.61
5	_	_	10.53
6	_	_	12.97
7	_	_	11.24
8	_	_	11.35
9	_	7.57	_

Table 4.3: Severity Grades According to Area Drawn By Clinician

Images	Mild	Moderate	Severe
1	_	_	15.39
2	_	_	10.86
3	_	9.38	_
4	_	_	13.23
5	_	9.72	_
6	_	_	12.94
7	_	_	11.29
8	_	_	11.86
9	_	5.59	_

4.3 METHOD 2- COMBINED WAVELET AND WATERSHED TRANSFORMATION BASED MOSAIC JET SEGMENTATION (CWWT-MJS)

In the proposed method a multistep algorithm has been applied. The first stage of the proposed algorithm is dual-tree complex wavelet transform. Next stage is the watershed transform and then similarity measure has been done to get the final segmented image. In this method wavelet transformation is for the reduction of the over-segmentation which is caused by the watershed algorithm. Using the dual tree complex wavelet transformation this can be utilized to get the texture features. The proposed method has ability to distinguish the real regurgitant jet which is mosaic pattern from the other color jet.

4.3.1 Algorithm for Jet Area Segmentation

Figure 4.10 shows the steps which have been carried out during the segmentation of regurgitation jet area.

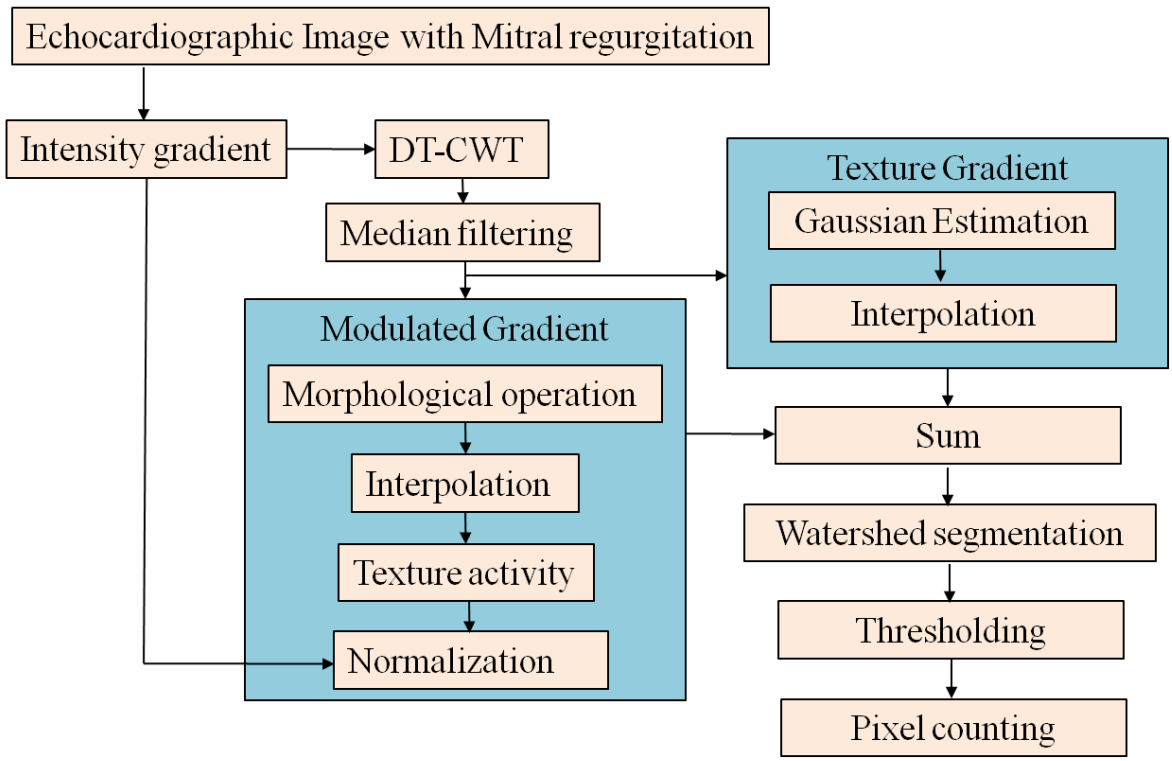

Figure 4.10 Block Diagram for Regurgitant Jet Area Segmentation using CWWT-MJS and Value Detection

4.3.1.1 Intensity Gradient

For getting intensity gradient if image first of all two dimensional sobel gradient operator have been used. This operator performs a 2-D spatial gradient measurement and emphasizes regions of high spatial gradient that corresponds to edges.

Here this operator is used to approximate absolute gradient magnitude at each point in an input grayscale image $I(x,y)$. However we have color image which is to be converted to gray scale first. This operator consists of a pair of 3×3 convolving mask, in which one is as it is and other is rotated by 90^0. As below h_x for horizontal derivative and h_y for vertical derivative. By using this operator multidimensional filtering has been performed with input values outside the bounds equal to nearest border.

h_x=

-1	0	+1`
-2	0	+2
-1	0	+1

and h_y=

+1	+2	+1
0	0	0
-1	-2	-1

Horizointal H_x and vertical H_y components of the image can be obtained as shown in equation 6.10.

$$H_x=\begin{bmatrix}-1 & 0 & +1\\ -2 & 0 & +2\\ -1 & 0 & +1\end{bmatrix}*I(x,y)\ and\ H_y=\begin{bmatrix}+1 & +2 & +1\\ 0 & 0 & 0\\ -1 & -2 & -1\end{bmatrix}*I(x,y) \tag{4.13}$$

The gradient magnitude is given by:

$$|H|=\sqrt{H_x^2+H_y^2} \tag{4.14}$$

4.3.1.2 Dual Tree Complex Wavelet Transform (DT-CWT)

For getting texture features DT-CWT [111] have been used here. It is an enhanced technique in the area of wavelet transform and having the structure as shown in fig. 4.11.

If the output from the DT-CWT can be denoted as $D_i(x,y)$. Its complex magnitude can be denoted as $|D_i(x,y)|$. Where i is the level DT-CWT.

DT-CWT having an approximate shift invariance and good selectivity. This filter has directionality in 2-D with other filters. By using short linear phase it is easy to get perfect reconstruction.

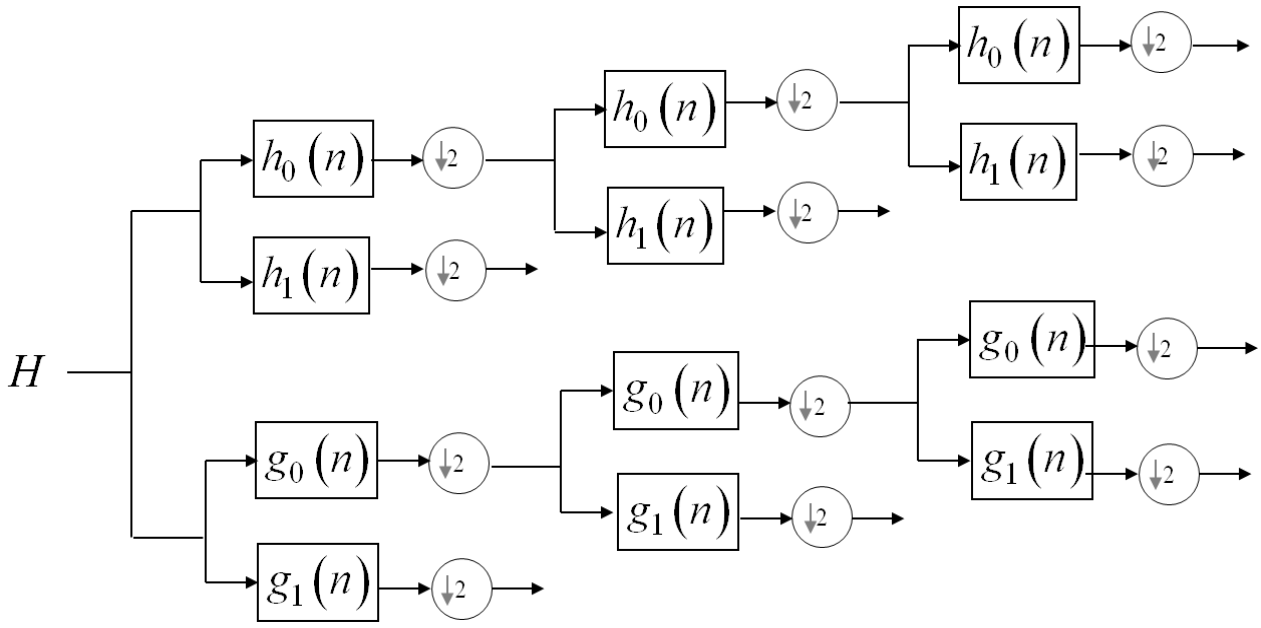

Figure 4.11 Analysis Diagram of Dual Tree Complex Wavelet Transform (DT-CWT)

Image from these feature area not of our use our main objective to segment out the jet area for this further processing is required to collect the other features.

4.3.1.3 Median Filtering

If we directly apply the watershed on this then there may be changes of spurious edges generation for this median filtering have been done which smoothes the image so that sharp edges and line will not produces a false recognition. Median filtering has been applied on each sub-band to avoid this problem

A 9 order median filtering has been applied here. Output of the median filter can be denoted as in eq. 4.15.

$$M_i(x,y) = median(|D_i(x,y)|) \tag{4.15}$$

Now next step is to get modulated intensity gradient and texture gradient from the median filtered sub-band features.

4.3.1.4 Modulated Intensity Gradient

As shown in fig. 6.13 this step consists of four sub steps. First step is to perform morphological operation to remove the noise which is introduced during the 1-D operation of median filtering. Morphological erosion here is defined as in eq.6.16

$$\left[\varepsilon_B(f)\right](x) = \bigcap_{b\in B} f(x+b) \tag{4.16}$$

Where $f(x)$ is the function which is defined over pixels x and B within the sterl mask.

Next step is to apply linear interpolation for up-sampling. Linear interpolation has the property of zero insertion and anti-image filtering. In case of two data points say (x_i, y_i) and (x_j, y_j) then the output of linear interpolation filter at points (x, y) is given by:

$$y = y_i + (y_j - y_i)\frac{(x - x_i)}{(x_j - x_i)} \tag{4.17}$$

And the sum of the up sampled sub-band features i.e. the texture energy is defined as:

$$E_{tex} = \sum \text{int}\,erp\left(\varepsilon_B\left(\frac{M_i(x,y)}{2^i}\right)\right) \tag{4.18}$$

For the correction of dc gain in wavelet filters the factor 2^i is introduced [218].

Now the modulated intensity gradient find out by measuring the texture activity. The aim of this activity is to suppress the intensity gradient in textured areas but leave by keeping in smooth regions unmodified.

The texture activity is given as in eq. (4.19)

$$TA(x,y) = e^{\Re_h\left(\frac{E_{tex}(x,y)}{\alpha} - \beta\right)} \tag{4.19}$$

Where $\Re_h(\varsigma)$ is just half-wave rectification to suppress negative exponents.

$$\Re_h(\varsigma)=\begin{cases}0: & \varsigma<0\\ \varsigma: & \varsigma\geq 0\end{cases} \tag{4.20}$$

β is the threshold below which activity measure is unity. Above this threshold activity measure increases due exponential with sensitivity which is determined by α . E_{tex} is the sum of the up sampled sub-band features and we can call it as texture energy.

After that normalization have been carried out by taking the output of texture activity and intensity gradient and obtained the modulated intensity gradient as in eq. (4.21)

$$M_{IG}(x,y)=\frac{\left|H(x,y)\right|}{TA(x,y)*\left(H_{median}(x,y)\right)} \tag{4.21}$$

Where M_{IG} is modulated intensity gradient and $H_{median}(x,y)$ is the median of intensity gradient, in case of [221], they take this value to four times to enhance the texture feature but we need both features in equal range so take the equation as mentioned above.

4.3.1.5 Texture Gradient

To find out texture gradient Gaussian derivative function is used [252]. Gaussian smoothing process occurs by the decrement in the noise amplification. It reduce blurring while maintaining the noise averaging.

After the application of gradient derivative function the texture gradient of each sub-band is given by:

$$T_{G_i}(x,y)=\sqrt{\left(M_i(x,y)*G_x^{'}\right)^2+\left(M_i(x,y)*G_y^{'}\right)^2} \tag{4.22}$$

where $G_x^{'}$ and $G_y^{'}$ are the partial derivative of Gaussian function in the x and y directions respectively and $*$ shows the convolution.

Gaussian approximation is given as:

$$T_{G_i} \approx \left|\nabla M_i\left(x,y\right)\right| \tag{4.23}$$

To get the single value from the different sub-band, interpolations of weighted sum of magnitudes has been carried out as ion eq. below:

$$T_G\left(x,y\right) = \sum_i \text{int}\, erp\left(w_i \times \hat{T}_{G_i}\left(x,y\right)\right) \tag{4.24}$$

$$\text{Where , } \hat{T}_{G_i}\left(x,y\right) = \frac{T_{G_i}\left(x,y\right)}{\max\limits_{x,y}\left(T_{G_i}\left(x,y\right)\right)} \tag{4.25}$$

$$\text{And , } \quad w_i = \frac{n_i}{\sum\limits_{x,y}\hat{T}_{G_i}\left(x,y\right)^2} \tag{4.26}$$

Where n_i is the pixels in sub-band image at level i.

So the texture gradient can be explained as follows:

$$T_G(x,y) = \frac{T_G\left(x,y\right)}{T_{Gmedian}} \tag{4.27}$$

Where $T_{Gmedian}$ is the median of texture gradient.

4.3.1.6 Sum of Gradients

To utilize the facility of both gradients need to find out the weighted sum up both modulated intensity gradient and texture intensity gradient. So final total image gradient can be obtained as below in eq. (4.28)

$$G_T\left(x,y\right) = M_{IG}\left(x,y\right) + T_G\left(x,y\right) \tag{4.28}$$

Where G_T is the total intensity gradient.

4.3.1.7 Watershed Segmentation

Watershed segmentation is applied on the image to get the segmented jet area. Gradient features have been used to overcome the problem of over segmentation.

Before applying watershed segmentation all minima from the image whose depth is less than h have been suppressed by H-minima transform. It removes the gray values of image to a minimal height.

Connected components of pixels with higher external boundary pixel value and having constant intensity value are the regional minima.

Assume that the image $I(x, y)$ is an element of the space $C(d)$ of a connected domain D then the topographical distance between points p and q in D is,

$$T_f(p,q) = \inf_\gamma \int \left\| \nabla f\left(\gamma(s)\right) \right\| ds \tag{4.29}$$

Where "$\inf_\gamma$"is over all paths (smooth curve) inside D, water shed is defined as:

Let $f \in C(D)$ have a minima $\{m_k\}_{k\in I}$, for some index set I. The catchment basin $CB(m_i)$ of a minimum m_i is defined as the set of points $C \in D$, which are topographically closer to m_i than to any other regional minimum m_j.

$$CB(m_i) = \left\{ X \in D \middle| \forall_j \in {I}/{\{i\}} : f(m_i) + T_f(x, m_i) < f(m_j) + T_f(x, m_j) \right\} \tag{4.30}$$

The watershed of f is the set of points which do not belong to any catchment basin;

$$W_{shed}(f) = D \cap \left(\bigcup_{i\in I} CB(m_i) \right) \tag{4.31}$$

Let W be some label, $W \in I$. The watershed transform of f is a mapping of $\lambda : D \to I \cup \{W\}$ such that $\lambda(p) = i$ if $p \in CB(m_i)$ and $\lambda(p) = W$ if $p \in W_{shed}(f)$. So the watershed transform of f assigns labels to the points D, such that (i) different catchment basins are uniquely labeled, and (ii) a special label W is assigned to all points of the watershed of f.

4.3.2 Jet Area Detection

Jet area can be calculated from the segmented image. This needs two steps explained in this section.

4.3.2.1 Thresholding

Here the aim of thresholding operation is convert the obtained segmented image to binary image so that the image divided into two regions. One is inside the jet area and other is the outside the jet area it can be explained as:

$$\begin{cases} if\ i \le T \quad then\, i \in J_{outside} \\ if\ i > T \quad then\, i \in J_{inside} \end{cases} \tag{4.32}$$

Where i denotes the pixel value, T denotes the threshold and $J_{outside}$ is the outside jet region the whereas J_{inside} is the inside region of jet.

4.3.2.2 Pixel counting

Pixel counting has been done on the binary image obtained from the thresholding operation. Jet area can be calculated as in eq. (4.33).

$$J_A = \sum_{x,y} i \in J_{inside} \tag{4.33}$$

4.3.3 Results

Figure 4.12 shows the images from patients suffering from mitral regurgitation (MR). These images are taken by the color Doppler echocardiography. Fig. 4.12a is the case of mild MR showing a small mosaic pattern called as MR jet. While other images fig. 4.12b to fig.4.12f having a large mosaic pattern or MR jet shows the severe MR.

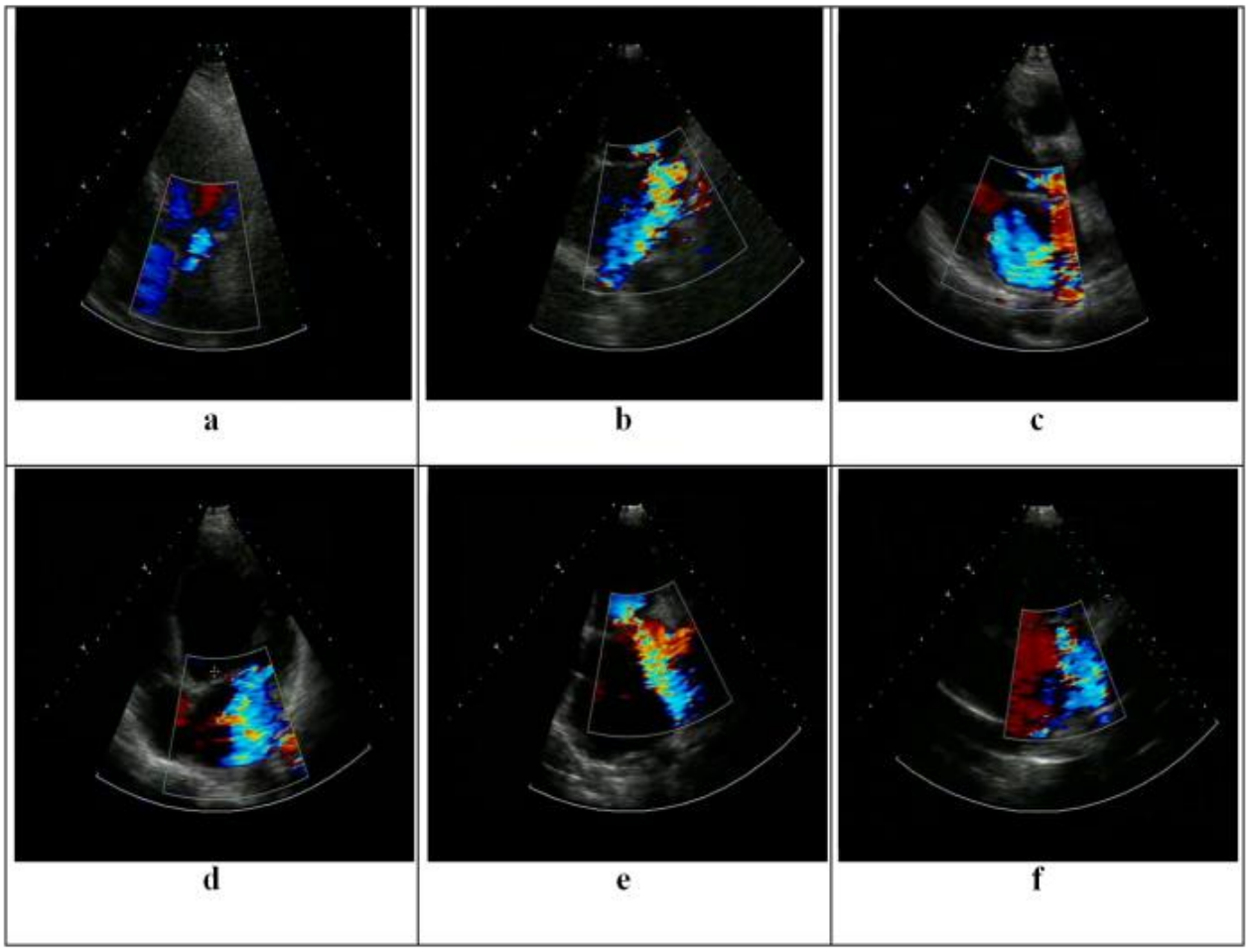

.

Figure 4.12 Color Doppler Echocardiographic Images of Patients with MR

Modulate intensity gradient images are shown in fig. 4.13. From this it can be analyzed that color region is highlighted with gradients. Here it can be seen a very interesting visualization having important features so in the proposed algorithm modulated intensity gradient used in the equal amount to get the gradients of the images.

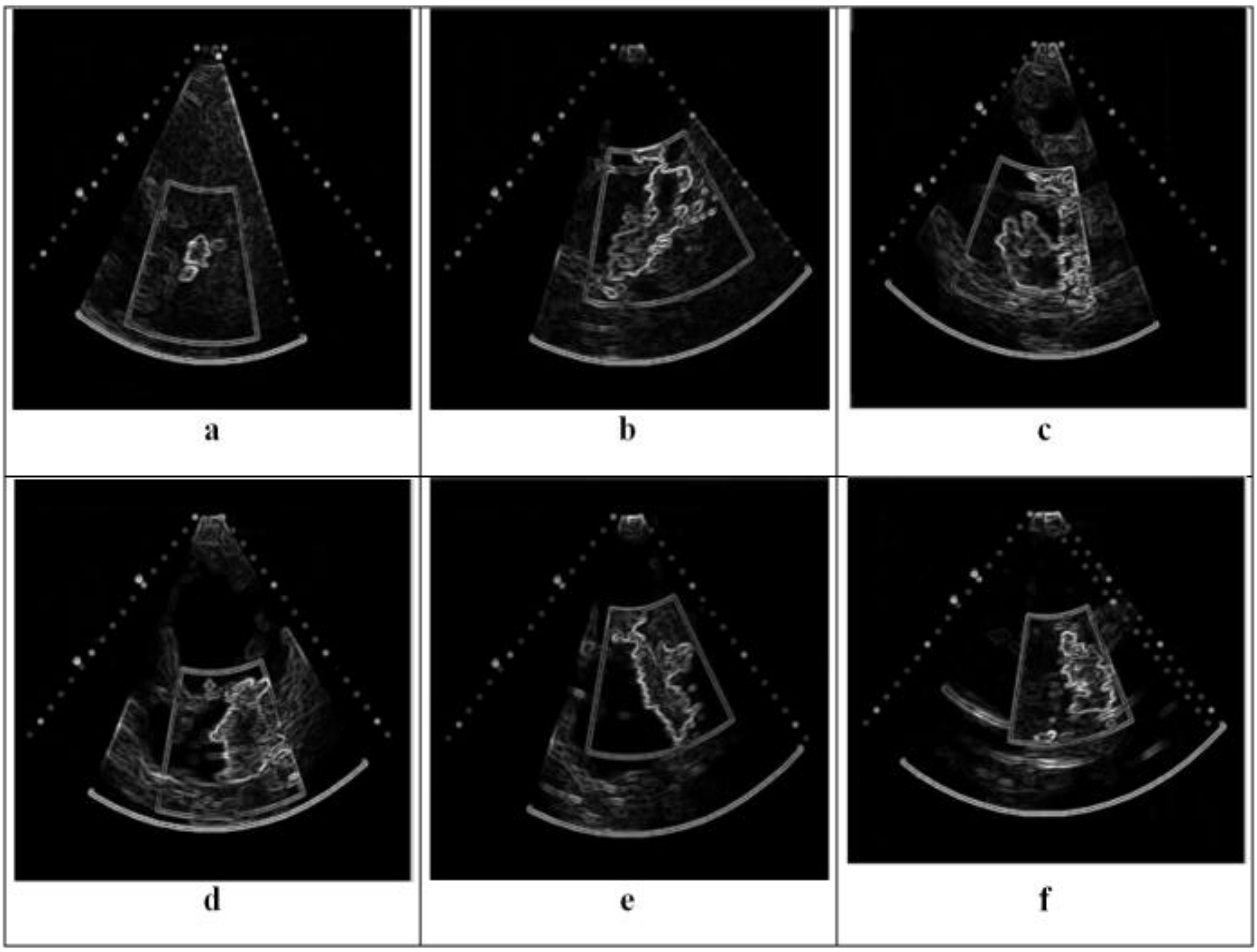

Figure 4.13 Modulated Intensity Gradient Images

Figure 4.14 shows the texture gradient images. The texture gradient is smoother than the modulated intensity gradient. From this image texture gradient images have been obtained which are already smoothed with median filtering.

It can be analyzed from these images that texture gradient relates to the ways in which one can perceive depth. Specifically, texture gradient is a monocular cue in which there is a gradual change in appearance of objects from coarse to fine - some objects appear closer because they are coarse and more distinct, but gradually become less and less distinct (and more fine) which makes the objects appear to get further and further away.

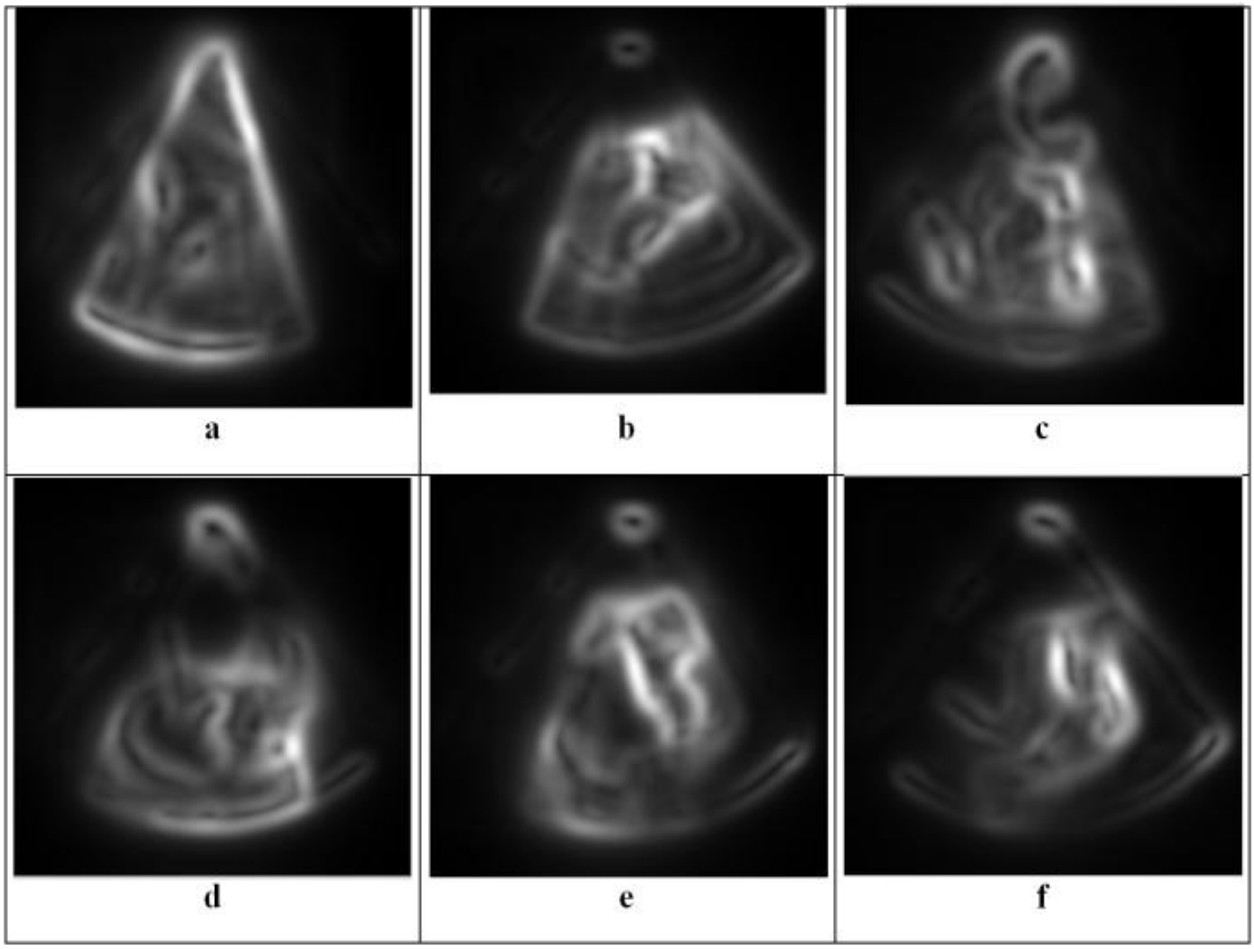

Figure 4.14 Texture Gradient Images

Total gradient of images shown in fig. 4.15 taken for getting the advantage of both gradients.

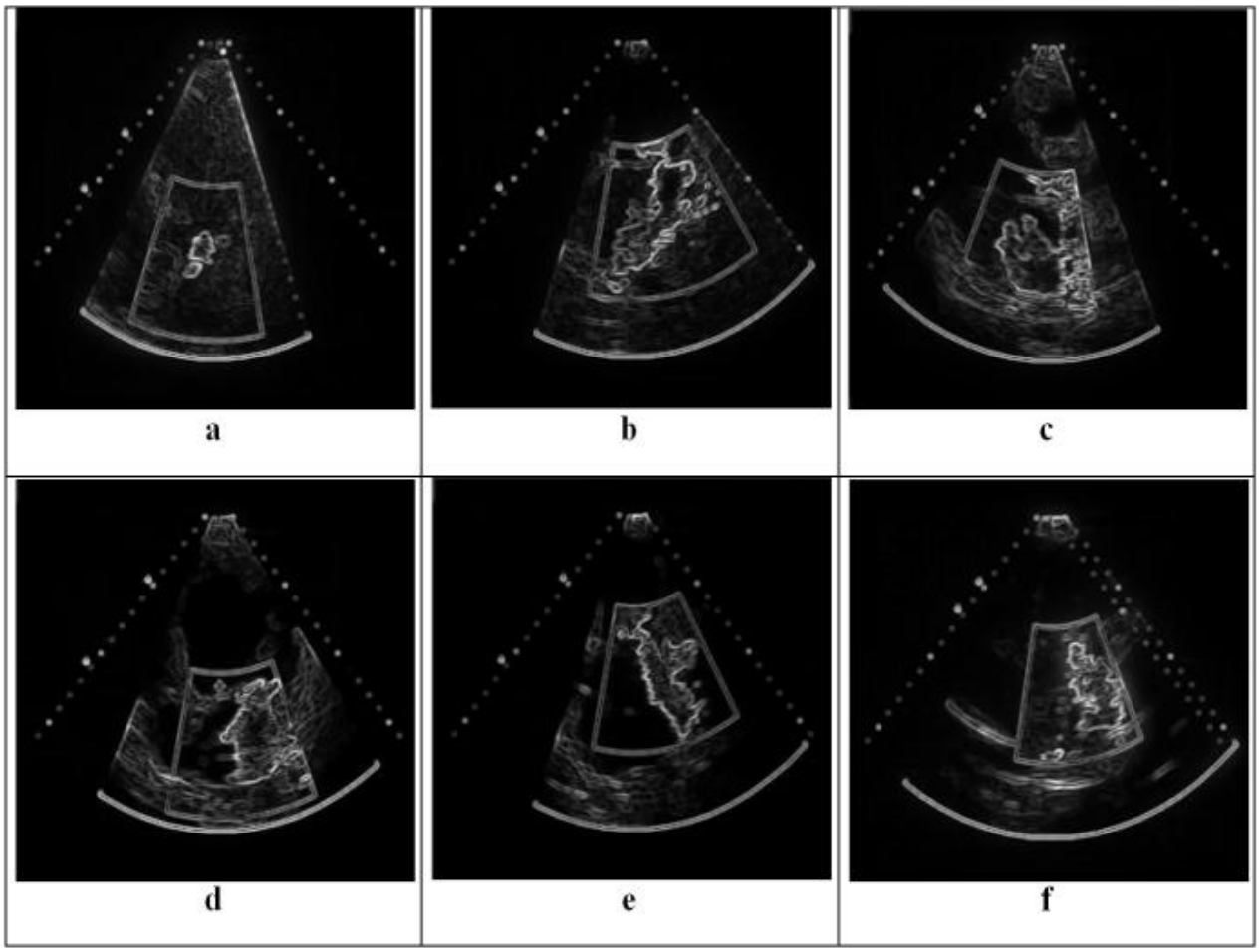

Figure 4.15 Combination of Modulated Intensity and Texture Gradients

Watershed segmentation is applied on the images with the utilization of gradient feature obtained as in fig 5.15 Output from the watershed transformation is shown in fig. 4.16. From fig. 4.16. It can be easy analyzed the jet area the purple region in fig. 4.16a, 4.16b, 4.16d, 4.16e and 4. 16f and in case of fig. 4.16c in green color is the MR jet area.

The result should be a close approximation of the continuous case. That is, the digital distances playing a role in the watershed calculation should approximate the Euclidean distance. The watershed method in its original form produces a severe over segmentation of the image, i.e., many small basins are produced due to many local minima in the input image. But from fig. 4.16 it can be seen that the over-segmentation is suppressed by utilizing the combination of gradients.

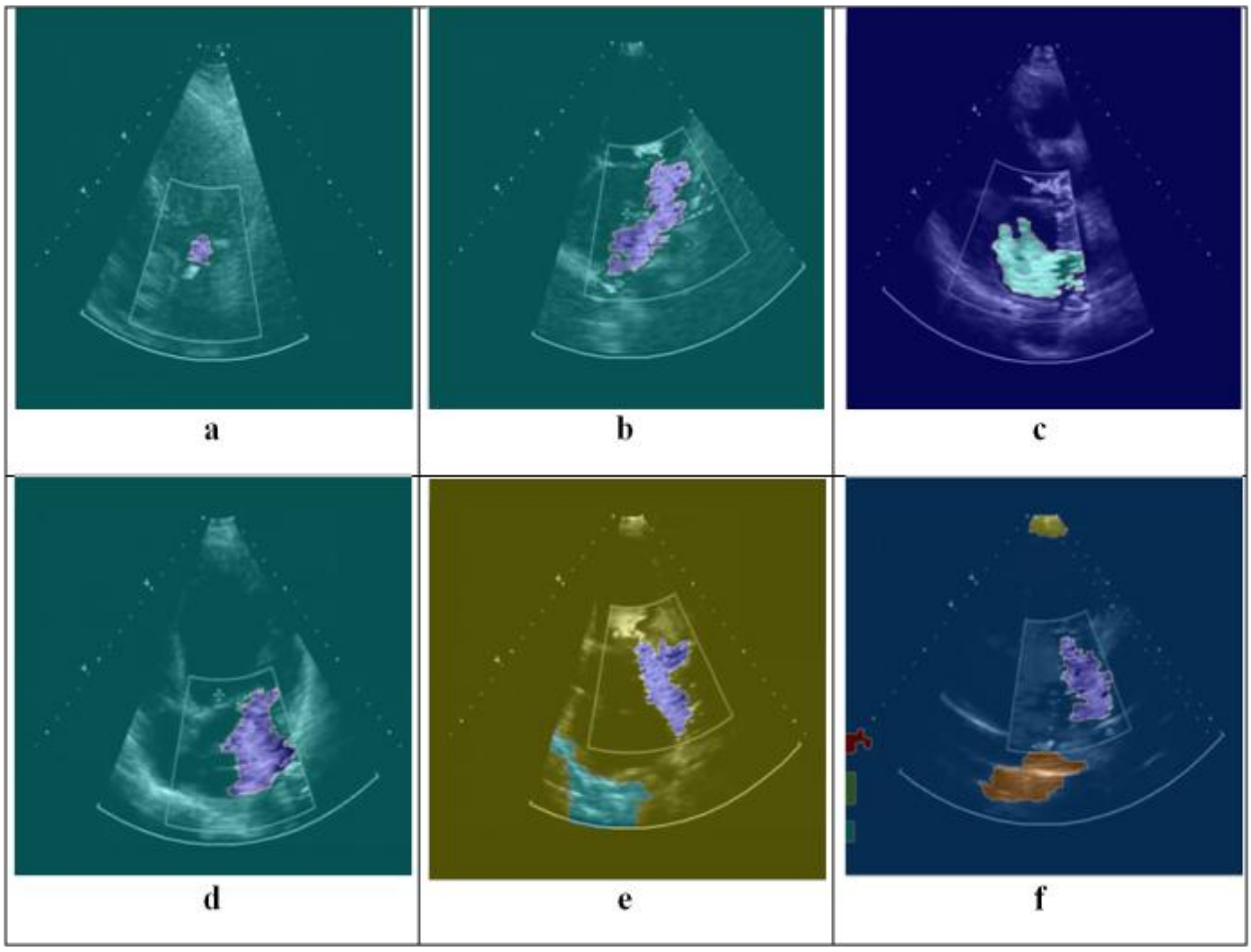

Figure 4.16 Watershed Segmented Images

To get the binary image for jet area thresholding operations has been applied and images obtained are shown in fig. 4.17.

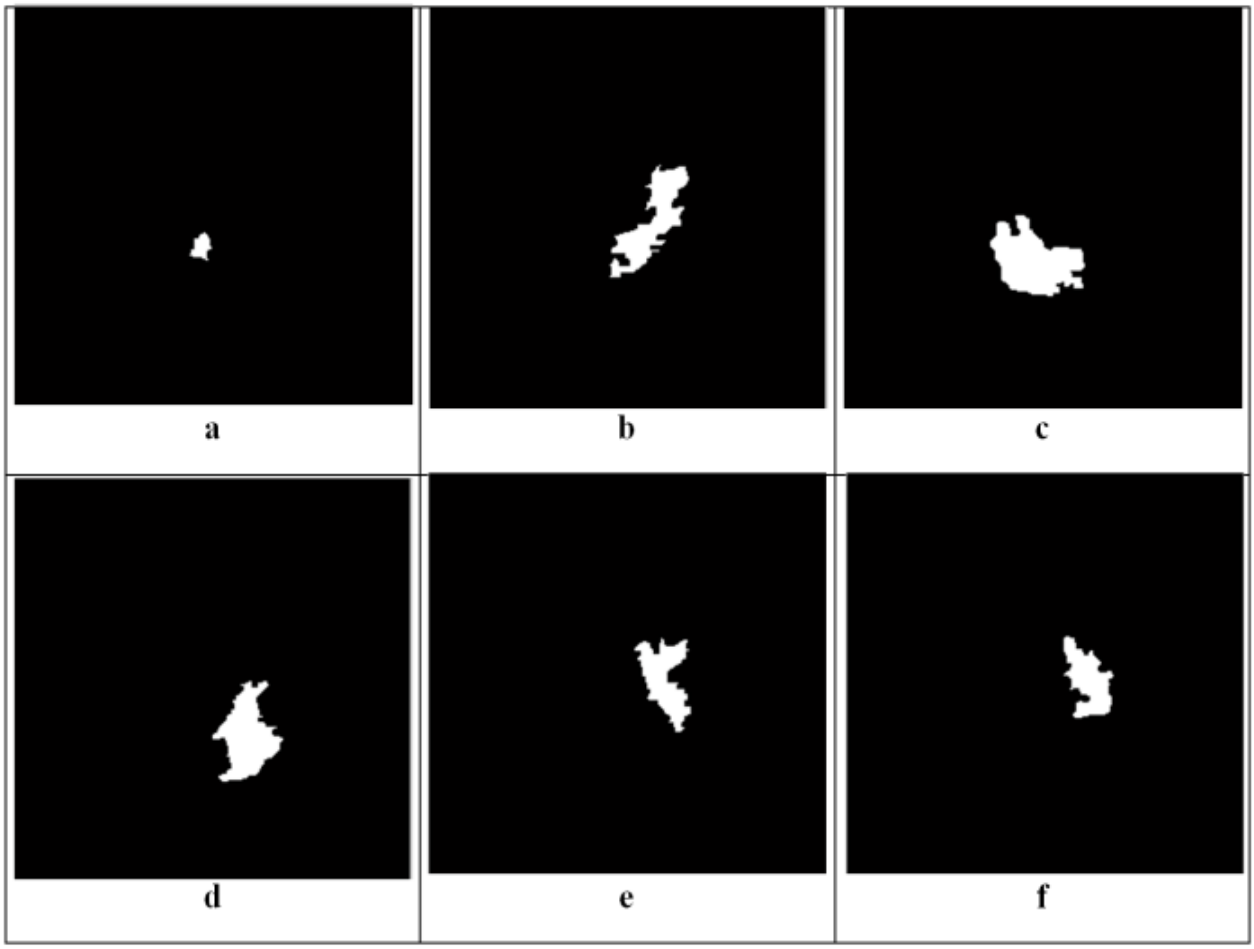

Figure 4.17 Binary Version of Segmented Images

From fig. 4.18 it can be noticed that value of jet area obtained by the proposed method and by a expert echocardiographer automatic segmentation proposed in this work and the one obtained by clinician are almost the same. There is very less variation in values. There difference is very-very close to zero line except in some values which are also quite near zero line.

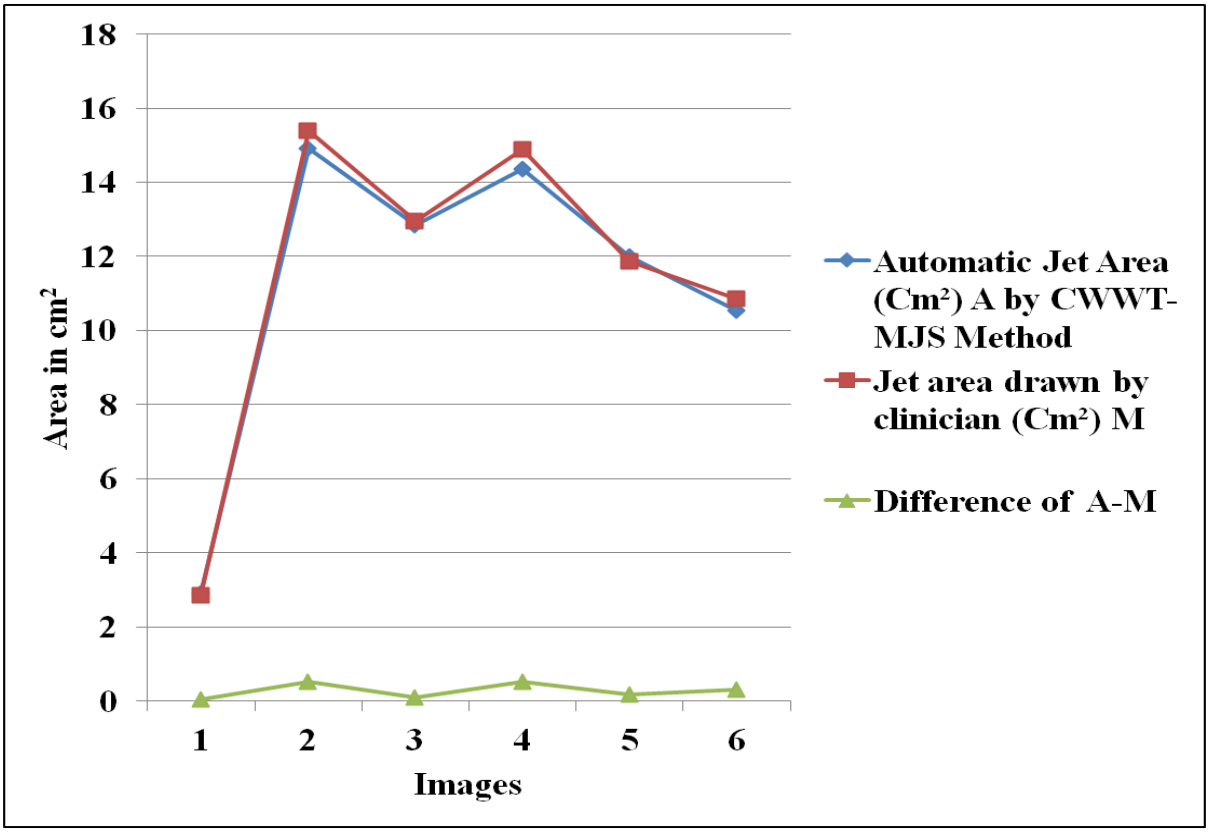

Figure 4.18 Comparison Between Regurgitant Jet Area from Proposed Algorithm CWWT-MJS and by Clinician

Table 4.4 shows the comparison between area detected by the clinician and by proposed automatic jet area detection method. Table 45.5 shows the patients with mild, moderate and severe mitral regurgitation with proposed algorithm and Table 4.6 presents the findings carried out by clinician. There is one case of mild regurgitation in both cases. Patients are the same in both the cases. Table 4.5 shows that proposed method categorized one patient in mild MR condition and 5 patients in severe condition. Patient having mild mitral regurgitation is patient 1 having jet area 2.91 cm^2. Patients 2, 3, 4, 5, 6 having severe regurgitation having jet area 14.92cm^2, 12.84 cm^2, 14.37cm^2, 12.01 cm^2, 10.55cm^2 respectively. Table 4.6 shows that according to area drawn by clinician one patient 1 with jet area 2.86 cm^2 is having mild mitral regurgitation; whereas the patients 2, 3, 4, 5 and 6 with jet area 15.39 cm^2, 12.94 cm^2, 14.89 cm^2, 11.86 cm^2, and 10.86 cm^2 having severe regurgitation.

Table 4.4: Comparison between Jet Areas Calculated by Proposed Method (CWWT-MJS) and Clinician

Images	Automatic Jet Area (Pixels) Using CWWT-MJS	Automatic Jet Area (Cm^2) A Using CWWT-MJS	Jet area drawn by clinician (Cm^2) M	Difference of A-M
1	320	2.91	2.86	0.05
2	8424	14.92	15.39	0.53
3	6230	12.84	12.94	0.10
4	7822	14.37	14.89	0.52
5	5455	12.01	11.86	0.18
6	4212	10.55	10.86	0.31

Table 4.5: Severity Grades according Area drawn by Proposed Automatic Method

Imag	Mild	Moderate	Severe
1	2.91	_	
2	_	_	14.92
3	_	_	12.84
4	_	_	14.37
5	_	_	12.01
6	_	_	10.55

Table 4.6: Severity Grades According to Area Drawn by Clinician

Images	Mild	Moderate	Severe
1	2.86	_	_
2	_	_	15.39
3	_	_	12.94
4	_	_	14.89
5	_	_	11.86
6	_	_	10.86

4.4 SUMMARY

This chapter deals with the automatic segmentation of regurgitant jet area and finding of the numerical value of that jet area. So far the clinicians have been drawing the jet area by hand. Main feature in the first proposed method RG-MJS is that it is very fast method to segment the jet area. Few seconds required to find out the desired object. All the results obtained have been crossed checked with the results obtained by the clinician and the findings are the same within very close limits. This work will enhance the clinician's capability in fast determining the extent of severity of mitral regurgitation. The algorithm developed is capable of removing the spurious areas during the process of segmentation. Removal of such type of areas is the part of the algorithm.

The proposed second method CWWT-MJS opens a way for clinicians to find out the regurgitating jet area automatically. Results show that there is very less difference between the area detected by proposed method and by clinicians. Combination of wavelet and watershed segmentation technique decrease the problem of over segmentation arises during watershed segmentation. Method utilizes the advantage of both features i.e. modulated intensity gradient and texture gradient.

CHAPTER 5

AUTOMATIC DETECTION OF VENA CONTRACTA WIDTH

5.1. INTRODUCTION

In this chapter an automatic method for vena contracta width detection for the severity of the mitral regurgitation (MR) has been developed. Vena contracta width is an efficient method for grading the severity of MR, but it is very difficult to locate this narrowest part exactly in transthoracic echocardiography (TTE) as well as in transesophageal echocardiography (TEE). So, indeed, there is a need to develop a method which is capable of finding out the vena contracta width. A comparison has also been made between the results obtained using the proposed computing method and the results obtained by the clinicians, manually.

At present interest in color Doppler imaging for vena contracta for the assessment of mitral regurgitation is increasing progressively [60], [262] and [203]. The vena contracta is the narrowest part of the regurgitant jet, that can also be called as 'neck' of the jet [297] and having location just downstream from the orifice and before the jet area [202] as shown in fig. 5.1.

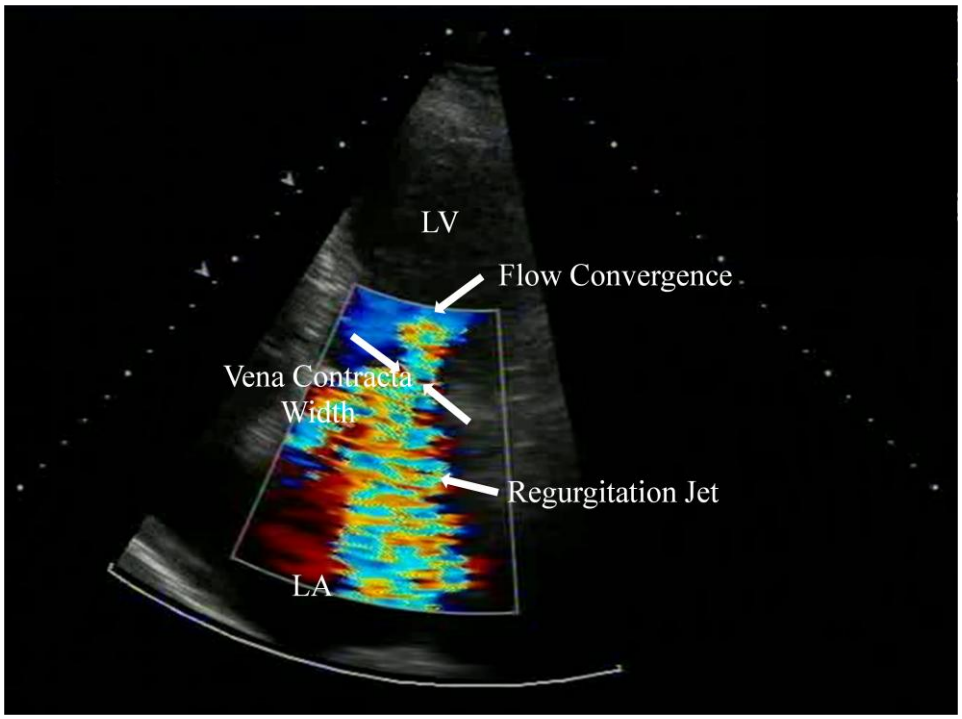

Figure 5.1 Color Doppler Image with Mitral regurgitation

The cross sectional area is directly related to the regurgitant orifice area. Due to the complex and the unpredictable shape, it is very difficult to measure the regurgitant orifice area. For such a measurement jet is to be imaged in the short axis plane. In clinical settings, it is very difficult to localize the narrowest area from the jet. So a correlation is measured between the VC width which is measured from the zoomed view of the parasternal long axis and the apical views, and the EROA, by quantitative Doppler [262]. Relationship between the EROA and the VC width given at many places in the literatures [228], [314] and [274]. This relationship shows good results even in eccentric MR [323]. The VC width is the one dimensional measurement whereas EROA is the two dimensional so there are some limitations also. But in [271] it shown that VC width is the much better tool for measurement of severity of MR. Such as VC width less than 0.3cm indicates the mild MR. If this value is in between 0.3 and 0.5 then it is the case of moderate MR. But if the VC width is more than 0.5cm than it indicates the severe MR.

In any view the localization of the VC width is very difficult. So an experienced clinician is required for the measurement of such a narrowest portion. This gets very time consuming also to locate the exact VC. Hence in the present work a technique has also been developed to locate the VC and also to find the VC width automatically.

5.2 Mathematical Treatment of Determination of Vena Contracta Width

Mathematically, blood flow is described by Darcy's law (which can be viewed as law relating to the fluid flow equivalent of Ohm's law) and approximately by Hagen-Poiseuille equation:

$$Darcy's\,law \;\; F = \Delta P \big/ R \tag{5.1}$$

$$Hagen-PoiseuilleEquation \;\; R = \left(\nu L \big/ r^4\right)\left(8 \big/ \pi\right) \tag{5.2}$$

Where F is blood flow, P is pressure, R is resistance, ν is fluid viscosity, L is length of tube, and r is radius of tube.

When blood passes through the orifice then the momentum flux is given as:

$$\frac{dp}{dt} = \rho\left(v_2^3 A_3 - v_1^2 A_1\right) \approx \rho v_3^2 A_3 \approx 2P_1 A_3 \tag{5.3}$$

Where A_1, A_2 and A_3 are the area of jet in ventricle, atrium and vena contracta; v_1, v_2 and v_3 are the velocities of the blood in the ventricle, atrium and vena contracta; and P_1, P_2 and P_3 are the pressures in the respective regions.

According to Bernoulli's equation in the limit that $P_3 << P_1$, the force that causes this momentum change is:

$$F \approx P_1 A_1 - \left[P_1 \left(A_1 - A_2 \right) + P_3 A_3 \right] = P_1 A_2 \approx P_1 A_2 \tag{5.4}$$

We can estimate the vena contracta to be:

$$A_3 = \frac{A_2}{2} \tag{5.5}$$

If the vena contracta is to be measured in two dimensional potential flow through the orifice, then a more accurate analysis can be done based on the velocity potential ϕ that exists when the flow is irrotational $\left(\nabla \times V = 0 \Rightarrow V = -\nabla \phi \right)$. If the fluid is incompressible, such that $\nabla . V = 0$, the velocity potential satisfies Laplace's equation $\nabla^2 \phi = 0$.

Any analytic function $w(z) = \phi + i\psi$ of the complex variable $z = x + iy$, obeys the Cauchy-Riemann equations,

$$\frac{\partial \phi}{\partial x} = \frac{\partial \psi}{\partial y} \tag{5.6i}$$

and

$$\frac{\partial \phi}{\partial y} = -\frac{\partial \psi}{\partial x} \tag{5.6ii}$$

which imply that $\nabla^2 \phi = 0 = \nabla^2 \psi$; i.e., any analytic function of a complex variable can, in principle, be related to the velocity potential of some two-dimensional, incompressible, irrotational fluid flow. Furthermore, the curves $\psi(x, y) =$ constant follow streamlines of the Potential $\phi(x, y)$ (and vice versa).

According to Kirchhoff if the fluid flow includes a free surface, on which the pressure is constant, then Bernoulli's equation implies that the velocity of the fluid flow is constant on this surface. This velocity can always be scaled to unity. Then, since $V = -\nabla\phi = -\left(\partial\phi/\partial x, \partial\phi/\partial y\right)$, the scaled flow on a free surface obeys

$$\left(\frac{\partial\phi}{\partial x}\right)^2 + \left(\frac{\partial\phi}{\partial y}\right)^2 = 1 \tag{5.7}$$

Furthermore, according to the Jacobian transformation of area elements

$$dx\,dy = J\,d\phi d\psi = JJ^{'}dx\,dy, \tag{5.8}$$

So, $JJ^{'} = 1$. The Cauchy-Riemann equations for $\phi + i\psi = w(x + iy)$ and $x + iy = w^{-1}(\phi + i\psi)$ allow us to write the Jacobian determinants as:

$$J = \frac{\partial\phi}{\partial x}\frac{\partial\psi}{\partial y} - \frac{\partial\phi}{\partial y}\frac{\partial\psi}{\partial x} = \left(\frac{\partial\phi}{\partial x}\right)^2 + \left(\frac{\partial\phi}{\partial y}\right)^2 \tag{5.9i}$$

and

$$J^{'} = \left(\frac{\partial x}{\partial\phi}\right)^2 + \left(\frac{\partial y}{\partial\phi}\right) \tag{5.9ii}$$

Then, the scaled flow on a free surface also obeys

$$\left(\frac{\partial x}{\partial\phi}\right)^2 + \left(\frac{\partial y}{\partial\phi}\right)^2 = 1 \tag{5.10}$$

Kirchhoff, extended Helmholtz' technique of functions $w(z)$, that are defined implicitly via knowledge of $z(w)$ by consideration of the derivative dz/dw defined as

$$\frac{dz}{dw} = -f(w) - \sqrt{f^2(w) - 1}, \tag{5.11}$$

arguing that if along some portion of a streamline ψ =constant the function f is real and $|f|$ less than 1, then $dx/d\phi = \mathrm{Re}\left(dz/dw\right) = -f$ and $dy/d\phi = \mathrm{Im}\left(dz/dw\right) = -\sqrt{1-f^2}$, such that eq. (5.10) is satisfied, and this portion of the streamline corresponds to a free surface of the fluid flow.

In particular, the function

$$f = e^{-w} = e^{-\phi}\cos\psi - ie^{-\phi}\sin\psi \tag{5.12}$$

obeys eq. (5.10) for $\psi = 0$ and $\phi > 0$. The free surface is defined by the equations

$$\frac{dx}{d\phi} = -f = e^{-\phi} \tag{5.13i}$$

and

$$\frac{dy}{d\phi} = -\sqrt{1-f^2} = -\sqrt{1-e^{-2\phi}} \quad (\phi > 0, \psi = 0) \tag{5.13ii}$$

which integrate to

$$x = e^{-\phi} - 1 \tag{5.14i}$$

and

$$y = \sqrt{1-e^{-2\phi}} - \ln\left(e^{\phi} + \sqrt{e^{2\phi}-1}\right) \quad (\phi > 0, \psi = 0) \tag{5.14ii}$$

Similarly, the streamline $\psi = \pi$ also obeys eq. (5.10) for $\phi > 0$, such that

$$\frac{dx}{d\phi} = e^{-\phi} \tag{5.15i}$$

and

$$\frac{dy}{d\phi} = -\sqrt{1-e^{-2\phi}} \quad (\phi > 0, \psi = \pi) \tag{5.15ii}$$

which integrate to

$$x = -x_0 + 1 - e^{-\phi} \tag{5.16i}$$

and

$$y = \sqrt{1-e^{-2\phi}} - \ln\left(e^{\phi} + \sqrt{e^{2\phi}-1}\right) \quad (\phi > 0, \psi = \pi) \tag{5.16ii}$$

On this streamline $dz/d\phi$ is real and negative for $\phi < 0$, so y is again constant at 0 while x decreases from $-x_0$ to $-\infty$.

Furthermore, on the streamline $\psi = \pi/2$, dz/ϕ , is purely imaginary so that x is constant (at $-x_0/2$), and this streamline is the symmetry axis of the flow.

The constant x_0 can be determined by noting that for large negative y the streamlines $0 \le \psi \le \pi$ are all in the y direction, so the corresponding equipotentials of ϕ are at constant y. Then, the velocity $V = -\nabla\phi$ is constant across the jet, with value unity, such that integrating across the jet at large negative y find, using the Cauchy-Riemann eq. (5.6)

$$\Delta\psi = \pi = \int_{-x_0+1}^{-1} \frac{\partial\psi}{\partial x}\,dx = -\int_{-x_0+1}^{-1} \frac{\partial\phi}{\partial y}dx = v\int_{-x_0+1}^{-1} dx = x_0 - 2 \tag{5.17}$$

and hence the width of the orifice is $x_0 = \pi + 2$. Thus, we determine the vena contracta to be

$$A_{contracted\ jet} = \frac{\pi}{\pi+2} A_{orifice} = 0.61 A_{orifice} \tag{5.18}$$

This is the case when we considered the mitral orifice as a circular aperture.

The mathematical treatment done above may give satisfactory results if all the quantitative data and the values of atrial and ventricular areas are accurately measured and substituted in the above equations. However, it might prove to be very time consuming and developed on the accuracies of measurement of involved parameters. Hence, a method which direct and automatic is also proposed based completely on the information taken from the echocardiographic images.

5.3 AUTOMATIC DETECTION OF VC WIDTH: THE PROPOSED METHOD

Block diagram in fig. 5.2 shows the steps of the proposed method for automatic detection of vena contracta width.

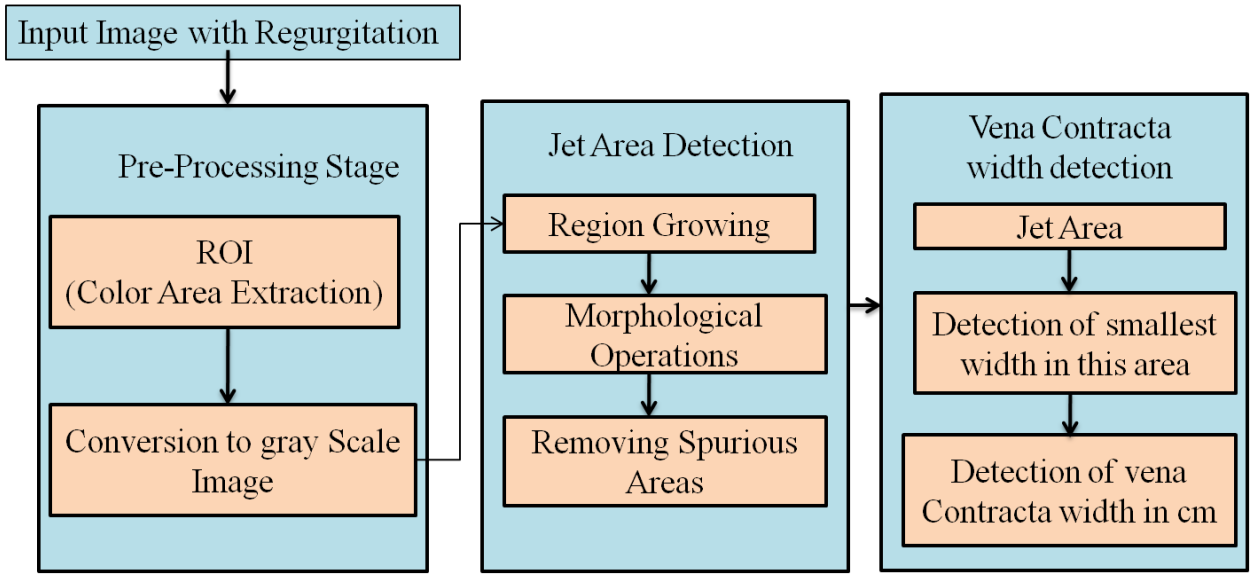

Figure 5.2 Algorithm for Vena Contracta Width Detection

For example, an i^{th}, pixel, p_i, is classified belonging to C_g and C_c, and can be written as,

$$if\ \left(d_1\ and\ d_2\ and\ d_3 = 0\right) or\ \left(d_1\ or\ d_2\ or\ d_3 \le T\right)$$
$$then\ C_g \leftarrow p_i$$
$$else\ C_c \leftarrow p_i$$

Where, d_1, d_2 and d_3 are the distances between RG, RB, and GB respectively. C_g and C_c are the class labels of grayscale or color pixels respectively. However, after this step the image will not give a distinct segment or object but instead it would show discontinuities called *islands.* These can be removed by pre-processing and post-processing such as Gaussian blur and morphological operations.

However the problem here is that there is mixture is mixture of colors in the gray portion too. The color area has been extracted as per the method developed in chapter 4. This extracted image is the region of interest (ROI) which is converted to gray scale for further processing as in the second building block of the first stage of fig. 5.2. This grayscale area is slightly bigger than the actual jet area due to the color aliasing.

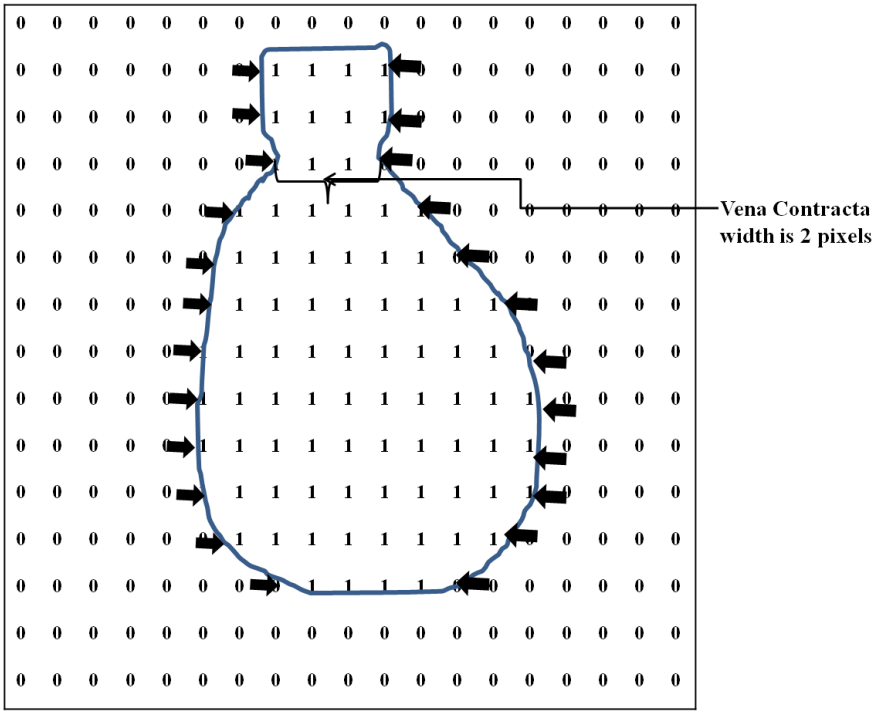

Figure 5.3 Counting for Elements inside the Object

Next step is to detect the jet area in which vena contracta exists. The spurious area which are generated due to the color aliasing are removed using the morphological operations while employing the method of extracting jet area is explained in chapter 4 in detail. The area so extracted is actually the accurate jet area in which contained is the vena contracta width.

The vena contracta width is determined from this area. The elements in each row in are counted throughout this jet area. As shown in fig. 5.3, the row showing the minimum number of pixels inside the jet area is the region where vena contracta exists. The number of pixels of that particular row gives the size of the VC width.

Total number of nonzero elements, E, within the two arrow heads, inside the object is given as in eq. (5.19)

$$E = \sum_{i=m}^{j=n} e_{ij} \tag{5.19}$$

Where e_{ij} is the ij^{th} element inside the object i.e., the element at the i^{th} row and j^{th} column.

Vena contracta width can be find out as in eq. (5.20)

$$VC_{width} = \min(E) \tag{5.20}$$

This value is in pixels. To compare it with clinical data it is good to convert this value to centimeters.

5.3 RESULTS

Figure 5.4 shows the color Doppler images with mitral regurgitation. Images in fig. 5.4a, fig. 5.4b and fig. 5.4h are the apical two chamber views of the heart with color Doppler. In these images the chambers enveloping the large color jet are the left atria. The chambers just above these atria of these images are the left ventricles. The junction layer of LA and the LV is the atrio-ventricular partition containing at the left extreme is the mitral valve.

The image of fig. 5.4c is the only image that is images in apical four chamber view. The LA and LV in this are shown on the left of the image. As usual the color jet is enveloped within the LA.

The image of fig. 5.4d through fig. 5.4g and fig. 5.4i are images in the parasternal long axis view. In these images also the chambers having large MR jet are the left atria, and just above atria and more right are the left ventricles.

Vena contracta width is just below the orifice of the mitral valve and it is just within the color portion of the images. This VC width is quite nearly shown in fig.5.1; which is just within the two arrow heads.

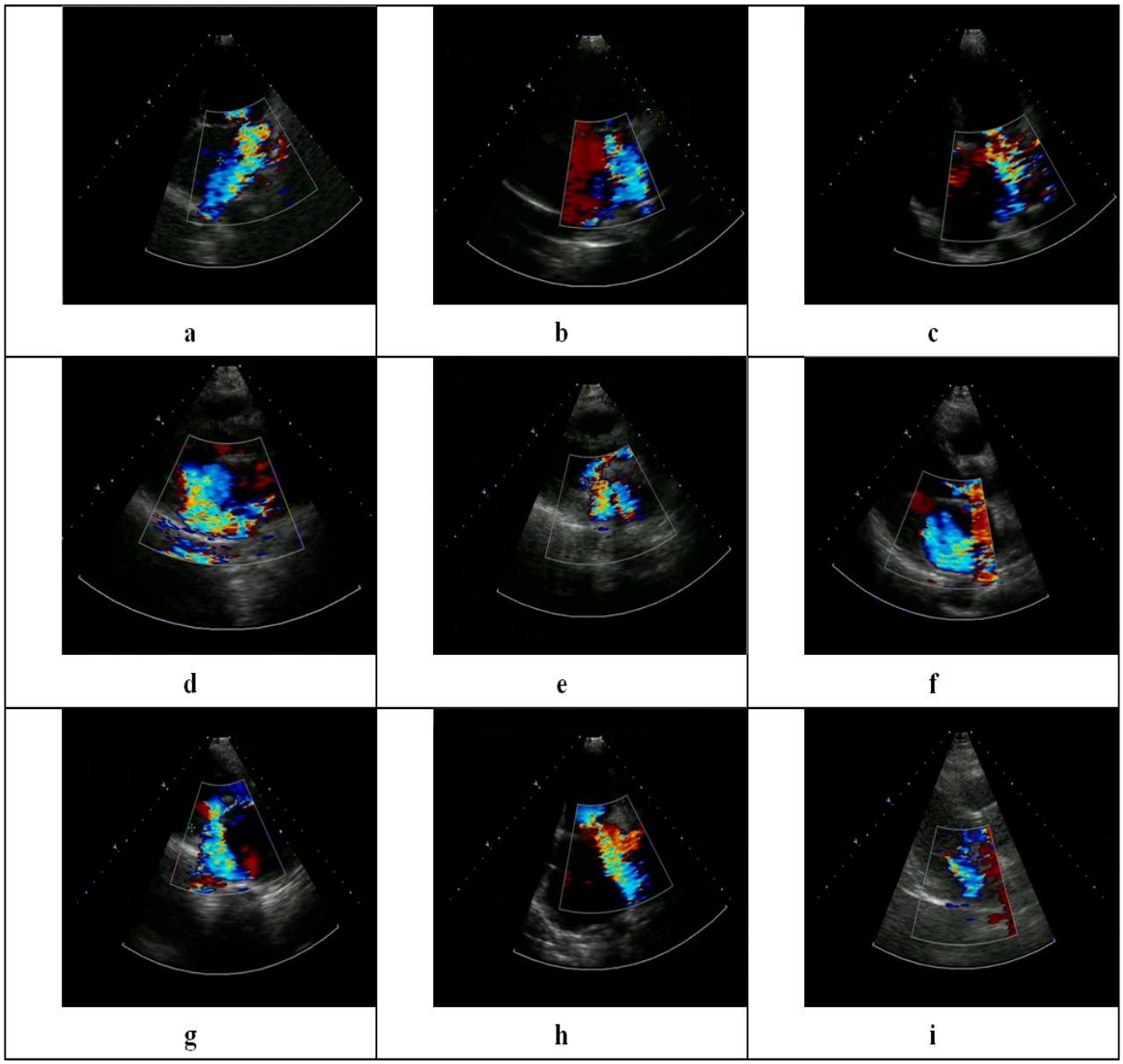

Figure 5.4 Color Doppler Images with Mitral Regurgitation

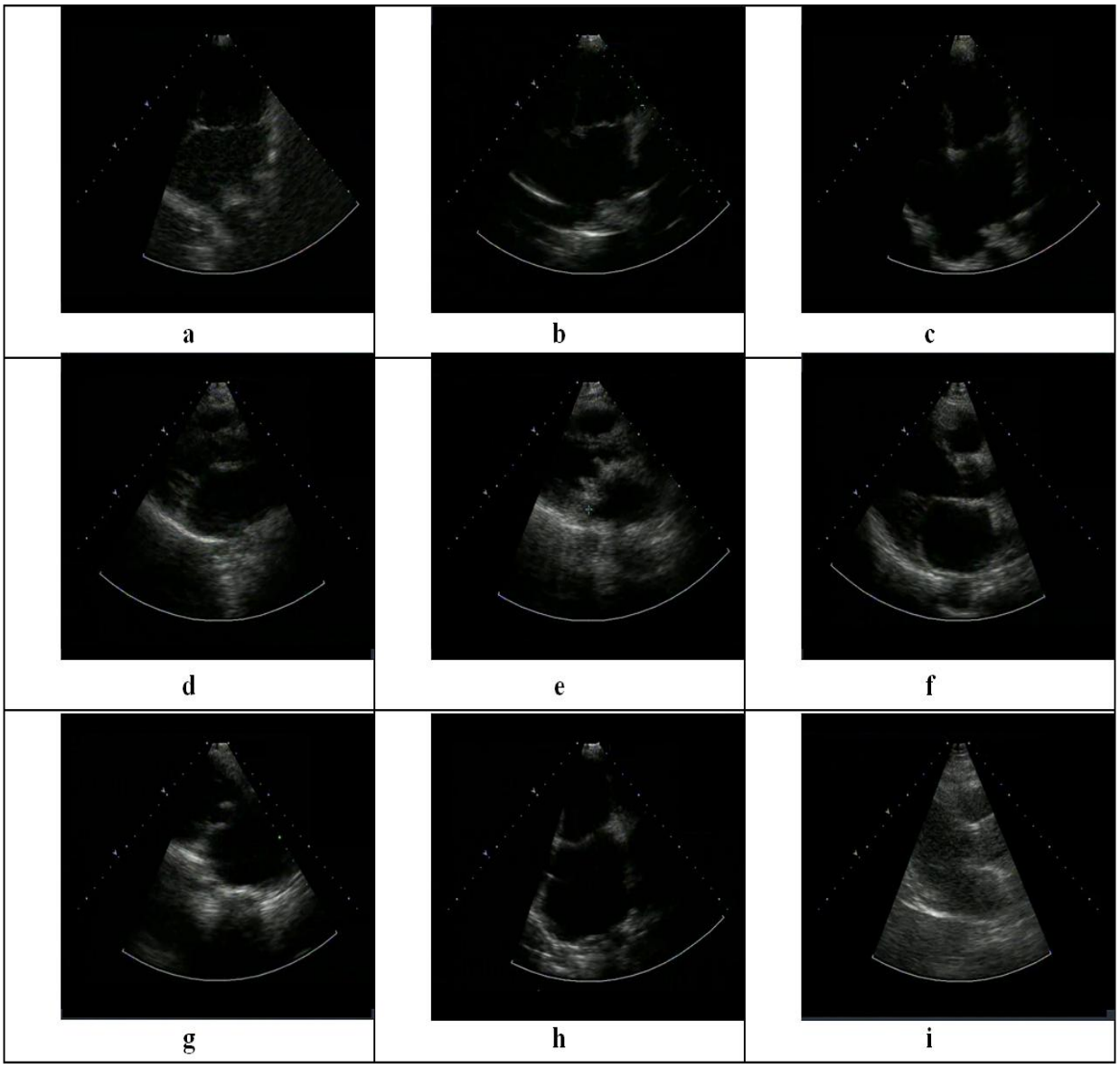

Figure 5.5 Background Images

To extract the color jet portion we need images without pseudo color superimposition. These images are background images shown in Fig.5.5.

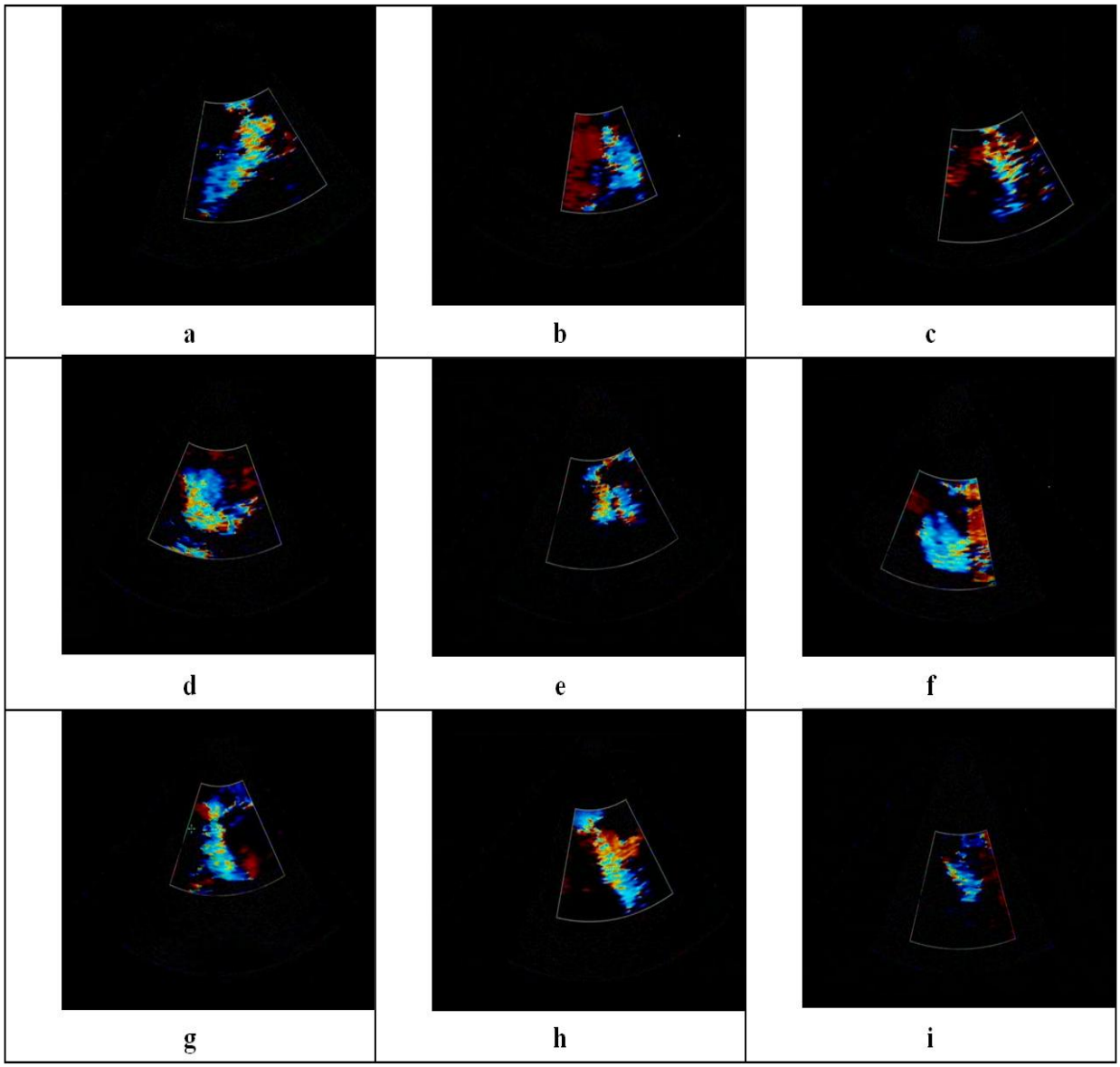

Figure 5.6 Object Extracted Images

Figure 5.6 shows the images with region of interest from where vena contracta width can be find out. This is the color area in which VC exists.

Figure 5.7 shows the images after application of segmentation process and applying the binary conversion by the way of assigning one's to intensity pixels which are within the jet area and the zero's to the area which is in the background.

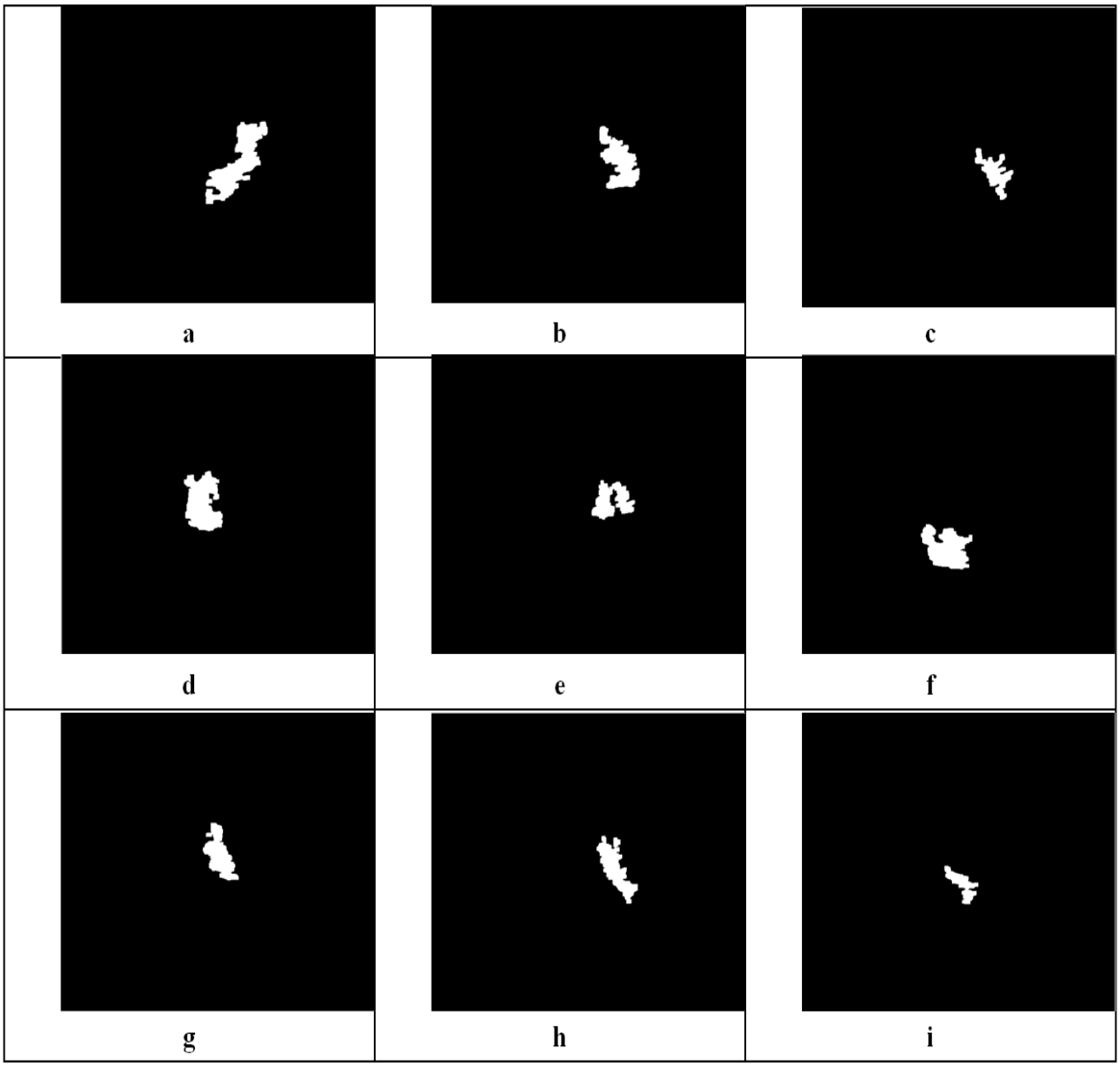

Figure 5.7 Final Segmented Images for Vena Contracta Width

It can be observed from the table 5.1 that the automatic vena contracta width detection method proposed here corroborate quite closely with the severity grades determined by the clinicians. If the cases 1, 2, 4, 6, 7 and 8 are viewed, the values of vena contracta width are greater than 0.5cm suggesting that the MR is of the severe grade. Whereas, in cases 3, 5, and 9, the VC widths observed are within 0.4 to 0.5 cm wide. This range of VC width suggests that the MR is of the moderate severity grade. The MR severity evaluation using proposed method corroborates 100% with MR severity gradation carried out by the clinicians.

Table 5.1: MR Severity Grade Checking on the Basis of Vena Contracta Width

Images	Vena Contracta width in (pixels)	Vena Contracta width (Cm)	MR Severity (by Proposed method)	MR Severity (by Clinicians)
1	13	0.58	severe	severe
2	14	0.61	severe	severe
3	8	0.46	moderate	moderate
4	12	0.56	severe	severe
5	8	0.46	moderate	moderate
6	12	0.56	severe	severe
7	11	0.54	severe	severe
8	11	0.54	severe	severe
9	9	0.39	moderate	moderate

5.4. SUMMARY

Vena contracta diameter is directly related to the effective regurgitant orifice area (EROA). Automatic detection of vena contracta width presented in this work offers time saving method for finding out the severity of MR. The proposed method does not require zooming out of the vena contracta width portion of the images MR jet. Zooming the view increases the blurring in the image. VCW is not load independent in MR because short-term changes in loading conditions produce dynamic changes in the regurgitant orifice. Cause of MR does not always predict accurately whether the regurgitant orifice is fixed or dynamic. Since, the algorithm of the proposed method is quit fast, the multiple images during the systole can be images and dynamicity of EROA can be examined.

CHAPTER 6

CONCLUSIONS AND FUTURE SCOPE

6.1 CONCLUSIONS

Estimation of mitral regurgitation is the one of the chief goals in clinical diagnosis. The clinical decision makings are greatly influenced by its severity. There are numerous echocardiographic techniques put-forth for enhanced quantification of valvular regurgitation. With the help of color Doppler mapping the existence of mitral regurgitation is diagnosed and detected. Approximately in about 40% of healthy normal persons there is a small color flow jets are observed prominently but they are graded under the normal persons. There are mainly three methods available for computing the severity of MR as; Regurgitant jet area, vena contracta and flow convergence (PISA). Jet is the comparatively less accurate method due to some disturbing parameters, but it is used extensively, because of its easy detection, however vena contracta gives the almost accurate results. On the other hand flow convergence or proximal isovelocity method is also reliable and accurate but are very time consuming.

The assessment of left ventricular function is an essential component of the evaluation of any patient with known or suspected heart disease. So, our main concentration has been on left ventricular volume and MR jet area detection. Similarly, the left atrium also does give information about the diseases.

On the basis of our research contributions, the conclusions drawn are as given below:

6.1.1 Data Base Collection

All the echocardiographic image data have been acquired from PGIMER, Chandigarh, India. All patients examined were suffering from the valvular disease mitral regurgitation. The Images in data base contain the three types of severity grading viz. mild MR, moderate MR, and severe MR. The echocardiographic views in data base are apical four chamber view, apical two chamber view and parasternal long axis view. Images obtained have been taken in two modes; 2-D echocardiography and color Doppler echocardiography. The echocardiography machine, from which data have been collected, is ‘ACUSON SEQUOIA C512 System’ of the Siemens manufacturer.

6.1.2 Contrast Enhancement of Echocardiographic Images

The existing log-transformation technique has been modified to make it suitable for the echocardiographer to enhance the different contrast images. This contribution helps the clinician to adjust the contrast in accordance with their requirement.

6.1.3 De-Speckling of Echocardiographic Images

Two methods for the removal speckle noise from echocardiographic images have been developed and proposed specially for the echocardiographic images. Speckle removing filters are designed to offer better visualization of the echocardiographic images. The proposed methods remove the speckle noise to an extent that makes the image speckle- free while at the same time retaining important information such as edges and the chamber partitioning. The proposed methods of de-speckling the echocardiographic images have offered high PSNR, good quality index, reduction in error and excellent visualization capabilities for the clinicians.

Five of the performance parameters, as suggested, exhibit excellent quality of these filters. These parameters demonstrate advantages with regard to the edge preservation and speckle filtering capabilities. In addition to the echocardiographic images used for the present work these filters can also be used for other medical images, such as, radar images and synthetic images.

6.1.4 Echocardiographic Images Boundary Detection

Two dimensional echocardiography has proved to be a very effective method of quantifying Left Ventricular (LV) functionality. A good amount of research work is found in literature to develop fully or semi-automatic LV boundary extraction algorithms, however, none of the algorithms has shown reasonable accuracy to render it clinically useful. The main problem is the poor quality of Echocardiographic images. They are inherently noisy with areas of weak or non-existent edges, as well as conflicting artifacts from mitral valves and papillary muscles. Most recent works have focused on the use of minimum energy contours to extract the desired LV boundaries. Two automatic boundary detection methods which detect the boundaries according to change in shape of left ventricle have been developed.

Automatic detection of boundaries enables the clinicians to determine the chambers efficiently and carry out easy and accurate diagnosis. The proposed methods are efficient in terms of detecting the proper boundaries with the highest clarity. These methods exhibit much higher CPU efficiency which is of high significance to the clinicians for carrying out speedy diagnosis.

6.1.5 Jet Area Evaluation

It is the most common approach for using color flow Doppler to quantize the mitral regurgitant jet severity. Mosaic pattern have been assigned as MR jet area. This measurement is relatively simple and has wide appeal. Unfortunately this approach for quantitating mitral regurgitation has many significant limitations. Numerous Instrument factors can influence the size of a Doppler flow jet. These factors include difference in color Doppler Display from one instrument to another, gain settings and the carrier frequency of the transducer.

Some data suggest that measuring the turbulent mosaic pattern is more accurate than including the non-high velocity flow that surrounds the mosaic turbulent blood. A jet flowing into the center of chamber is able to develop to its fullest. If, however, Jet is directed eccentrically and strikes one of the walls of the chamber, then flow will be distorted by that wall and a totally different jet area will be recorded. Measuring the area of the turbulent multicolored jet directed toward the left atrium would be misleading in evaluating severity of the mitral regurgitation.

So far, the clinicians have been drawing the jet area by hand manually. The main feature of the proposed methods is that both the methods are need based very fast methods to segment the MR jet area. Only a few seconds are required to evaluate the desired object. All the results determined have been cross checked with the results obtained by the clinician and the findings are nearly the same, within very close limits. This present repeating of development enhances the clinician's capability in terms of fast and corroboratively accurately determining the extent of severity of mitral regurgitation.

6.1.6 Vena Contracta Width Detection

Vena contracta diameter is directly related to the effective regurgitant orifice area (EROA). Automatic detection of vena contracta width presented in the present thesis offers a time saving method for finding out the severity of MR. There is no need to zoom out the vena contracta width portion in this method. Zooming the view increase the blurring in the image. VCW is not load independent in MR because short-term changes in loading conditions produce dynamic changes in the regurgitant orifice. Proposed method offers the eligibility to find out vena contracta width automatically. Comparison with clinical results shows that this method will proved to be helpful to the clinicians in carrying out fast diagnosis.

6.2 FUTURE SCOPE OF THE WORK

When we started review of literature on processing of echocardiographic images with the view to evaluate MR severity, there were no research papers available on processing of MR mosaic jet images and computer aided detection of vena contracta width. The work is directed to offer corroborative support to the manually drawn MR jet area and marking of VCW by the clinicians.

Significant technical and clinical progress can still be made in the field of image de-speckling and mosaic jet segmentation, to advance understanding of the diagnosis and treatment of cardiac diseases.

Our proposed contrast enhancement technique can be used for the enhancement of synthetic images such as for SAR images, for natural images, for the other medical images such as MRI, CT, and X-ray images. Proposed de-speckling techniques may be experimented on SAR images, other ultrasound images for example on liver images in future. Boundary detection methods proposed here for echocardiographic images can be used to segment natural images, synthetic images, other medical image and can be enhanced for 3-D echocardiographic images, which will positively improve the diagnostic performance. Proposed Jet area detection methods can be used for tricuspid regurgitation and aortic regurgitation also, Detection of mosaic pattern of mitochondrial DNA alterations indifferent populations of cells from the same endometrial tumor, for human face recognition and for the detection and characterization of abnormal vascular patterns in automated cervical image analysis. Vena contracta width detection method proposed in this thesis can be used for automatic vehicle detection in satellite images, line recognition in large-size images, measuring the width of a sheet of material and detection and interpretation of landslides.

REFERENCES

[1] A. A. Amini, T. E. Weymouth, and R. C. Jain, "Using Dynamic Programming for Solving Variational Problems in Vision," IEEE Trans. Patt. Anal. Mach. Intell., Vol.12, No.9, pp. 855–867, 1990.

[2] A. Achim, A. Bezerianos, P. Tsakalides, "Novel Bayesian Multiscale Method for Speckle Removal in Medical Ultrasound Images," IEEE Trans. Med. Imag., Vol. 20, No. 8, pp. 772-783, 2001.

[3] A. Achim, P. Tsakalides, A. Bezerianos, "SAR Image Denoising via Bayesian Wavelet Shrinkage based on Heavy-Tailed Modelling," IEEE Trans. Geosc. Remote Sens., Vol. 41, No. 8, pp. 1773-1784, 2003.

[4] A. Aldroubi, M. Unser, Wavelets in Medicine and Biology, CRC Press, 1996.

[5] A. Araújo, S. Barbeiro and P. Serranho , "Stability of Finite Difference Schemes for Complex Diffusion Processes, DMUC report , pp. 10–2, 2010.

[6] A. B. Hamza, Escamilla, P.L., Aroza, J.M., Roldan, R.: "Removing Noise and Preserving Details with Relaxed Median Filters", J. Math. Imaging Vis. 11, pp. 161–177, 1999.

[7] A. Blake and A. Zisserman, "Visual Reconstruction. Boston", MIT Press, 1987.

[8] A. Bovik, Handbook of "Image & Video Processing", Academic Press, 2000.

[9] A. Bravo, M. Vera, R. Medina, "Edge Detection in Ventriculograms Using Support Vector Machine Classifiers and Deformable Models", CIARP 2007, LNCS, Vol. 4756, pp. 793–802, 2007.

[10] A. C. Guyton and J. E. Hall, "Heart Muscle; The Heart as a Pump and Function of the Heart Valves," in Textbook of Medical Physiology 11th ed. China: Elsevier Inc., 2006, ch. 9, pp 104.

[11] A. D. Goldfinger, "Estimation of Spectra from Speckled Images," IEEE Trans. Aerospace Elect. Syst., Vol. AES-18, pp. 675–681, 1982.

[12] A. Diplaros, N. Vlassis, and T. Gevers, "A Spatially Constrained Generative Model and an EM Algorithm for Image Segmentation", IEEE transactions on neural networks, Vol. 18, No. 3,pp. 798-808, May 2007.

[13] A. F. Bolger, N. L. Eigler, J. M. Pfaff, K. J. Resser, G. Maurer, "Computer Analysis of Doppler Color Flow Mapping Images for Quantitative Assessment of in Vitro Fluid Jets", J Am Coll Cardiol, Vol. 12 , pp. 450 –457, 1988.

[14] A. Garrido, N. PeHrez de la Blanca, "Applying Deformable Templates for Cell Image Segmentation", Pattern Recognit, Vol. 33, pp. 821– 832, 2000.

[15] A. H. Torp, S. I. Rabben, A. Støylen, H. Ihlen, K. Andersen, L-Å ke Brodin, B. Olstad, "Automatic Detection and Tracking of Left Ventricular Landmarks in Echocardiography", IEEE Ultrasonics Symposium, pp. 474–477, 2004.

[16] A. Ioannidis, D. Kazakos, D. D. Watson, "Application of the Median Filter on Nuclear Medicine Scintigram Images', Proceedings of the 7th International Conference on pattern recognition, pp. 33–6, 1984.

[17] A. J. Worth, N. Makris, V. S. Caviness, and D. N. Kennedy, "Neuroanatomical Segmentation in MRI: Technological Objectives," Int'l J. Patt. Recog. Artificial Intell., Vol.11, pp. 1161–1187, 1997.

[18] A. K. Jain, Fundamentals of Digital Image Processing. Englewood Cliffs, NJ: Prentice-Hall, 1989.

[19] A. Khare, M. Khare , Y. Jeong, H. Kim, M. Jeon, "Despeckling of Medical Ultrasound Images using Daubechies Complex Wavelet Transform", Signal Processing, Vol. 90, pp. 428–439, 2010.

[20] A. L. Taylor, E. J. Eichhorn, M. E. Brickner, R. C. Eberhart, P. A. Grayburn, "Aortic Valve Morphology: An Important in Vitro Determinant of Proximal Regurgitant Jet Width by Doppler Color Flow Mapping", J Am Coll Cardiol, Vol. 16, pp. 405–412, 1990.

[21] A. Lopes, E. Nezry, R. Touzi, H. Laur, "Maximum A Posteriori Speckle Filtering and First Order Texture Model in SAR Images," Proc. of the Int. Geoscience and Remote Sensing Symposium (IGARSS'90), pp. 2409-2412, 1990.

[22] A. Lopes, E. Nezry, R. Touzi, H. Laur, "Structure Detection and Statistical Adaptive Speckle Filtering in SAR Images," Int. J. Remote Sensing, Vol.14, No.9, pp. 1735-1758, 1993.

[23] A. M. Badawi, M. A. Rushdi, "Speckle Reduction in Medical Ultrasound: A Novel Scatterer Density Weighted Nonlinear Diffusion Algorithm Implemented as a Neural-Network Filter", IEEE 28th Annual International Conference on Engineering in Medicine and Biology, pp. 2776-2782, 2006.

[24] A. M. Kizilbash, D. L.Willett, M. E. Brickner, S. K. Heinle, P. A. Grayburn, "Effects of Afterload Reduction on Vena Contracta Width in Mitral Regurgitation" , J Am Coll Cardiol. , Vol. 32, pp. 427-431, 1998.

[25] A. M. Wink, J. B. T. M. Roerdink, "Denoising functional MR images: A Comparison Of Wavelet Denoising and Gaussian Smoothing," IEEE Trans. Med. Imag., Vol. 23, No. 3, pp. 374-387, 2004.

[26] A. Madabhushi, J. K. Udupa and A. Souza, "Generalized Scale: Theory, Algorithms, Properties and Application to Image Inhomogeneity Correction", Comp. Vis. Image Understan, Vol. 101, pp.100–121, 2006.

[27] A. Mark, X. W. Schulze Qing, "Noise Reduction in Synthetic Aperture Radar Imagery using a Morphology-Based Nonlinear Filter", Proceedings of DICTA , Vol. 95, pp. 661-666, 1995.

[28] A. Mehnert, P. Jackway, "An Improved Seeded Region Growing Algorithm", Pattern Recognition Letters, Vol. 18, pp. 1065–1071, 1997.

[29] A. Mishra, P. K. Dutta, and M. K. Ghosh, "A GA based Approach for Boundary Detection of Left Ventricle with Echocardiographic Image Sequences," Image Vis. Comput., Vol.21, pp. 967 976, 2003.

[30] A. Moghaddamzadeh and N. Bourbakis, "A Fuzzy Region Growing Approach for Segmentation of Color Images," Patt. Recogn. Vol. 30, No. 6, pp. 867–88, 1997.

[31] A. P. Richard II, "A New Algorithm For Image Noise Reduction Using Mathematical Morphology", IEEE Transactions On Image Processing, Vol. 4, No. 3, pp. 554-568, 1995.

[32] A. P. Yoganathan, E. G. Cape, H. W. Sung, F. P. Williams, A. Jimoh, "Review of Hydrodynamic Principles for the Cardiologist: Applications to the Study of Blood Flow and Jets by Imaging Techniques", J Am Coll Cardiol, Vol. 12, pp.1344 –53, 1988.

[33] A. P. Zijdenbos and B. M. Dawant, "Brain Segmentation and White Matter Lesion Detection in MR Images," Critical Reviews in Biomedical Engineering, Vol.22, pp. 401– 465, 1994.

[34] A. Pizurica, W. Philips, I. Lemahieu, M. Acheroy, "Despeckling SAR Images using Wavelets and a New Class Of Adaptive Shrinkage Estimators," IEEE ICIP, Thessaloniki-Greece, pp. 233-236, 2001.

[35] A. Vichik, R. Keshet, D. Malah, "Self-Dual Morphology on Tree Semilattices and Applications", Proceedings of the 8th International Symposium on Mathematical Morphology, Rio de aneiro Brazil MCT/INPE Vol. 1, pp. 49– 60, 2007.

[36] A. Yezzi, S. Kichenassamy, A. Kumar, P. Olver, and A. Tennenbaum, "A Geometric Snake Model for Segmentation of Medical Imagery," IEEE Trans. Med. Imag., Vol.16, pp. 199–209, 1997.

[37] B. B. Kimia, A. R. Tannenbaum, and S. W. Zucker, "Shapes, Shocks, and Deformations I: The Components of Two-Dimensional Shape and the Reaction-Diffusion Space," Int'l J. Comp. Vis., Vol.15, pp. 189–224, 1995.

[38] B. B. Kimia, Conservation Laws and a Theory of Shape. Ph.D. thesis, McGill Centre. for Intelligent Machines, McGill University, Montreal, Canada, 1990.

[39] B. Dawant, A. Zijidenbos, R. Margolin, "Correction of Intensity Variations in MR Images of Computer-Aided Tissue Classification," IEEE Trans. Med. Imag., Vol. 12, pp. 770-781, Dec. 1993.

[40] B. Deka, P. K. Bora, "A Versatile Statistical Model for Despeckling of Medical Ultrasound Images", Proc.in IEEE India conference (INDICON), pp. 1-4, Dec 2009.

[41] B. E. A. Saleh and M. Rabbani, "Linear Filtering of Speckled Images," Opt. Commun., Vol. 35, pp. 327–331, 1980.

[42] B. K Khandeira, A. J. Tajik, G. S. Reedrer, M. J. Callahan, R. A. Nishimura, F. A. Miller, J. B. Seward, "Doppler Color Flow Imaging: A New Technique for Visualization And Characterization of the Blood Flow Jet in Mitral Stenosis". Mayo Clin Proc. Vol. 61, pp.623-630, 1986.

[43] B. M. Carvalho, C. J. Gau, G. T. Herman, and T. Y. Kong, "Algorithms for Fuzzy Segmentation," Patt. Anal. Applicat., Vol. 2, pp. 73–81, 1999.

[44] B. Widrow, "The "Rubber-Mask" Technique," Pattern Recognition, Vol.5, pp. 175– 211, 1973.

[45] C. A. Davatzikos and J. L. Prince, "An Active Contour Model for Mapping the Cortex," IEEE Trans. Med. Imag., Vol.14, pp. 65–80, 1995.

[46] C. B. Burckhardt, "Speckle in Ultrasound B-Mode Scans," IEEE Trans. on Sonics and Ultrasonics, Vol. SU-25, No. 1, pp. 1-6, 1978.

[47] C. Chen, J. D. Thomas, J. Anconia, et al., "Impact of Impinging Wall Jet on Color Doppler Quantification of Mitral Regurgitation", Circulation, Vol.84, pp. 712–20, 1991.

[48] C. Chu, J.K. Aggarwal, "The Integration of Image Segmentation Maps Using Region and Edge Information", IEEE Transactions on Pattern Analysis and Machine Intelligence, Vol. 15, No.2, pp. 1241–1252, 1993.

[49] C. I. Christodoulou, C. Loizou, C.S. Pattichis, M. Pantziaris, E. Kyriakou, M.S. Pattichis, C.N. Schizas, A. Nicolaides, "De-Speckle Filtering In Ultrasound Imaging of the Carotid Artery," Second Joint Conf. Engineering in Medicine and Biology and Biomedical Engineering Society (EBMS/BMES), Houston, TX USA, pp. 1027-1028, Oct. 23-26, 2000.

[50] C. J. Oliver, "Review Article: Information from SAR Images," J. Phys. D: Appli. Phys., vol. 24, pp. 1493–1514, 1991.

[51] C. Junqing, N. Thrasyvoulos, M. P. Aleksandra and E. R. Bernice, "Adaptive Perceptual Color-Texture Image Segmentation" , IEEE transactions on image processing, Vol. 14, No. 10, pp. 1524-1536, October 2005.

[52] C. Lantu_ejoul, La squelettisation et. al. Son Application Aux Mesures Topologiques Des Mosa_Ques Polycristallines. PhD thesis, Ecole des Mines, Paris, 1978.

[53] C. Loizou , C. Christodoulou, C.S. Pattichis, R. Istepanian, M. Pantziaris, A. Nicolaides, "Speckle Reduction in Ultrasound Images of Atherosclerotic Carotid Plaque," DSP 2002, Proc., IEEE 14th Int. Conf. Digital Signal Proces., Santorini-Greece, pp. 525-528, July 1-3, 2002.

[54] C. Loizou, Speckle Reduktion in Medizinischer Ultraschallbildern, University of Kaisserslautern, Germany, Master's Thesis, pp. 1-157, 1990.

[55] C. M. Li, C. Y, Xu, C. F. Gui, M. D. Fox, "Level Set Evolution Without Re-Initialization: A New Variational Formulation", in: IEEE Conference on Computer Vision and Pattern Recognition, San Diego, pp. 430–436, 2005.

[56] C. Oliver and S. Quegan, Understanding Synthetic Aperture Radar Images. Norwood, MA: Artech House, 1998.

[57] C. P. Loizou, C.S. Pattichis, C.I. Christodoulou, R.S.H Istepanian, M. Pantziaris, A. Nicoliades, "Comparative Evaluation Despeckle Filtering in Ultrasound Imaging of the Carotid Artery," accepted, IEEE Trans. of Ultras. Ferroel. and Frequency. Control, 2005.

[58] C. R. Jung, "Combining Wavelets And Watersheds for Robust Multiscale Image Segmentation", Image and Vision Computing, Vol. 25, pp. 24–33, 2007.

[59] C. Samson, L. Blanc-Feraud, G. Aubert, and J. Zerubia, "A Variational Model For Image Classification and Restoration" , IEEE Trans. Patt. Anal. Mach. Intell., Vol. 22, No. 5, pp. 460- 472, 2000.

[60] C. Tribouilloy, W.F. Shen, J. P. Quere, J. L. Rey, D. Choquet, H. Dufosse, J.P Lesbre, "Assessment of Severity of Mitral Regurgitation by Measuring Regurgitant Jet Width at its Origin with Transesophageal Doppler Color Flow Imaging", Circulation, Vol. 85, pp.1248 – 1253, 1992.

[61] C. Xu and J. L. Prince, "Generalized Gradient Vector Flow External Forces for Active Contours," Signal Processing—An International Journal, Vol.71, No.2, pp. 131–139, 1998.

[62] C. Xu and J. L. Prince, "Snakes, Shapes, and Gradient Vector Flow," IEEE Trans. Imag. Proc., Vol.7, No.3, pp. 359–369, 1998.

[63] C. Y. Xiao, Z. Su, Y. Z. Chen, "A Diffusion Stick Method for Speckle Suppression in Ultrasonic Images", Pattern Recogn Lett, Vol. 25, pp. 1867–77, 2004.

[64] C. Yu-Chou, D. J. Lee and Y. G. Wang, "Color-Texture Segmentation of Medical Images Based on Local Contrast Information", Proceedings of the 2007 IEEE Symposium on Computational Intelligence in Bioinformatics and Computational Biology (CIBCB 2007), pp 488-493.

[65] D. Adalsteinsson and J. A. Sethian, "The Fast Construction of Extension Velocities in Level Set Methods," J. Computational Physics, Vol.148, pp. 2–22, 1999.

[66] D. Adam, S. Beilin-Nissan, Z. Friedman, V. Behar, "The Combined Effect of Spatial Compounding and Nonlinear Filtering on The Speckle Reduction in Ultrasound Images", Ultrasonics Vol. 44, pp. 166-181, 2006.

[67] D. F. Switzer, A. P. Yoganathan, N. C. Nanda, Y. R. Woo, A. J. Ridgway, "Calibration of Color Doppler Flow Mapping During Extreme Hemodynamic Conditions in Vitro: A Foundation for A Reliable Quantitative Grading System for Aortic Incompetence", Circulation, Vol. 75, pp. 837– 846, 1987.

[68] D. F. Switzer, N. C. Nanda NC, "Doppler Color Flow Mapping", Ultrasound Med Biol Vol. 11, pp. 403-416, 1985.

[69] D. J. Sahn, "Instrumentation And Physical Factors Related to Visualization of Stenotic and Regurgitant Jets by Doppler Color Flow Mapping", J Am Coll Cardiol , Vol. 12, pp. 1354–1365, 1988.

[70] D. J. Sahn, L. M. Valdes Cruz, "New Advances in Two Dimensional Doppler Echocardiography", Prog Cardiovasc Dis, Vol. 28, pp 367-382, 1986.

[71] D. J. Skorton, S. M. Collins, E. G. Garcia, E. A. Geizer, W. Hillard, W. Koppes, D. Linker, G.Schwartz, "Digital Signal and Image Processing in Echocardiography", Am Heart J , Vol. 110, pp. 1266-1283, 1985;

[72] D. J. Williams and M. Shah, "A Fast Algorithm for Active Contours and Curvature Estimation," CVGIP: Imag. Under., Vol.55, No.1, pp. 14–26, 1992.

[73] D. Kuan, A. Sawchuk, T. Strand, P. Chavel , "Adaptive Restoration of Images with Speckle," IEEE Trans. Acoust., Speech, Signal Processing, Vol. ASSP 35, pp. 373–383, 1987.

[74] D. L. Chopp, "Computing Minimal Surfaces via Level Set Curvature Flow," J. of Comp. Phys., Vol.106, pp. 77–91, 1993.

[75] D. L. Donoho, De-Noising by Soft Thresholding, "IEEE Trans. Inform. Theory, Vol. 41, pp. 613, 627, May 1995.

[76] D. MacDonald, D. Avis, and A. C. Evans, "Multiple Surface Identification and Matching in Magnetic Resonance Images," in SPIE Proc. Visualization in Biomedical Computing, Vol.2359, pp. 160–169, 1994.

[77] D. Mumford, J. Shah, "Optimal Approximation by Piecewise Smooth Function and Associated Variational Problems", Communication on Pure and Applied Mathematics, Vol. 42, pp. 577– 685, 1989.

[78] D. S. Bach, G. Michael Deeb, S. F. Boiling, "Accuracy of Intraoperative Transesophageal Echocardiography for Estimating the Severity of Functional Mitral Regurgitation", Am J Cardiol, Vol. 76, pp. 508–512, 1995.

[79] D. T. Kuan, A. A. Sawchuk, T. C. Strand, and P. Chavel, "Adaptive Noise Smoothing Filter for Images with Signal-Dependent Noise," IEEE Trans. Pattern Anal. Machine Intell., Vol. PAMI-2, pp. 165–177, 1985.

[80] D. T. Kuan, A. A..Sawchuk, T. C. Strand , P. Chavel , "Adaptive Restoration of Images with Speckle" , IEEE Trans. Acoust., Speech, Signal Processing, Vol. ASSP-35, pp. 373–383, 1987.

[81] D. T. Kuan, A.A. Sawchuk, "Adaptive Noise Smoothing Filter for Images with Signal Dependent Noise", IEEE Trans. on Pattern Analysis and Mach. Intellig., Vol. PAMI-7, No.2, pp.165-177, 1985.

[82] D. T. Kuan, A.A. Sawchuk, T.C. Strand, P. Chavel, "Adaptive Restoration of Images with Speckle," IEEE Trans. on Acoustic speech and Signal Processing, Vol. ASSP-35, No.3, pp.373 383, 1987.

[83] D. Terzopoulos and D. Metaxas, "Dynamic 3D Models with Local and Global Deformations: Deformable Superquadrics," IEEE Trans. Patt. Anal. Mach. Intell., Vol.13, pp. 703–714, 1991.

[84] D. Terzopoulos and K. Fleischer, "Deformable Models," The Visual Computer, Vol.4, pp. 306–331, 1988.

[85] D. Terzopoulos, "On Matching Deformable Models to Images." Technical Report 60, Schlumberger Palo Alto research, 1986. Reprinted in Topical Meeting on Machine Vision, Technical Digest Series, Vol.12, 1987, 160-167.

[86] D. Terzopoulos, A. Witkin, and M. Kass, "Constraints on Deformable Models: Recovering 3D Shape and Nonrigid Motion," Artificial Intelligence, Vol.36, No.1, pp. 123, 1988.

[87] E. A. Geiser, D.C.Wilson, G.L. Gibby, J. Billett and D.A. Conetta, 'A Method for Evaluation of Enhancement Operations in Two-Dimensional Echocardiographic Images', J. Amer. Soc. Echocardiogr., Vol. 4, No. 3, May, pp.235–246, 1991.

[88] E. I. Dana and F. W. Paul, "An Adaptive Unsupervised Segmentation Algorithm Based on Color-Texture Coherence", IEEE transactions on image processing, Vol. 17, No. 10, pp. 1926-1939, October 2008.

[89] E. Izquierdo, M. Ghanbari, "Nonlinear Gaussian Filtering Approach for Object Segmentation," IEEE Proc. Vision, Image and Signal Proces., Vol. 146, No. 3, pp. 137-143, 1999

[90] E. Nezry, F.Y.-Simen, "Family of Distribution-Entropy Filters for Polarimetric SAR Data, and for Single or Multi-Channel Detected and Complex SAR Images," Private Experts in Remote Sensing, Great Bay Marina, Netherlands Antiles, 2000.

[91] F. A. Monroy, J. G. Sucerquia , "Increment of Lateral Resolution In Digital Holography by Speckle Noise Removal", optic, Vol. 121, pp.2049-2052, 2010.

[92] F. Ferri. and E. Vidal, "Color Image Segmentation and Labeling through Multiunit Condensing", Pattern Recognition Letters, Vol. 13, No. 8, pp. 561-568, 1992.

[93] F. Helmcke, N. C. Nanda, M. C. Hsiung, et al., "Color Doppler Assessment of Mitral Regurgitation with Orthogonal Planes", Circulation, Vol.75, pp. 175–183, 1987.

[94] F. L. Valverde, N. Guil, J. Muñoz, "Segmentation of Vessels from Mammograms using a Deformable Model", Comput Methods Programs Biomed , Vol. 73, pp. 233–247, 2004.

[95] F. Meyer, "Color Image Segmentation," in Proc. 4th IEEE Conf. Image Process. Applicat., Thessaloniki, Greece, Oct. 7–10, 2001, Vol. 354:53, pp. 303–306, 1992.

[96] F. N. S Medeiros, N.D.A. Mascarenhas, R.C.P Marques, C.M. Laprano, "Edge Preserving Wavelet Speckle Filtering," 5th IEEE Southwest Sympos. on Image Anal. and Interpret., Santa Fe, New Mexico, pp. 281-285, 7-9 April 2002.

[97] F. Sery, D.D.-Gambart, A. Lopes, R. Fjortoft, E.C.-Castan, P. Marthon, "Multisource Classification of SAR Images with the use of Segmentation, Polarimetry, Texture and Multitemporal Data," Society of Photo-Optical Instrumentation Engineers, 1996.

[98] F. T. Ulaby, "Regional stability of an ERS/JERS-1 classifier," in The Plenary Session of IGARSS'96, Lincoln, NE, May 1996.

[99] F. T. Ulaby, F. Kouyate, and B. Brisco, "Textural Information in SAR Images," IEEE Trans. Geosci. Remote Sensing, Vol. GE-24, pp. 235–245, 1986.

[100] G. Borgefors, "Distance Transformations in Arbitrary Dimensions," Comp. Vis. Graph. Imag. Proc., Vol.27, pp. 321–345, 1984.

[101] G. Cincotti, G. Loi, M. Pappalardo, "Frequency Decomposition of Ultrasound Medical Images with Wavelet Packets," IEEE Trans. Med.l Imag., Vol. 20, No. 8, pp. 764-771, Aug. 2001.

[102] G.D. Joshi, J. Sivaswamy, "A Simple Scheme for Contour Detection", In: Proc. of the Conference on Computer Vision Theory and Applications", pp. 236–242, 2006.

[103] G. Gilboa , N. Sochen , Y. Y. Zeevi, "Image Enhancement and Denoising by Complex Diffusion Process", IEEE Trans. Pattern Anal. Mach. Intell. Vol. 25, No. 8, pp. 1020-1036, 2004.

[104] G. Gilboa, Y.Y. Zevi, N. Sochen, "Image Enhancement Segmentation and De-Noising by Time Dependent Non-Linear Diffusion Process," ICIP 2001, Thessaloniki-Greece, pp. 134-137, 2001.

[105] G. Liu, X. Zeng, F. Tian Z. Li, K. Chaibou, "Speckle Reduction by Adaptive Window Anisotropic Diffusion", Signal Processing, Vol. 89, pp. 2233–2243, 2009.

[106] G. P. Zhu, S. Q. Zhang, Q. S. Zeng, C. H. Wang, "Boundary-Based Image Segmentation Using Binary Level Set Method", Optical Engineering , Vol. 46, No.5. pp. 050501-1-3, 2007.

[107] G. Sapiro and A. Tannenbaum, "Affine Invariant Scale-Space," Int'l J. Comp. Vis., Vol.11, No.1, pp. 25–44, 1993.

[108] G. Sapiro, "Geometric Partial Differential Equations in Image Analysis: Past, Present, and Future," in Proc. IEEE Int'l Conf. Imag. Proc., Vol.3, pp. 1–4, 1995.
[109] G. Stippel, I. Duskunovic, W. Philips, A. Zedic, P. Govaert, I. Lemahieu, "A New Filtering Method for Ultrasound Images Incorporating Prior Statistics Concerning Medical Features," IEEE ICIP, Thessaloniki-Greece, pp. 821-824, 2001.
[110] H. Aotsuka, K. Tobita, H. Hamada, M. Uchishiba, S. Tateno, K. Matsuo, T. Fujiwara, K. Niwa, "Validation of the Proximal Isovelocity Surface Area Method for Assessing Mitral Regurgitation in Children", Pediatr Cardiol , Vol. 17, No. 6, pp. 351–359, 1996.
[111] H. Baumgartner, H. Kratzer, G. Helmreich, P. Kuhn, "Quantitation of Aortic Regurgitation by Color Coded Cross-Sectional Doppler Echocardiography". Eur Heart J, Vol. 9, pp. 380 –387, 1988.
[112] H. Baumgartner, H. Schima, P. Kuhn, "Value and Limitations of Proximal Jet Dimensions for the Quantitation of Valvular Regurgitation: An In Vitro Study Using Doppler Flow Imaging", J. Am. Soc Echocardiography, Vol. 4, pp. 57-66, 1991.
[113] H. D. Cheng, X. H. Jiang, Y. Sun, and J. Wang, "Color Image Segmentation: Advances and Prospects," Patt. Recogn., Vol. 34, No. 12, pp.2259–2281, 2001.
[114] H. Delingette, "Simplex Meshes: A General Representation for 3D Shape Reconstruction," Tech. Rep. TR2214, INRIA, Sophia-Antipolis, France, 1994.
[115] H. H. Chang, D. J. Valentino, "An Electrostatic Deformable Model for Medical Image Segmentation" Comput Med Imaging Graph, Vol. 32, pp. 22–35, 2008.
[116] H. Heijmans, "Self Dual Morphological Operators and Filters", Journal of Mathematical Imaging and vision, Vol. 6, No.1, pp. 15-36, 1996.
[117] H. L. Eng, K. K. Ma, "Noise Adaptive Soft-Switching Median Filter," IEEE Trans. Image Process., Vol. 10, No. 2, pp. 242-251, 2001.
[118] H. Lange, "Advanced Gray-Scale Morphological Filters for the Detection of Sea Mine in Side Scan Sonar Imagery", Proc. SPIE 4038, pp. 362-372, 2000.
[119] H. Mewada, S. Patnaik, "Variable Kernel Based Chan-Vese Model for Image Segmentation", Proc.in IEEE India conference (INDICON), ,pp. 1-4, Dec 2009.
[120] H. M. Salinas, D. C. Fernández , "Comparison of PDE-based Nonlinear Diffusion Approaches for Image Enhancement and Denoising In Optical Coherence Tomography", IEEE Trans. Med. Imaging , Vol. 26, No. 6, pp. 761–771, 2007.
[121] H. Rifai, I. Bloch, S. Hutchinson, J. Wiart, L. Garnero, "Segmentation of the Skull in MRI Volumes using Deformable Model and taking the Partial Volume Effect into Account" , Med Image Anal, Vol. 4, pp. 219–233, 2000.
[122] H. Tek and B. B. Kimia, "Volumetric Segmentation of Medical Images by Three Dimensional Bubbles," Comp. Vis. Imag. Under., Vol.65, pp. 246–258, 1997.
[123] H. W. Muller-Gartner, J. M. Links, J. L. Prince, R. N. Bryan, E. McVeigh, J. P. Leal, C. Davatzikos, and J. J. Frost, "Measurement of Radiotracer Concentration in Brain Gray Matter using Positron Emission Tomography: MRI-Based Correction for Partial Volume Effects," J. Cereb. Blood Flow Metab., Vol.12, pp. 571–583, 1992.
[124] I. A. Hunter, J. J. Soraghan, T. McDonaght, "Fully Automatic Left Ventricular Boundary Extraction in Echocardiographic Images", Comput Cardiol, pp. 741–744, 1995.
[125] I. Cohen, L. D. Cohen, and N. Ayache, "Using Deformable Surfaces to Segment 3- D Images and Infer Differential Structures," CVGIP: Imag. Under., Vol.56, No.2, pp. 242–263, 1992.
[126] I. N. Bakman, Handbook of Medical Imaging, Processing and Analysis, Academic Press, © 2000.

[127] I. Vanhamel, I. Pratikakis, and H. Sahli, "Multiscale Gradient Watersheds of Color Images," IEEE Trans. Image Process., Vol. 12, pp. 617–626, June 2003.
[128] J. A. Sethian, "An Analysis of Flame Propagation". Ph.D. thesis, Dept. of Mathematics, University of California, Berkeley, CA, 1982.
[129] J. A. Sethian, "A Review of Recent Numerical Algorithms for Hypersurfaces Moving With Curvature Dependent Speed," J. Differential Geometry, Vol.31, pp. 131–161, 1989.
[130] J. A. Sethian, "Curvature and Evolution of Fronts," Commun. Math. Phys., Vol.101, pp. 487–499, 1985.
[131] J. A. Sethian, Level Set Methods and Fast Marching Methods: Evolving Interfaces in Computational Geometry, Fluid Mechanics, Computer Vision, and Material Science. Cambridge, UK: Cambridge University Press, 2nd ed., 1999.
[132] J. Bartunek, P. J. Vantrimpont, B. De Bruyne, "Left Atrial Volume Determination by Echocardiography. Validation by Biplane Angiography in the Setting of Mitral Balloon Valvuloplasty", Intern J Card Imaging Vol. 10, pp. 263–268, 1994.
[133] J. Chen, P. Saint-Marc, and G. Medioni, "Adaptive Smoothing: A General Tool for Early Vision," IEEE Trans. Pattern Anal. Machine Intell., Vol. 13, pp. 514–529, June 1991.
[134] J. D. Bronzino, The Biomedical Engineering Handbook.: CRC Press, 1995.
[135] J. Djamal Boukerroui, A. Noble and M. Brady "Feature Enhancement in Low Quality Images with Application to Echocardiography", in Insana, M.F. and Leahy, R.M. (Eds.): IPMI 2001, LNCS, Vol. 2082, pp.453–460, 2001a.
[136] J. Djamal Boukerroui, A. Noble, M. C. Robini and M. Brady, "Enhancement of Contrast Regions in Suboptimal Ultrasound Images with Application to Echocardiography", Ultrasound in Med. & Biol., Vol. 27, No. 12, pp.1583–1594, 2001b.
[137] J. F. Haddon, J.F. Boyce," Image Segmentation by Unifying Region and Boundary Information", IEEE Transactions on Pattern Analysis and Machine Intelligence, Vol. 12 No. 10, pp. 929–948, 1990.
[138] J. Fan, D.K.Y. Yau, A.K. Elmagarmid, W.G. Aref, "Automatic Image Segmentation by Integrating Color-Edge Extraction and Seeded Region Growing", IEEE Transactions on Image Processing, Vol. 10, No.10, pp. 1454–1466, 2001.
[139] J. G. Abbott, F. Thurstone, "Acoustic Speckle: Theory and Experimental Analysis", Ultrason Imag , Vol. 1, pp. 303–324, 1979.
[140] J. Hansegård, E. Steen, S. I. Rabben, A. H. Torp, S. Frigstad, B.Olstad , "Knowledge based Extraction of the Left Ventricular Endocardial Boundary From 2D = Echocardiograms", In: IEEE International Ultrasonics, Ferroelectrics, and Frequency Control Joint 50th Anniversary Conference, pp 2121–2124, 2004.
[141] J. K. Andre Souza, and A.M. Udupa, "Image Filtering via Generalized Scale", Medical Image Analysis, Vol. 12, pp.87–98, 2008.
[142] J. K. Udupa and S. Samarasekera, "Fuzzy Connectedness and Object Definition: Theory, Algorithms, and Applications in Image Segmentation," Graph. Model Image Process., Vol. 58, No. 3, pp. 246–261, May 1996.
[143] J. L. Mateo, A. F. Caballero, "Finding Out General Tendencies In Speckle Noise Reduction In Ultrasound Images", Expert Systems with Applications, Vol.36, pp.7786–7797, 2009.
[144] J. Lie, M. Lysaker, X. C. Tai, "A Binary Level Set Model and Some Application to Munford–Shah Image Segmentation", IEEE Transaction on Image Processing, Vol. 15, pp. 1171–1181, 2006.

[145] J. Lu and Jr. Healym, "Contrast Enhancement of Medical Images using Multiscale Edge Representation", Wavelet Applications, Proc. SPIE, Orlando, FL, Vol. 2242, pp.711–719, (1996).
[146] J.Manivannan , M. Ramasubba Reddy , S. Thanikachalam, R. Ajay Kumar, "Left Ventricular Systolic Dysfunction Identification by Motion Analysis", Proc. of the 2005 IEEE Engineering in Medicine and Biology 27th Annual Conference Shanghai, China, September 1-4, 2005.
[147] J. M. Kellndorfer, M. C. Dobson, and F. T. Ulaby, "Regional Stability of an ERS/JERS-1 Classifier," in Proc. IGARSS, Lincoln, NE, 1996, pp. 1093–1095.
[148] J. O. Robert 'Callaghan and R. David Bull, "Combined Morphological Spectral Unsupervised Image Segmentation,"IEEE Tran. on image process. Vol. 14, No. 1, pp., Jan. 2005.
[149] J. P. Quere, C. Tribouilloy, M. Enriquez-Sarano, "Vena Contracta Width Measurement: Theoretic Basis and usefulness in the Assessment of Valvular Regurgitation Severity", Curr Cardiol Rep , Vol. 5 , pp. 1101–1115, 2003.
[150] J. R. Klepper, "The Physics of Doppler Ultrasound and its Measurement Instrumentation", In: Spencer MP, ed. Cardiac Doppler diagnosis. Boston, Martinus Nijhoff Publishers, pp. 19-31, 1983.
[151] J. S. Lee, "A Simple Speckle-Smoothing Algorithm for Synthetic Aperture Radar Images," IEEE Trans. System Man and Cybernetics, Vol. SMC-13, No.1, pp. 85-89, 1983.
[152] J. S. Lee, "Digital Image Enhancement and Noise Filtering by use of Local Statistics," IEEE Trans. on Pattern Analysis and Machine Intelligence, Vol. PAMI-2, No. 2 pp. 165-168, 1980.
[153] J. S. Lee, "Digital Image Smoothing and the Sigma Filter," Comp. Graph.Image Proces, Vol. 24, pp. 255-269, 1983.
[154] J. S. Lee, "Refined Filtering of Image Noise using Local Statistics," Comp. Graph.Image Proces., Vol. 15, pp. 380-389, 1981.
[155] J. S. Lee, "Speckle Analysis and Smoothing of Synthetic Aperture Radar Images," Computer Graph. and Imag. Proces., Vol. 17, pp. 24-32, 1981.
[156] J. S. Lee, "Speckle Suppression and Analysis for Synthetic Aperture Radar," SPIE Int. Conf. Speckle, Vol. 556, pp. 170-179, 1985.
[157] J. S. Won, J.H. Ryu, H.Y Kim, "Radarsat SAR investigation over the south coast of Korea: Coastal zone management perspective," Dept. of Earth System Sciences, Yonsei University, Seodaemun-Ku, Shinchon-dong 134, Seoul, Korea, 1996.
[158] J. Saniie, T. Wang, N. Bilgutay, "Analysis of Homomorphic Processing for Ultrasonic Grain Signal Characterization," IEEE Trans. Ultrasonics, Ferroelectrics, Frequency Control, Vol. 3, pp. 365-375, 1989.
[159] J. Serra, Image Analysis and Mathematical Morphology. Academic Press, New York, 1982.
[160] J. Shi and J. Malik, "Normalized Cuts and Image Segmentation," IEEE Trans. Patt. Anal. Mach. Intell., Vol. 22, No. 8, pp. 888–905, Aug. 2000.
[161] J. W.Goodman, "Some Fundamental Properties of Speckle", J. Opt. Soc. Am. Vol. 66, pp.1145–1150, 1976.
[162] J. Weickert, B.M. ter H. Romery, M. Viergever, "Efficient and Reliable Schemes for Nonlinear Diffusion Filtering," IEEE Trans. Image Proc., Vol. 7, No. 3, pp. 398-410, March 1998.
[163] J. Xu, A. Janowczyk, S. Chandran, A. Madabhushi, "A Weighted Mean Shift, Normalized Cuts Initialized Color Gradient Based Geodesic Active Contour Model: Applications to Histopathology Image Segmentation", In: Proc. of SPIE. 2010;7623:76230Y.

[164] J. Y. Yan and T. Zhuang, "Applying Improved Fast Marching Method to Endocardial Boundary Detection in Echocardiographic Images," Pattern Recognit. Lett., Vol.24, No.15, pp. 2777–2784, Nov. 2003.
[165] J. Yu, J. Tan, Y. Wang, "Ultrasound Speckle Reduction by A SUSAN-Controlled Anisotropic Diffusion Method", Pattern Recognition, Vol. 43, pp. 3083–3092, 2010.
[166] K. Abd-Elmonien, A.-B. Youssef, Y. Kadah, "Real-Time Speckle Reduction and Coherence Enhancement in Ultrasound Imaging via Nonlinear Anisotropic Diffusion," IEEE Trans. Biomed. Eng., Vol. 49, No. 9, pp. 997-1014, Sept. 2002.
[167] K. Djemal, "Speckle Reduction in Ultrasound Images by Minimization of Total Variation" IEEE International Conference on Image Processing, Vol. 3, No.III, pp. 357-60, 2005.
[168] K. Miyatake, S. Izumi, M. Okamoto, et al., "Semiquantitative Grading of Severity of Mitral Regurgitation by Real-Time Two-Dimensional Doppler Flow Imaging Technique", J Am Coll Cardiol, Vol. 7, pp. 82–88, 1986.
[169] K. Siddiqi, Y. B. Lauzi`ere, A. Tannenbaum, and S. W. Zucker, "Area And Length Minimizing Flows for Shape Segmentation," IEEE Trans. Imag. Proc., Vol.7, pp. 433– 443, 1998.
[170] K. Z. Abd-Elmoniem, A. B. M. Youssef, Y. M. Kadah, "Real-Time Speckle Reduction And Coherence Enhancement in Ultrasound Imaging via Nonlinear Anisotropic Diffusion", IEEE Trans Biomed Eng Vol. 49, No. 9, pp. 997–1014, 2002.
[171] K. Zhang, L. Zhang, H. Song, W. Zhou, "Active Contours With Selective Local or Global Segmentation: A New Formulation and Level Set Method", Image and Vision Computing, Vol. 28, pp. 668–676, 2010.
[172] L. Alvarez, F. Guichard, P. L. Lions, and J. M. Morel, "Axioms and Fundamental Equations of Image Processing," Archive for Rational Mechanics and Analysis, Vol.123, No.3, pp. 199–257, 1993.
[173] L. Chen, Y. Zhou, Y. G. Wang and Yang, "GACV: Geodesic-Aided C-V Method", Pattern Recognition, Vol. 39, pp. 1391-1395, 2006.
[174] L. D. Cohen and I. Cohen, "Finite-Element Methods for Active Contour Models and Balloons for 2-D and 3-D Images," IEEE Trans. Patt. Anal. Mach. Intell., Vol.15, No.11, pp. 1131–1147, 1993.
[175] L. D. Cohen, "On Active Contour Models and Balloons," CVGIP: Imag. Under., Vol.53, No.2, pp. 211–218, 1991.
[176] L. Dennis, T. Parker, J. Allan pryor and R. Douglas, "Enhancement of Two Dimensional Echocardiographic Images By Lateral Filtering", Computers and Biomedical Research, Vol. 12, pp.265–277, 1979.
[177] L. J. Busse, T.R. Crimmins, J.R. Fienup, "A Model based Approach to Improve the Performance of the Geometric Speckle Reduction Algorithm," IEEE Ultrasonic Symposium, pp. 1353-1356, 1995.
[178] L. J. Porcello, N.G. Massey, R.B. Ines, J.M. Marks, "Speckle Reduction in Synthetic Aperture Radar Images," J. Opt. Soc. Am., Vol. 66, No. 11, pp. 1305-1311, Nov. 1976
[179] L. Najman, M. Schmitt, "Geodesic Saliency of Watershed Contours and Hierarchical Segmentation", IEEE Transactions on Pattern Analysis and Machine Intelligence, Vol.18 No.12, pp. 1163–1173, 1996.
[180] L. P. Yaroslavskii, N. S. Merzlyakov , "Methods of Digital Holography, (Translated From Russian by D. Parsons)", New York: Consultants Bureau, 1989.
[181] L. Pi, J. Fan and C.M. Shen, "Color Image Segmentation for Objects of Interest with Modified Geodesic Active Contour Method", Math. Image and Vis, Vol. 27, pp. 51-57, 2007.

[182] L. Priese and V. Rehrmann, “On Hierarchical Color Segmentation and Applications", Proc. CVPR'93, New York, USA, pp. 633-634, 15 -17 June 1993.
[183] L. Vincent and P. Soille, “Watersheds in Digital Spaces: An Efficient Algorithm based on Immersion Simulation,” IEEE Trans. Patt. Anal. Mach. Intell., Vol. 13, No. 6, pp. 583–597, Jun. 1991.
[184] M. A. Fischler and R. A. Elschlager, “The Representation and Matching of Pictorial Structures,” IEEE Trans. on Computers, Vol.22, No.1, pp. 67–92, 1973.
[185] M. A. Grayson, “Shortening Embedded Curves,” Annals of Mathematics, Vol.129, pp. 71–111, 1989.
[186] M. A. Morales, R. Amyot, E.M. Ferdeghini, L. Caruso and D. Rovai “Spatial and Temporal Variability in Myocardial Contrast Enhancement after Intravenous Echo Contrast Injection”, Computers in Cardiology, Vol. 27, pp.33–36, 2000.
[187] M. Black, G. Sapiro, D. Marimont, D. Heeger, “Robust Anisotropic Diffusion,” IEEE Trans. Image Pro., Vol. 7, No. 3, pp. 421-432, March 1998.
[188] M. Brand, “A Short Note On Local Region Growing By Pseudophysical Simulation”, Proc. CVPR'93, New York City, pp. 782-783, USA, 15- 18 June 1993.
[189] M. D. Smith, J. M. Cassidy, J. C. Gurley, A. C. Smith, D. C. Booth, “Echo Doppler Evaluation of Patients with Acute Mitral Regurgitation: Superiority of transesophageal echocardiography with color flow imaging”, Am Hear J, Vol. 129, No. 5, pp. 167–174, 1995.
[190] M. Datcu, K. Seidel, and M.Walessa, “Spatial Information Retrieval from Remote Sensing Images,” IEEE Trans. Geosci. Remote Sensing, vol. 36, pp. 1431–1445, Sept., 1998.
[191] M. Enriquez-Sarano, A. J. Basmadjian, A. Rossi, K. R. Baile, J. B. Seward, A. Jamil Tajik, “Progression of Mitral Regurgitation. A Prospective Doppler Echocardiographic Study”, J Am Coll Cardiol Vol. 34, No. 4, pp. 1137–1144, 1999.
[192] M. Enriquez-Sarano, A. J. Tajik, K. R. Bailey, et al. , “Color Flow Imaging Compared With Quantitative Doppler Assessment of Severity of Mitral Regurgitation: Influence Of Eccentricity of Jet And Mechanism of Regurgitation”, [erratum appears in J Am Coll Cardiol 1993;22:342]. J Am Coll Cardiol , Vol. 21, pp. 1211–1219, 1993.
[193] M. Enriquez-Sarano, L. Sinak, A. Tajik, R. Kent, Bailey, B. James, M. D. Seward, “Changes on Effective Regurgitant Orifice Throughout Systole on Patients with Mitral Valve Prolapse. A Clinical Study using the Proximal Isovelocity Surface Area Method”, Circulation, Vol. 92 , pp. 2951–2958, 1995.
[194] M. Enriquez-Sarano, W.K. Freeman, C. M. Tribouilloy. "Functional Anatomy of Mitral Regurgitation: Accuracy and Outcome Implications of Transesophageal Echocardiography", Journal of the American College of Cardiology, Vol. 34, pp. 1129-1136, 1999.
[195] M. F. Insana, T.J. Hall, G.G. Cox, J.S. Rosenthal, “Progress in Quantitative Ultrasonic Imaging,” Proc. SPIE, Medical Imag. III, Image Formation, Vol. 1090, pp. 2-9, 198
[196] M. G. Spain, M. D. Smith, P. A. Grayburn, et al., “Quantitative Assessment of Mitral Regurgitation by Doppler Color Flow Imaging: Angiographic and Hemodynamic Correlations”, J Am Coll Cardiol, Vol.13, pp.585–590, 1989.
[197] M. H. Yaou and , W.T. Chang, “Fast Surface Interpolation using Multiresolution Wavelet Transform”, IEEE Trans. Pattern Anal. Machine Intell., Vol. 16, pp.673–688, 1994.
[198] M. Hellemans, E.G. Pieper, A. C. Ravelli., "Prediction of Surgical Strategy in Mitral Valve Regurgitation based on Echocardiography", American Journal ofCardiology, Vol. 79, pp. 334-8, 1997.

[199] M. Hellemans, E.G. Pieper, A.C. Ravelli, "Comparison of Transthoracic and Transesophageal Echocardiography with Surgical Findings in Mitral Regurgitation", The ESMIR research group, American Journal of Cardiology, Vol. 77, pp. 728-33, 1996.

[200] M. Hild, Y. Shirai, and M. Asada, "Initial Segmentation for Knowledge Indexing". Proc. 11th International Conference on Pattern Recognition. vol. 1, conf. A: Computer Vision and Applications. 1A, pp. 587-590, Den Hague, Netherlands. 30 Aug – 3 Sept 1992.

[201] M. I. Miller, G. E. Christensen, Y. Amit, and U. Grenander, "Mathematical Textbook of Deformable Neuroanatomies," Proc. National Academy of Science, Vol.90, pp. 11944–11948, 1993.

[202] M. Ishii, M. Jones, T. Shiota, I. Yamada, R. S. Heinrich, S. R. Holcomb, A. P. Yoganathan, D. J. Sahn, "Evaluation of Eccentric Aortic Regurgitation by Color Doppler Jet and Color Doppler-Imaged Vena Contracta Measurements: An Animal Study of Quantified Aortic Regurgitation", Am Heart J, Vol .132, pp. 796–804, 1996.

[203] M. Ishii, M. Jones, T. Shiota, I. Yamada, R. S. Heinrich, S. R. Holcomb, A. P. Yoganathan, D. J. Sahn, "Quantifying Aortic Regurgitation by Using the Color Doppler-Imaged Vena Contracta: A Chronic Animal Model Study", Circulation, Vol. 96, pp. 2009 –2015, 1997.

[204] M. J. Lester, J. F. Brenner and W. D. Selles, 'Local Transforms for Biomedical Image Analysis', Comput. Graphics, Image Processing, Vol. 13, pp.17–30, 1980.

[205] M. Karaman, M. Alper Kutay, G. Bozdagi, "An Adaptive Speckle Suppression Filter for Medical Ultrasonic Imaging," IEEE Trans. Med. Imag., Vol. 14, no. 2, pp. 283-292, 1995.

[206] M. Kass, A. Witkin, and D. Terzopoulos, "Snakes: Active Contour Models," Int'l Comp. Vis., Vol.1, No.4, pp. 321–331, 1987.

[207] M. Krinidis and I. Pita, "Color Texture Segmentation Based on the Modal Energy of Deformable Surfaces", IEEE transactions on image processing, Vol. 18, No. 7, pp. 1613-1622, July 2009.

[208] M. Mignotte and J. Meunier, "A Multiscale Optimization Approach for the Dynamic Contour Based Boundary Detection Issue," Comput. Med. Imag. Graph., Vol.25, No.3, pp. 265–275, May Jun. 2001.

[209] M. Mulet-Parada and J.A. Noble, "2D+T Acoustic Boundary Detection in Echocardiography", Medical Image Analysis, Vol. 4, pp.21–30, 2000.

[210] M. N. Ahmed, S.M. Yamany, N. Mohamed, A.A. Farag, T. Moriarty, "A Modified C-Means Algorithm to Bias Field Estimation and Segmentation of MRI Data," IEEE trans. Med. Imag., vol. 21, No.3, pp. 193-199, March 2003.

[211] M. Nagao, T. Matsuyama, "Edge Preserving Smoothing," Comp. Graph. Image Proc., Vol. 9, pp. 394-407, 1979.

[212] M. Walessa and M. Datcu, "Model-Based Despeckling and Information Extraction from SAR Images," IEEE Trans. Geosci. Remote Sensing, Vol. 38, pp. 2258–2269, Sept. 2000.

[213] M. Zhang, L. O. Hall, and D. B. Goldgof, "A Generic Knowledge-Guided Image Segmentation and Labeling System using Fuzzy Clustering Algorithms", IEEE transactions on systems, man, and cybernetics—part b: cybernetics, Vol. 32, No. 5, pp.571-582, October 2002.

[214] N. Ayache, P. Cinquin, I. Cohen, L. Cohen, F. Leitner, and O. Monga, "Segmentation of Complex Three-Dimensional Medical Objects: A Challenge and a Requirement for Computer-Assisted Surgery Planning and Performance," in Computer-Integrated Surgery: Technology and Clinical Applications (R. H. Taylor, S. Lavallee, G. C. Burdea, and R. Mosges, eds.), pp. 59–74, MIT Press, 1996.

[215] N. Born, J. De Boo, H. Rijsterborgh: On The Aliasing Problem 181 in Pulsed Doppler Cardiac Studies, J Clin Ultrasound, Vol. 12, pp. 55-567, 1984.
[216] N. D. A. Maskarenhas, L.F. Costa, F.N.S. Medeiros, "Speckle Noise Filtering in SAR Images by MAP Approach," Cybernetic Vision Group, IFSC-University of Sao Paulo, Caixa Postal, 369, SP, Brasil, 1991.
[217] N. KaChanoura, A. Delouche, A. Herment, F. Frouin, B. Diebold, "Automatic Detection of End Systole Within a Sequence of Left Ventricular Echocardiographic Images Using Autocorrelation and Mitral Valve Motion Detection", In: Proceedings of the 29th Annual International Conference of the IEEE EMBS Cité Internationale, pp 4504–4507, Lyon, France, 2007.
[218] N. Kingsbury, "Complex Wavelets for Shift Invariant Analysis and Filtering of Signals," J. Appl. Comput. Harmonic Anal., Vol. 10, No. 3, pp. 234–253, May 2001.
[219] N. Paragios, R. Deriche, "Geodesic Active Contours and Level Sets for Detection and Tracking of Moving Objects", IEEE Transaction on Pattern Analysis and Machine Intelligence, pp. 221–15, 2000.
[220] N. R. Pal and S. K. Pal, "A Review on Image Segmentation Techniques," Patt. Recogn., Vol. 26, No. 9, pp. 1277–1294, 1993.
[221] N. Rougon, F. Preteux, "Controlled anisotropic diffusion," Dept. Signal et Image, Institute National des Telecommunications, Evry, France, Conference on Non-linear Image Processing VI at IS&T/SPIE Symposium on Electronic Imaging, Science and Technology 95.
[222] O. J. Morris, J. Lee, and A. G. Constantinides, "Graph Theory for Image Analysis: An Approach Based on the Shortest Spanning Tree," IEE Proc., pt. F, Vol. 133, No. 2, pp. 146–152, 1986.
[223] O. T. von Ramm and S. W. Smith, "Real Time Volumetric Ultrasound Imaging System," J. Digit. Imag., Vol.3, No.4, pp. 261–266, Nov. 1990.
[224] P. A. Grayburn, W. Fehske, H. Omran, M. E. Brickner, B. Luderitz, "Multiplane Transesophageal Echocardiographic Assessment of Mitral Regurgitation by Doppler Color Flow Mapping of the Vena Contracta", Am J Cardiol , Vol. 74, pp. 912–917, 1994.
[225] P. E. Danielsson, "Euclidean distance mapping," Comp. Graph. Imag. Proc., Vol.14, pp. 227–248, 1980.
[226] P. Felzenszwalb and D. Huttenlocher, "Image Segmentation using Local Variation," in Proc. IEEE Conf. Comput. Vision Patt. Recogn., pp.98–104, 1998.
[227] P. George and P. Kimon Valavanis, "A Color Texture Based Visual Monitoring System For Automated Surveillance", IEEE transactions on systems, man, and cybernetics—part c: applications and reviews, vol. 29, no. 1, pp. 298-307, Feb 1999.
[228] P. Grayburn, W. Fehske, H. Omran, M. E.Brickner, B. Lüderitz, "Multiplane Transesophageal Echocardiographic Assessment of Mitral Regurgitation by Doppler Color Flow Mapping of the Vena Contracta" , Am J Cardiol, Vol. 74, pp.912–917, 1994.
[229] P. Jackway, "Gradient Watersheds in Morphological Scale-Space," IEEE Trans. Image Processing, Vol. 5, pp. 913–921, June 1996.
[230] P. M. Shankar, J. Reid, H. Ortega, C.W. Piccoli, B.B. Goldberg, "Use on Non-Rayleigh Statistics for the Identification of Tumors in Ultrasound B-Scan of The Breast," IEEE Trans. Med. Imag., Vol. 12, No. 4, pp. 685-692, 1993.
[231] P. Marsgos, "Differential Morphology and Image Processing", IEEE Transaction on Image Processing, Vol. 5, No.6, pp. 922-937, 1996.
[232] P. Moulin, "A Multiscale Image Decomposition and Wavelets, In Handbook of Image & Video Processing, Ed. By A. Bovik, Academic press, pp. 289-300, 2000.

[233] P. N. Watton, X. Y. Luo, M. Yin, G. M. Bernacca, D. J. Wheatley, " Effect Of Ventricle Motion on the Dynamic Behaviour of Chorded Mitral Valves", J Fluids Struct , Vol. 24, pp. 58–74, 2008.
[234] P. Perona and J. Malik, "Scale Space snd Edge Detection using Anisotropic Diffusion," IEEE Trans. Pattern Anal. Machine Intell., Vol. 12, pp. 629–639, 1990.
[235] P. Puvanathasan, K . Bizheva, "Speckle Noise Reduction Algorithm for Optical Coherence Tomography Based on Interval Type II Fuzzy Set", Opt. Express , Vol. 15, No. 24, pp. 15747–15758, 2007.
[236] P. Salembier and L. Garrido, "Binary Partition Tree as an Efficient Representation for Image Processing, Segmentation, and Information Retrieval," IEEE Trans. Image Process., Vol. 9, No. 4, pp. 561–576, Apr. 2000.
[237] P. Salembier, "Morphological Multiscale Segmentation for Image Coding", Signal Processing, Vol. 38, No.3, pp. 359–386, 1994.
[238] P. Salembier, J. Serra, "Flat Zones Filtering, Connected Operators and Filters by Reconstruction", IEEE Transactions on Image Processing, Vol. 4, No.8, pp. 1153-1160, 1995.
[239] P. Scheunders, "Wavelet Thresholding of Multivalued Images," IEEE Trans. Image Proces., Vol. 13, No. 4, pp. 475-483, 2004.
[240] P. Slomka, J. Mandel, A. Fenster, D. Downey, "Automated 3-D Registration of Magnetic Resonance Angiography, 3D Power Doppler, and 3D B-Mode Ultrasound Images of Carotid Bifurcation," Med. Imag. Proc. SPIE, Vol. 3979, pp. 332-341, 2000.
[241] P. Soillel, "Morphological Image Analysis", Springer-Verly, Berlin, New-York, 1999.
[242] P. Taylor, "Invited review: computer aids for decision-making in diagnostic radiology —a literature review," Brit. J. Radiol., Vol.68, pp. 945–957, 1995.
[243] P. W. Vachon and J. C. West, "Spectral Estimation Techniques for Multilook SAR Images Of Ocean Waves," IEEE Trans. Geosci. Remote Sensing, Vol. 30, pp. 568–577, May 1992.
[244] R. Adams, L. Bischof, "Seeded Region Growing", IEEE Transactions on Pattern Analysis and Machine Intelligence, Vol. 16, No.6, pp. 641–647, 1994.
[245] R. C. Gonzalez and R.E. Woods: "Digital Image Processing", Addison-Wesley Publishing company, 1992.
[246] R. Courant and D. Hilbert, Methods of Mathematical Physics, Vol.1. New York: Interscience, 1953.
[247] R. F. Wagner, M.F. Insana, S.W. Smith, "Fundamental Correlation Lengths of Coherent Speckle in Medical Ultrasonic Images," IEEE Trans. Ultrasonics, Feroelectrics and Frequency Control, Vol. 35, No. 1, pp. 34-44, Jan. 1988.
[248] R. F. Wagner, S. W. Smith, J. M. Sandrik, H. Lopez, "Statistics of Speckle in Ultrasound B-Scans", IEEE Trans Son Ultrason, Vol.30, No. 3, pp. 156-163, 1983.
[249] R. Fjortoft, A. Lopes, Frederic Adragna, "Radiometric and Spatial Aspects of Speckle Filtering," Proc. IGARSS, Honolulu, Hawaii, 24-28 July, pp. 1-3, 2000.
[250] R. Gonzalez, R. Woods, Digital Image Processing, Second edition, Prentice-Hall Inc., 2002
[251] R. I. Taylor and P. H. Lewis, "Color Image Segmentation using Boundary Relaxation", Proc. 11th IAPR Int. Conf. on Pattern Recognition, Den Hague, Netherlands, 30 Aug.-3 Sept. 1992, vol.III, conf. C: Image, Speech, and Signal Analysis, pp. 721-724, 1992.
[252] R. J. O'Callaghan and D. R Bull "Combined Morphological Spectral Unsupervised Image Segmentation", IEEE trans on image process., Vol. 14, No. 1, pp., Jan. 2005.
[253] R. Kimmel, A. Amir, and A. M. Bruckstein, "Finding Shortest Paths on Surfaces using Level Sets Propagation," IEEE Trans. Patt. Anal. Mach. Intell., Vol.17, No.6, pp. 635– 640, 1995.

[254] R. L. Engle Jr., “Attempts to use Computers as Diagnostic Aids in Medical Decision Making: A Thirty Year Experience,” Perspectives in Biology and Medicine, Vol. 35, No. 2, pp. 207-217, 1992.
[255] R. M. Berne and M. N. Levy, Cardiovascular Physiology 8th ed. St. Lous: Mosby, inc., 2001.
[256] R. Malladi, J. A. Sethian, and B. C. Vemuri, “Shape Modeling with Front Propagation: A Level Set Approach,” IEEE Trans. Patt. Anal. Mach. Intell., Vol.17, No.2, pp. 158– 175, 1995.
[257] R. Omoto, “Color Atlas of Real-Time Two-Dimensional Doppler Echocardiography”, Shindan-To-Chyrio Company, Tokyo, pp. 9-29, 1984.
[258] R. Ronfard, “Region-Based Strategies for Active Contour Models”, Int. 1.Comp. Vis., Vol. 13, No. 2, pp. 229-251, 1994.
[259] R. Srivastava, J. R. Gupta, P. H. Parthasarthy , “Comparison of PDE Based and Other Techniques for Speckle Reduction from Digitally Reconstructed Holographic Images”, Optics and Lasers in Engineering , Vol. 48, pp. 626–635, 2010.
[260] R. T. Whitaker, “Volumetric Deformable Models: Active Blobs,” Tech. Rep. ECRC-94- 25, European Computer-Industry Research Centre GmbH, 1994.
[261] R. Touzi, S. Goze, T. Le Toan, A. Lopès, "Optimization of polarimetric Discriminators In SAR Images”, Proc. International Geoscience and Remote Sensing Symposium (IGARSS'90), Ref IEEE90CH2825-8, Washington DC, USA, 20-24 May 1990, pp. 1683-1686.
[262] S. A. Hall, M. E. Brickner, D. L. Willett, W. N. Irani, I. Afridi, P. A. Grayburn, “Assessment of Mitral Regurgitation Severity by Doppler Color Flow Mapping of the Vena Contracta”, Circulation, Vol 9 , pp. 636–642, 1997.
[263] S. Acton, "Diffusion Based Edge Detectors, In Handbook of Image & Video Processing", Ed. by A. Bovik, Academic press, pp. 433-447, 2000.
[264] S. Beucher, “Segmentation D’images et Morphologie Mathematique,” Ph.D. dissertation, School of Mines, Paris, France, 1990.
[265] S. Beucher, and C. Lantu_ejoul, "Use of Watersheds In Contour Detection. In Proc. International Workshop on Image Processing, Real-Time Edge and Motion Detection/Estimation", Rennes, september, 1979.
[266] S. Beucher, and F. Meyer, "The Morphological Approach To Segmentation: The Watershed Transformation.", In Mathematical Morphology in Image Processing, E. R. Dougherty, Ed. Marcel Dekker, New York, ch. 12, pp. 433-481, 1993.
[267] S. Bhachu, "A New Method to Quantify Mitral Regurgitation", 4th year Medicine, TSMJ, Vol. 5, Review Article, pp. 37-40, April 2004.
[268] S. E. Umbaugh, R. H. Moss, W. V. Stoecker, and G. A. Hance, “Automatic Color Segmentation Algorithms with Application to Skin Tumor Feature Identification”, IEEE Engineering in Medicine and Biology, Vol. 12, No. 3, pp. 75-82, 1993.
[269] S. F. Yiu, M. Enriquez-Sarano, C. Tribouilloy, J. B. Seward, A. J. Tajik, “Determinants of the Degree of Functional Mitral Regurgitation in Patients with Systolic Left Ventricular Dysfunction: A Quantitative Clinical Study”, Circulation, Vol. 102, pp. 1400–1406, 2000.
[270] S. H. Kwok and A. G. Constantinides, “A Fast Recursive Shortest Spanning Tree for Image Segmentation and Edge Detection,” IEEE Trans. Image Process., Vol. 6, No. 2, pp. 328–332, Feb. 1997.
[271] S. Hall, M. Brickner, D. Willett, et al., “Assessment of Mitral Regurgitation by Doppler Color Flow Mapping of the Vena Contracta”, Circulation, Vol. 95, pp.636–642, 1997.

[272] S. Heinle, S. Hall, E. Brickner, D. L. Willett, P. A. Grayburn, "Comparison of Vena Contracta Width by Multiplane Transesophageal Echocardiography With Quantitative Doppler Assessment of Mitral Regurgitation", Am J Cardiol, Vol. 81, pp. 175–179, 1998.

[273] S. Jin, Y. Wang, J. Hiller, "An Adaptive Non-Linear Diffusion Algorithm for Filtering Medical Images," IEEE Trans. on Inform. Technol. in Biomed., Vol. 4, No.4, pp.298-305, Dec. 2000.

[274] S. K. Heinle, S. A. Hall, M. E. Brickner, D. L.Willett, P. A. Grayburn, "Comparison of Vena Contracta Width by Multiplane Transesophageal Echocardiography with Quantitative Doppler Assessment of Mitral Regurgitation", Am J Cardiol, Vol. 81, pp.175-179, 1998.

[275] S. K. Holland, S. C. Orphanoudakis, C. C. Jaffe, "Frequency Dependent Attenuation Effects in Pulsed Doppler Ultrasound: Experimental Results", IEEE BME , 1984.

[276] S. K. Pal and D. D. Madjumadar, "Fuzzy Mathematical Approach to Pattern Recognition" New York: Wiley, 1986.

[277] S. Kichenassamy, A. Kumar, P. Olver, A. Tennenbaum, and A. Yezzi, "Conformal Curvature Flows: From Phase Transitions to Active Vision," Arch. Rational Mech. Anal., Vol.134, pp. 275–301, 1996.

[278] S. M. Ali, R.E. Burge, "New Automatic Techniques for Smoothing and Segmenting SAR Images," Signal Proces., Vol. 14, pp. 335-346, North-Holland, 1988.

[279] S. M. Collins, D. J Skorton, E. A. Geiser, J.A. Nichols, D. A. Conetta, N.G. Pandian, and R.E. Kerber, "Computer-Assisted Edge Detection in Two-Dimensional Echocardiography: Comparison With Anatomic Data", J. Amer. Soc. Echocardiogr., Vol. 53, pp.1380–1387 , 1984.

[280] S. M. Larie and S. S. Abukmeil, "Brain Abnormality in Schizophrenia: A Systematic and Quantitative Review of Volumetric Magnetic Resonance Imaging Studies," J. Psych.,Vol.172, pp. 110–120, 1998.

[281] S. Makrogiannis, G. Economou, and S. Fotopoulos, "A Graph Theory Approach for Automatic Segmentation of Color Images," in Proc. Int. Workshop Very Low Bitrate Video Coding., Athens, Greece, Oct. 11–12, 2001, pp. 162–166.

[282] S. Makrogiannis, G. Economou, S. Fotopoulos, and N. G. Bourbakis, "Segmentation of Color Images Using Multiscale Clustering and Graph Theoretic Region Synthesis", IEEE transactions on systems, man, and cybernetics—part a: systems and humans, Vol. 35, No. 2, pp. 224-238, March 2005.

[283] S. Makrogiannis, I.Vanhamel, H. Sahli, and S. Fotopoulos, "Scale-Space Segmentation of Color Images using Watersheds and Fuzzy Region Merging," in Proceedings of International Conf. Image Process., Vol. 1, pp. 734–737, Thessaloniki, Greece, Oct. 7–10, 2001.

[284] S. Osher and J. A. Sethian, "Fronts Propagating with Curvature-Dependent Speed: Algorithms Based on Hamilton-Jacobi Formulations," J. Computational Physics, Vol.79, pp. 12–49, 1988.

[285] S. Pradhan, D. Patra, "Unsupervised Brain Magnetic Resonance Image Segmentation using HMRF-FCM framework**",** Proc.in IEEE India conference (INDICON), pp. 1-4, Dec 2009.

[286] S. S. Mader, "The Cardiovascular System," in Understanding Human Anatomy and Physiology 5th ed.: The McGraw−Hill Companies, 2004, ch. 12. pp. 227.

[287] S. T. Acton, "De-Convolution Speckle Reducing Anisotropic Diffusion", IEEE International Conference on Image Processing, Vol.1, No. I, pp. 5-8, 2005.

[288] S. T. Acton, J. A. Molloy, Y. Yu, "Three-Dimensional Speckle Reducing Anisotropic Diffusion", IEEE Conference Record of the 37th Asilomar Conference on Signals, Systems and Computers, Vol. 2, pp. 1987- 1991, 2003.

[289] S. Tang, “Experiment of image enhancement with homomorphic filtering,” Computers science department, University of Nevada, Reno, NV 89557, internal report, e-mail: tang@cs.unr.edu.
[290] S. Wang and J. M. Siskind, “Image Segmentation with Ratio Cut”, IEEE transactions on pattern analysis and machine intelligence, Vol. 25, No. 6, pp. 675- 690, June 2003.
[291] S. Y. Yu, Y. Zhang, Y. Wang, and J Yang, “Color-Texture Image Segmentation By Combing Region and Photometric Invariant Edge Information”, in: MCAM 2007, Vol. 4577, pp. 286-294, 2007.
[292] S. Zhong, V. Cherkassky, “Image Denoising Using Wavelet Thresholding and Model Selection,” Proc. of IEEE Int. Conf. Image Proces., Vancouver, Canada, pp.1-4, Nov. 2000.
[293] T. Binder, “Three-Dimensional Echocardiography—Principles and Promises,” J. Clin. Basic Cardiol., Vol.5, No.2, pp. 149–152, 2002. 11 Hill, C. R., Bamber, J. C., and ter Haar, G. R. Physical principles of medical ultrasonics, 2nd edition, 2004 (John Wiley, Chichester, UK).
[294] T. Chan, L. Vese, “Active Contours Without Edges”, IEEE Trans Image Process, Vol. 10, No. 2, pp. 266–277, 2001.
[295] T. Greiner, C. Loizou, M. Pandit, J. Mauruschat, F.W. Albert, “Speckle Reduction in Ultrasonic Imaging for Medical Applications,” Proc. of the ICASSP91, 1991 Int. Conf. acoustic Signal speech and Processing, Toronto Canada, May 14-17, pp. 2993-2996, 1991.
[296] T. H. Le, S.W. Jung, K.-S. Choi and S.-J. Ko, “Image Segmentation Based on Modified Graph-Cut Algorithm”, Electronics Letters, Vol. 46 No. 16, 5th August 2010.
[297] T. Irvine, X. K. Li, D. J. Sahn, A. Kenny, “Assessment of Mitral Regurgitation, Heart”, Vol. 88(Suppl IV), pp. iv11–iv19, 2002.
[298] T. McInerney and D. Terzopoulos, “A Dynamic Finite Element Surface Model for Segmentation snd Tracking in Multidimensional Medical Images with Application to Cardiac 4D Image Analysis,” Comp. Med. Imag. Graph, Vol.19, No.1, pp. 69–83, 1995.
[299] T. Pavlidis, Y.T. Liow, “Integrating Region Growing and Edge Detection”, IEEE Transactions on Pattern Analysis and Machine Intelligence, Vol. 12, No. 3, pp.225–233, 1990.
[300] T. R. Crimmins, “Geometric Filter for Speckle Reduction,” Applied optics, Vol. 24, No. 10, pp. 1438-1443, 1985.
[301] T. Shiota, M. Jones, D. Teien, et al., “Color Doppler Regurgitant Jet Area for Evaluating Eccentric Mitral Regurgitation: An Animal Study with Quantified Mitral Regurgitation”, J Am Coll Cardiol , Vol. 24, pp. 813–819, 1994.
[302] T. Vlachos and A. G. Constantinides, “Graph-Theoretical Approach to Color Picture Segmentation and Contour Classification,” IEE Proc. I, Vol. 140, No. 1, pp. 36–45, 1993.
[303] T. Vlachos and A.G. Constantinides, “A Graph-Theoretic Approach to Color Image Segmentation and Contour Classification", Proc. IEE Int. Conf. on Image Processing and its Applications, Maastricht, Netherlands, pp. 298-302, 7 - 9 April 1992.
[304] T. Westman, D. Harwood, T. Laitinen, and M. Pietikainen, “Color segmentation by Hierarchical Connected Components Analysis with Image Enhancement by Symmetric Neighborhood Filters", Proc. 10th Int. Conf. on Pattern Recognition 1990, Atlantic City, New Jersey, USA, pp. 96-802, 16- 21 June 1990.
[305] U. Grenander, Y. Chow, and D. M. Keenan, Hands, "A Pattern Theoretic Study of Biological Shapes", New York: Springer-Verlag, 1991.
[306] V. Caselles, F. Catte, T. Coll, and F. Dibos, “A Geometric Model for Active Contours,” Numerische Mathematik, Vol.66, pp. 1–31, 1993.
[307] V. Caselles, R. Kimmel, G. Sapiro, “Geodesic Active Contours”, in: Processing of IEEE International Conference on Computer Vision’95, Boston MA, pp 694–699, 1995.

[308] V. Dutt, "Statistical Analysis of Ultrasound Echo Envelope," Ph.D. dissertation, Mayo Graduate School, Rochester, MN, 1995.
[309] V. Metzler, M. Puls, T. Aach, "Restoration of Ultrasound Images by Non-Linear Scale-Space Filtering," Institute of signal processing, Medical university of Luebeck, D-23538 Luebeck, Germany, 1999.
[310] V. S Frost, J. A. Stiles, K. S. Shanmugan, J. C. Holtzman, "A Model For Radar Images and its Application to Adaptive Digital Filtering of Multiplicative Noise", IEEE Trans. Pattern Anal. Machine Intell. Vol. PAMI-4, pp.157–166, 1982.
[311] V. S. Frost, J.A. Stiles, K.S. Shanmungan, J.C. Holtzman, "Edge Detection for Synthetic Aperture RADAR and other Noisy Images," Proc. of the Int. Geoscience and Remote Sensing symposium (IGARSS'82), Sec. FA2, pp.4.1-4.9, 1982.
[312] V. S. Khoo, D. P. Dearnaley, D. J. Finnigan, A. Padhani, S. F. Tanner, and M. O. Leach, "Magnetic Resonance Imaging (MRI): Considerations and Applications in Radiotheraphy Treatment Planning," Radiother. Oncol., Vol.42, pp. 1–15, 1997.
[313] W. E. L. Grimson, G. J. Ettinger, T. Kapur, M. E. Leventon,W. M.Wells, et al., "Utilizing Segmented MRI Data in Image-Guided Surgery," Int'l J. Patt. Recog. Artificial Intell., Vol.11, pp. 1367–1397, 1997.
[314] W. Fehske , H. Omran , M. Manz , J. Köhler, A. Hagendorff, B. Lüderitz, "Color-Coded Dopplerimaging of the Vena Contracta as a Basis for Quantification of Pure Mitral Regurgitation", Am J Cardiol, Vol. 73 pp. 268–274, 1994.
[315] W. Hagg and M. Sties, "Efficient Speckle Filtering of SAR Images," in Proc. IGARSS, Pasadena, CA, 1994, pp. 2140–2142.
[316] W. J. German and C. L. Stanfield, Principles of Human Physiology 2nd ed. San Francisco: Benjamin Cummings, 2005.
[317] W. J. Niessen, B. M. ter Haar Romeny, M. A. Viergever, "Geodesic Deformable Models for Medical Image Analysis", IEEE Trans Med Imaging, Vol. 17, No.4, pp. 634–641, 1998.
[318] W. Ohyama, T. Wakabayashi, F. Kimura, S. Tsuruoka, K. Sekioka, "Automatic Left Ventricular Endocardium Detection In Echocardiograms based on Ternary Thresholding Method", In: Proceedings 15th International Conference On Pattern Recognition, pp 181–183, 2000.
[319] W. P. Santamore, F. N. Dimeo, P. R. Lynch, "A Comparative Study of Various Single-Plane Cineangiocardiographic Methods to Measure Left-Ventricular Volume", IEEE Trans Biomed Eng BME, Vol. 20 , No. 6, pp. 417–421, 1973.
[320] X. Hao, S. Gao, X. Gao, "A Novel Multiscale Nonlinear Thresholding Method for Ultrasonic Speckle Suppressing," IEEE Trans. Med. Imag., Vol. 18, No. 9, pp. 787-794, 1999.
[321] X. Liao, D. C. Liu, "Numerical Analysis of A Deformable Model for Ultrasound Border Detection", APCMBE 2008, IFMBE Proc Vol. 19, pp. 537–541, 2008.
[322] X. Wang, X. Huang, F. Hui, "A Color-Texture Segmentation Method to Extract Tree Image in Complex Scene", International Conference on Machine Vision and Human-machine Interface, pp.621-625, 2010.
[323] X. Zhou, M. Jones, T. Shiota, I. Yamada, D. Teien, D. J. Sahn, "Vena Contracta Imaged by Doppler Color Flow Mapping Predicts the Severity of Eccentric Mitral Regurgitation Better than Color Jet Area: A Chronic Animal Study", J Am Coll Cardiol, Vol. 30, pp. 1393– 1398, 1997.
[324] X. Zong, A. Laine, E. Geiser, "Speckle Reduction and Contrast Enhancement of Echocardiograms via Multiscale Nonlinear Processing, "IEEE Trans. Med. Imag.," Vol. 17, No. 4, pp. 532-540, 1998.

[325] Y. Deng, B.S. Manjunath, "Unsupervised Segmentation of Color Texture Regions in Images and Video", IEEE Transactions of Pattern Analysis and Machine Intelligence, Vol. 23, No.8, pp. 800 810, 2001.
[326] Y. Frank Shih, S. Cheng, "Automatic Seeded Region Growing for Color Image Segmentation", Image and vision computing, Vol. 23, pp. 877–886, 2005.
[327] Y. H. Kuan, C. M. Kuo, and N. C. Yang, "Color-Based Image Salient Region Segmentation Using Novel Region Merging Strategy", IEEE transactions on multimedia, Vol. 10, No. 5, pp. 832-845, August 2008.
[328] Y. H. Yang and J. Liu, "Multiresolution Image Segmentation," IEEE Trans. Patt. Anal. Mach. Intell., Vol. 16, No. 7, pp. 689–700, Jul. 1994.
[329] Y. Huang, J.L. van Genderen, B.S. van Veen, ITC Filter, "A New Adaptive Filter for SAR Speckle Reduction," Int. Institute for AeroSpace survey and earth science (ITC), 1996.
[330] Y. J. Yu, S. T. Acton, "Speckle Reducing Anisotropic Diffusion", IEEE Trans Image Process Vol. 11, pp. 1260–70, 2002.
[331] Y. M. Yoo, F. Zhang , L. M. Koh, Y. Kim, "Nonlinear Diffusion in Laplacian Pyramid Domain for Ultrasonic Speckle Reduction", IEEE transaction on Medical Imaging, Vol. 26, pp. 200-211, 2007.
[332] Y. Su, H. Wang, Yi. Wang, Y. Guo, H. Cheng, Y. Zhang, J. Tian, "Speckle Reduction Approach for Breast Ultrasound Image and its Application to Breast Cancer Diagnosis", European Journal of Radiology, Vol.75, pp. 136–141, 2010.
[333] Y. W. Lim. and S. U. Lee, "On the Color Image Segmentation Algorithm based on the Thresholding and the Fuzzy C-Means Techniques", Pattern Recognition, vol. 23, no. 9, pp. 935-952, 1990.
[334] Y. Yongjian and T. Scott Acton, "Speckle Reducing Anisotropic Diffusion "IEEE Transactions on Image Processing, Vol. 11, No. 11, November 2002.
[335] Y. Yu, J. A. Molloy, S. T. Acton, "Generalized Speckle Reducing Anisotropic Diffusion for Ultrasound Imagery", 17th IEEE Symposium on Computer-Based Medical Systems, pp.279-284, 2004.
[336] Y. Zimmerand R. Tepper and S. Akselrod. "A Two-Dimensional Extension of Minimum Cross Entropy Thresholding for the Segmentation Of Ultrasound Images", Ultrasound Med. Biol., Vol.22, pp. 1183–1190, 1996.
[337] Z. K. Huang, P. W. Li, S. Q. Wang , L. Y. Hou, "Using FCM for Color Texture Segmentation based Multirscale Image Fusion", International Conference on e-Education, e-Business, e-Management and e-Learning, pp. 84-87, 2010.
[338] Z. Wang and R. Boesch, "Color and Texture-Based Image Segmentation for Improved Forest Delineation", IEEE transactions on geoscience and remote sensing, Vol. 45, No. 10, pp. 3055-3062, October 2007.
[339] Z. Wu and R. Leahy, "An Optimal Graph Theoretic Approach to Data Clustering: Theory And its Application to Image Segmentation," IEEE Trans. Patt. Anal. Mach. Intell., Vol. 15, No. 11, pp. 1101–1113, Nov. 1993.
[340] Z. Ying, L. Guangyao, S. Xiehua, and X. Xinmin, "Geometric Active Contours without Re-Initialization for Image Segmentation", Pattern Recogn., Vol. 42, No.9, pp.1970-1976, 2009.

USER MANUAL

Type Command Echocardiography in MATLAB command window

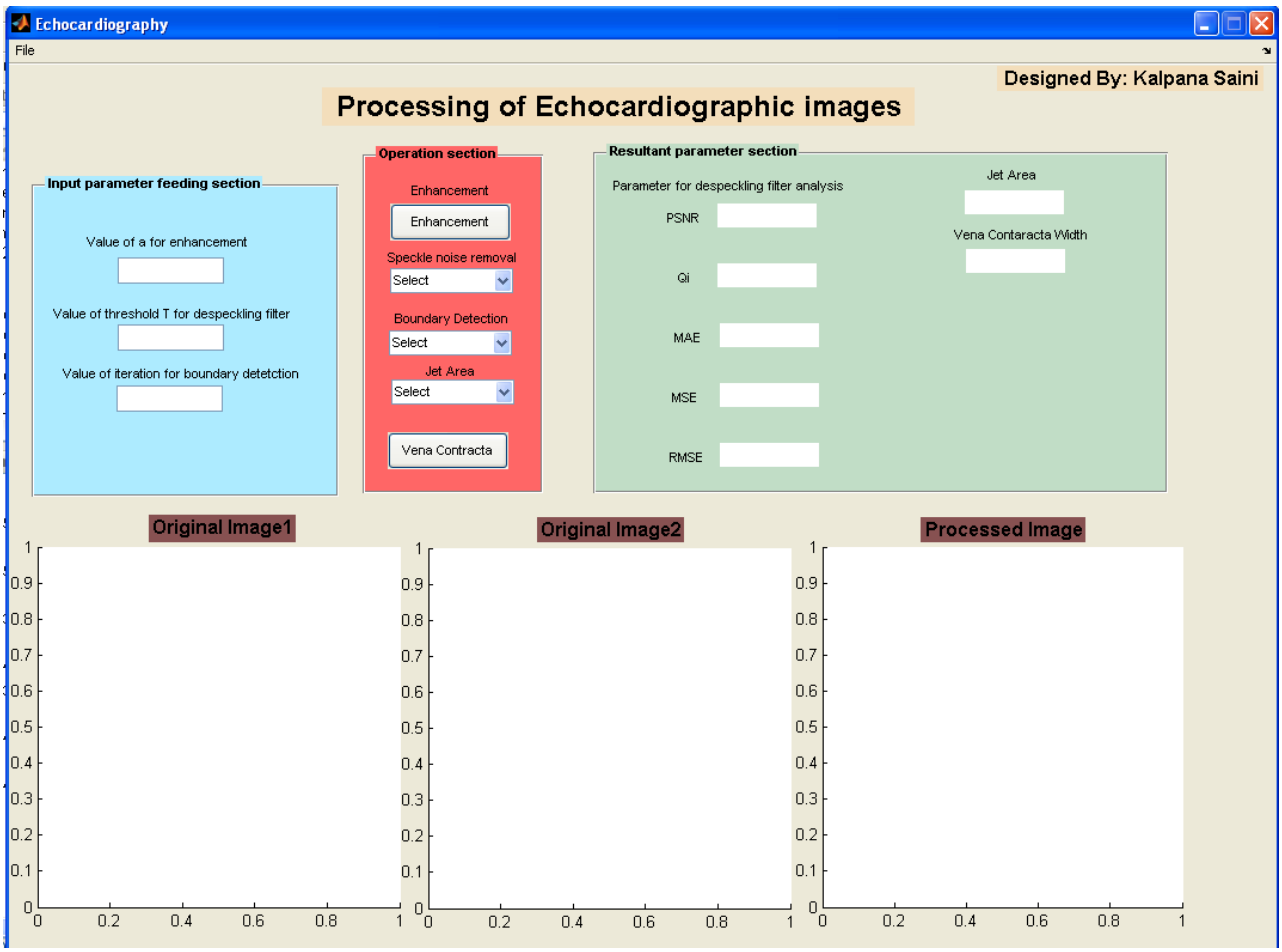

Figure M.1 The User Interface of the "Processing of Echocardiographic Images System". The three windows, namely, the 'Original Image1', the 'Original Image2' and the 'Processed Image' are used to show the Images before and after a transaction respectively.

As can be seen from the figures M.1 to M.10 there are three sections on the top of the MATLAB GUI. The first section is the input parameter feeding section. This section is subdivided into three blocks. First block of input parameter feeding section is, namely, the 'value of 'a' for enhancement'. In this block some value of 'a' has to be chosen in accordance with the different contrast images. For example, for low contrast images the value of 'a' will be high. The next block of this section, is namely, the 'value of threshold T for de-specking'. In this block a threshold value will have to be fed which is nothing but the number of iterations desired. Generally 25 iterations are sufficient for the echocardiographic images and may vary for other modality images. The third

block of parameter feeding section is the ‘value of iterations for boundary detection’. In this block the number of iterations will assigned for the convergence of boundary detection methods. This value may vary according to the particular method.

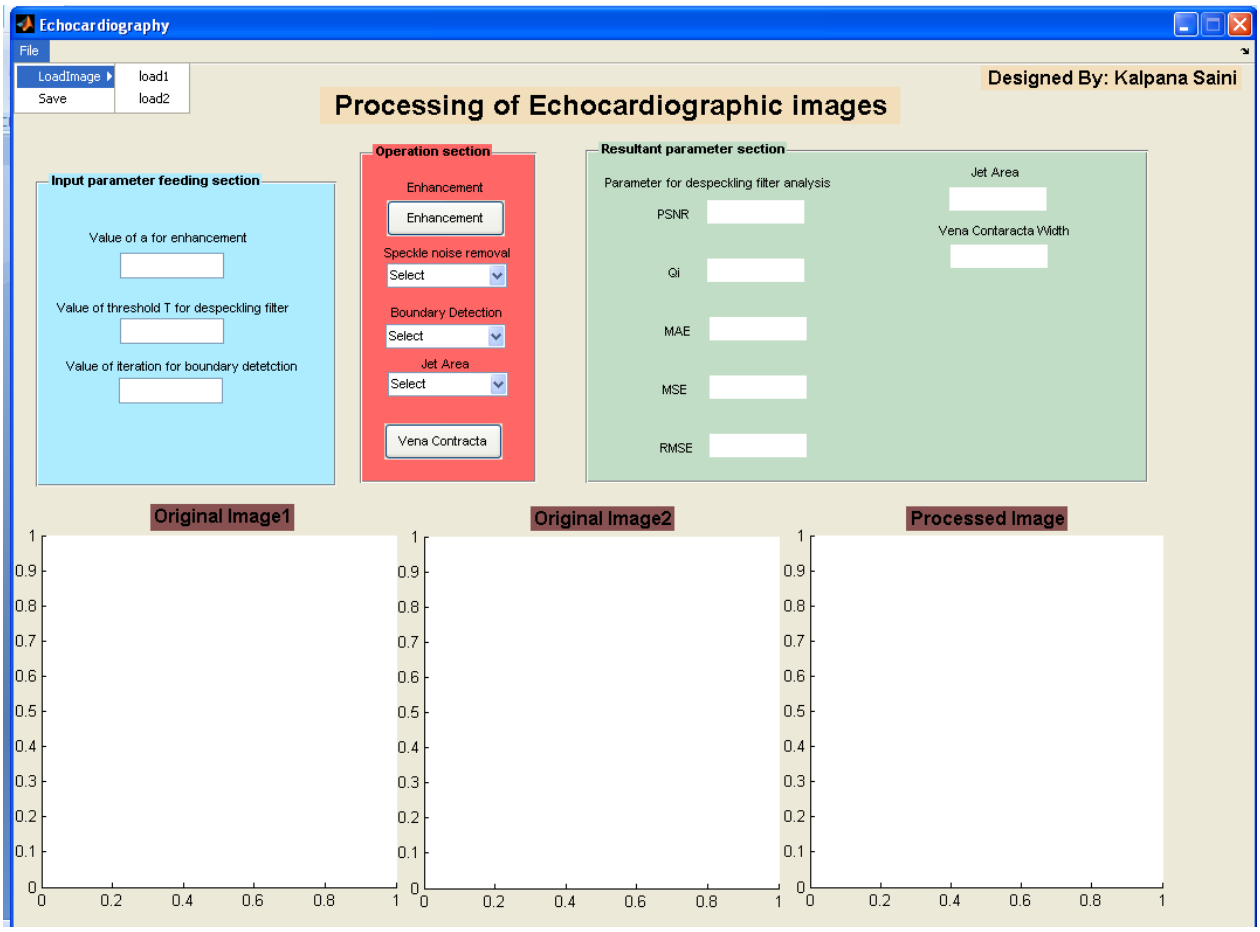

Figure M.2 Load an Echocardiographic Image from a Drive Specified by the Users

Second section is the operation section. This section is subdivided into five blocks. First block of operation selection section is a push button, namely the ‘Enhancement’ push button. Second block is a pop-up menu type button, namely, the ‘Speckle noise removal’ button. In the menu , listed are the existing and the proposed. The third block is named as the ‘Boundary detection’ operation block. This is also a pop-up menu type button and having options of boundary detection methods including some pervious boundary detection methods and the proposed boundary detection method for echocardiographic images. The fourth block is named as the ‘Jet Area’ display block. The pop-up menu of the ‘jet area’ block having the two new proposed methods

listed for MR jet area segmentation. The last block of this section is the push button named as 'Vena Contracta'.

The third section is the resultant parameter section, which shows the comparative value of parameters between the various de-speckling filters by showing values of PSNR, Qi, MAE, MSE, and RMSE. This section also has the blocks on which the value of jet area and vena contracta width will printed automatically.

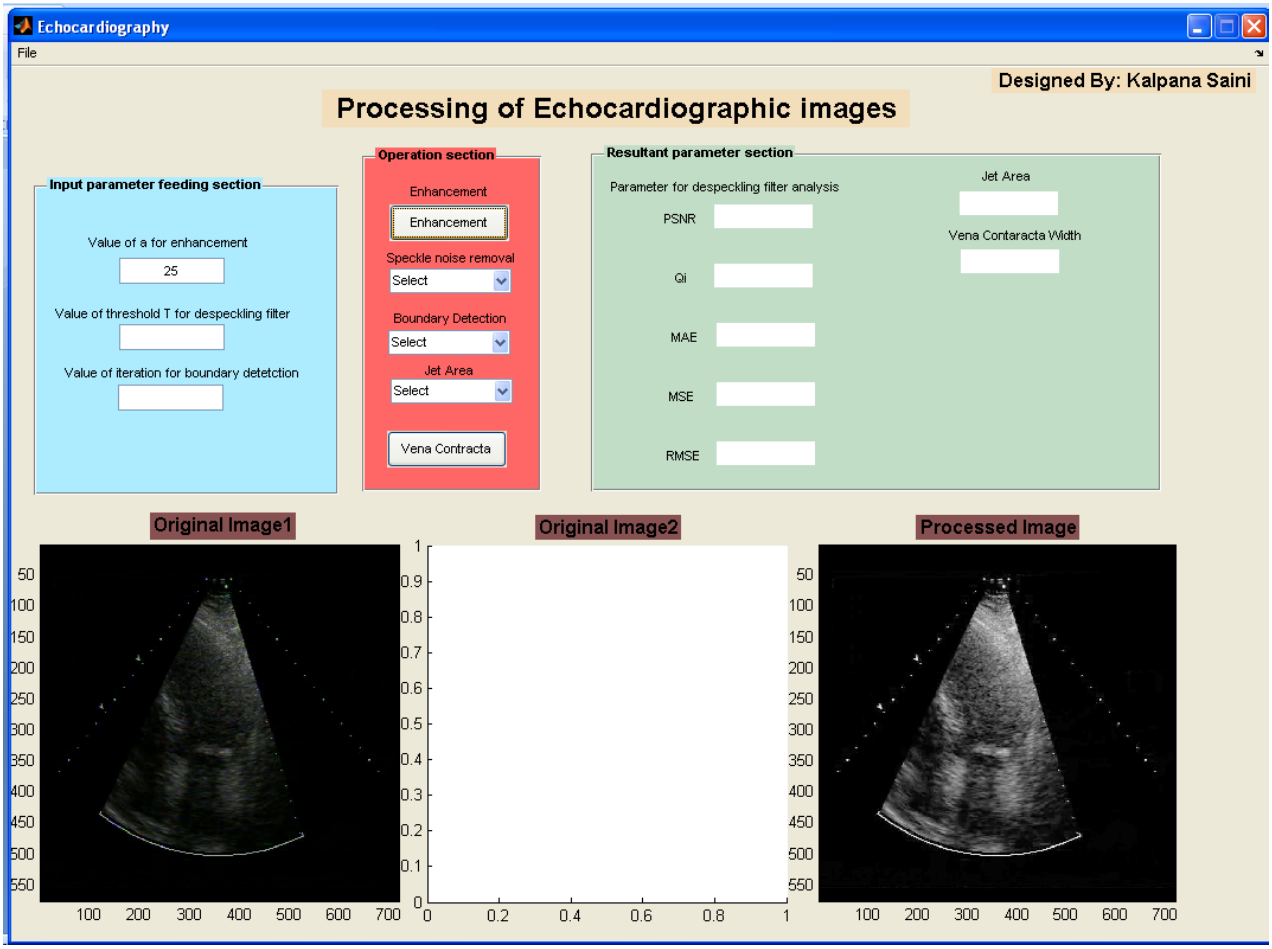

Figure M.3 After Enhancement Process; the Enhanced Image is Shown in the Processed Image Block

LOAD IMAGES

In the fig. M.1, above, there are blocks for feeding the input parameters, selection of operation and output parameters. There are three windows for image representation. The first two blocks are for the input images and the third block is for showing the resultant image.

At the menu bar there is a popup menu named file. In fig M.2 it can be seen that by dropping down the file menu there appear options of Load Image and Save. Under the Load tool, options are available to select ‘load 1’ and ‘load 2’ options according to the requirement. Save menu is given if one wants to save the image in the desired location.

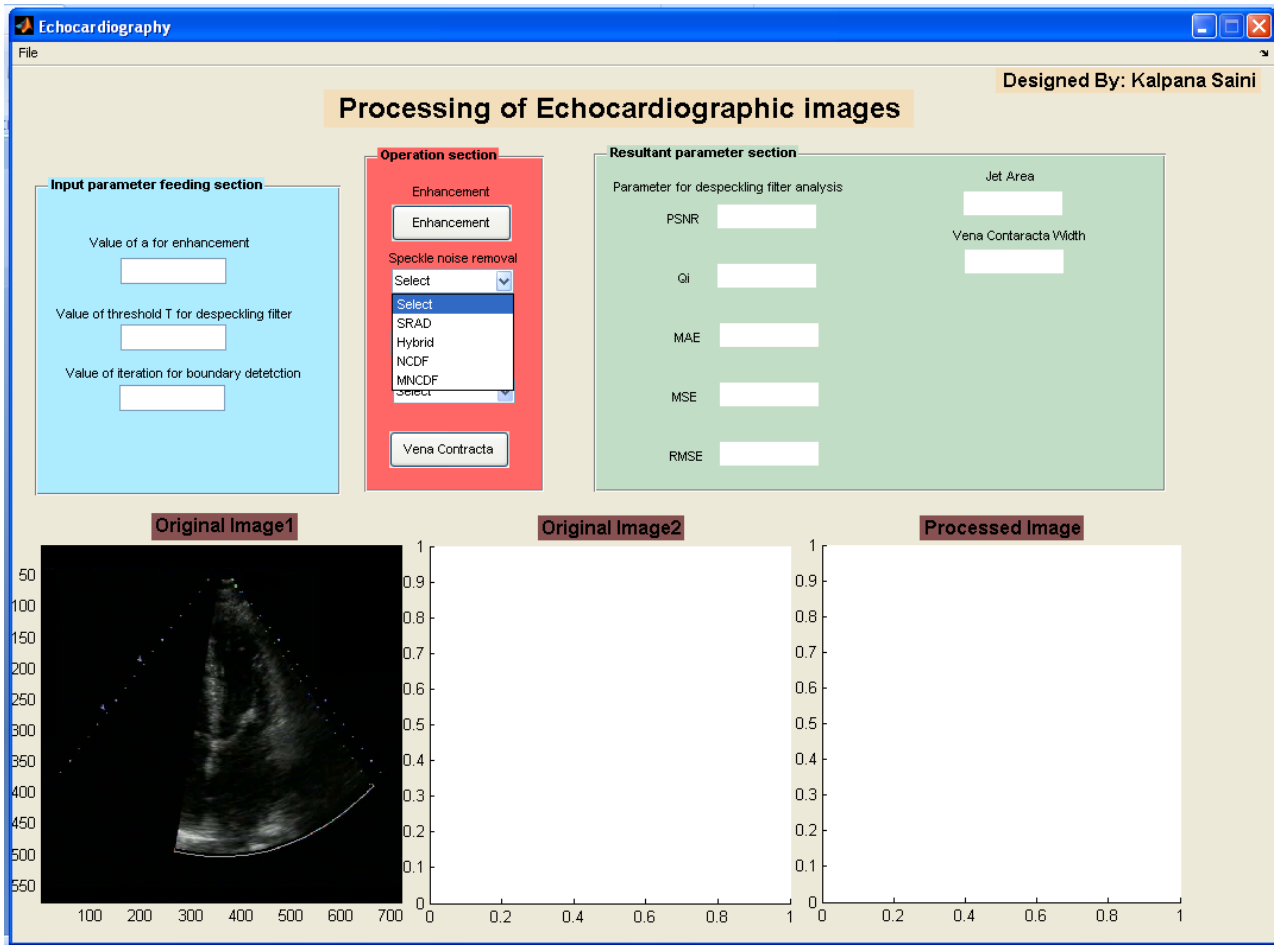

Figure M.4 Selection of De-Speckling Method

ENHANCEMENT

For performing enhancement operation one needs to first load the image using the ‘load1’ option as shown in fig.M.3. After loading the image one needs to assign a value to the parameter a which is in accordance with the kind of image. Now the next step is to go through the operation block and select the option Enhancement. The resultant image appears in the processed image block. Proposed transformation is suitable for different kinds of low contrast images. There is no requirement of different transformation function for different kind of images as in the case of

conventional transformations. Parameters are specified automatically and the enhancement procedure can work as an automatic enhancement tool. This is applicable to gray-scale images, color images, 3-D echocardiographic images also.

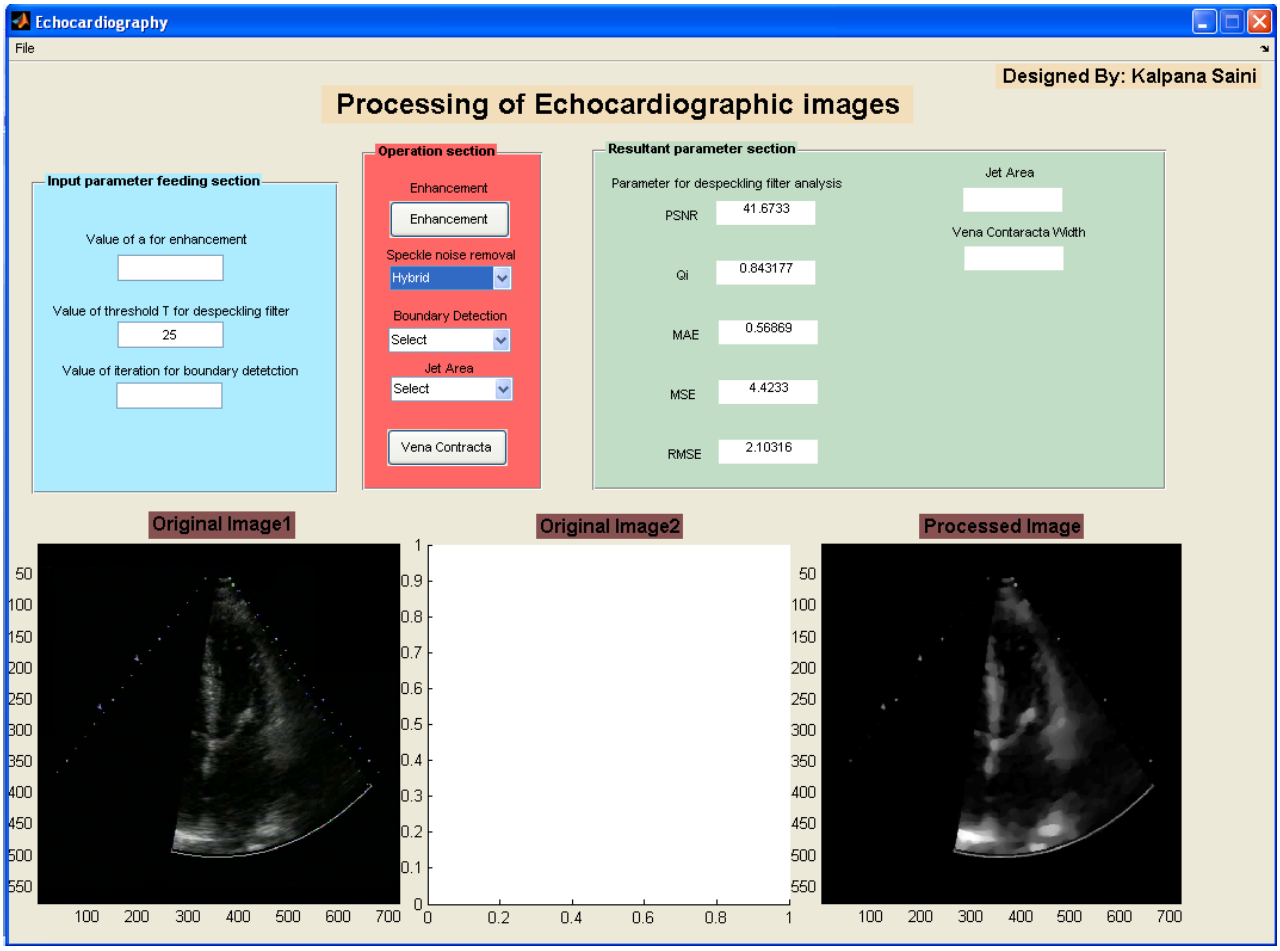

Figure M.5 After the Selection of De-Speckling Method; The De-Speckled Image is shown in the Processed Image Block

SPECKLE NOISE REMOVAL

For the removal of speckle noise load the image as in fig M.4 and then enter the threshold value in the block ‘value of threshold T for de-speckling filter’ of the input parameter feeding section. After setting the threshold value T, select the operation from the ‘speckle noise removal’ popup menu of the operation section.

After selecting one of the de-speckling methods one can see the resultant image in the ‘Processed Image’ Block, and the analysis parameters can be read in the ‘resultant parameter section’ as shown in fig. M.5. These outputs are as obtained using the selected de-speckling

method. These parameters are PSNR, Qi, MAE, MSE, and RMSE. For example, proposed filter HSRAD has been selected in fig. M.5.

BOUNDARY DETECTION

For boundary detection of heart chambers from the echocardiographic images, first load the image as described earlier, and then, put the iteration values in the 'Value of Iterations for Boundary Detection' block in the input parameter feeding section. The value of iterations is boundary detection method specific. Hence, one needs to choose the boundary detection method from amongst the various listed methods as shown in fig. M. 6.

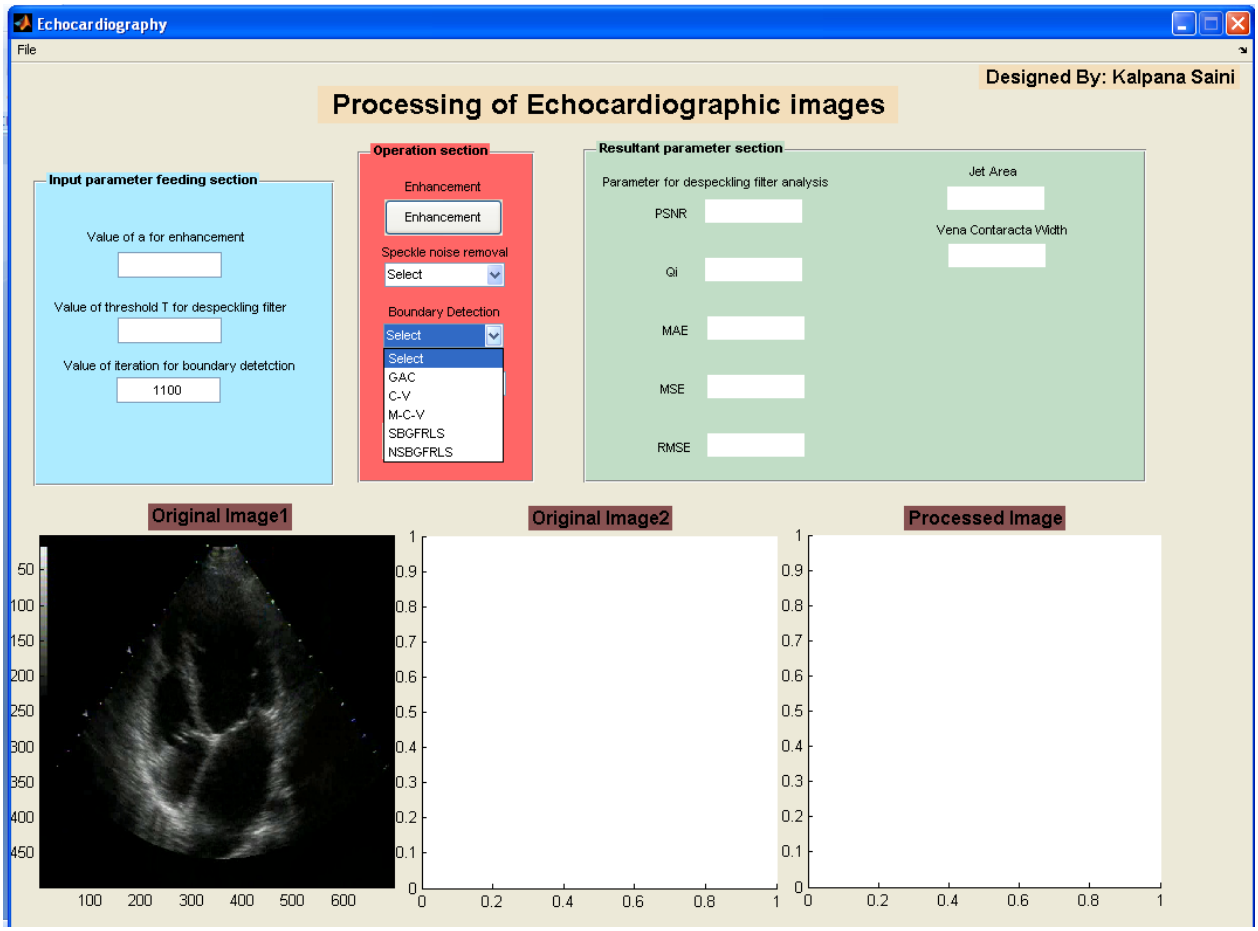

Figure M.6 Selection of Boundary Detection Method

Output processed image can be viewed in the processed block and boundaries can be seen in the 'Original Image1' block as shown in fig M.7.

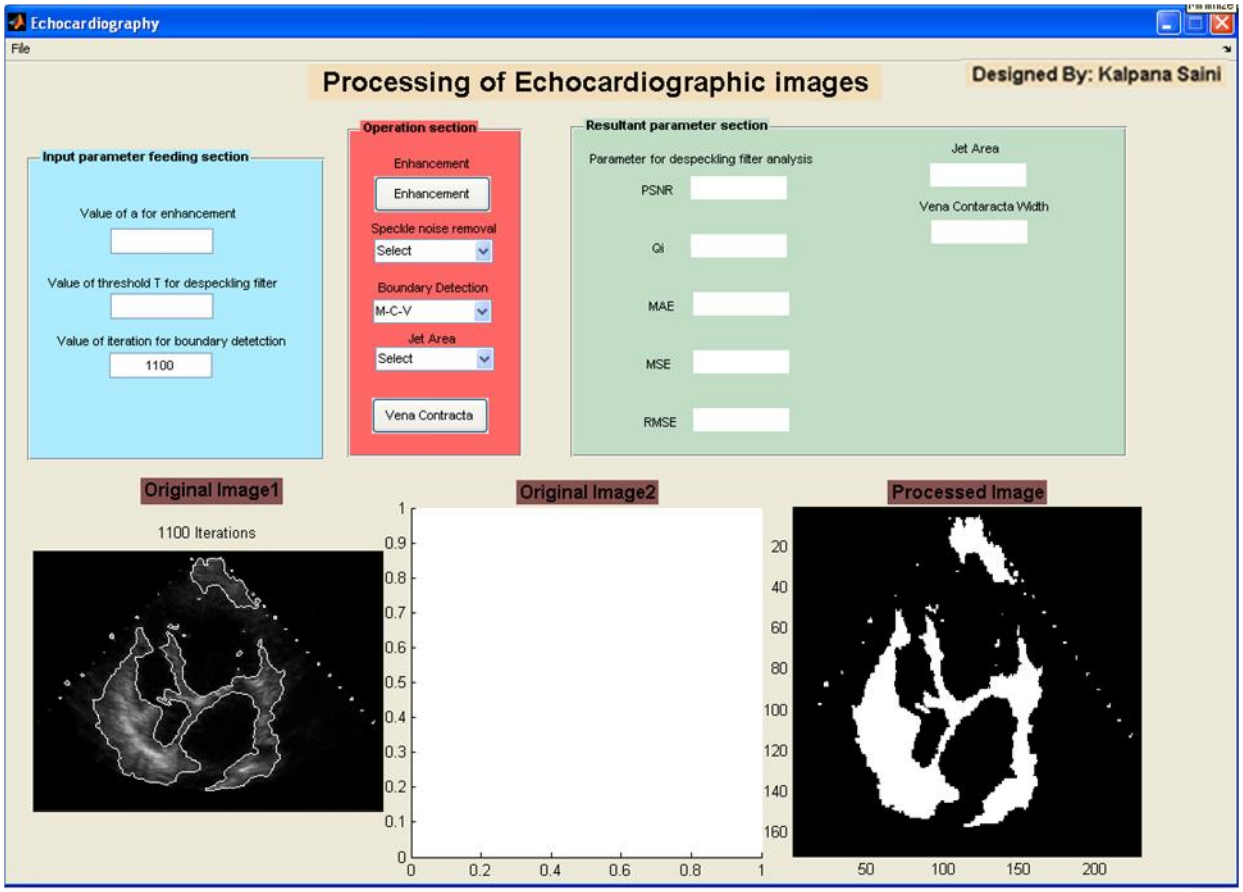

Figure M.7 After Applying Boundary Detection Method on the Original Image, Boundaries are Superimposed on the Original Image and the Processed Image Block shows Segmented Image

JET AREA DETECTION

For evaluating the area of the regurgitant jet one needs to load two images. One of the images is the color Doppler jet image and the other one is the background image for the case of region growing method as shown in fig. M.8. However, for the other method i.e., the combined method of wavelet and watershed only the colored jet image is sufficient. This selection of methods can be made from the 'Jet Area' drop down menu of the operation section.

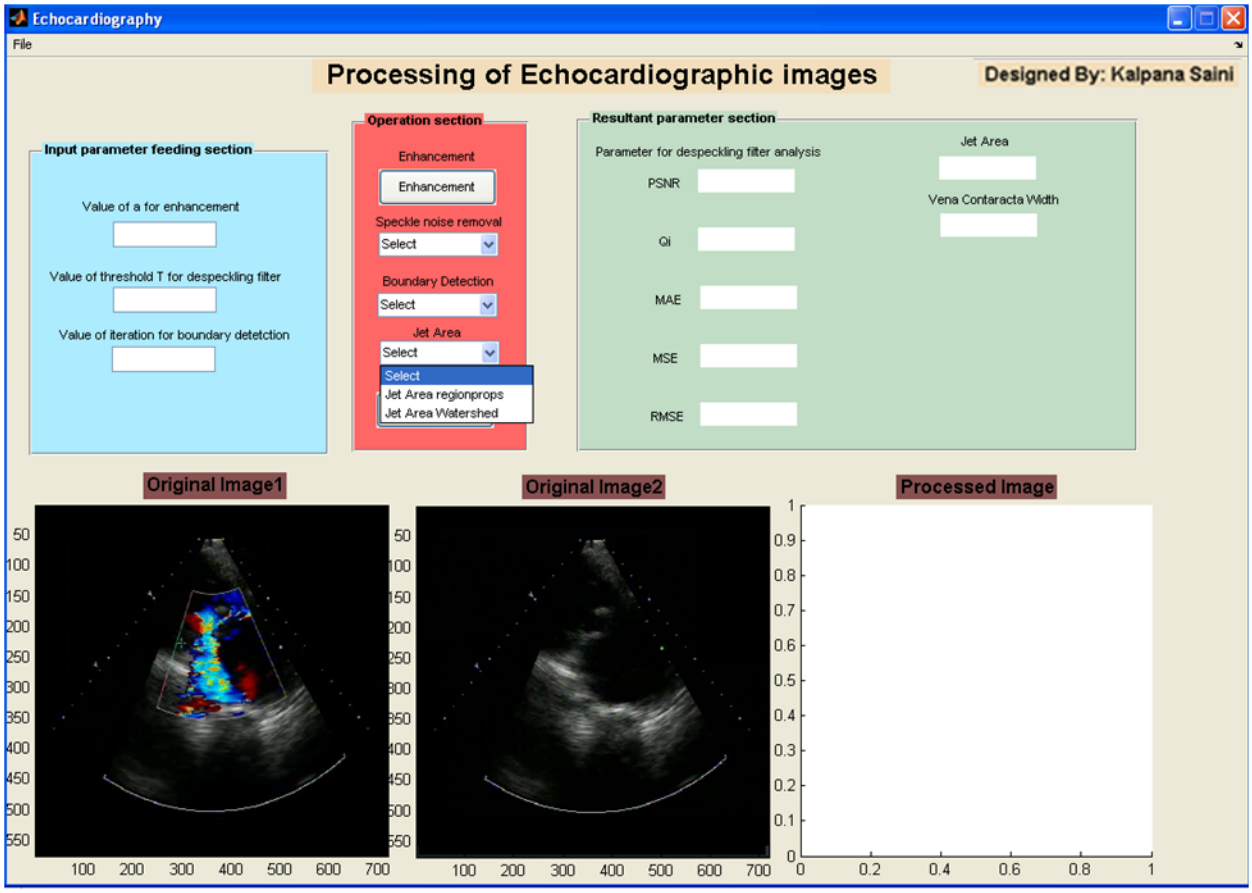

Figure M.8 Loading of Images for Jet Area Segmentation

Jet area is shown in processed image block and the calculated jet area is shown in the 'Jet Area block' of the resultant parameter section as shown in fig. M. 9. During systole, the left atrium is usually free from color in normal cases. In abnormal cases the increased velocity and the turbulence caused through the closed valve orifice, result in aliasing and it appears as a mix of color mosaic patterns. Severity of valvular regurgitation is based approximately on the configuration and the size of the regurgitant jet. Very small jets, localized just to the proximal side of the regurgitant valve, usually signify mild valvular regurgitation. Large jets that fill the receiving chamber usually indicates sever valvular regurgitation.

If the value of jet area in the 'Jet Area' block of the resultant section is less than $4cm^2$ than the MR is in the category of mild MR. If this value is in between $4cm^2$ and $10cm^2$ than it is categorized in the moderate MR. If the value of jet area increases beyond $10cm^2$, than it shows severe MR.

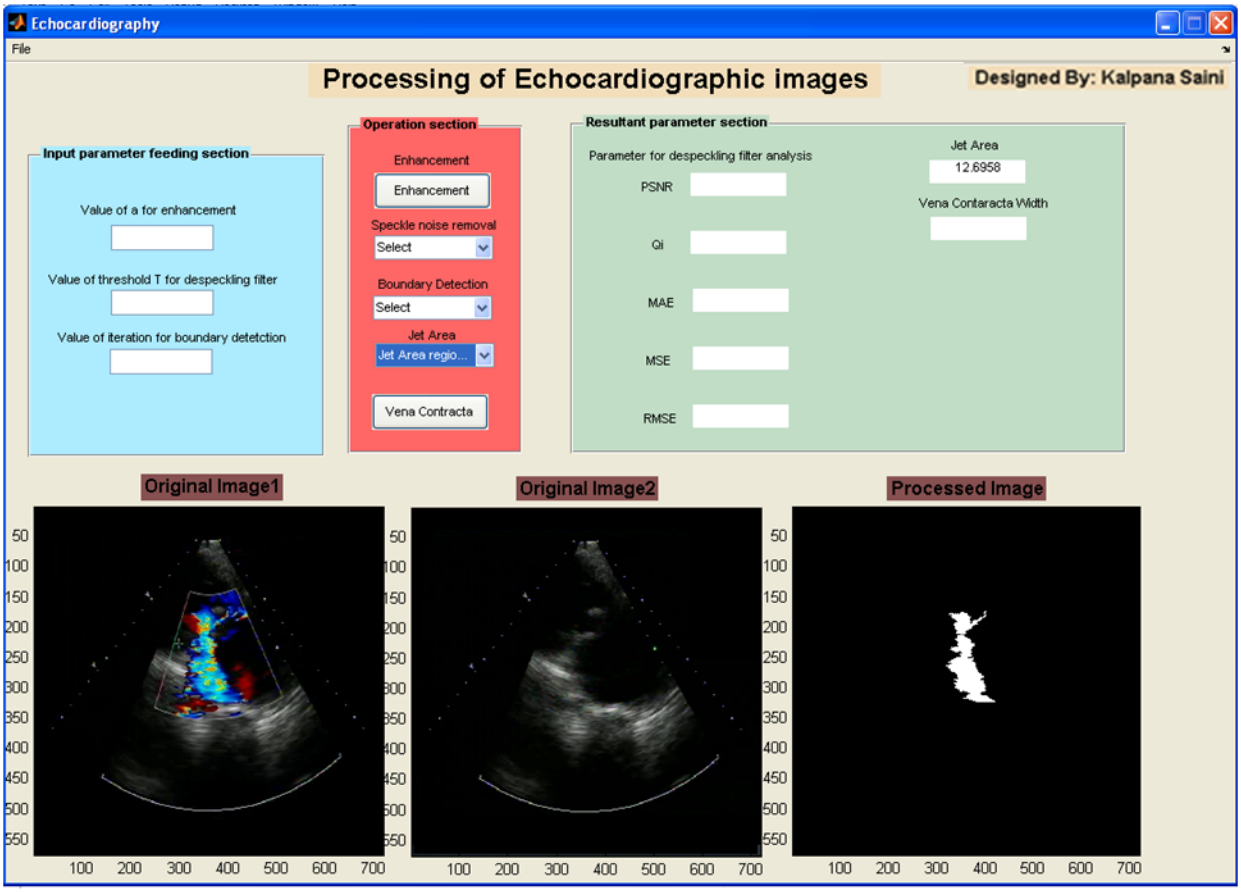

Figure M.9 After Applying Jet Area Detection, the Jet Area Segmented Image is shown in the Processed Image Block. The Value of Jet Area is Printed in Jet Area Resultant Block

VENA CONTRACTA WIDTH DETECTION

Measurement of vena contracta width is an efficient method of grading the severity of MR, but it is very difficult to locate this narrowest part exactly in transthoracic echocardiographic (TTE) as well as in transesophageal echocardiographic (TEE) images. For getting the automatic vena contracta width load the color Doppler image as well as the background image and then press the 'Vena Contracta' push button fixed on the panel within the operation section as shown in fig. M.10.

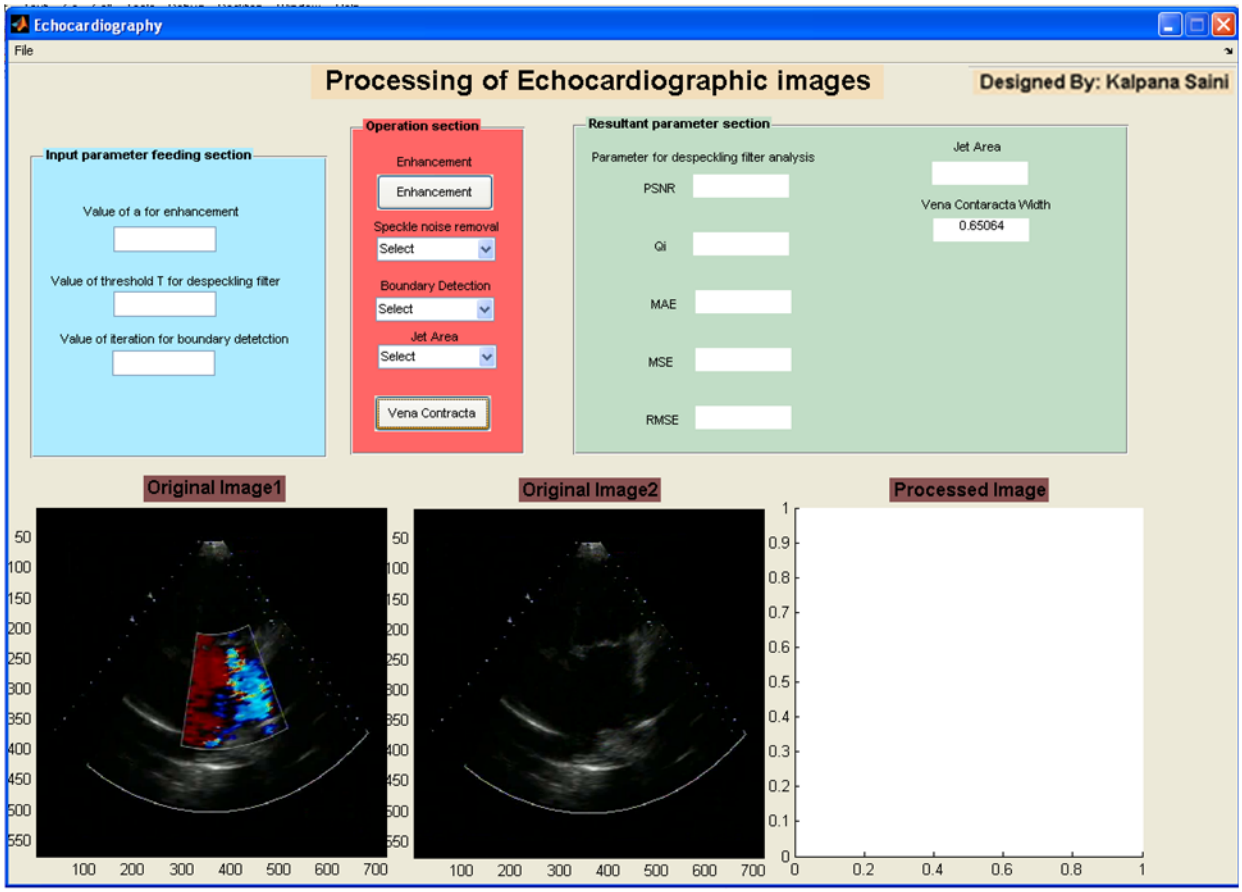

Figure M.10 After Applying Vena Contracta Width Detection. Value of Vena Contracta is printed in the Vena Contracta Width Resultant Block

Vena contracta width is displayed in the 'Vena Contracta Width' block of the resultant parameter section. The VC width less than 0.3cm indicates the mild MR. If this value is in between 0.3 and 0.5 then it is the case of moderate MR. But if the VC width is more than 0.5cm than it indicates the severe MR.

APPENDIX I

ECHOCARDIOGRAPHY MACHINE DESCRIPTION AND OPERATION

AI.1 ACUSON SEQUOIA C512 SYSTEM

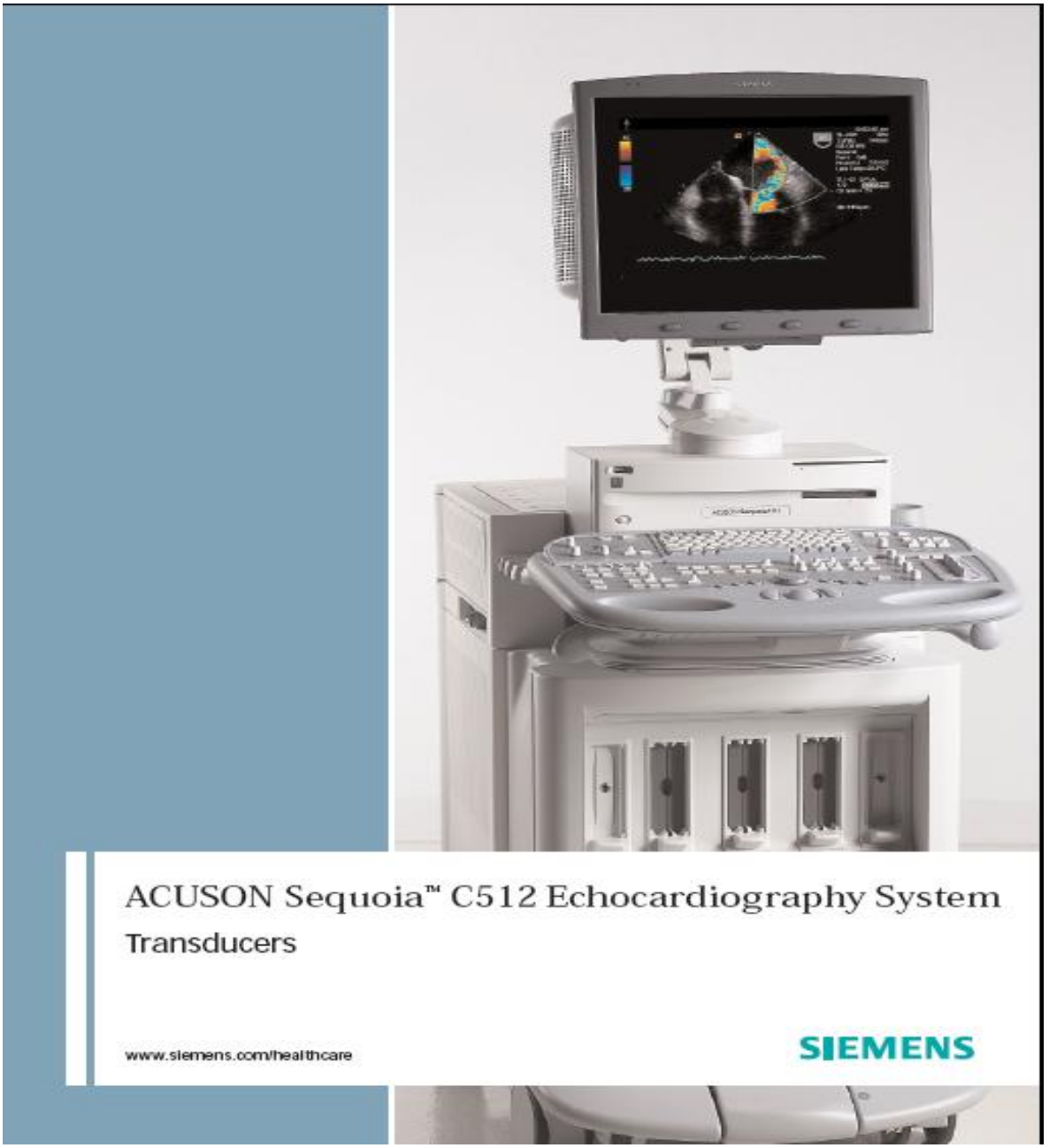

Figure AI.1 ACUSON Sequoia™ C512 Echocardiography system

Sequoia systems are specially designed to help you perform radiology, obstetrics, gynecology, cardiac, and/or vascular exams. They offer a wide range of standard and optional operating modes and transducer formats. This manual explains all standard and optional features. Your system may not have all of these features installed. In which Sequoia C512 is for echocardiography.

AI.2. SEQUOIA SYSTEM COMPONENTS

The Sequoia system is equipped with either a flat panel monitor or a cathode ray tube monitor.

Sequoia System with Flat Panel Monitor

1. Monitor and Speakers
2. DVD/CD Drive
3. MO Disk Drive
4. Transducer Holders
5. Cable Holder
6. Storage Compartment
7. Wheel Lock/Steering Controller
8. Footswitch Connector (hidden)
9. MP Transducer Ports (3)
10. MP Storage Port
11. Control Panel/ Keyboard
12. Power Button
13. USB Port
14. Soft Keys (4)
15. Monitor Controls

Sequoia system with flat monitor

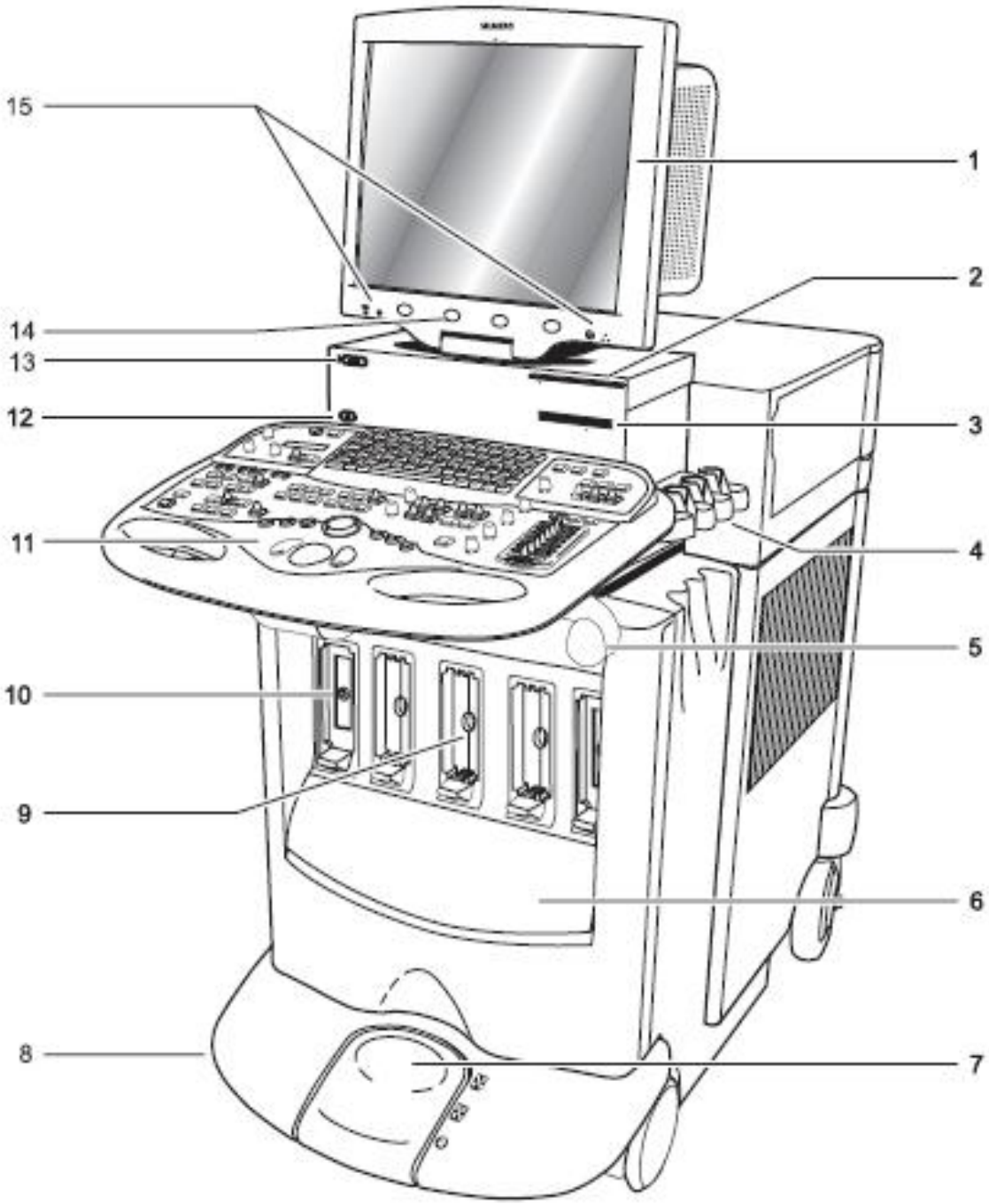

Figure AI.2 Sequoia System Components with flat panel monitor

Sequoia System with Cathode Ray Tube Monitor

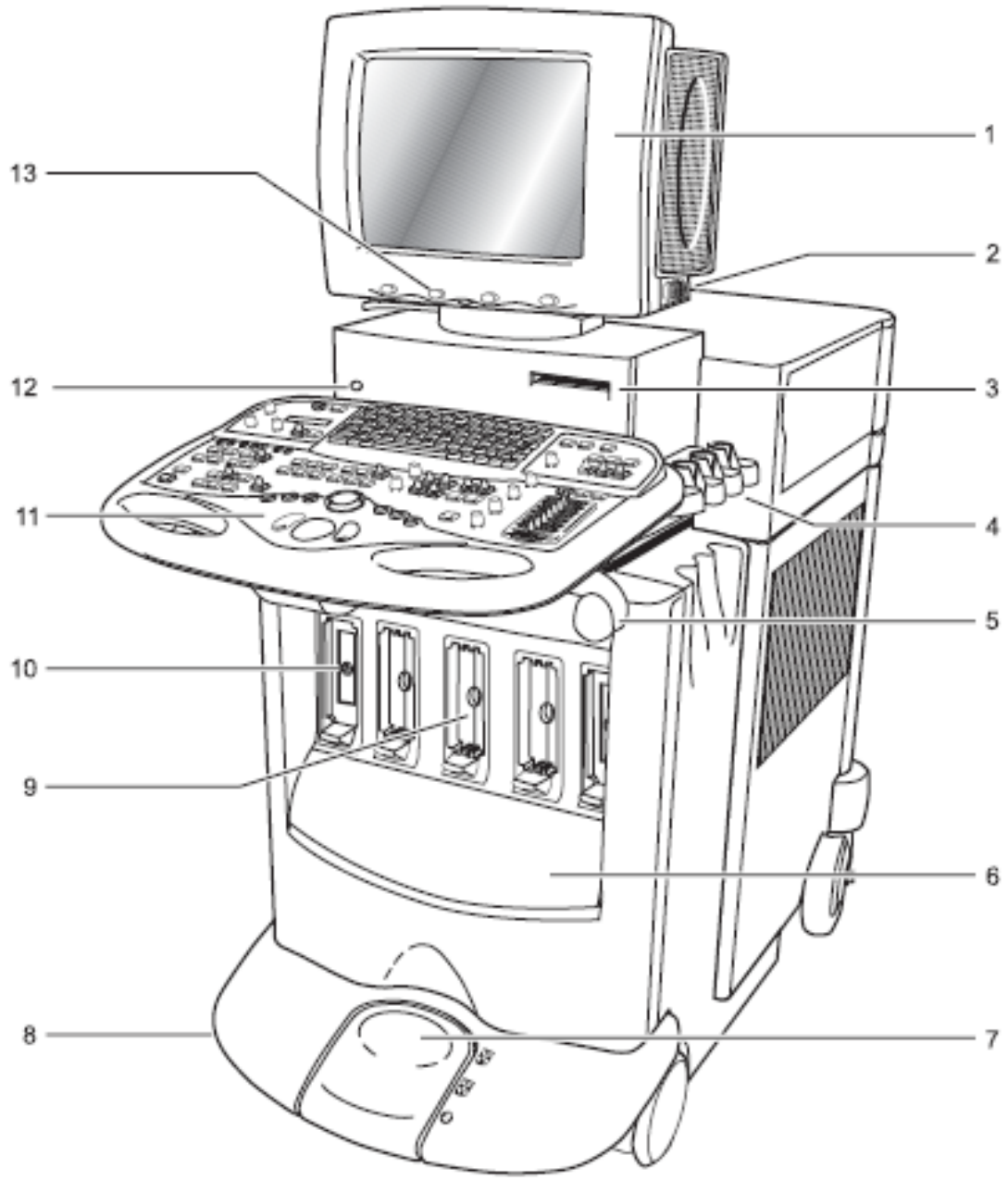

Figure AI.3 Sequoia System Components with cathode ray tube monitor

1. Monitor and Speakers
2. Monitor Controls
3. MO Disk Drive

4. Transducer Holders
5. Cable Holder
6. Storage Compartment
7. Wheel Lock/Steering Controller
8. Footswitch Connector
9. MP Transducer Ports
10. MP Storage Port
11. Control Panel/Keyboard
12. Power Button
13. Soft Keys (4)

AI.3. IMAGING MODES

The Sequoia system displays ultrasound information in several imaging modes. The modes available to depend on the options installed on your system and the transducer that you are using.

Table AI.1: Description of Imaging Modes

Mode	Description
2-d mode	The system displays a two-dimensional image of the tissues that lie within the scan plane. For example, you can use 2-D imaging mode to observe organs such as the heart and peripheral vasculature. Because the system displays 2-D images in real-time, you can observe organs in motion.
Spectral doppler mode	Spectral Doppler capabilities allow you to monitor the flow of blood through vessels or within the heart. You can display Doppler information either by itself or simultaneously with the 2-D image.
Color doppler imaging mode	Color Doppler imaging allows real-time spatial visualization of blood flow patterns in the heart and discrete vessels. It also provides Doppler shift information related to moving cardiac tissue. There are several imaging options you can use within Color Doppler mode. See Chapter 10 for more information on Color Doppler Mode. Subsequent chapters provide details about different Color Doppler options.

High frame rate tissue Doppler	High frame rate Tissue Doppler (HTD)
M-mode	In M-mode the system displays a graphic representation of a line of interest (within the 2-D image) and displays a graph that shows how that line changes over time. Use M-mode to document cardiac function and precisely measure chamber dimensions. See Chapter 16 for more information on M-mode.
Color m-mode	Color M-mode displays M-mode together with Color Doppler mode. Color M-mode displays timing information from the Color Doppler display, and supports the display characteristics and features of standard M-mode.

AI.4. TRANSDUCER CONNECTIONS

The Sequoia system is configured with three active MP transducer ports. You must use transducers that are compatible with the connectors on your system. Two of these ports are high-density (one on the left and one on the right). This configuration allows the connection of two highdensity transducers at once. When using the left high-density port, the middle port must be empty. The following table shows valid transducer combinations:

Table AI.2: Transducer Connections

Left port	Middle port	Right port
Non-high density	Non-high density	Any
High Density	None	Any

To connect a transducer to the system:

1. Insert the transducer connector into one of the active transducer ports. Insert MP transducers with the cable up. The sliding doors that cover the MP transducer port open automatically.
2. Rotate the transducer lock handle clockwise to lock the transducer connector in place.

To disconnect a transducer from the system:

1. Rotate the transducer lock handle counterclockwise to unlock the transducer.
2. Pull the transducer connector away from the port.
3. Properly store the transducer.

AI.5 CHANGING TRANSDUCER FREQUENCY

In 2-D imaging mode, Native Tissue Harmonic Imaging (NTHI) mode, PW Doppler, Color Doppler (CD) imaging mode, M-mode, and Color M-mode, the MultiHertz multiple frequency imaging feature extends the usefulness of several transducers by enabling them to operate at multiple, independent imaging frequencies. This capability on a single transducer provides better 2-D resolution at higher frequencies and better 2-D and CD penetration at lower frequencies. In addition, the lower frequencies provide increased CD velocity scales to reduce aliasing.

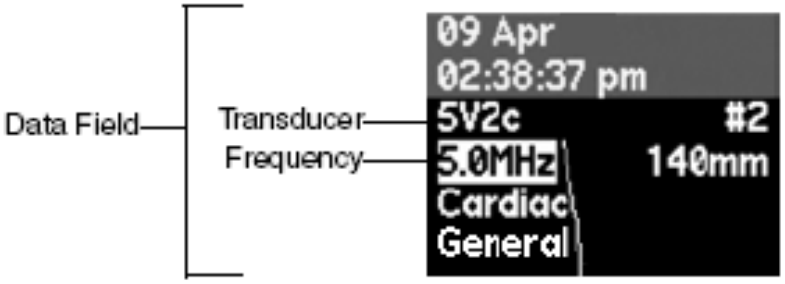

Figure AI.4 Transducer Frequency Selection

AI.6. CHANGING THE TRANSDUCER OUTPUT POWER LEVEL

To change the imaging frequency, toggle MULTIHZ.

Currently within the United States, the FDA has established guideline ultrasound power limits for various clinical applications. Within the United States, manufacturers may not market diagnostic equipment for routine clinical use in a particular application if it exceeds the relevant guideline levels. For more information about power limits, guideline levels, and power values provided by specific transducers. The Exam Preset that you are using determines the default power level.

To change the output power level for the active transducer, turn the power knob clockwise to increase the power level or counterclockwise to decrease the power level.

The current power level always appears in the Output Display monitor, on the keyboard. See “Output Display”, next. You can set up the system to also display the power level on the screen.

AI.7. OUTPUT DISPLAY

The Sequoia system includes a built-in Output Display system that lets you monitor acoustic output levels for the active transducer and imaging modes during an exam. The Output Display provides an indication of the potential for bio-effects that might be caused by the ultrasound energy being emitted. With this information, you can better control the diagnostic ultrasound equipment and examination to ensure that needed diagnostic information is obtained with minimum risk to the patient. The Output Display system provides the following output measurements:

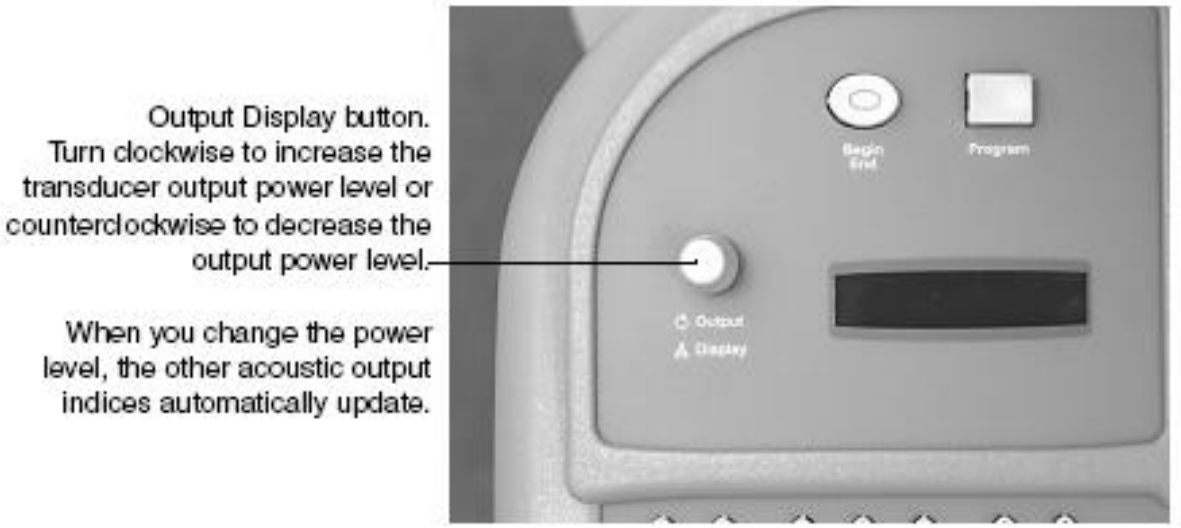

Figure AI.5 Power Output Level

Table AI.3: Output Measurements

Abbreviation	Measurement	Description
Mi	Mechanical Index	If there is more than one active imaging mode, the system displays the highest MI and adds an indicator to show which mode it is from.

Indicator	Mode
MI2d	2-D
MImm	M-Mode
MIcd	Color Doppler
MIpw	Pulsed Wave Spectral Doppler
MIcw	Continuous Wave or Auxiliary Continuous

			Wave Spectral Doppler
Tic	Thermal Index, Bone at Surface	Recommended for adult or neonatal cephalic scanning.	
Tib	Thermal Index, Bone at Focus.	Recommended for second and third trimester fetal scanning	
Tis	Thermal Index, Soft Tissue at Surface	Recommended for soft-tissue scanning; may also be used for second and third trimester fetal scanning depending on position of fetus.	
Tisf	Thermal Index, Soft Tissue at Focus	Indicates focal region TIS for M-mode, Pulsed Wave Doppler, and Continuous Wave Doppler modes.	

AI.8. SETTING UP THE OUTPUT DISPLAY

To set up the Output Display, press SETUP and select OUTPUT from the Setup menu.

1. For 2-D mode, select the transducer power value or None to display in the first column. MI appears in the third column.
2. For M-mode, Color M-mode, Color Doppler, and Spectral Doppler modes, select the output value for each column.
3. Press EXIT to return to the imaging screen.

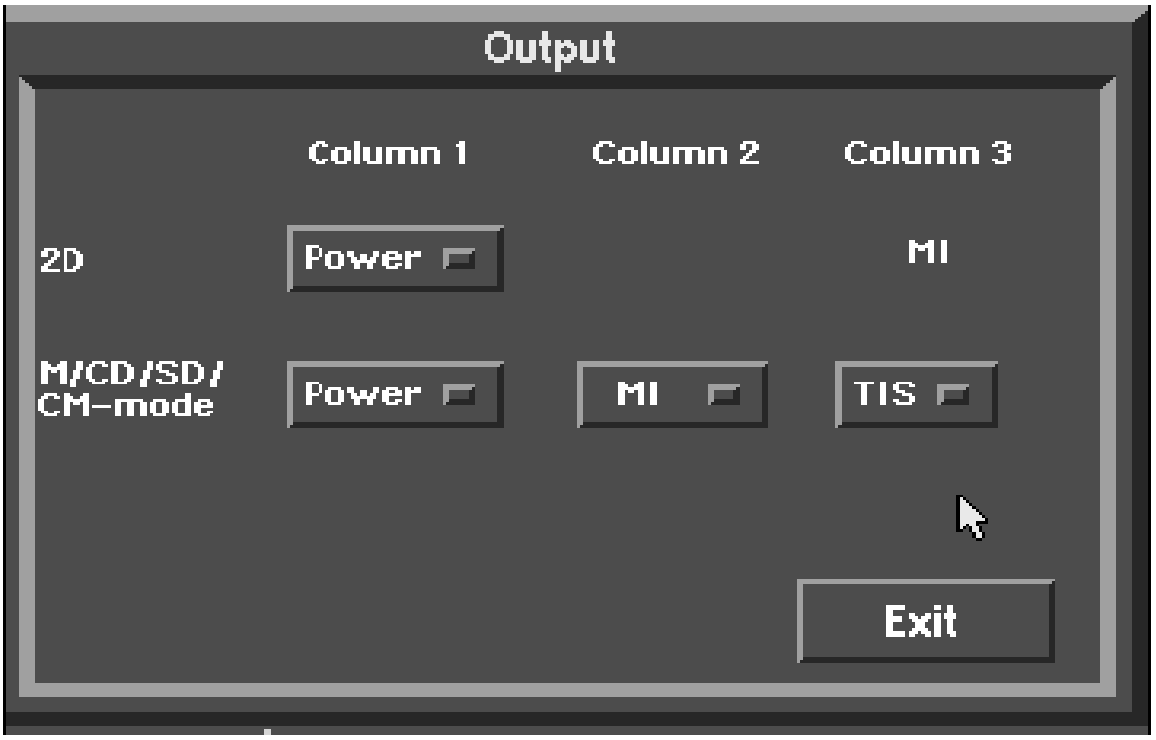

Figure AI.6 Operating Controls That Can Cause a Change in Radiated Field

Table AI.4: Output Modes

Mode	Control
B-mode	Transmit Power, Gain, Depth, Dynamic Range, Transmit Focus location, Transmit Focus number, RES, MultiHertz, SpaceTime, Edge, DELTA, Color DELTA, DGC, Frame Rate, Update, Trigger
M-mode	Transmit Power, Gain, Depth, Dynamic Range, Transmit Focus location, Transmit Focus number, RES, MultiHertz, SpaceTime, Edge, DELTA, Color DELTA, Frame Rate, Update, Trigger
Color Doppler	Transmit Power, Gain, Depth, Dynamic Range, Transmit Focus location, RES, MultiHertz, SpaceTime, Edge, Gate, Filter, Scale, Options, Frame Rate, Update, Trigger
Spectral Doppler (PWD, CWD)	Transmit Power, Gain, Depth, Dynamic Range, Transmit Focus location, RES, Edge, Gate, Scale, Doppler type, Frame Rate, Update, Trigger

AI.9. SYSTEM CONTROLS

This section explains basic techniques for using the keyboard and controls.

Keyboards

The controls on the keyboard are grouped by function to make it easier for you to find the control you need.

Code Keys

To access some functions that appear in black on an alphanumeric key, press the CODE key and then press the alphanumeric function key. There are two CODE keys, one at each side of the alphanumeric function keypad. When this guide describes how to use a function that requires you to press the CODE key, it instructs you to press CODE + the alphanumeric key. For example, press CODE + DATA POS.

Soft Keys

The four unlabeled keys immediately below the screen are soft keys. They correspond to soft key menus that appear at the bottom of the screen. The labels and functions of the soft keys change depending on the function you are using. To select a menu option, press the corresponding soft key. When there are no options to select, no soft key menu is displayed. This manual displays soft keys in brackets, for example: [MODIFY].

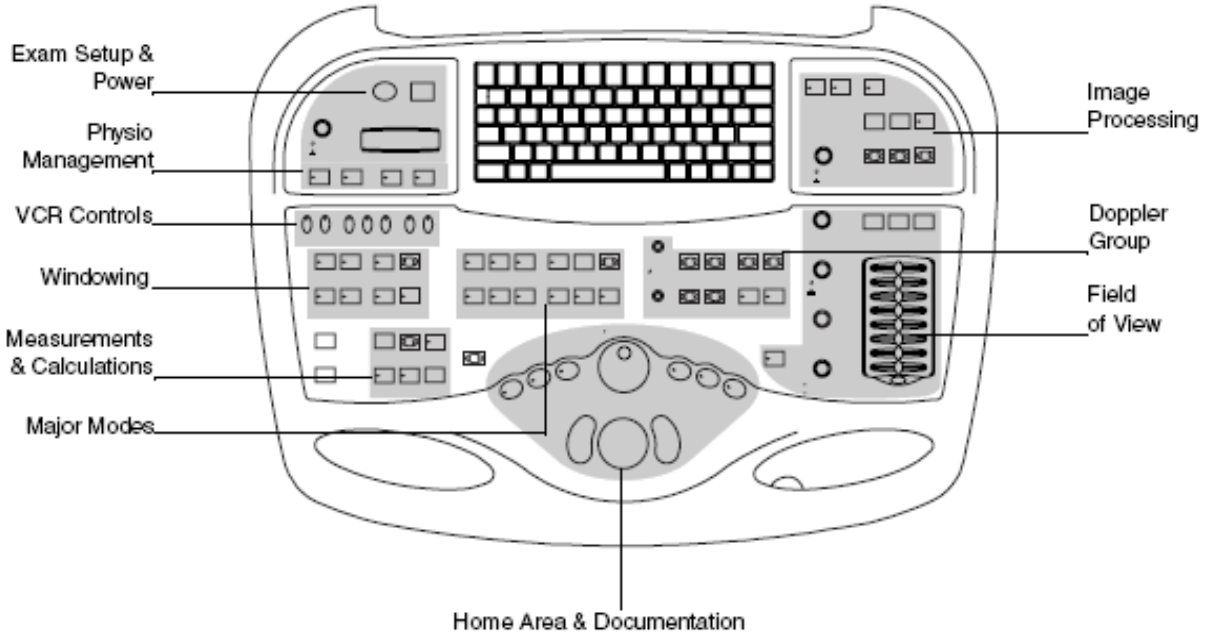

Figure AI.7 Keyboard Controls

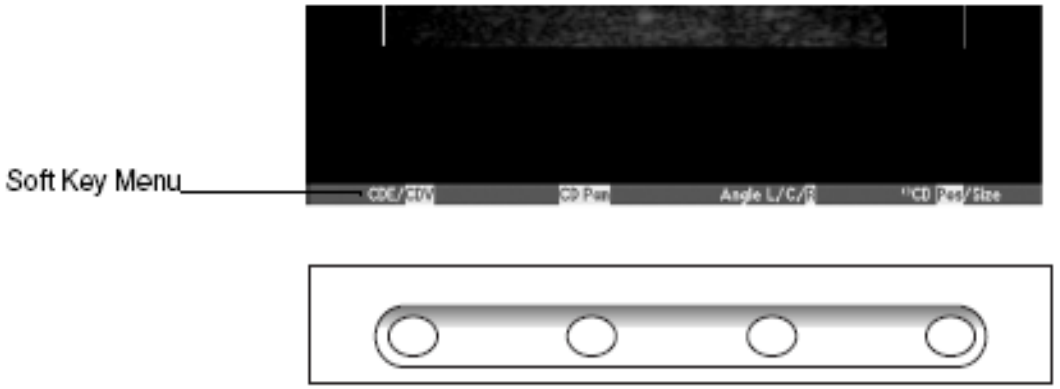

Figure AI.8 Soft Keys

There are two types of toggling soft keys:

• One type toggles between two or more options in the soft key label. Press the soft key until the option you want is highlighted.

• The other type of soft key displays only the active option. Press the soft key until the one you want appears. In most cases, you can remove a soft key menu by pressing RETURN.

Trackball

You use the trackball to move a pointer and other objects on the display. Roll the trackball in the direction that you want to move the pointer.

To change the trackball's function, toggle PRIORITY until the function you want is active.

Select Keys

The SELECT KEYS on either side of the trackball are like mouse buttons. You click them to select objects, choose items from menus, and so on. You can also double click (click quickly twice) to access other functions.

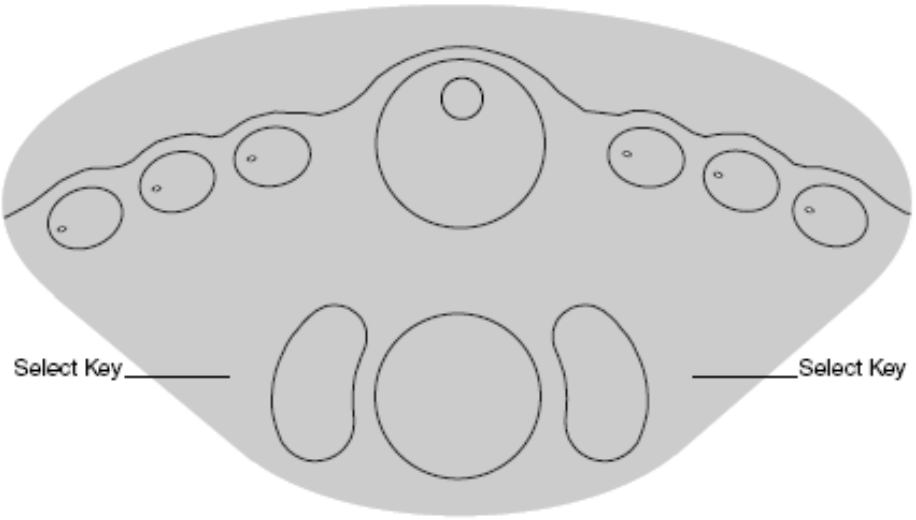

Figure AI.9 Trackball

When you see the single-click icon (()) in a soft key label (for example, [()END TRACE]), you can select that menu item by clicking either SELECT KEY once. If you see the double click icon ((())), you can select that item by quickly clicking either SELECT KEY twice.

Pop-up Menus

Some functions display a pop-up menu that contains a list of choices. Unlike toggling soft keys, a highlighted item is only active when it is selected.

Table AI.5: Pop-Up Menu List

Control	Use
Trackball	Roll up or down until the item you want is highlighted.
[Select]	Press to select the item and remove the menu.
[Hide menu] return	Press either key to remove a menu without choosing an item. Or, press the key that activated the menu.

Dialog Boxes

Dialog boxes contain pop-up menus, option buttons, and command buttons that you use to customize a function.

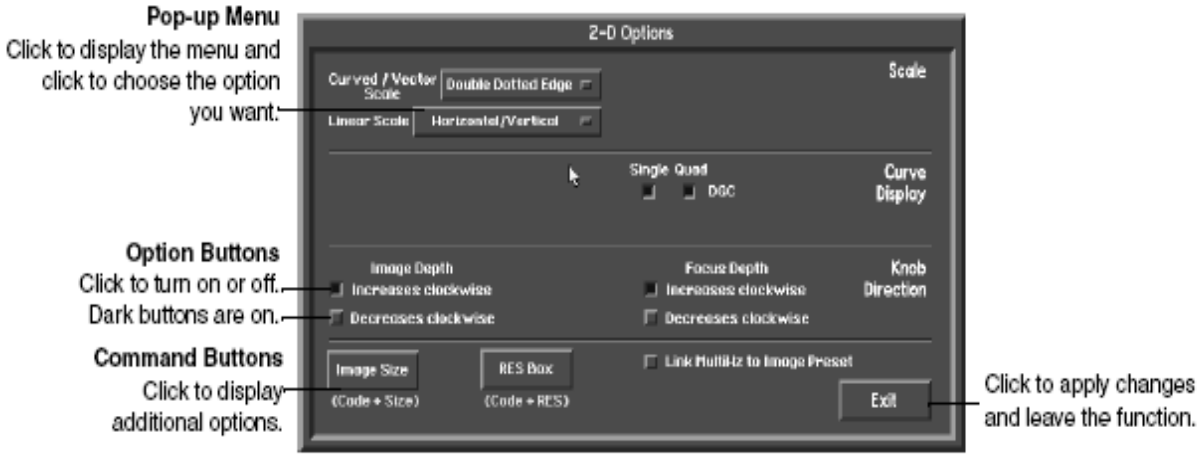

Figure AI.10 Popup menu

AI.10. MOVING THE DATA DISPLAY BOX

The system uses a data display box to display on-screen information from measurements and calculations. You can move the data display box, and save its location.

To move the data display box, press CODE + DATA POS.

1. Use the trackball to move the box to the desired location or press the first soft key to cycle quickly between five different preset locations and growth directions.
2. To choose the number of lines of information to be displayed, press [8 LINES/12 LINES] to select either 8 or 12 lines.
3. To lock the data display box into place, press [SET POSITION].
4. To exit, press [EXIT].

AI.11. EDITING TEXT

There are two different formats for entering text with the alphanumeric keys on the Sequoia system.

• Text fields that you can edit appear shaded. Text fields appear in dialog boxes, several reports, and the Begin-End page.

• In the annotation function, you can make notes directly on an ultrasound image. Use these controls for editing text. Chapter 6 describes additional controls for annotating images.

Table AI.6: Text editing

Control	Use
Cursor	Shows the current type-in point. This is where any text that you type appears.
Space bar	Press to move the cursor to the right within a text field.
Return tab	Press or use the trackball to move the cursor between text fields or to the next line.
Home	Moves the cursor to its home position, usually the upper-left corner of the display or upper-most text field.
Backspace	Press to erase the character before the cursor.
Code + caps lock	Press to switch between typing uppercase or lowercase letters. The system default is uppercase.
Shift	Hold down while pressing an alphanumeric key to override the CAPS LOCK setting for that keystroke.
[Delete]	Press to delete the current value in a report field and replace it with the default value.

AI.10. USING THE SYSTEM STOP WATCH

You can use the stop watch function to time events during any live imaging mode. Upon starting the stop watch, the start time and an elapsed timer are displayed in the data display box as shown.

Entering Cine or Freeze modes changes the time stamp display as shown.

The elapsed timer continues counting but is now displayed below the stop watch stop time. The elapsed timer is always highlighted.

To start the stop watch, press STOP WATCH.

1. Use the following soft keys with the stop watch.

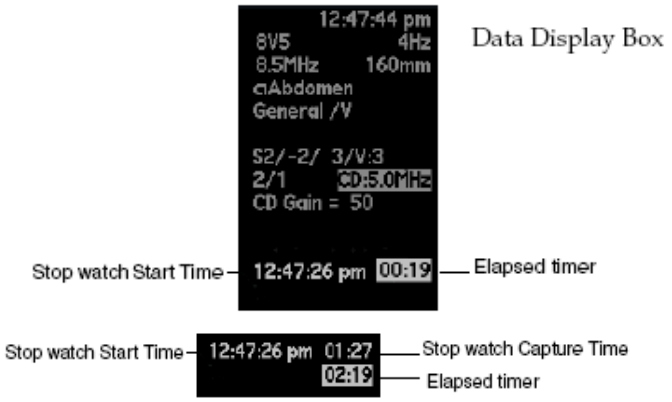

Figure AI.11 Stop watch

Table AI.7: Stop watch key functions

Control	Use
[Exit]	Exits the stop watch function. Removes the time stamp and stop watch soft key menu.
[Reset]	Resets the elapsed time field to 00:00 and removes the time stamp.
[Start timer]	Starts the stop watch and displays a time stamp that shows the system time when started and the elapsed time. While the elapsed timer is counting, this soft key label changes to [STOP TIMER].
[Stop timer]	Stops timing and leaves the time stamp on the screen. While the elapsed timer is stopped, the soft key label changes to [START TIMER].
Freeze and cine	Freezes the image display and displays the elapsed timer if the stop watch was running upon entering Cine or Freeze. When frozen, scroll through the captured frames to replay the time stamp as it was captured with the image. Press GAIN/FRZ/RUN or CINE again to return to real-time imaging.

2. Press [EXIT] or STOP WATCH to leave the stop watch function.

APPENDIX II

CARDIAC CALCULATIONS

AII.1 USES

The cardiac calculation package can be used to:

• Take measurements and perform standard cardiac calculations.

• Store the measurements and calculations on your system.

• View and print reports with the results of these studies. Cardiac calculation pop-up menus are divided into two sections. The top, gray section displays a hierarchical navigation history. The bottom section displays a sub-menu of choices that are one hierarchical level below the last item in the navigation history.

• Study

• Category

• Cluster

• Measurement

The cardiac calculation pop-up menu displays submenus that show a list of measurements related to each selection of Study, Cluster and Measurement combination. Each list show measurements that must be performed in the current selection combination, and related measurements in other modes of operation that must also be collected for the current study. Studies with more than one measurement listed on a pop-up menu allow the user to leap frog through the measurement list, with the next measurement starting where the first one ended until all the measurements on the list have been collected. As you navigate through the cardiac calculation pop-up menu, you select items in this order.

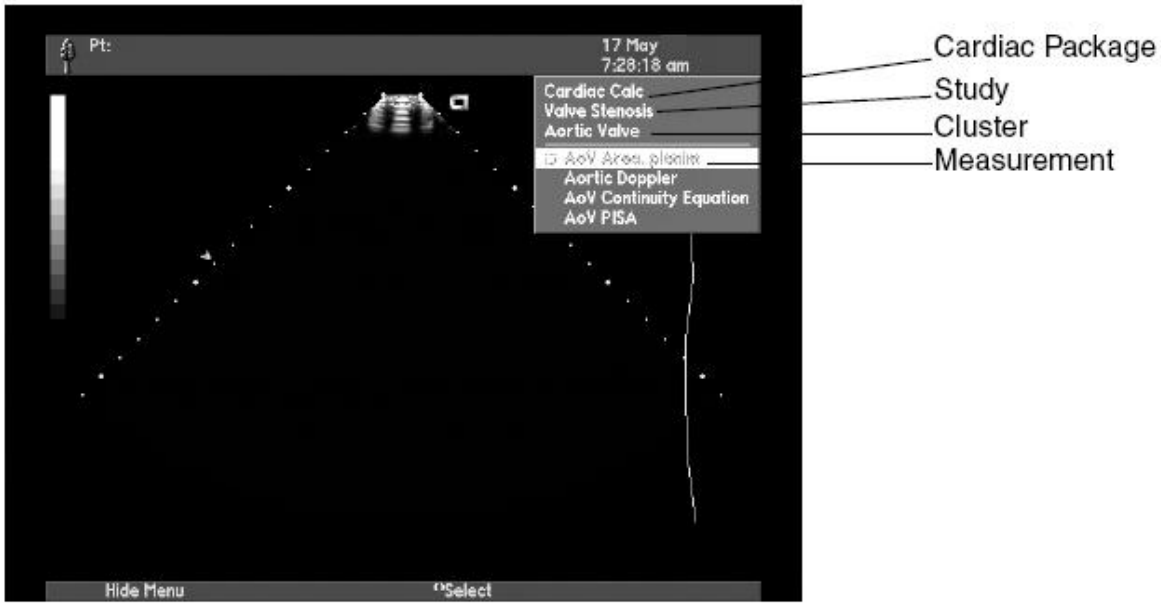

Figure AII.1. Cardiac Calculations

AII.2. ENTERING AND EXITING THE CARDIAC CALCULATION PACKAGE

You can enter and exit the calculation package at any time during a study. Calculation data is saved until you end the study. To take cardiac measurements in strip modes, you must first press FREEZE or CINE to stop the strip.

To enter the cardiac calculation package:

1. Press CALC.

2. Select the item you want from the pop-up menu. When you choose a measurement from the pop-up menu, the pop-up menu disappears, the measurement tool and soft key menu are activated, and the data display box appears.

3. Press CALC to exit the cardiac calculation package.

Types of Measurements

The following table describes the types of measurement the cardiac calculation package contains and general steps for performing the measurement.

To perform any measurement:

1. Freeze the image and enter the cardiac calculation package.

2. Follow the steps below for the type of measurement you want to take.

Table AII.1: Measurements for Cardiac Calculations

Measurement	Procedure
Distance	1 Select a distance measurement. 2 Place the first caliper on the object to be measured. 3 Press a select button to place the second caliper on the object to be measured. 4 Enter the measurement.
2-d area and volume	1 Select an area measurement. 2 Trace the outline of the area. For LV or RV volume measurements, begin the trace at one side of the annulus and end at the opposite side of the annulus. 3 End the trace.1 4 Enter the measurement.
Velocity time integral	1 Select a VTI measurement. 2 Start the trace at the beginning of the Doppler spectrum to be measured. 3 Trace the VTI of the Doppler spectrum to be measured. The tool will automatically correct to baseline if you start above or below the line. 4 End the trace.1 5 Enter the measurement. 1. You can reposition the axis by using the trackball. Be sure to end the trace after editing.
Velocity	1 Select a velocity measurement. 2 Move the caliper to the velocity you want to measure. 3 Enter the measurement.
Color Doppler velocity or PISA	1 Select a color Doppler velocity or PISA measurement. 2 Move the caliper to the origin (vena contracta) of the color Doppler jet to be measured near the orifice of the valve. 3. Press a select button to place a second caliper at the first color aliasing zone of the PISA. 4 Enter the measurement.

Table AII.2: Mitral Valve Regurgitation Study

Category	Cluster	Measurement
Mitral valve	Pulmonary Venous Flow	RUPV measurements RLPV measurements LUPV measurements LLPV measurements
	MR Volume by PISA	MR PISA Radius MR Alias Velocity MR Vmax MR VTI MV Diam MV VTI, annulus
	MR Volume by Dop/Dop	MV Prox Diam MV VTI, Annulus Site 2 Diam Site 2 VTI MR VTI
	MR Volume by 2-D/Doppler	LV Area, A4C, d & s LV Major, A4C, d & s LV Vol, A4C MOD, d & s LV Area, A2C, d & s LV Major, A2C, d & s LV Vol, A2C MOD, d & s Site 2 Diam Site 2 VTI AR VTI

APPENDIX III

ECHOCARDIOGRAPHIC TRANSDUCERS

AIII.1 10V4C TRANSDUCER

Frequency Bandwidth:	10 – 4 MHz
Compatible With:	ACUSON Sequoia™ 512 ultrasound system
Applications:	Neonatal and pediatric echocardiography

Features:

• MICROSON™ high resolution transducer

• Vector™ wide-view imaging format phased array

• User-selectable Wideband MultiHertz™ multiple frequency imaging

AIII.2 8V3C TRANSDUCER

Frequency Bandwidth:	8 – 3 MHz
Compatible With:	ACUSON Sequoia 512 ultrasound system
Applications:	Pediatric and fetal echocardiography

Features:

• Hanafy lens transducer technology

• Vector imaging format phased array

• User-selectable Wideband MultiHertz imaging.

AIII.3 4V1C TRANSDUCER

Frequency Bandwidth:	4 – 1 MHz
Compatible With:	ACUSON Sequoia 512 ultrasound system
Applications:	Contrast agent studies, coronary artery imaging, stress echo, transcranial with 12.0 and vascular option, transthoracic adult and pediatric echocardiography

Features:

• Hanafy lens transducer technology

• Vector imaging format phased array

• User-selectable Wideband MultiHertz imaging

• RF shielding

AIII.4 4V1C TRANSDUCER

Frequency Bandwidth:	4 – 1 MHz
Compatible With:	ACUSON Aspen™ ultrasound system ACUSON Sequoia 512 ultrasound system
Applications:	General and deep abdominal vascular

Features:

• Hanafy lens transducer technology

• Vector imaging format phased array

• User-selectable Wideband MultiHertz imaging

• Excellent penetration

AIII.5 6C2 TRANSDUCER

Frequency Bandwidth:	4 – 1 MHz
Compatible With:	ACUSON Aspen ultrasound system ACUSON Sequoia 512 ultrasound system
Applications:	Abdominal vascular, fetal heart

Features:

• Curved vector imaging format

• Hanafy lens transducer technology

• Wide view phased array

• User-selectable Wideband MultiHertz imaging

AIII.6 4C1 TRANSDUCER

Frequency Bandwidth:	4 – 1 MHz
Compatible With:	ACUSON Sequoia 512 ultrasound system ACUSON Aspen ultrasound system
Applications:	Abdominal vascular, fetal heart, technically difficult and typical patients

Features:

• Curved vector imaging format

• Hanafy lens transducer technology

• Wide view phased array

• User-selectable Wideband MultiHertz imaging

• Excellent penetration

AIII.7 17L5 HD TRANSDUCER

Frequency Bandwidth:	17–5 MHz
Compatible With:	ACUSON Sequoia 512 ultrasound system
Applications:	Contrast agent imaging, superficial vascular

Features:

• Hanafy lens transducer technology

• Patented ergonomic design with Elastogrip™ ergonomic grip coating

• Linear and Vector wide-view imaging format

• User-selectable Wideband MultiHertz imaging

AIII.8 15L8W TRANSDUCER

Frequency Bandwidth:	15–8 MHz
Compatible With:	ACUSON Sequoia 512 ultrasound system
Applications:	Superficial vascular

Features:

• MICROSON imaging

• Hanafy lens transducer technology

• User-selectable Wideband MultiHertz imaging

• Extra long cable

AIII.9 9L4 TRANSDUCER

Frequency Bandwidth:	9–4 MHz
Compatible With:	ACUSON Sequoia 512 ultrasound system
Applications:	Cerebrovascular, contrast agent imaging, peripheral vascular, superficial vascular

Features:

• 1.25 Multi-D array

• Multi-D™ matrix array transducer technology

• Linear and Vector wide-view imaging format

• Triplex imaging

• User-selectable Wideband MultiHertz imaging

AIII.10 8L5 TRANSDUCER

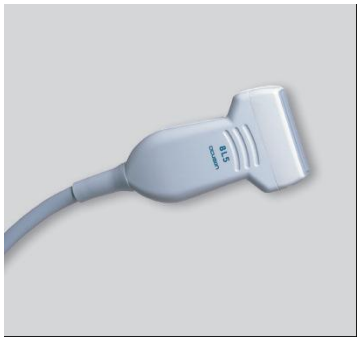

Frequency Bandwidth:	9–4 MHz
Compatible With:	ACUSON Sequoia 512 ultrasound system
Applications:	Cerebrovascular, contrast agent imaging, peripheral vascular, superficial vascular

Features:

• User-selectable Wideband MultiHertz imaging

AIII.11 6L3 TRANSDUCER

Frequency Bandwidth:	6–3 MHz
Compatible With:	ACUSON Sequoia C256 echocardiography system ACUSON Sequoia 512 ultrasound system
Applications:	Extracranial vascular, medium and deep arterial and venous studies, peripheral vascular

Features:

• User-selectable Wideband Multi Hertz imaging

AIII.12 V7M TRANSDUCER

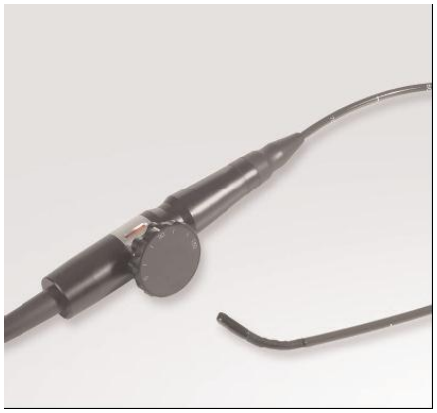

Frequency Bandwidth:	8–3 MHz
Compatible With:	ACUSON Sequoia C256 echocardiography system ACUSON Sequoia 512 ultrasound system
Applications:	Pediatric and adult transesophageal mini-multi-plane echocardiography

Features:

• Endoscope dimensions: diameter = 7.0, length = 70 cm, patient weight = 3.5 kgs and above

• Small tip size for increased patient comfort: width = 10.9 mm, thickness = 8.0 mm, circumference = 22 mm

• Ergonomic design featuring one-hand control

• Manual rotation: -10° – 190°

• Vector imaging format phased array

• User-selectable Wideband MultiHertz imaging

• DTI™ Doppler tissue imaging capability

AIII.13 V5MS TRANSDUCER

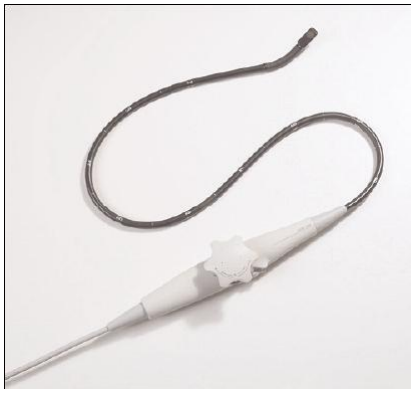

Frequency Bandwidth:	7–3 MHz
Compatible With:	ACUSON Sequoia C256 echocardiography system ACUSON CV70™ cardiovascular system ACUSON Cypress™ cardiovascular system ACUSON Aspen ultrasound system ACUSON 128XP/10C™ echocardiography system ACUSON Sequoia 512 ultrasound system
Applications:	Transesophageal multiplane echocardiography

Features:

• Endoscope diameter = 10.5, length = 110 cm

• Adult tip size: width = 14.5, height = 11.5

• Ergonomic design featuring one-hand control with variable speed rotation – 90° per sec.

• RF shielding

• Vector imaging format phased array

• User-selectable Wideband MultiHertz imaging

• DTI capability

• *syngo*® *four*Sight™ TEE view

• *syngo*® Mitral Valve Assessment (MVA)

AIII.14 ACUNAV 8F

Frequency Bandwidth:	2–10 MHz
Compatible With:	ACUSON Sequoia C256 echocardiography system ACUSON CV70 cardiovascular system ACUSON Cypress cardiovascular system ACUSON Sequoia 512 ultrasound system
Applications:	Adult intracardiac echocardiography

Features:

• 8 french catheter (2.7 mm diameter)

• 110 cm insertable length

• Sterile, single-use advanced miniaturization AcuNav ultrasound catheter family

• Reusable SwiftLink™ catheter connector

• Four-way steering in two planes: 160° in each direction

• Logitudianal side-fire imaging

• Vector imaging format phased array

• DTI capability

AIII.15 Aux CW

Frequency Bandwidth:	2 MHz
Compatible With:	ACUSON Sequoia C256 echocardiography platform ACUSON Aspen echocardiography platform ACUSON Aspen ultrasound platform ACUSON Sequoia 512 ultrasound system
Applications:	Non-imaging, transthoracic adult and pediatric, continuous wave spectral Doppler echocardiography

Features:

• Continuous wave spectral Doppler mode

• Excellent intercostal, suprasteral and subcostal access

• Excellent penetration